Spring 1-1-2017

Impact of High-Latitude Ionospheric E Region Enhancements on Global Positioning System Scintillations in the Alaskan Sector

Diana C. Loucks
University of Colorado at Boulder, loucksd@colorado.edu

Impact of High-latitude Ionospheric E Region Enhancements on Global Positioning System Scintillations in the Alaskan Sector

by

Diana C. Loucks

B.S., Texas Christian University, 1996

M.S., University of Colorado, 2008

A thesis submitted to the

Faculty of the Graduate School of the

University of Colorado in partial fulfillment

of the requirements for the degree of

Doctor of Philosophy

Department of Aerospace Engineering Sciences

2017

This thesis entitled:
Impact of High-latitude Ionospheric E Region Enhancements on Global Positioning System Scintillations in the Alaskan Sector
written by Diana C. Loucks
has been approved for the Department of Aerospace Engineering Sciences

_____
Prof. Scott Palo

_____
Dr. Marcin Pilinski

_____
Prof. Delores Knipp

Date _____

The final copy of this thesis has been examined by the signatories, and we find that both the content and the form meet acceptable presentation standards of scholarly work in the above mentioned discipline.

Loucks, Diana C. (Ph.D., Aerospace Engineering Sciences)

Impact of High-latitude Ionospheric E Region Enhancements on Global Positioning System Scintillations in the Alaskan Sector

Thesis directed by Prof. Scott Palo

A reduction in Arctic sea ice extent is driving an increase in Arctic Circle ship traffic and a requirement for communications in the region. High-latitude ionospheric behavior can significantly impact Ultra High Frequency (UHF) transmissions including degradation of Global Positioning System (GPS) position solutions. To address these operational concerns, a need arises to identify and understand the ionospheric structures that lead to disturbed conditions in Arctic latitudes. This research focuses on determining those structures that occur within the Alaskan high-latitude sector, and comparing their local relative importance to that across the broader northern high-latitudes. The goal is to identify correlative features between GPS scintillation, electron densities and their gradients, as seen by ground GPS receivers in Alaska and the Poker Flat Incoherent Scatter Radar (PFISR), as well as other instruments and models available for context.

Several case studies are examined, specifically global and local geomagnetically disturbed times that allow for the isolation of ionospheric sources associated with GPS scintillation. Upon determination of known scintillating E and F region structures, the relative importance of each is compared in terms of the frequency, duration, and extent of operational impact. These results are compared across the broader high-latitude region to gain insight into the timing and location of physical mechanisms that drive GPS scintillations in the Arctic. Analysis indicates that E region auroral activity is the primary driver in Alaska. This differs from the Arctic European sector where F region auroral blobs structured by precipitating particles have been reported as the primary causal structures. Geomagnetic conditions vary greatly across the Arctic, so differences between sectors is not surprising. While further modeling and studies are required to understand why the differences exist, the observed differences themselves give observational insight into potential

causes. The uniqueness of this work lies in the use of a predictive conjunction analysis between the PFISR beam array and known GPS satellite signal paths to determine experiment times and both single and multi-beam experiment configurations. This is coupled with all sky imagery for broader contextual interpretation; and, the approach can be transitioned to future work conducted across other high-latitude sectors.

Dedication

To my beloved husband Gary, our late pup and forever navigator Max, and our inqisitive and playful Beagles Ruby and Leo. You are forever my calming force and my inspiration. $T = HB^2$!

Acknowledgements

Remember those who led you, who spoke the word of God to you; and considering the result of their conduct, imitate their faith - Hebrews 13:7

I would like to thank my primary advisory team, Professor Scott Palo and Doctor Marcin Pilinski, who spent countless hours guiding me, and allowed me great latitude in the directions associated with my research (University of Colorado and NSF Grant PLR-#1543446). I would also like to thank Doctor Geoff Crowley, along with the employees of Atmospheric & Space Technology Research Associates LLC, who provided scientific and technical guidance as well as GPS CASES observations data. ASTRA staff were supported by NSF Grant PLR #1243225. Thank you also to my committee members Professors Jeffrey Thayer, Delores Knipp, Kristine Larson and Dmitri Uzdensky for all of your insight and guidance, as well as to the Colorado Center for Astrodynamics Research, University of Colorado, Boulder for facilities and on-site support.

Thank you to the Primary Investigators of Poker Flat Research Range. Doctors Mike Nicolls and Roger Varney (SRI International) provided countless hours of experiment support to include design assistance and data processing for PFISR experiments. PFISR is operated on behalf of the US National Science Foundation under NSF Cooperative Agreement AGS-1133009 (data resides in the Open Madrigal Web: `http://cedar.openmadrigal.org/`). Dr. Don Hampton, Geophysical Institute, provided optical imagery support including assistance with processing and interpretation.

A special thanks to my husband, Gary, to our pups Max, Leo and Ruby, to my family and friends, and to the many mentors I have been blessed with over the years. You were especially patient with me as I struck out on this adventure and I could not have done it without you.

Contents

Chapter

Tables

Table

Figures

Figure

Chapter 1

Introduction

1.1 Research Motivation

Over the course of one year, the Arctic sea ice extent currently varies from as much as sixteen million square kilometers in the winter, to under seven million square kilometers in summer. This variation at the extremes of nine million square kilometers opens up over two and a half million square nautical miles of trafficable ocean. A trip across the Atlantic or Pacific Oceans that takes one to two weeks can be significantly reduced by transiting the Arctic Ocean. This diminishes the associated costs for both commercial and government entities by opening access to the northernmost sea ports. For reference, the extremes of the 2016 sea ice extent from the months

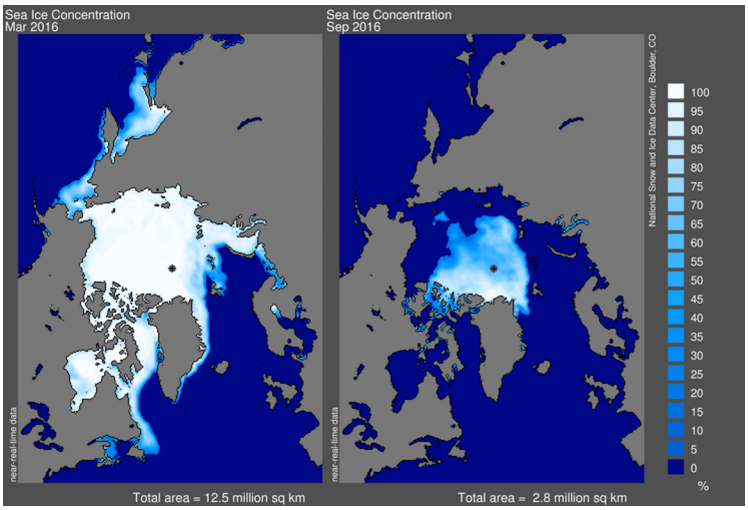

Figure 1.1: 2016 sea ice extent extremes during the Months of (a) March and (b) September. Source: `https://nsidc.org/`.

of March (maximum extent) and September (minimum extent) are shown in Figure 1.1 (*NSIDC*, 2016). Note that there are open channels of transit through the Canadian archipelago and along the Russian coast.

Today a handful of countries own, operate and maintain Global Navigation Satellite Systems (GNSS) that provide location and timing services to commercial and military users world-wide, including the Arctic (*Misra and Enge*, 2006). GNSS are used in a number of commercial and scientific applications including precision landing and navigation, GNSS-based plate-tectonics and, particular to this work, GNSS-based ionospheric research (*Davis*, 1996). GNSS systems include Galileo (European), GLONASS (Russian) and BeiDou (Chinese) (*Misra and Enge*, 2006). The US-based Global Positioning System (GPS), which is one of the current GNSS systems, provides navigation and timing solutions to users world wide and is the subject of the research. Within the same frequency band as GPS exist both government and civilian communications systems that support these users (*Matassa*, 2011). Iridium and INMARSAT are both UHF commercial communications systems that provide satellite based cellular services including voice, text and data. Ultra High Frequency (UHF) Follow-On (UFO) is a legacy Department of Defense (DoD) satellite constellation providing mobile UHF wide and narrow-band communications services, especially to users over the ocean. Mobile User Objective System (MUOS) is DoD's successor program to UFO. Each of these and their relative frequencies to GPS are shown in Figure 1.2. According to the Office of the Undersecretary of Defense for Policy, a secure and navigable Arctic is essential to United States security and defense operations in the region:

> ...vast distances, obsolete or deteriorating polar communications architecture, limitations of geostationary communication satellites, harsh weather conditions, high-latitude ionic disturbances, and geomagnetic storms (space weather) combine to make reliable, secure communications in the Arctic difficult.

Because of this the DoD will continue to update systems which are '...essential for Arctic operations.' This includes GPS, which an suffer radio signal degradation caused by the space environment. Much current research focuses on helping military and civil users understand, predict and mitigate environmentally-caused signal loss.

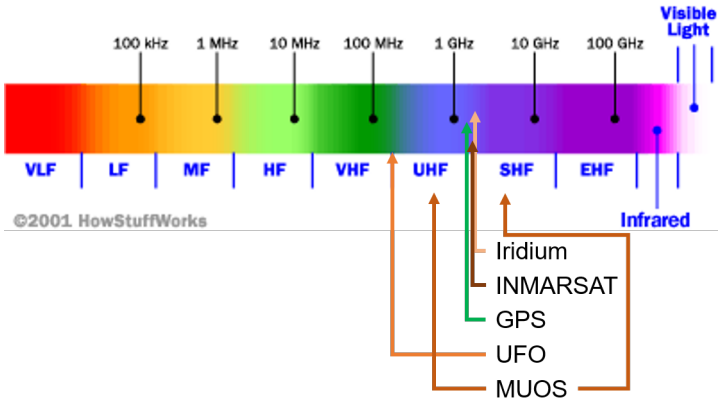

Figure 1.2: Relative frequencies of several civilian and military satellite systems including GPS. These are overlaid onto a snapshot of the electromagnetic spectrum for reference. Source: `http://electronics.howstuffworks.com/radio-spectrum.htm`.

1.2 Scintillation Science: The History of a Debate

For over a half century, scientists and engineers have known that space-based signals are disturbed prior to their arrival at ground-based receivers. Initial observations reported by *Hey et al.* (1946) of fluctuations in signals from the Cygnus constellation, followed with observations by *Smith* (1950) excluding the possibility of these fluctuations emanating from the source due to a lack of correlation over large distances, led to the conclusion they must be caused by Earth's atmosphere. Additionally, *Briggs et al.* (1950) observed diffraction ground patterns produced from radio waves reflected off of an irregular ionosphere. In the same paper, they pointed out that the velocities associated with those irregularities could be measured using appropriately spaced and oriented ground receivers. *Booker et al.* (1950) proposed the theory of *diffraction by a random screen* as a way to model the source of the fading observed in signals reflected from the ionosphere, and *Hewish* (1951) proposed a similar theory as it applied to signals from radio stars. Over the next several decades, efforts were put towards advancing the diffraction screen theory in multiple situations by many including *Ratcliffe* (1956), *Salpeter* (1967) and *Buckley and Road* (1975). *Booker* (1958) noted that the scale sizes associated with ionospheric irregularities and scintillation were determined to be approximately a kilometer for amplitude scintillation, and that scintillation was most notable

parallel to Earth's magnetic field. The linkage of scintillation to the changes in electron density (ΔN_e) along the signal path was formalized by *Yeh and Liu* (1982).

The advent of GPS in the late 1970s and 1980s, especially with the disabling of *selective availability* in 2000,[1] provided the scientific community a publically accessible, highly controlled and constantly transmitting signal, that could be used for furthering our understanding of Earth's ionosphere.[2] Consistent with historical observations from radio stars, one of the greatest error sources for GPS signals comes from transiting Earth's ionosphere (*Kintner and Ledvina*, 2005; *Misra and Enge*, 2006). These errors can range from meters to tens of meters in position if left uncorrected (*Kintner and Ledvina*, 2005).[3] Early scintillation research focused on the densely populated low- and mid-latitudes (*Basu et al.*, 1980; *Basu and Basu*, 1981, 1985; *Beach*, 1998; *Beniguel et al.*, 2011; *Ghafoori and Skone*, 2015; *Joshi et al.*, 2015; *Ledvina et al.*, 2004; *Kintner*, 2004; *Kintner et al.*, 2007; *Kumar and Singh*, 2012; *Psiaki et al.*, 2008; *Rama Rao et al.*, 2006; *Warnant and Pottiaux*, 2000). At low-latitudes ionospheric irregularities linked to electron density gradients in plasma depletions are known to be the primary source of GPS scintillation (*Basu et al.*, 2002; *Kintner et al.*, 2007; *Sridhar et al.*, 2014). At mid-latitudes during heightened solar and geomagnetic activity *subauroral ion drifts (SAID)* can be an electron density gradient source for scintillation (*Kintner et al.*, 2007; *Ledvina et al.*, 2004). In the low and mid-latitudes scintillation most often appears in the form of either amplitude scintillation (measured with the S_4 index) or phase scintillation (measured with the phase scintillation index or σ_ϕ). By contrast and as will be discussed later, scintillation in the high-latitudes appears primarily on the signal phase and much less so on its amplitude.

It is the current theory that *diffraction* and *refraction* of radio waves around and through a medium of appropriately scaled gradients in electron density cause the scintillation observed radio systems operating at or near GPS wavelengths. The morphology and climatology of plasma

[1] GPS was designed and implemented as a military application. Congress was successfully lobbied by the American public, and in 2000, *selective availability*, or the associated extra error that was introduced into the transmit signal of the publically accessible course acquisition code (C/A), was removed.

[2] Many other scientific applications using GPS signals include plate tectonics, soil moisture, snow depth, shore-line heights and sea-level changes. For more details see http://www.gps.gov/applications/.

[3] See Section 3.2.3

structures linked to high-latitude signal scintillation, and how these compare across high-latitude sectors are currently being debated. *Plasma patches* of substantially increased electron density convect across the polar cap, eventually convecting into the auroral oval where they are called *auroral blobs* (*Crowley et al.*, 2000). Since their source is dayside plasma from photoionization, these patches and blobs are located at altitudes of ∼150-400 km. Also present in the high-latitudes are the aurora: a beautiful emission display that is in part the result of energetic particle precipitation. This precipitation leads to ionization of the neutral atmosphere at ∼90-150 km altitudes, depending on particle energy. At high-latitudes phase scintillation of GPS signals has been linked to electron density gradients associated with both of these phenomena(*Aarons*, 1997; *Kintner et al.*, 2007).

One of the earliest climatology papers on high-latitude ionospheric scintillation related to GPS was published by *Aarons* (1997), who noted that '[d]ifferent regions of the [auroral] oval ... may have differing mechanisms responsible for phase and amplitude scintillation.' Since then, studies linking GPS scintillation to the ionospheric sources of electron density gradients are divided into two primary categories: those that assert ionospheric F region dominance (i.e., plasma patches and auroral blobs created by photoionization), and those that maintain that E region phenomena are paramount (i. e. , impact ionization due to energetic particle precipitation). But studies conducted over the last decade including the analyses presented in this work, and those conducted by *Clausen et al.* (2016) and *Jin et al.* (2014), have found that the location of a site relative to the auroral oval dictates the dominant ionospheric scintillation source. In the case of *Clausen et al.* (2016), satellite data was used to define the auroral oval, and a correlation analysis was run between the occurrence of increased phase scintillation and the size and location of the polar cap. In *Jin et al.* (2014), emission and phase scintillation data were compared. In both cases, the focus was on distinguishing the scintillation behavior in the polar cap and in the auroral boundary regions. Both studies found that scintillation was enhanced in convecting polar cap patches that were influenced by particle precipitation as they passed through the poleward auroral boundary.

1.3 Research Focus

The core of this work is focused on the detection and attribution of ionospheric structures that are the source of GPS scintillation over the Alaskan sector. High-latitudes, and in particular the northern Alaskan coastline, are of interest due in large part to the increase of military and commercial traffic that will occur thanks to melting sea ice extent, and also to the unique geometric orientation of this region to the networks of available GPS. The instruments and data used in this study include but are not limited to: radars, imagers, GPS receivers, contextual models, and global and regional indices to interpret the data. Specific science questions to be answered are as follows:

(1) What are the plasma structures driving UHF scintillations near GPS frequencies in the Alaskan high-latitude sector?

(2) What is the relative importance of E and F region structures in the Alaskan high-latitude sector with respect to L-band scintillation?

(3) How do the scintillating structures and their relative importance compare to those in other high-latitude sectors?

To simplify the discussion a few definitions are required. As used here, the *Alaskan sector* is defined to be the high-latitude ionosphere constrained to the geographic borders of Alaska that

(1) can be sensed by the Poker Flat Incoherent Scatter Radar (PFISR)

(2) can be transited by GPS signals, specifically those received at Poker Flat Research Range (PFRR), Fort Yukon, Toolik, Kaktovic, Eagle, and Gakona - all locations of Connected Autonomous Space Environment Sensor (CASES) GPS receivers

(3) can be imaged by all-sky imagers at these and potentially other locations.

Note that observations made during the Arctic summer (May through September), during which use of all-sky imagers is impractical, are not considered here. Second, *scintillations* are either phase or amplitude scintillations above a predetermined statistical threshold within the region. Lastly, *scintillating structures* are those plasma structures in the ionosphere that exist within the *sector* which temporally and/or spatially correlate to *scintillations* and existing global and regional environmental indices.

Each of the science questions can be further refined by the tools and data required to answer them. Climatologically the high-latitude region regularly sees phase scintillation (σ_ϕ) and rarely sees amplitude scintillation (S_4). Further it is also known that convecting blobs and particle precipitation are correlated with scintillation (*Moen et al.*, 2013; *Kintner et al.*, 2007). Chapter 4 describes the multi-instrument approach and associated analysis techniques that confirm and explain these climatological results.

Once *scintillating structures* are confirmed, their relative location and importance can be determined. Chapters 6, 7 and 8 investigate the relative importance and contribution of the E and F region ionosphere to phase scintillation. Lastly, the relative importance of Alaskan scintillating structures will be compared to those from other sectors in other high-latitudes regions. Sectors of comparable geographic and/or geomagnetic location will be considered. These include areas in Canada, northern Europe, and northern Asia. At many of these locations, similar studies are being conducted. Where there are not studies being conducted, the potential exists to apply the techniques used in this research to observational tools available in those sectors.

1.4 Document Structure

Chapter 2 presents a discussion of the broader aerospace environment, and is followed by a detailed discussion of the scintillation of radio waves and GPS signals in Chapter 3. Chapter 4 discusses observational and contextual tools used to achieve the goals of this dissertation. Two case studies are evaluated in Chapters 5 and 6. In Chapter 5, the time frame surrounding the geomagnetic storm of 17 March 2013 is discussed and analyzed. Lessons learned from this analysis lead directly to the formulation of an experiment set used to analyze the 20-21 December 2015 geomagnetic storm in Chapter 6. Chapter 7 discusses a climatology campaign conducted throughout the months of March and April 2016 using the experimental methods of Chapter 6. A second climatology campaign covering the months October and November 2016 is analyzed and discussed in Chapter 8. Chapter 9 provides a detailed review of work done across other sectors of the Arctic, and their comparison to the results from Alaska. In Chapter 10 the three science questions along with

their answers are summarized and discussed, and concluding remarks and future work are presented. Lastly, the Appendices contain a list of physical constants and acronyms (Appendices A.1 and A.2); a brief synopsis with references for the coordinate systems used in this work (Appendix B); and a list of experiments conducted with dates, times and figures (as indicated) (Appendix C).

Chapter 2

Aerospace Environment

The sun is a dynamic star that can both protect and harm the earth. It is the source of the solar wind and of the *interplanetary magnetic field (IMF)*, which serve both as Earth's shield to cosmic phenomena and a pathway for solar particles to directly access the earth via its magnetic field. Through this interaction we see the beautiful visual effect known as the aurora, as well as a degradation of transionospheric radio signals: an unwanted and potentially dangerous manifestation (*Knipp*, 2011). Understanding the core physical processes of the near-space environment is a key element for conducting the research associated with this dissertation. Presented in this chapter is a broad overview of core scientific tenants that are required to understand the interaction of transionospheric signals with the overall aerospace environment.

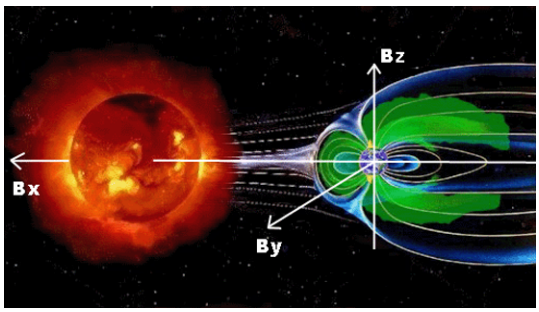

Figure 2.1: Depiction of the orientation of the Interplanetary Magnetic Field (IMF) components in the Geocentric Solar Ecliptic (GSE) coordinate system. Source: `https://www.spaceweatherlive.com/en/help/the-interplanetary-magnetic-field-imf`.

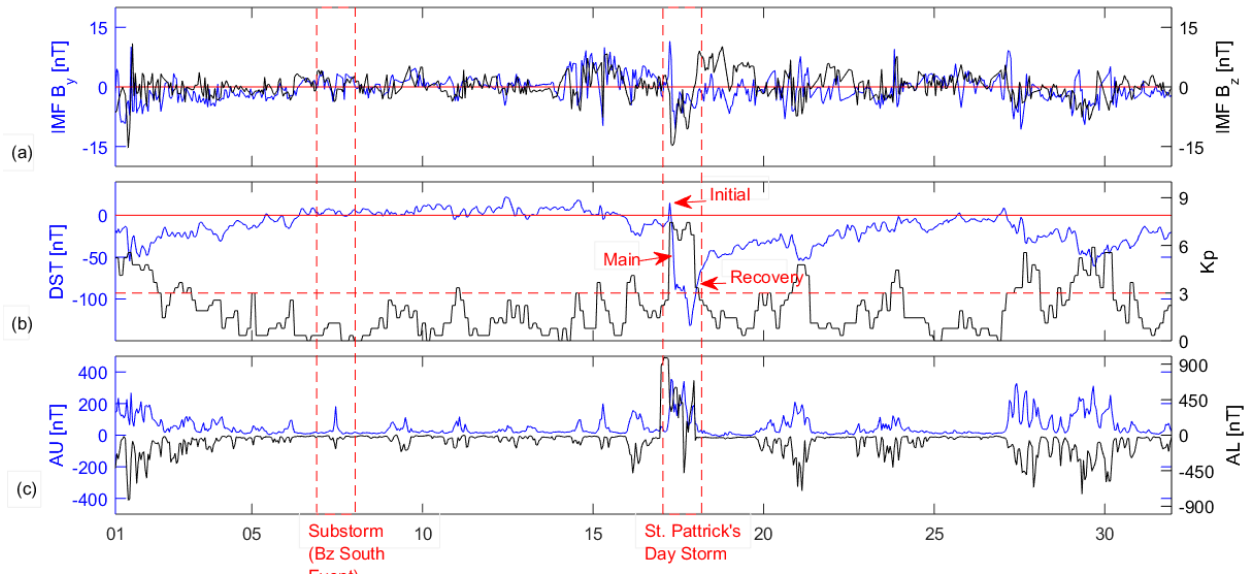

Figure 2.2: Indices for the month of March 2013. (a) Interplanetary Magnetic Field (IMF) components as measured by the Advanced Composition Explorer (ACE) satellite (B_y, blue, and B_z, black); see Section 2.1. (b) Disturbance Storm Time (DST) (blue) with geomagnetic storm phases highlighted, Kp (black); see Sections 2.2 and 2.3.1. (c) Auroral Upper (AU) (blue), Auroral Lower (AL) (black); see Section 2.3.2.

2.1 The Interplanetary Magnetic Field

As the sun rotates, the solar wind flows outward and the IMF traces out what is known as the *Parker Spiral* (*Parker*, 1958). Whether spiral or non-spiral the IMF links to Earth's geomagnetic field allowing for transfer of energy and momentum between the two. The transfer is most efficient when the vertical component of the IMF is directed opposite Earth's magnetic field. Several tools have been developed to easily evaluate the state of the geomagnetic environment associated with the sun-earth system. Measurements from the Advanced Composition Explorer (ACE) satellite stationed at the L1 Lagrange point provide valuable information. Note that the L1 Lagrange point is an orbital point of equilibrium in the sun-earth system (*Christian and Davis*, 2012; *Vallado*, 2007). Included in these measurements are the composition, density and speed of the solar wind (not discussed here). Also measured are components of the interplanetary magnetic field (IMF), which are depicted in Figure 2.1 as represented by the Geocentric Solar Ecliptic (GSE) coordinate

system and are defined as follows:

- B_x: x-axis points from the earth to the sun
- B_z: z-axis points north and perpendicular to the ecliptic (the earth's orbital plane about the sun)
- B_y: y-axis completes the right-handed coordinate system in the ecliptic

The earth's magnetic field (B_E) is approximated at a distance of four Earth radii as a magnetic dipole. Field lines are oriented south to north, being horizontal at the equator and near vertical at the poles (inward at the north magnetic pole while outward at the south).[1] *Magnetic reconnection* of the IMF with Earth's magnetic field[2] provides an effective pathway for charged particles into the earth's geomagnetic environment. This occurs when the IMF is counter-oriented to B_E, or when IMF B_z is southward ($B_z < 0$), and is further described in Section 2.3.4 (*Dungey*, 1961; *Crooker*, 1975; *Sandholt et al.*, 1998, 2004). It is worth noting here that, although not depicted, the earth's rotation axis is tilted by 23.5° with respect to the ecliptic, with a magnetic field that is titled approximately 11° with respect to the axis of rotation. This gives a range of angles over which the earth's magnetic field is tilted with respect to the ecliptic. Therefore, one must also consider that effects of IMF B_y, as it projects onto the earth's magnetic field lines, are both enhancing and damping Sun-Earth interactions associated with IMF B_z (*Russell and McPherron*, 1973; *Barkhatov et al.*, 2012).

Characteristics of the equinoctial interaction between the interplanetary medium and the geomagnetic field are revealed in Figure 2.2a. Shown are the IMF B_y (left axis) and B_z (right axis) components for the month of March 2013. A pattern emerges as multi-day intervals of small rapid IMF fluctuations associated with high speed stream flow, which project the IMF B_y component onto Earth's dipole to produce periods of alternating quiet and active conditions (*Russell*, 2001). Extended times of B_z north preceed some of these intervals and are often referred to as the *Calm Before the Storm* in that they precondition the earth's geomagnetic environment when followed by a geomagnetic storm (*Borovsky and Steinberg*, 2006; *Borovsky and Denton*, 2009). This low-to-

[1] See Appendix B.1.
[2] See Section 2.3.4.

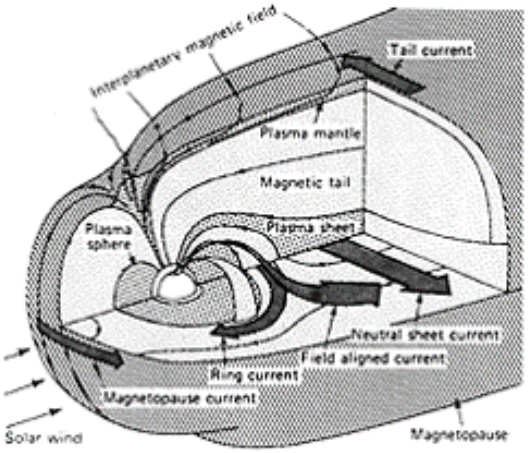

Figure 2.3: The earth's magnetosphere and associated currents, specifically the magnetopause (Section 2.2), ring (Section 2.2), and field aligned currents (Section 2.3.4). Source: Figure 4 of *Russell* (2001).

moderate activity pattern can be disrupted by large solar wind transients (coronal mass ejections) that drive significant geomagnetic storms (*Dungey*, 1961; *Crooker*, 1975; *Sandholt et al.*, 1998, 2004).

2.2 Geomagnetic Activity

Generally, the result of the earth's interaction with the solar wind is that the earth's magnetic field separates charged particles in the solar wind as they travel around it, establishing an electric field (E_{sep}) that the IMF's associated electric field will either enhance or reduce: northward IMF ($B_z > 0$) will exist with a counter-oriented electric field thus reducing E_{sep}, while a southward IMF ($B_z < 0$) will enhance it. A time series of ACE measured IMF components is shown in Figure 2.2a for the month of March 2013, with blue representing IMF B_y, black IMF B_z. A period of time exists (6 to 14 March) where B_z stays primarily north ($B_z > 0$) and B_y primarily east ($B_y > 0$). On 17 March 2013, by contrast, conditions indicate the arrival of a coronal mass ejection (CME) that arrived at Earth on 17 March 2013 [e.g., *Verkhoglyadova et al.* (2016)]. For this storm, IMF B_z turned decidedly south and IMF B_y decidedly west (both B_y and B_z were negative). The resulting changes in the mid- and low-latitude geomagnetic field near the surface of the earth are caused by

the ring current, formed by the solar wind interaction with the earth's magnetic field. Charged particles of higher energies penetrate further into the magnetosphere and cluster in the equatorial region at approximately four Earth radii ($4R_E$). The net current is opposite the direction of the earth's rotation creating an induced magnetic field that enhances B_E outside of the ring current, and acts against B_E on the earth's surface (*Knipp*, 2011). During a geomagnetic storm, the ring current intensifies to maintain the earth's exterior magnetic field, taking away from the earth's surface field.

These changes are reflected in the Disturbance Storm Time (DST) index, which is the average of horizontal component variations of the earth's magnetic field computed from four reference observatories near the magnetic equator. The DST is a direct measure of geomagnetic storm levels and indirectly measures the ring current (*Knipp*, 2011). Although it is a global measure, it does not always depict the local geomagnetic activity at any given point on the earth. A depiction of the earth's magnetosphere is shown in Figure 2.4, including the magnetopause and ring currents. Figure 2.2b shows a time series of the DST (left axis), also for the month of March 2013. Notice the three storm stages highlighted on the 17 March: *Initial*, *Main* and *Recovery* (*Kamide et al.*, 1998; *Knipp*, 2011). This pattern is easily spotted in DST data taken during a CME, and it is interesting to note that his storm was the result of a CME that interrupted high-speed solar wind flows (*Brito et al.*, 2015; *Verkhoglyadova et al.*, 2016). [3]

2.3 The Earth's Ionosphere

Most GNSS systems operate in the plasmasphere at approximately 20,000 km altitude, and transmit their signals through the ionosphere[4] to ground users (*Misra and Enge*, 2006). The ionosphere is a region that starts around 70 km above the earth's surface,[5] and is home to free electrons and ions. While altitude delineations between ionospheric layers are approximate, the

[3] The solar storm in question was actually a G2 Coronal Mass Ejection. For more information on the storm see Section 5.1 and `https://www.nasa.gov/mission_pages/sunearth/news/News031513-cme.html`.

[4] A good beginners guide to the ionosphere can be found at `http://www.arm.ac.uk/summerschool2012/Aylward.pdf`.

[5] Depending on many of the conditions discussed earlier in this chapter, the base altitude can be as low as 50 km or as high as 80-90 km.

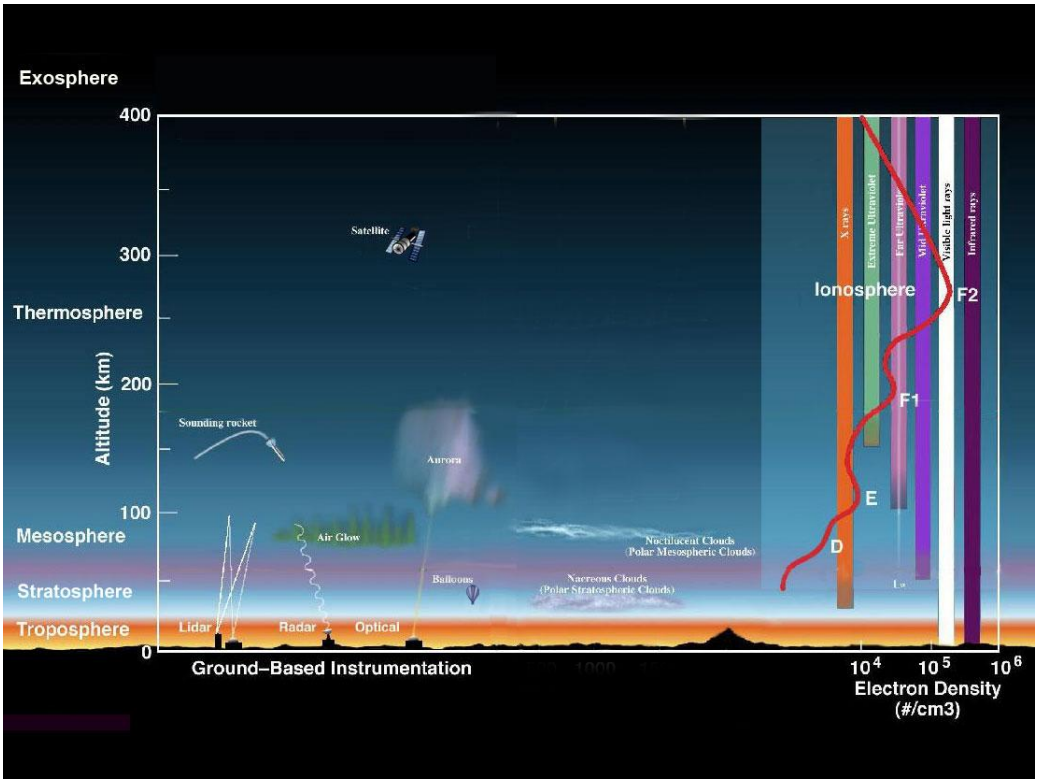

Figure 2.4: A canonical depiction of the earth's ionosphere. Indicated are its co-existence with other atmospheric layers, examples measurement sensors, and the ability of various types of electromagnetic radiation to penetrate it. Source: `https://www.nasa.gov/sites/default/files/images/463940main_atmosphere-layers2_full.jpg`.

overall ionosphere extends out to approximately 1,000 km in altitude but can vary significantly depending on solar activity. It is comprised of five layers, depending on the time of day. The day-side ionosphere begins with the D-region at or above 50 km, and has ionized nitric oxide (NO^+) and ionized molecular oxygen (O_2^+) as its major constituents. It extends up to ~90 km. This is followed by the E-region, where the primary constituents flip in order (O_2^+ and NO^+), and which reaches up to ~150 km in altitude. The F-region starts at the top of the E-region, extends to ~400km, and splits into two distinct layers: $F1$ (lower) and $F2$ (upper), with the separation near 200km. Both primarily contain ionized atomic oxygen (O^+), while the $F1$ layer additionally contains some NO^+ (*Knipp*, 2011; *Schunk and Nagy*, 2009).

The ionosphere's composition and structure are largely defined by its interaction with the sun

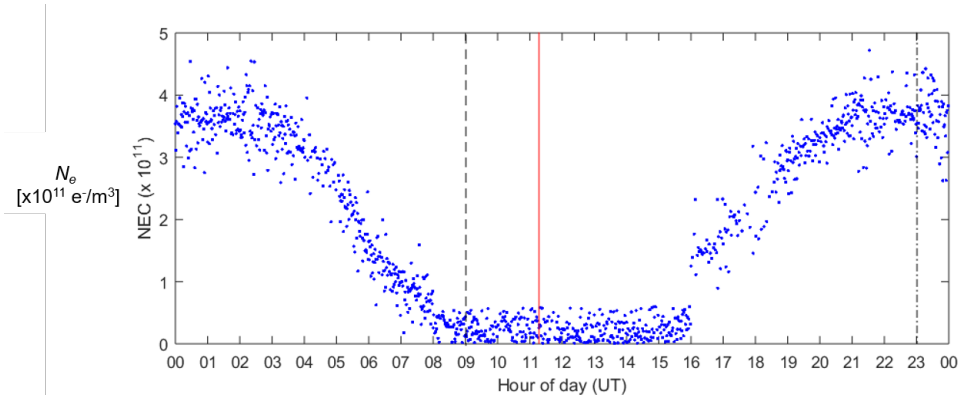

Figure 2.5: Electron density, N_e in e^-/m^3, baseline for March 2013. Local midnight (black dashed line), local 1400 (dash-dotted black line), and magnetic midnight (solid red line) are marked.

and varies with the solar cycle, season and time of day. The earth's rotation allows for dayside heating and night-side cooling of the atmosphere. During the day, extreme ultra-violet (EUV) energy from the sun causes photoionization of atmospheric constituents and hence increased quantities of free electrons. This is predominantly through the interaction of EUV radiation with atomic oxygen in the F-region.

$$O + h\nu \rightarrow O^+ + e^- \tag{2.1}$$

Here O is atomic oxygen, h is Planck's constant, ν is the photon frequency, and e^- is the electron. At night the ions and free electrons recombine without the presence of solar radiation. This is primarily done through collisions:

$$O^+ + O_2 \rightarrow O_2^+ + O \tag{2.2}$$

$$O^+ + N_2 \rightarrow NO^+ + N \tag{2.3}$$

followed by dissociative recombination

$$O_2^+ + e^- \rightarrow O + O \tag{2.4}$$

$$NO^+ + e^- \rightarrow O + N \tag{2.5}$$

where N is atomic nitrogen.(*Knipp*, 2011; *Schunk and Nagy*, 2009)

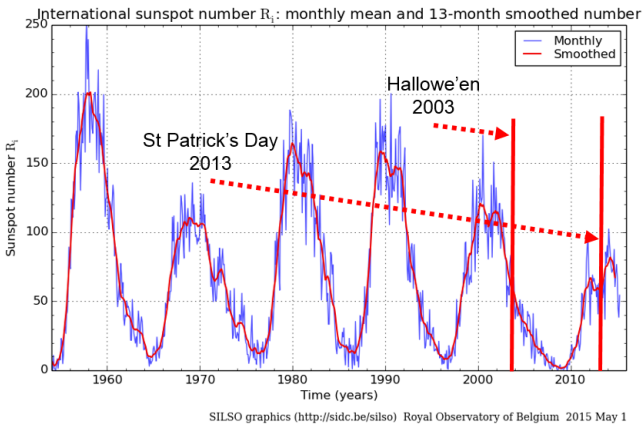

Figure 2.6: The international sunspot number as a function of time from around 1950. Highlighted are the approximate times for the Hallowe'en Storms of 2003, and the St. Patrick's Day Storm of 2013.

At sundown, the D-region recombines and essentially disappears with the loss of solar radiation. The E-region recombines as well, but lasts much further into the night-time hours, especially with increased solar activity. In the F layer, ions in the $F1$ region recombine after sundown with lingering remnants of ionization, and the $F2$ region loses much of its ion and electron populations, but still persists through the night. The Topside layer extends beyond 400km, has as its primary constituents O^+ and H^+, and exists during both day and night (*Knipp*, 2011; *Schunk and Nagy*, 2009). The focus herein will be on E and F-region night-side high-latitude phenomenology, as will be discussed further in Section 2.3.2.

The ionosphere's diurnal structuring is reflected in the 24-hour baseline electron density profile shown in Figure 2.5. In the figure, local midnight is indicated by a vertical dashed black line, magnetic midnight by a vertical solid red line.[6] Clearly visible is the dayside ionization peak around 1400 local (2 pm, 2300 UT) indicated by a dash-dotted black line. This baseline was formed using electron density measurements from the Poker Flat Incoherent Scatter Radar (PFISR), near Fairbanks, Alaska, and taken at 363 km altitude.[7]

Daily ionospheric electron density (N_e) variations are known to occur due to dayside pho-

[6] Magnetic midnight is defined as the time, either local or UT, when the sun, the earth's magnetic pole, and a particular site align, in that order.

[7] The radar's description and a detailing of how this baseline was formed can be found in Section 4.1.3.

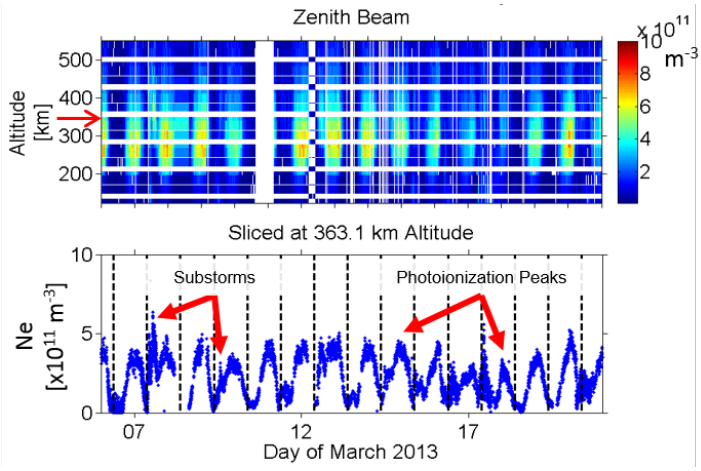

Figure 2.7: Electron Density ($\times 10^{11} e^{-}/m^{-3}$, colorbar at right) over time for 6-20 March 2013 from the zenith beam. (a) All altitudes, all times of radar operation. (b) Single altitude slice at 363 km.

toionization. Irregularly occurring enhancements due to phenomena discussed here and other known phenomena also occur. This is evident in the color plots in Figure 2.7 covering 6-20 March 2013, for the zenith beam at PFISR. An example slice at 363.1 km altitude is also shown in Figure 2.7. Local midnight is indicated with black dashed lines. Note the daily photoionization peaks (occur following local noon) and the irregular night time substorms (occur quasi-nightly just after local midnight). Examples of each are highlighted on the altitude slices in Figure 2.7. An easy way to differentiate between solar driven geomagnetic storms and substorms is to look at the peak photoionization N_e levels and see that they drop during the period of the geomagnetic storm (17 March 2013 in Figure 2.7) and recover back to normal levels following (*Knipp*, 2011; *Schunk and Nagy*, 2009). This is because of several factors that cause a drop in the O/N_2 ratio during storm times (summarized in *Kil et al.* (2011)).

While the diurnal cycle of the ionosphere is caused by the earth's rotation on its axis, the earth's orbit about the sun also provides for a seasonal dependence (*Crooker et al.*, 1992). The relative inclination of the earth's magnetic field to the ecliptic is most conducive to an enhanced storm-time response during the equinoxes, as the earth's magnetic field and the IMF are more apt to counter-align (*Russell and McPherron*, 1973; *Barkhatov et al.*, 2012). As it turns out,

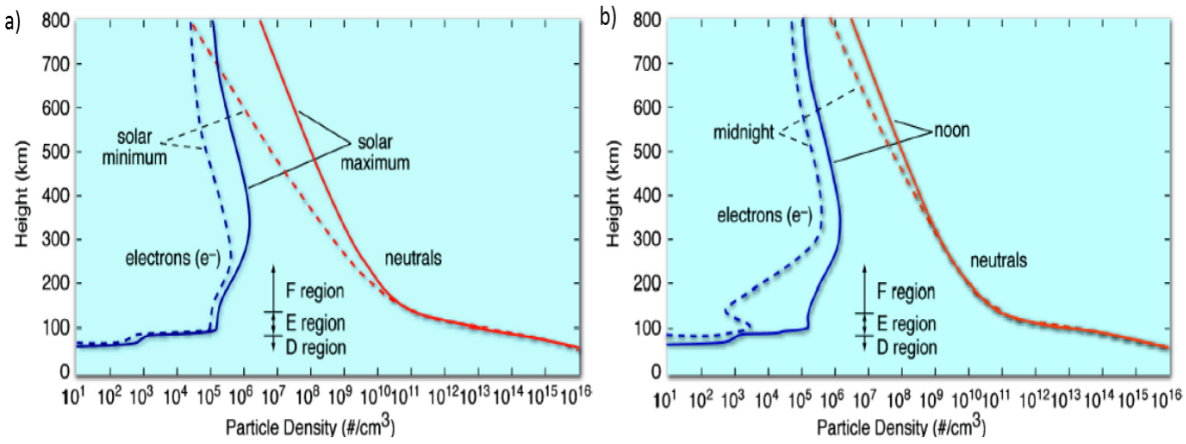

Figure 2.8: Average electron and neutral density profiles for (a) solar cycle extrema and (b) the diurnal cycle as discussed in Section 2.3. Approximate altitudes for ionospheric layers are also shown (*Knipp*, 2011).

quasi-annually there does exist a St. Patrick's Day geomagnetic storm because of its proximity to the Vernal Equinox; and, storms in the northern hemisphere near the Autumnal Equinox are statistically more prominent (*Cliver et al.*, 2000). The reasons for this asymmetry in the seasonal storm statistics is the subject of current research (*Falayi and Beloff*, 2009; *O'Brien and McPherron*, 2002; *Oh and Yi*, 2011; *Rangarajan and Iyemori*, 1997).

Representative vertical profiles showing average electron densities by altitude can be found throughout the literature. As was previously discussed, these profiles vary daily, seasonally, and with the solar cycle. Solar activity, as indicated by the sunspot cycle shown in Figure 2.6, has a roughly 11 year periodicity, minimum to minimum. Peak electron densities for both day and night-side ionosphere can be up to an order of magnitude greater during solar maximum than during solar minimum. In general they are represented by the profiles in Figure 2.8. Shown are electron density and neutral profiles for the extremes of the solar cycle (a), as well as the diurnal cycle (b).

2.3.1 The Low- and Mid-latitude Ionosphere

In addition to temporal variations, the earth's ionospheric structure also depends on geomagnetic latitude;[8] and, is broken into three major regions: low-, mid- and high-latitudes. The low-latitude ionosphere is defined as the region within $\pm 20^o$ of the geomagnetic equator; and, the high-latitudes encompass the auroral oval and the polar cap (*Aarons*, 1982; *Jiao and Morton*, 2015). The mid-latitude ionosphere is everything in between. In the low-latitude ionosphere, the magnetic field is horizontal and electron densities reach a global dayside peak. During pre-peak hours, the sun warms the thermosphere and hence the ionosphere. These regions lift and their plasma, which elongates along magnetic field lines, flows poleward on the slightly declined lines away from the magnetic equator. This creates the *Appleton Anomalies*, which are two bands of F-region plasma with enhanced densities at $\pm 15^o$ geomagnetic latitude (*Appleton*, 1946; *Basu et al.*, 2002; *Kintner et al.*, 2007; *Ledvina et al.*, 2004; *Sridhar et al.*, 2014). Although the night-side ionosphere experiences recombination after sunset, at low-latitudes the F-region plasma remains suspended by horizontal magnetic field lines and an $\vec{E} \times \vec{B}$ drift from an eastward E-region electric field. Pockets of lower electron densities in the lower F-region, called *depletions*, are generated through the evolution of the Rayleigh-Taylor instability, an effect that essentially keeps ionized plasma and neutral atmosphere from mixing (*Chiu and Straus*, 1979; *Huang et al.*, 2011). These depletions rise and create bubbles that flow poleward, leading to the existence of ionospheric irregularities and gradients in electron density (*Basu et al.*, 2002; *Kintner et al.*, 2007; *Sridhar et al.*, 2014).

The mid-latitude ionosphere is less dynamic compared to low- and high-latitudes, except during times of heightened solar and geomagnetic activity. Geographically, it covers the continental US and similar regions of Europe, Africa, Asia and Australia. It experiences the aforementioned diurnal ionization cycles and is one source of plasma associated with high-latitude phenomena discussed later (Section 2.3.2). Here magnetic field lines continue to point northward and begin to see increasing declinations.[9] During times of moderate to severe geomagnetic activity, storm

[8] For a full description of magnetic coordinate systems, refer to Appendix B.1
[9] Full definitions of geomagnetic coordinate systems, see Appendix B.1

enhanced densities exist with steep gradients at the storms' main phase, and hence high bulk velocities called *subauroral ion drifts (SAID)* (*Kintner et al.*, 2007; *Ledvina et al.*, 2004).

The mid-latitude region is home to 13 reference observatories that provide us a measure of the earth's geomagnetic activity through the K_p index. It is calculated as the average of K indices from observatories in the US, Canada, Europe and Australia (*Knipp*, 2011). Figure 2.2 on page 10 also shows the March 2013 time series for K_p. Generally a K_p value less than three is considered magnetically quiet (*Knipp*, 2011). It just so happens that the quiet time shown corresponds to that given by the *Calm Before the Storm* time indicated in Figure 2.2b ($B_z > 0$).

2.3.2 The High-latitude Ionosphere

A more in-depth look at the sun-earth interaction is required to fully appreciate the dynamics of the high-latitude ionosphere, unique in that it coexists with the earth's magnetic poles and open field lines. The diurnal activity previously defined is complicated and often dominated by its interaction with the magnetosphere and the broader space environment. The high-latitudes are defined as the region above approximately 60 degrees latitude in each hemisphere. Because of their proximity to the magnetic poles, the earth's magnetic field approaches a vertical orientation in the high-latitudes. Some of these field lines connect with the IMF and act as pathways for incoming charged particles (especially near the cusp, less so towards the night-side) and allow them to propagate into Earth's near-space environment (open field lines). Other field lines create a connection between the polar ionosphere and the magnetosphere, essentially completing an electric circuit along which charged particles (both ions and electrons) are exchanged.

The electric field generated by the IMF-B_E interaction, $\vec{E}_{SEP}$, translates across the poles (now denoted the *polar cap electric field* ($\vec{E}_{PC}$) and creates a zonal current (east-west oriented) known as the *Pederson Current*. Pederson Currents close the circuit via their connection to the magnetosphere by way of the *Field Aligned Currents* (currents aligned with magnetic field lines), with Region I currents connecting to the magnetopause and Region II to the ring current (refer back to Figure 2.4). Ions and electrons drift horizontally in the F-region due to an $E \times B$ drift

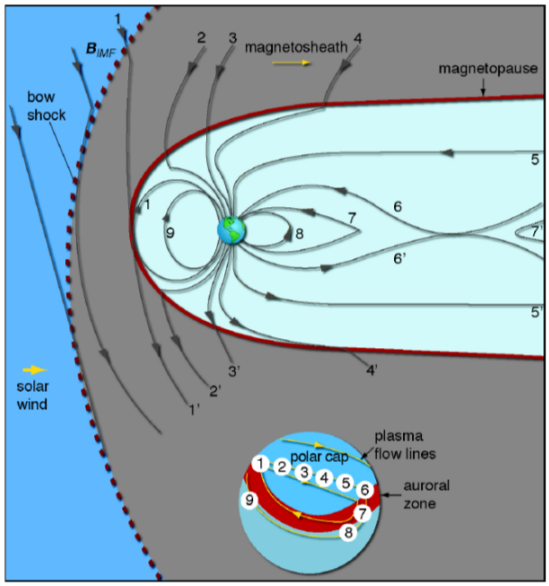

Figure 2.9: A step-by-step representation of the process of magnetic reconnection starting with (1) dayside and moving through (6) nightside reconnection (Section 2.3.4) (*Knipp*, 2011; *Cowley*, 1996).

with a velocity given by

$$\vec{v} = \frac{\vec{E}_{PC} \times \vec{B}_E}{B_E^2} \tag{2.6}$$

When applying the right hand rule, we see that electrons and ions drift antisunward. Since ions are more collisional with the thermospheric neutral constituents due to their larger cross-section, the ions will transfer momentum to the neutrals (called ion drag) and be slowed, thus the electrons will drift faster than the ions. The net result during geomagnetically quiet times is a two-cell convection pattern where the current flows sunward across the polar cap, and anti-sunward at dawn and dusk through the auroral zone, known as *Hall Currents*. Hall currents act in line with polar circulation and potential patterns, to be discussed later (*Schunk and Nagy*, 2009; *Knipp*, 2011; *Johnsen*, 2011). Segments of the Hall Currents, those flowing sunward through the auroral zone, are also known as the *auroral electrojets*.

2.3.3 Convection Phenomena

Previously mentioned was the concept of magnetic reconnection of the IMF with B_E. When this occurs on the dayside, the response discussed above is seen. A depiction of this interaction is given in Figure 2.9. Here the sun-earth system is seen from the dusk sector, sliced in the north-south plane, with the earth's rotation axis pointing up and lying in the plane of the page. When reconnection occurs on the dayside (depicted with a '1' in Figure 2.9), a flux of solar plasma enters the magnetosphere, and particles become trapped. Pressure from reconnection with B_z south conditions builds, and the newly open field lines are forced across the polar cap ('2', '3', and '4' in Figure 2.9) (*Schunk and Nagy*, 2009; *Knipp*, 2011; *Johnsen*, 2011).

The process of magnetic reconnection is what drives the convection of plasma into and across the polar cap (*Moen et al.*, 2015). The mid-latitude ionosphere is one source of plasma that feeds into this convection pattern (*Crowley et al.*, 2000). It is thought that solar particles entering the earth's atmosphere along open field lines in the dayside cusp region are another (*Zhang et al.*, 2013). The discussion that follows summarizes the processes associated with the former, and is presented in Figure 2.10. Regardless of the source of the convection phenomena, the fact of their existence plays a key role in GPS scintillation at the high-latitudes. This process begins with *subauroral polarization streams (SAPS)* that are westward flowing plasma streams just outside the auroral oval in the dusk sector at F-region altitudes. During a geomagnetic storm, these SAPS can also flow poleward and drag ions with them, yielding *storm enhanced densities (SED)* in the noon cusp region[10] (*Erickson et al.*, 2011). If IMF B_z south conditions persist long enough, these plumes are convected into the polar cap through the cusp as *tongues of ionization (TOI)*, which can segment into *polar cap plasma patches*. Patches continue to move about the polar cap until they are eventually convected into the auroral oval where they are called *blobs*. Patches (blobs) are regions of enhanced F-region electron density that are two times or more the background density

[10] The dayside polar cusps are defined as the narrow border regions near either pole where the earth's magnetic field lines no longer close on the day or nightside of the earth, and are open at the earth but connected (closed) to the IMF. Solar particles may directly access the ionosphere in these locations, near 75^o geomagnetic latitude (*Knipp*, 2011).

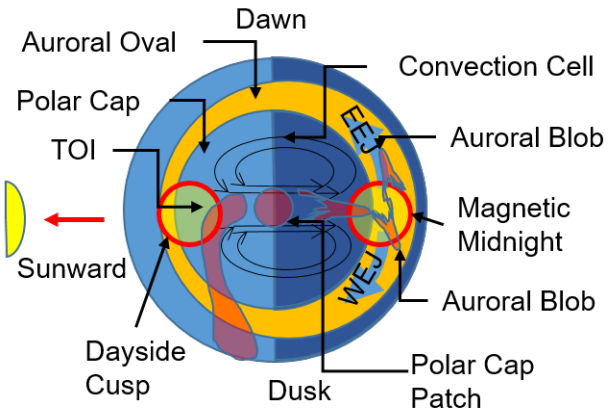

Figure 2.10: Representative diagram of the northern high-latitude region polar convection phenomena and their progression. Labeled are (clockwise from the top): the dawn sector and the Auroral Oval, convection cells, an auroral blob, the magnetic midnight sector, patches and blobs, the dusk sector, a sub-auroral polarization stream (SAPS), a region of storm enhanced density (SED), and a tongue of ionization (TOI), the dayside cusp and the Polar Cap. See Section 2.3.3.

(*Crowley*, 1996; *Crowley et al.*, 2000; *Foster et al.*, 2005; *Moen et al.*, 2013). In the auroral zone, auroral blobs can form independent of convection phenomena; and are thought to be caused by particle precipitation, but otherwise behave in the same manner as patches (blobs) (*Crowley et al.*, 2000; *Moen et al.*, 2013; *Jin et al.*, 2014)

While the mechanism(s) and theory underlying the formation and structure of patches is being debated, their structure is well documented. Patches are smooth at the leading edge, with minimal gradients in electron density, with significant variation on the trailing edge and tails that are composed of vast and large electron density gradients (∇N_e) (*Crowley*, 1996; *Crowley et al.*, 2000; *Moen et al.*, 2013). As the patches convect through an electrodynamically complex polar cap with evolving circulation cells, the patches can rotate and become twisted, and their tails even further elongated (*Hosokawa et al.*, 2011; *Thomas et al.*, 2015). At magnetic midnight and under B_z south conditions, their journey continues as they cross into the auroral oval, and *Thomas et al.* (2015) concluded that '...patches exiting the polar cap on the nightside are subject to extensive reshaping and quickly lose the spatial imprint of their dayside formation mechanism.' As mentioned previously, patches that have traveled into, or developed inside the auroral zone are known as blobs.

Blobs can be broken down into three categories:

- boundary blobs: exist near the equatorward auroral boundary, still in the auroral zone
- subauroral blobs: exist just outside of the equatorward boundary and in the ionospheric trough; potentially left over when auroral oval retreats during storm recovery phase.
- auroral blobs: assumed to be formed by particle precipitation (*Crowley et al.*, 2000).

A consistent manifestation of patch (blob) structuring is the unique airglow signature associated with it at 630.0 nm. This line is the result of the forbidden transition of atomic oxygen, and is from collisions of the plasma with the neutral atmosphere. (*Rees and Luckey*, 1974; *Akasofu*, 2009; *Colpitts*, 2016). By contrast, airglow emission intensities are much lower than those of the aurora [Hosokawa et al., 2011; van der Meeren et al., 2014]. For example, auroral intensities measured throughout this research are thousands to tens of thousands of Rayleigh; whereas, normal ambient airglow emission intensities are hundreds to thousands of Rayleigh (*Hosokawa et al.*, 2011).

2.3.4 The Aurora

The Dungey cycle shown in Figure 2.9 is also a driver behind particle precipitation. When the earth's magnetic field lines finally make it to the its night-side, they eventually and explosively reconnect (depicted with a '5' and '6' in Figure 2.9). This gives trapped plasma enough energy to precipitate along field lines into the auroral zones ('7' and '8'). In the north we see this physically manifest in the *Aurora Borealis* (in the south, the *Aurora Australis*) (*Schunk and Nagy*, 2009; *Knipp*, 2011; *Johnsen*, 2011). A good summary of the association of particle precipitation of this form is given in *Chua et al.* (2004), but suffice to say that this process results in what is called discrete aurora. Discrete aurora appear in the form of striated curtains that appear to shimmer across the night sky (*Akasofu*, 2009). This is far different from diffuse aurora which are the result of particles that interact with the neutral atmosphere as part of pitch angle diffusion and results in broad swaths of lighted sky (*Newell et al.*, 2009). The primary focus of this work is on discrete aurora, while both discrete and diffuse aurora are evident in the analyses presented in this work.

Succinctly, the auroral zone refers to geographic locations in which the aurora are known

to occur, whereas the auroral oval is the region in which the aurora are actually occurring and varies with geomagnetic activity. *Jones* (1974) also noted that the most intense aurora occur in the magnetic midnight region of this oval: magnetic midnight coincides with night-side magnetic reconnection (*Johnsen*, 2011). When the 'explosion' of particles from the magnetotail occurs, the electrons (and sometimes protons) collide with atmospheric constituents and produce the aurora.[11] Green (557.7 nm) emissions originate from the excitation of atomic oxygen (O) and are visible down to around 100 km. The blue-violet (427.8 nm) auroral emissions are the brightest band generated by ionized molecular nitrogen (N_2^+). Red (630.0 nm) auroras are the result of a forbidden transition of atomic oxygen (O), detected above 250 km due to collisions of plasma with neutral atmosphere and are not normally visible to the naked eye (*Rees and Luckey*, 1974; *Akasofu*, 2009; *Colpitts*, 2016). The red emission line is also associated with patch and blob convection in the high-latitudes and is not to be confused with emissions from energetic particle precipitation: airglow emission intensities are much lower (by at least half) than those of the aurora (*Hosokawa et al.*, 2011; *van der Meeren et al.*, 2014).

Alaska lies within the auroral zone, which rotates with the earth in and out of the auroral oval that is fixed with respect to the sun and expands or contracts with changes in the geomagnetic environment (*Akasofu*, 2009). During increased activity, linked to solar activity and IMF orientation, the auroral oval expands equatorward, and during decreased activity it contracts poleward (*Akasofu*, 2009; *Milan et al.*, 2009). It is important to note that when the auroral oval expands, both boundaries move equatorward (*Akasofu*, 2009; *Milan et al.*, 2009). *Milan et al.* (2009) noted that '...the polar cap expands and contracts during the substorm cycle...but during storm times remains enlarged above its quiet-time size.' This allows for sites that rotate in and out of the poleward boundary to, during extreme quiet times, potentially rotate in and out of the equatorward boundary. *Aarons* (1997) specifically states that in times of extreme quiet, '...the irregularity region moves considerably poleward of the auroral oval or may even fail to exist at various levels of

[11] Only those lines of the aurora that are pertinent to this analysis are discussed here. For a more thorough outline see *Jones* (1974).

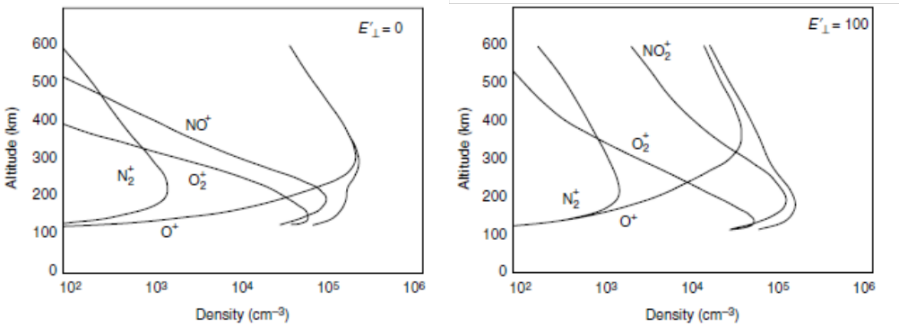

Figure 2.11: Representative ion and electron density profiles for the high-latitude ionosphere. See Section 2.3.4 for discussion. *Schunk and Nagy* (2009)

intensity.'[12] [13] Nearly always present in the oval is diffuse aurora - the result of electron precipitation due to pitch angle diffusion. When the geomagnetic environment is active, precipitation in the form of auroral arcs appear in the sky within the oval. *Jones* (1974) noted that the most intense aurora occur in the magnetic midnight region of the oval. This is consistent with the climatology of GPS scintillation discussed in Section 3.3. In a dynamic high-latitude ionosphere the time scales associated with a changing aurora are on the order of seconds and the focus of this analysis is on the highly variable discrete auroral arcs with vertical striations.

The processes that cause the aurora create a precipitation of energetic electrons (at least $35eV$) which collide with the background neutral thermospheric constituents. If sufficient energy is transferred to the neutral atom or molecule, then impact ionization occurs. Because of this, a slightly different electron density profile and constituent population exists at high-latitudes.[14] Collisions of plasma energized in the magnetotail at reconnection with atmospheric constituents are the cause of the bulk of the aurora. One can estimate the associated auroral electron energies from a ratio of emission intensities. Using this ratio, one can then estimate the associated electron flux; and, finally cross-reference this with impact ionization rates for particles of various energies (*Rees and Luckey*, 1974). This allows for a prediction of which altitudes increased electron densities are

[12] More discussion on this and its impacts are found in Chapter 9.
[13] *Aarons* (1997) defined the irregularity region as a subset of the auroral oval that was based on the intensity of the detected irregularities.
[14] See Figure 2.11 for example.

most likely to be detected by a radar. Note that green emissions result from particles with higher energies that, because of their energies, are able to further penetrate the neutral atmosphere. Note also that during storm time, the O/N_2 ratio decreases, increasing the supply of nitrogen and decreasing the supply of oxygen available for emission, again disproportionately affecting the green emission line (*Strickland et al.*, 1989; *Grubbs*, 2016).

As will be further discussed in Section 4.1.3, only estimates of enhancement altitudes are required. Therefore, detailed estimates of energies are not required; and, adjustments based on O/N_2 ratios are not necessary (*Strickland et al.*, 1989; *Grubbs*, 2016). Without correction there is the potential to underestimate the intensities and hence underestimate the precipitating particle energies. Ratios of green to blue, red to blue and red to green are calculated and shown, and can be used to estimate precipitating particle energies; but, because the green emission is most sensitive to the O/N_2 ratio, only the red to blue ratio was used to estimate precipitating particle energies per the final recommendation of *Rees and Luckey* (1974).

2.3.5 Geomagnetic Sub-storms

Auroral activity occurs in conjunction with geomagnetic storms as well as during substorms. As was discussed in Section 2.2, geomagnetic storms are a result of the earth's interaction with solar storms (e.g., coronal mass ejections), and their intensity is a direct result of the IMF orientation during the interaction, in addition to other factors (*Knipp*, 2011; *Chua et al.*, 2004; *Rostoker*, 2000). Substorms, on the other hand, are often driven by the orientation of the IMF in the solar wind and do not necessarily have a solar storm driver (*Knipp*, 2011; *Chua et al.*, 2004; *Rostoker*, 2000; *Kamide et al.*, 1998). As such, the DST and Kp do not always accurately reflect geomagnetic activity in the Arctic region; and, in lieu of these, the Auroral Electrojet (AE) indices are often used. These measure high-latitude currents and are comprised of a computational total of horizontal component variations of the earth's magnetic field from the east and westward auroral electrojets (EEJ, WEJ) and the zonal current (Pederson Current). They are measured at observatories in Canada, Alaska, and Russia, as well as others throughout the Auroral Zone, and appear in four forms:

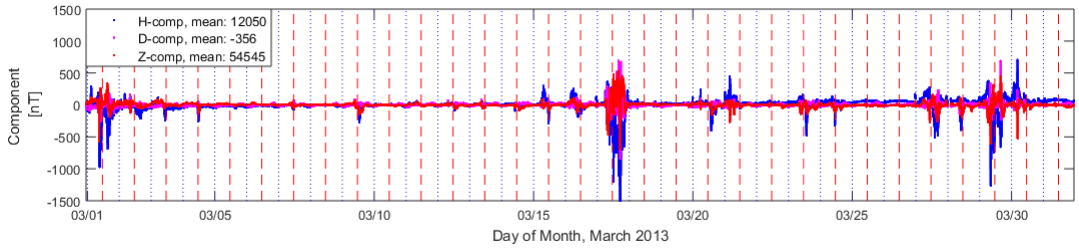

Figure 2.12: PFRR magnetometer data for the month of March 2013. Each component (H, D, Z) is defined in Appendix B.1, and each is plotted as a deviation from the mean for the time period shown.

- Auroral Upper (AU): measures eastward auroral electrojet (EEJ, part of Hall Currents)
- Auroral Lower (AL): measures westward auroral electrojet (WEJ, part of Hall Currents)
- Their Average (AO): measures equivalent zonal current (Pederson Currents)
- Their Difference (AE): reflects net effect of the current systems (*Magnetism and Space*, 2016; *Knipp*, 2011).

These indices are used in a variety of methods to determine Arctic geomagnetic conditions. Amongst these, AU is indicative of the geomagnetic response to changes in the IMF; and, AL is a good tool to understand substorm phasing (*Magnetism and Space*, 2016; *Knipp*, 2011). Shown in Figure 2.2c is a time series of AL and AU. Here indications in the data of B_z south driven *substorms* (quasi-nightly), as well as the geomagnetic storm on St. Patrick's Day can be clearly observed. Note that when compiling and averaging the AE indices, only the most extreme measurement set is used; and, hence the AE is a range index that is not always a representation of local geomagnetic activity in the auroral zone (*Gjerloev et al.*, 2004; *NCEI*, 2017). For the purposes of the analyses presented in this work, local magnetometer data are used in order to validate activity over Poker Flat and across the research range. Three components of the magnetic field are measured at each location and are described in Appendix B.1, with representative data shown in Figure 2.12 for the times matching Figure 2.2.

Chapter 3

Introduction: Scintillation Science

Presented in this chapter is a summary of the basics of scintillation science as they pertain to the subject of this dissertation. The basics of radio wave propagation through a medium are presented and scintillation is defined. This is followed by an overview of the Global Positioning System (GPS), a Global Navigation Satellite System (GNSS), including a review of the basic observables used in calculating position as well as the phase scintillation index, σ_ϕ, as calculated by specialized receivers. The chapter is closed with a review of the known scintillation climatology for the high-latitudes, as well as a summary of more recent studies in the region.

3.1 Radio Waves

3.1.1 Propagation

The theory of electromagnetic radiation and its propagation through space is founded in *Maxwell's Equations* (*Griffiths*, 1999; *Halliday et al.*, 2008), displayed in differential form in Equations 3.1 through 3.4.

$$\nabla \cdot \vec{E} = \frac{\rho}{\epsilon_0} \tag{3.1}$$

$$\nabla \times \vec{B} = \mu_0(\vec{J} + \epsilon_0 \frac{\partial \vec{E}}{\partial t}) \tag{3.2}$$

$$\nabla \times \vec{E} = -\frac{\partial \vec{B}}{\partial t} \tag{3.3}$$

$$\nabla \cdot \vec{B} = 0 \tag{3.4}$$

Here, $\vec{E}$ is the electric field and ρ is the associated charge density, $\vec{B}$ is the magnetic field and $\vec{J}$ source current density, and ϵ_0 and μ_0 are the dielectric constant and permittivity of free space (vacuum). This set of equations tells us that charges establish electric fields (*Gauss' Law*, Equation 3.1); that moving charges and/or changing electric fields create current, which in turn, creates a magnetic field (*Ampere's Law*, Equation 3.2); that a changing magnetic field results in a changing electric field (*Maxwell-Faraday Law*, Equation 3.3); and, that there are no magnetic monopoles (*Gauss' Law for Magnetism*, Equation 3.4) (*Griffiths*, 1999; *Halliday et al.*, 2008).

Combined, we can achieve a particular solution to these equations: that of an electromagnetic wave propagating through a vacuum. To obtain this solution, we first assume that there are no charges as sources ($\nabla \cdot \vec{E} = 0$ and $\vec{J} = 0$), and Equations 3.1 through 3.4 reduce to Equations 3.5 and 3.6.

$$\nabla^2 \vec{E} = \mu_0 \epsilon_0 \frac{\partial^2 \vec{E}}{\partial t^2} \tag{3.5}$$

$$\nabla^2 \vec{B} = \mu_0 \epsilon_0 \frac{\partial^2 \vec{B}}{\partial t^2} \tag{3.6}$$

Equations 3.5 and 3.6 are in the form of a wave equation, with a wave that is propagating at the speed of light in a vacuum, $c = 1/\sqrt{\mu_0 \epsilon_0}$. These have solutions of the form:

$$E_i = E \sin(kx_i - \omega t) \tag{3.7}$$

$$B_i = B \sin(kx_i - \omega t) \tag{3.8}$$

where E_i is the ith component of the electric field corresponding to the x_i direction. Also note here that $k = 2\pi/\lambda$ is the wave number, $\lambda = c/f$ is the wavelength, $f = \omega/2\pi$ is the frequency (*Griffiths*, 1999; *Halliday et al.*, 2008).

This assumes propagation of the wave through a vacuum. When electromagnetic waves travel through a medium other than a vacuum, ϵ_0 is replaced by ϵ, and μ_0 by μ, corresponding to the particular medium. The speed of light in the medium is defined as in Equation 3.9.

$$v = \frac{1}{\sqrt{\epsilon \mu}} \tag{3.9}$$

The ratio of the speed of light in a vacuum (c) to that in a medium (v) gives the index of refraction (n) of a medium, Equation 3.10 (*Griffiths*, 1999; *Halliday et al.*, 2008).

$$n = \frac{c}{v} \tag{3.10}$$

During GPS scintillation, discussed further in the sections that follow, the radio wave is transiting a medium that is not a vacuum. The index of refraction, n, is used to describe this medium and is given by the ratio of the speed of light in a vacuum (c) to that in a medium (v), and reduces to unity the closer a medium is to a vacuum. For the ionosphere n varies with the electron density (N_e) and is inversely proportional to the square of the transmission frequency (f). Higher frequency signals traversing the same ionosphere will experience an index of refraction closer to unity (*Knipp*, 2011; *Schunk and Nagy*, 2009). For reference, the index of refraction in the ionosphere at an electron density of 10^9 e^-/m^3 for the L1 signal (1575.42 GHz) is 0.99999998.

3.1.2 Scintillation

It is well known that radio wave scintillation in the form of abrupt changes to signal phase or amplitude is caused by the phenomena of wave *diffraction* and *refraction*. Simply put, diffraction results when waves bend around objects, whereas refraction occurs when waves bend through a medium. One of the most well-known examples of diffraction is single-slit diffraction, where an incident plane wave encounters a small slit in a screen and produces alternating regions of light and dark on a nearby wall or viewing screen. These are caused by constructive and destructive interference of the wave with itself, and produces both phase and amplitude scintillation. A simple example of refraction is that of a pencil or straw sitting in a glass of water. The section of pencil outside of the water appears misaligned with, or at an angle to, the submerged section. This is because the speed of light varies with the medium (*Griffiths*, 1999; *Halliday et al.*, 2008; *Kintner et al.*, 2007). As was discussed in Section 3.1.1, the index of refraction, n, of a given medium gives us the ratio of the speed of light in the medium to that of a vacuum. For the ionosphere the index of refraction varies with electron density, N_e [e^-/m^3], and is alternatively defined as shown

in Equation 3.11.

$$n \approx \sqrt{1 - \frac{80.6 N_e}{f^2}} \tag{3.11}$$

Note the dependence here of the index of refraction, n, with the signal's transmission frequency, f [Hz].

The spatial delineation between when diffraction and refraction occurs is known as the Fresnel Length (*Ratcliffe*, 1956; *Booker and Majidiahi*, 1981; *Kintner et al.*, 2007). Normally it is discussed for antennas that are separated by some distance on the ground. For satellite signals, it is focused around the distance, R, from an interfering ionospheric structure to the receiver. Combined with the signal's wavelength (λ), the Fresnel length is given by Equation 3.12.

$$r_F = \sqrt{2\lambda R} \tag{3.12}$$

Diffractive effects are seen when the ionospheric structure in the ray path has a size on the order of or smaller than r_F. Refractive effects occur when the size is much larger than r_F.[1] For context, Table 3.1 includes approximate Fresnel lengths for each GPS transmit frequency used in the current experiments (discussed in Section 3.2.1). These are calculated assuming a 350 km altitude (R) for the commonly used ionospheric pierce point (IPP), associated with the assumption that the bulk of ionospheric effects on GPS signals occur at or near the F-region peak (*Misra and Enge*, 2006). Also provided in the table are the Fresnel lengths for an E region altitude of 135 km, which are approximately 40% smaller than their F region counterparts. Shown in the last column are time scales associated with structures on the order of r_F at 350 km that are moving at 1 km/s (discussed in Section 2.3.3). These are calculated as $\tau \sim r_F/v$, where v is the structural drift velocity (*Ratcliffe*, 1956).

Electron density gradients resulting from fast moving and/or changing structures in the high-latitude ionosphere generate a high variation of the index of refraction along the signal ray path from satellite to receiver. This is the source of the abrupt changes to the signal phase and/or amplitude at a ground receiver for a space based signal. More discussion of these topics can be

[1] See Section 3.2.1 for Fresnel Radii associated with GPS signals.

Table 3.1: US Global Positioning System (GPS) Parameters

Carrier Label	**Frequency** [MHz]	**Codes**	**Fresnel Radius (r_F)** @ 350 km [m]	@ 135 km [m]	**Time Scale (τ)** @ 350 km [s]
L1	1575.42	C/A & P(Y)	˜365	˜227	0.365
L2	1227.60	C & P(Y)	˜413	˜257	0.413
L5	1176.45	LC	˜422	˜262	0.422

found in *Aarons* (1997); *Kintner and Ledvina* (2005); *Kintner et al.* (2007); *Knipp* (2011); *Schunk and Nagy* (2009); *Yeh and Liu* (1982). The net effect of the ionosphere on a wave's propagation through it is to change the *phase* and *group* velocities. Previously defined in Equation 3.9 as the speed of light in a medium, the phase velocity is further refined to include factors depending on the electron density (N_e), and hence the plasma frequency (ω_{pe}), as is shown in Equation 3.13.

$$v_\phi = \frac{c}{\sqrt{1 - \omega_{pe}^2/\omega^2}} \tag{3.13}$$

Similarly the group velocity is defined in Equation 3.14.

$$v_g = c\sqrt{1 - \omega_{pe}^2/\omega^2} \tag{3.14}$$

Note that ω is the angular frequency in radians of the propagating electromagnetic wave. In both cases, the plasma frequency is given by Equation 3.15, where q is the electron's charge and m_e is the electron's mass.

$$\omega_{pe} = \sqrt{\frac{N_e q^2}{\epsilon m_e}} \tag{3.15}$$

When multiplied together, the product of Equations 3.13 and 3.14 quantities is the speed of light squared, and so it is easy to see that when one increases, the other must decrease to maintain the accepted constancy of the speed of light (*Kintner and Ledvina*, 2005).

One last parameter particular to plasmas and critical to detection of electron densities is the *Debye length*: a plasma specific characteristic distance that essentially tells one the distance of influence in a plasma. It is defined as:

$$\lambda_D = \sqrt{\frac{k_B T_e \epsilon_0}{N_e q^2}} \tag{3.16}$$

where k_B is Boltzmann's constant, T_e is the temperature of the plasma electrons, and ϵ_0 is the permittivity of free space. If within λ_D, particles will exhibit individual behaviors, while outside collective behaviors take over. More specifics on all of these topics including derivations can be found in many of *Kintner's* publications including *Kintner and Ledvina* (2005); *Kintner et al.* (2007), any number of space environment or plasma physics texts (*Knipp*, 2011; *Schunk and Nagy*, 2009), or in papers like *Yeh and Liu* (1982).

3.2 Global Navigation Satellite Systems

GNSS are used in a number of commercial and scientific applications including precision landing and navigation, GNSS-based plate-tectonics and, particular to this work, GNSS-based ionospheric research (*Davis*, 1996). Other GNSS systems include Galileo (European), GLONASS (Russian) and BeiDou (Chinese) (*Misra and Enge*, 2006). While these may be included in future efforts, this work focuses solely on GPS.

3.2.1 System Architecture

The GPS constellation is one of several GNSS on orbit that provide real time position, navigation and timing (PNT) to global users, and reached full operating capacity in 1995. Its first well-known operational application came in OPERATIONS DESERT SHIELD and DESERT STORM, where it succeeded far beyond the hopes of its designers (*Dissinger*, 2008). Since then, it continues to undergo various system upgrades, and with each, improves on the capabilities provided to its users. The GPS constellation reached full operating capacity in 1995. GPS satellites are configured at a 55° orbital inclination across six orbital planes, spaced evenly around the globe, giving near global coverage. Its orbital geometry, frequency configuration, public signal structure and near omnipresence allow GPS to provide a means to measure the variable high-latitude ionosphere (*Misra and Enge*, 2006). GPS operates in the UHF band and transmits a variety of signals used for positioning calculations including the course/acquisition (C/A) on L1, and civil codes on L2C and L5; and Department of Defense only codes precision (P(Y)) and M

on L1 and L2. These frequencies and the codes modulated on them are summarized in Table 3.1. With the most recent upgrade, the system capabilities on orbit are formed by satellites that are part of Blocks IIR (completed in 2004), IIR (M) (completed in 2009), and IIF (completed in 2016). The next generation of the so-named modernized satellites, dubbed GPS III, are scheduled to begin launch starting in 2017[2] (*Dissinger*, 2008; *Misra and Enge*, 2006). For the purposes of this research, efforts will focus solely on the L1 C/A signal.

3.2.2 Ephemeris and Orbit Prediction

Users on the ground receive a file after first acquiring GPS satellites known as *broadcast ephemeris*. It contains within it all of the information needed for the receiver to know where to look for satellites in the sky. Unfortunately, this file is only good for about two hours. Several times each week, *yuma almanac* files are made publically available and have far more detail in them regarding the orbital elements of the constellation, and can be propagated for up to 24 hours. If even more precision is needed, *SEM* files can be downloaded and used. For the purposes of this research the *yuma almanac* will suffice as precision only on the order of decameters to kilometers is required,[3] (*Misra and Enge*, 2006).

Sidera is a software package developed to show GPS visibility based on published ephemeris data. It is as accurate as the ephemeris file used (*Bradley*, 2014). Because of the GPS orbital inclination, visibility as a receiver position approaches the poles becomes more and more limited, with the highest visible elevation angle decreasing proportional to latitude. At Poker Flat Research Range (PFRR), the highest elevation angle of a GPS satellite that is visible is near zenith, but most fall well short as shown in Figure 3.1. Note here that a unique design feature of GPS is its predictability: the orbits were specifically designed to coincide with a sidereal day, with the effect that each orbit precesses by approximately four minutes per day (*Axelrad and Larson*, 2006; *Misra and Enge*, 2006), i.e., satellites follow the same orbital track but get four minutes earlier each day.

[2] Additional information found at `http://www.gps.gov/`
[3] See Section 3.3

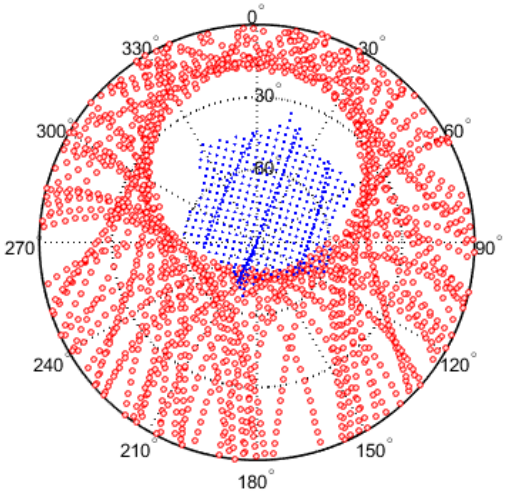

Figure 3.1: Polar plot showing visibility, and equivalently trajectories, of GPS satellites as seen by the CASES receivers at Poker Flat Research Range (PFRR, $\phi_{gd} = 65.13°$, $\lambda_{gd} = -147.47°$). Satellite positions in the sky are marked with red circles for the entire 24 hour period of 21 December 2015. The elevation mask is 10^o. See Section 3.2.2. Also shown is the Poker Flat Incoherent Scatter Radar (PFISR) beam array pattern (blue dots forming a curved hexagon, discussed in Section 4.1.3.

To a user, this means that the antenna is looking in roughly the same direction from day to day to find a given satellite at a given time, which is helpful if a broadcast ephemeris file has yet to download or is somehow corrupt. For this research, the predictability of the GPS constellation comes into play when requesting radar time for future passes. Screening GPS rays against the radar beams (discussed in Section 4.2.2), entails being able to predict up to a month in advance when a particular satellite will be at a certain location in the sky. Yuma files are obviously not valid for this extended interval, but if four minutes per day are subtracted from the visibility windows, with a small buffer on either side for orbital perturbations, then it is reasonable to predict when a conjunction is likely to occur.

3.2.3 Positioning Calculations and Error Sources

There are two ways that a GPS receiver calculates position. First, through the use of a pseudorange measurement, the distance between the receiver and a satellite whose signal it receives can

Table 3.2: Typical sources of GPS positioning errors (uncorrected) associated with Equations 3.17 and 3.18. Ranges are given where appropriate (*Kintner and Ledvina*, 2005; *Misra and Enge*, 2006).

Source	**Variable**	**Uncorrected Error [m]**
Clocks	$c[\delta_r - \delta^s]$	2
Troposphere (wet,dry)	ρ_{trop}	0.3, 3
Ionosphere	ρ_{ion}	5-40
Multipath	ρ_{multi}	3-5

be estimated. It is calculated based on the difference between the time the signal was transmitted and time the signal was received along a straight propagation path. Second, it estimates the number of cycles that a signal has propagated through along its path from a satellite to the receiver. Either can be used to perform a positioning calculation, and it is through the continuous update of these measurements and corresponding calculations that a receiver provides accurate time and position information. Note that a minimum of three satellites is required for a position solution, with a fourth providing a timing solution (*Misra and Enge*, 2006). The observable equations associated with the pseudorange and corresponding phase measurements are as follows:

$$P_i = \rho_r^s + c[\delta_r - \delta^s] + \rho_{trop} + \rho_{ion} + \rho_{multi} + \rho_{rel} + \epsilon_i \tag{3.17}$$

$$\phi_i \lambda_i = \rho_r^s + c[\delta_e - \delta^s] + \rho_{trop} - \rho_{ion} + \rho_{multi}^{\phi} + \rho_{rel} + \epsilon_{\phi_i} + N_i \lambda_i \tag{3.18}$$

Here ρ_r^s is observation either in meters or cycles; $c[\delta_r - \delta^s]$ is the difference in the receiver (δ_r) and satellite (δ^s) clock biases respectively; ρ_{trop}, ρ_{ion}, ρ_{multi} and ρ_{rel} are errors due to the troposphere, ionosphere, multipath and relativity, respectively; and, ϵ_i and ϵ_{ϕ_i} are noise terms. Note the sign differences in the two equations and that the phase equation (Equation 3.18) has an additional term for the phase ambiguity $N_i \lambda_i$. Variables found in these equations, along with typical values for the associated errors if left uncorrected are found in Table 3.2. Normally, corrections to these equations are made to minimize errors and calculate a position solution (e.g., differencing of the same measurement across two frequencies).[4] Under storm time conditions, whether local or global, ionospheric errors are not always able to be corrected (*Kintner and Ledvina*, 2005).

[4] For details on exactly how errors are corrected and measurements processed for a position and/or timing solution, see, e.g., *Misra and Enge* (2006).

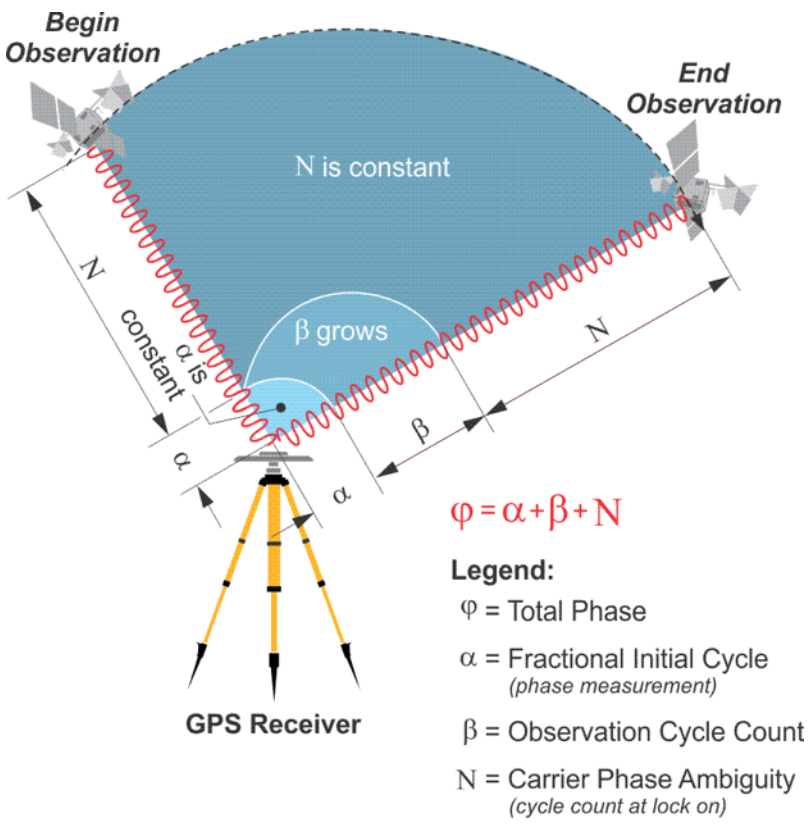

Figure 3.2: A pictorial representation of the components of the GPS carrier phase measurement, ϕ_i. Image source: `https://www.e-education.psu.edu/geog862/node/1729`.

Looking at the phase measurement of Equation 3.18 from the perspective of the electron density at each point along the signal path, n_e, each phase measurement ϕ_i, can also be written as is shown in Equation 3.19 (*Kintner et al.*, 2007).

$$\phi_i = \frac{q^2}{2c\epsilon_0 m_e f (2\pi)^2} \int n_e \mathrm{d}\rho \tag{3.19}$$

The quantity at the end, $\int n_e \mathrm{d}\rho$, defines the total electron content (TEC) along the signal path, and the equation includes previously defined quantities plus the electron charge, q, and mass of an electron, m_e. A single TEC unit (TECU) is defined as 10^{16} e/m^2, and the standard deviation of phi, σ_ϕ, is discussed later as calculated from the phase measurement presented in Equation 3.18 (*Kintner et al.*, 2007; *Misra and Enge*, 2006). It is worth noting here that 1 TECU is the equivalent of 0.16 m in the pseudorange observable (*Skone and Shrestha*, 1999).

A GPS receiver's measurement of ϕ_i has several components, and a depiction of these is

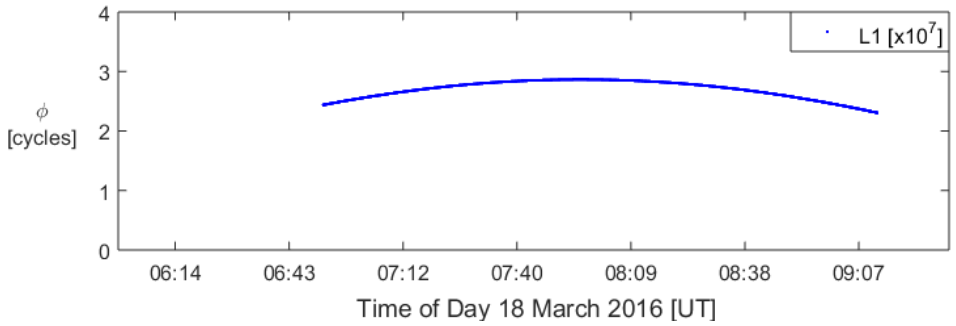

Figure 3.3: Phase data recorded by the CASES receiver on L1 at PFRR on 21 December 2015.

shown in Figure 3.2. First, the receiver records the initial fractional phase (α), and then estimates the carrier phase ambiguity (N), which are both constant during a series of observations unless the receiver loses lock and then N is reset. Finally the receiver accumulates the cycle count (β) during the satellite pass, which grows with Doppler shift. The carrier phase measurement is then the sum of these: $\phi_i = \alpha + \beta + N$. A graphical representation of this measurement is shown in Figure 3.3, which shows a series of phase measurements on the GPS L1 signal from a Connected Autonomous Space Environment Sensor (CASES) receiver at PFRR on 21 December 2015. Note that the plot shows an inverted parabola that indicates the motion of the satellite: as the satellite is ascending in the sky relative to the receiver the phase count increases, and as the satellite is descending in the sky the phase count decreases.

Unlike CASES receivers, many other types of receivers record observations in a RINEX format which has predefined standards for how the values are represented. The pseudorange measurement presented in Equation 3.17 as recorded in a RINEX file has the shape of an up-right parabola with the estimated range to the satellite decreasing as the satellite ascends to its peak elevation in the sky, and increasing as the satellite descends. RINEX formatting standards set the carrier phase observable to have a similar format, and as such the measurement is recorded proportional to negative Doppler shift and has the shape of an inverted parabola as is shown by the blue line in the top plot of Figure 3.4.[5] Here is seen the carrier phase observable on L1 (blue) as reported by

[5] For all RINEX observable definitions see `https://igscb.jpl.nasa.gov/igscb/data/format/rinex211.txt`.

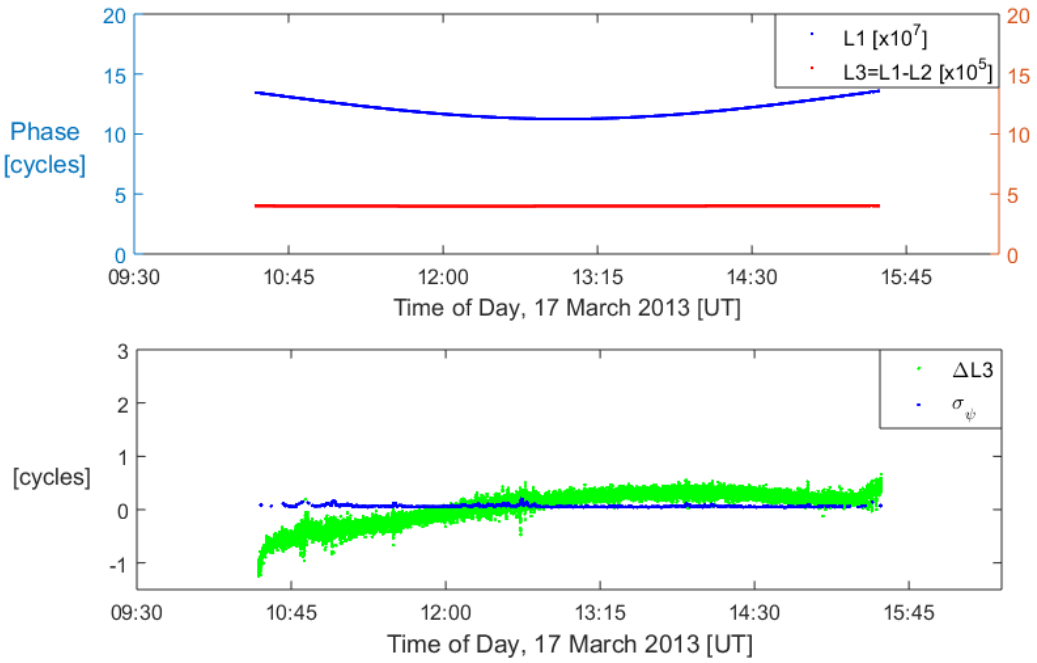

Figure 3.4: Phase data recorded by the NETR8 receiver at Toolik, Alaska on 17 March 2013; all units are in cycles. (a) L1 adjusted carrier phase data (blue) and $L3 = L1 - L2$ (red). (b) $\Delta L3$ (green) and σ_ψ (blue).

a NETR8 receiver at Toolik, Alaska. Other quantities in this figure are discussed in Section 3.2.4.

Scintillation can degrade a signal through associated power and/or phase fluctuations of the signal at the receiver. In some instances the degradation is so severe that one of two things, if not both, can occur. First, in the presence of amplitude scintillation, the receive signal power drops below the receiver threshold; and, it is no longer able to acquire or track the satellite (*Skone and De Jong*, 2000; *Kintner et al.*, 2007). Second, and the subject of this research, abrupt changes in phase cause an inability to track the phase because of an induced Doppler shift (*Skone and De Jong*, 2000; *Kintner et al.*, 2007). In both cases, errors, both large and small, are introduced into the positioning solution (*Skone and De Jong*, 2000; *Morrissey et al.*, 2004; *Kintner*, 2004; *Kintner et al.*, 2007).

3.2.4 The Phase Scintillation Index

Scintillation intensity is measured by the phase scintillation index, σ_ϕ. First the geometry-free observable (range or phase measurement with geometric effects of the satellite orbit removed), shown in Equation 3.20 is calculated, where L_1 and L_2 are the phase measurements on each of the two frequencies for a particular satellite, recorded in cycles.

$$\phi_g = L_1 - L_2 \tag{3.20}$$

Shown in Figure 3.4 are four quantities: the raw L1 carrier phase measurements presented at 1 Hz (top plot, blue arc), along with ϕ_g, i.e., L3 (top plot, red line). Note that it is 'flat-lined' which is an indication that geometric effects have been removed. The next step in the calculation is to take the difference of ϕ_g between two consecutive epochs for which there are no phase slips and divide it by the change in time as show in Equation 3.21.

$$\psi_i = \frac{(\phi_g^{t_i} - \phi_g^{t_{i-1}})}{(t_i - t_{i-1})} \tag{3.21}$$

This is represented graphically in Figure 3.4 (bottom plot, green), and this is the first time in the process where variations are plainly evident. From this calculation the standard deviation over a total of N measurements is taken and then updated epoch by epoch as shown in Equation 4.13 (*Ghoddousi-Fard et al.*, 2013). This calculation is also shown in Figure 3.4 (bottom plot, blue).

$$\sigma_\phi = \sqrt{\frac{1}{n}\sum_{i=1}^{n}(\bar{\tilde{\psi}}_i - \tilde{\psi}_i)^2} \tag{3.22}$$

Note that as part of the calculation for ϕ_g, measurements were eliminated if any of the pseudorange or phase measurements on either L1 or L2C were zero (*Misra and Enge*, 2006). It is worth noting here that in receivers where the sampling rate is ~1 Hz, the phase scintillation index calculated in this manner is known as the delta phase rate (σ_ψ). But when the sampling rate is at least 50 Hz and a single frequency's measurements are detrended prior to the final calculation, it is know as σ_ϕ (*Ghoddousi-Fard et al.*, 2013). This work focuses solely on the phase scintillation index as calculated by Connected Autonomous Space Environment Sensors (CASES) GPS receivers, discussed in Section 4.2.1.

3.3 GPS Scintillation Climatology

Although scintillation of GPS signals can happen any place in the globe at any time, certain regions of the globe are more prone to GPS scintillation at specific times of the day, during specific seasons, and at different years in the solar cycle (*Kintner et al.*, 2007; *Prikryl et al.*, 2010). These dependencies align with the variability of the ionosphere's structure on these time scales (see Sections 2.3 and 2.3.2). Generally speaking, increases in scintillation at high-latitudes also go with increases in geomagnetic activity, linked to the solar cycle (*Prikryl et al.*, 2015a). Many studies have been conducted at equatorial, mid and high-latitudes, and most agree with the geomagnetic activity dependence, although at mid- and low-latitudes it can both enhance and suppress scintillation (*Fejer*, 1991). While both phase and amplitude scintillation can occur globally, statistically phase scintillation dominates at high-latitudes (*Kintner et al.*, 2007; *Moen et al.*, 2013; *Prikryl et al.*, 2010; *Spogli et al.*, 2009a). The causes of scintillation were previously discussed; and simply put, when the signal experiences diffractively caused scintillation, both the phase and amplitude are affected. When refractive scintillation is occurring, primarily phase scintillation is seen. This leads to the natural conclusion that signal scintillation at the magnetic equator is primarily the result of diffractive scintillation, while that at the poles is primarily due to refractive scintillation (*Aarons*, 1997; *Kintner*, 2004; *Kintner et al.*, 2007).

Although a few of the more recent scintillation studies in the high-latitudes have been in the North American sector of the auroral oval (e.g., *Bergeot et al.* (2014); *Datta-Barua et al.* (2015); *Jin et al.* (2014); *Skone et al.* (2008); *Garner et al.* (2011)), most have been in Europe, specifically inside the polar cap, and they have been focused on evaluating the formation and evolution of polar cap patches and their linkage to magnetic reconnection in the cusp regions (*Goodwin et al.*, 2015; *Hosokawa et al.*, 2011, 2014; *Jin et al.*, 2014; *Liu et al.*, 2015; *Mitchell*, 2005; *van der Meeren et al.*, 2014, 2015). It has been shown that the bulk of the active high-latitude regions for scintillation are in the cusp region, extending into the dayside polar cap, and also in the nightside auroral oval near the boundaries (*Prikryl et al.*, 2011, 2015a). The vast majority of studies agree that

scintillation climatology within the polar cap differs from that of the auroral oval for one primary reason: particle precipitation linked to magnetic reconnection (*Yeh and Liu*, 1982; *Aarons*, 1997; *Spogli et al.*, 2009a; *Prikryl et al.*, 2010). There is also general agreement that scintillations are most often caused by electron density gradients associated with polar cap patches (blobs within the auroral zone), but can also be caused during times of active aurora, especially discrete auroral arcs (*Moen et al.*, 2013; *Prikryl et al.*, 2011, 2015a). *Prikryl et al.* (2011) specifically noted that during the solar minimum of 2008-2009:

> In the nightside auroral oval the phase scintillation was associated with auroral arc brightening and auroral substorms. Around local noon, the phase scintillation occurred in the cusp ionosphere that is perturbed by intense and dynamic convection.

What is not in agreement is which of the two phenomena dominate across the high-latitudes (the subject of this work).

As to temporal dependencies, scintillations have a magnetic local time dependence (*Aarons et al.*, 2000). *Prikryl et al.* (2011) found that phase scintillations '... primarily occur in the nighttime auroral oval and in the ionospheric cusp.' The reason for this, and the source of the debate, was that the aurora are linked to magnetic reconnection and particles precipitate from night-side magnetic reconnection at or near magnetic midnight, but also that polar cap patches convect into the auroral oval near magnetic midnight. Otherwise, the most severe scintillation occurs pre-midnight statistically more than post-midnight, and linked to '...auroral arc brightening and auroral substorms.' Also noted in the same study was that in the cusp region, scintillation was linked more to convection phenomena, but in the auroral zone it was linked to field alignment. The seasonal dependence is also different: the polar cap sees a winter increase (peaking in November), while in the auroral oval, scintillation is linked to the equinoxes, with the fall equinoctial season seeing slightly more than the spring (*Aarons*, 1997; *Aarons et al.*, 2000; *Prikryl et al.*, 2015a). Scintillations are also highly localized: a signal from the north could be potentially unperturbed while one from the south could be drastically impacted (*Yeh and Liu*, 1982; *Spogli et al.*, 2009a; *Moen et al.*, 2013; *Datta-Barua et al.*, 2015). Climatologies conducted by *Yeh and Liu* (1982); *Aarons* (1997); *Spogli*

et al. (2009a); *Azeem et al.* (2013) statistically link the most intense high-latitude scintillation to magnetic midnight and earlier times.

3.4 Recent Scintillation Studies

The current debate in this area of research is determining the relative importance of each of the known sources of scintillation as part of event driven and climatological studies. Although it has been known for some time that electron density gradients associated with patches are a source of scintillation, what is not known is the relative contribution of these phenomena to GPS scintillation across different high-latitude geomagnetic sectors. Many studies have been conducted across the polar cap and at the poleward boundary of the auroral oval, some specifically designed to answer this question. *Jin et al.* (2014) presented evidence that near magnetic midnight the most intense scintillation of GPS signals was seen from auroral blobs: polar cap patches that were further structured by auroral precipitation as they convected into the auroral zone. In other words, strong electron density gradients from plasma patches and auroral precipitation that existed at both E and F region altitudes along the path of the GPS signal caused the most intense scintillations. The aforementioned study was conducted at Ny-Ålesund with simultaneous GPS and all-sky imagery observations. Only 630.0 nm intensities were considered, and no radar was used to confirm enhancement altitudes. In *Jin et al.* (2016), two types of auroral blobs were further evaluated. First, those that originated as patches in the polar cap, convected into the auroral oval, and were then structured by particle precipitation. Second, those that were formed in the auroral oval solely from particle precipitation. They concluded that the former were the source of the greatest scintillation, which further specified the results from their study in 2014. *van der Meeren et al.* (2015) confirmed that the strongest scintillation occurs at the poleward edge of the auroral oval as patches convect into the auroral oval and particle precipitation structures them.

An earlier study in this region conducted by *Forte et al.* (2013), compared the relative contributions of the ionospheric layers over Tromsø, Norway, during geomagnetically quiet conditions. The European Incoherent Scatter Scientific Association (EISCAT) radar was used to track a par-

ticular GPS satellite, but used no other means to determine enhancement altitudes. Although E region ionization was present, results from this study led to the hypothesis that an F region patch moving across the line of site between the GPS receiver and the satellite in question provided the bulk of the scintillation producing enhancements. In *Forte et al.* (2016), the model of *Booker and Majidiahi* (1981) was used to causally link both E and F region structures to experienced GPS scintillation. They concluded that

> ...large-scale structures associated with the poleward edge of the ionospheric trough, with auroral arcs in the night side auroral oval and with particle precipitation at the onset of a substorm were indeed identified as responsible for enhanced phase scintillation at L band.

A study by *Kinrade et al.* (2013) at the geographic South Pole used both GPS and all-sky imagery observations, but radar measurements are not available at the South Pole to confirm enhancement altitudes. This time a correlative analysis was conducted between the scintillations observed and the intensities of the 557.7 nm and 630.0 nm emission lines. The authors assumed a fixed altitude for each emission (120 km and 200 km, respectively), and concluded that observed scintillation was more correlated to the 557.7 nm emissions. They speculated that this was due to the relative intensities of the two lines, stating that '...green emissions are characteristically a factor greater than red emissions.' Closer to the location of this analysis, a study by *Garner et al.* (2011) in Fairbanks, Alaska, compared the impacts of an auroral arc that interfered with the line of site of multiple satellites to near-collocated GPS receivers. Energy estimates after *Rees and Luckey* (1974) were used to determine that precipitating electrons with energies ranging from 2.5 to 4 keV resulted in E region ionization enhancements, but the analysis was again conducted without the benefit of radar data for confirmation.

Chapter 4

Observational and Contextual Tools

Presented in this chapter is a summary of the observational tools used in this dissertation. Each ground sensor is located at Poker Flat Research Range (PFRR), near Fairbanks, Alaska. The instruments, in the order they are discussed, are the Poker Flat Incoherent Scatter Radar (PFISR), Atmospheric Space Technology Research Associates' (ASTRA) Connected Autonomous Space Environment Sensor (CASES) GPS Receiver, and the digital all sky camera (DASC) at PFRR run by the Geophysical Institute at the University of Alaska, Fairbanks.

4.1 Radars

The impact of RADAR (RAdio Detection And Ranging) on society is unmistakable. This includes military uses such as the detection and identification of remote objects, civilian uses such as air traffic control and collision avoidance systems, and scientific uses including precipitation radars, wind radars and synthetic aperture radars. The concept is eloquently simple:

(1) send out a radio signal

(2) listen for its reflection

(3) determine the distance to the target from the time between transmit and receive

There are many parameters other than the distance to a target that can be detected based on the strength and shape of the return signal. This section will provide a brief overview of the broad basics of radars, and will specifically outline how these apply to the peculiarities of sensing the ionosphere with an *incoherent scatter radar (ISR)*.

4.1.1 Ranging Basics and the Radar Equation

The simplest parameter associated with radar returns is the distance to the target. If a signal is transmitted, assuming its velocity is the speed of light, c [m /s], and assuming that it is traveling through a volume, then the distance, r [m], that it travels in time t [s] is given by the relationship:

$$r = vt = ct \tag{4.1}$$

where v is its speed, and we assume nothing accelerates it along the way. This does not take into account the index of refraction of the transmission medium. Since a radar signal must travel to the target and back, the distance we are looking for is covered in half the time:

$$R = c\frac{t}{2} \tag{4.2}$$

where R is now the range to the target in meters, assuming the transmitter and receiver are co-located.

An electromagnetic wave that is intended to sense the ionosphere from the ground experiences environmental and system *losses*, as well as enhancements made by the system at both transmit and receive, known as *gains* (*Richards et al.*, 2010). These are taken into the account when estimating the receive strength of the signal, P_r in Watts [W], by the radar equation shown below. Note that gains typically appear in the numerator, while losses typically appear in the denominator.

$$P_r = \frac{P_t G_t G_r \lambda^2 \sigma}{(4\pi)^3 R^4 L} \tag{4.3}$$

Here P_t is the transmit power [W], G_t and G_r are the gains of the transmit and receive antennas respectively, λ is the transmit wavelength [m], and σ is the target's radar cross-section [m^2]. A full derivation of this equation is presented in many texts including the *Principles of Modern Radar* series and *Introduction to Airborne Radar* (*Melvin and Scheer*, 2013; *Richards et al.*, 2010; *Skolnik*, 2008; *Stimson*, 1998).

As a radio wave propagates through space, its power decreases proportional to $1/R^2$, hence the $1/R^4$ dependency for P_r. Antenna gains are a function of their geometry and of the radar's

operational wavelength, and a target's radar cross section is dependent upon its size, composition and radar signal wavelength. Transmit power is a function of cost and target size, and there are a variety of system gains and losses that are rolled up into the loss term, (L). These losses are typically either system losses or losses due to the propagation medium, and those appropriate to this research are discussed in the sections that follow (*Richards et al.*, 2010; *Stimson*, 1998).

4.1.2 Incoherent Scatter Radar

A particular type of radar, the *incoherent scatter radar (ISR)*, will be used for the purposes of this research. An ISR uses a series of pulses, each with a pulse width τ, to detect a target. The transmitter sends out an electromagnetic wave with many cycles lasting for time, τ, then listens for the returns, then sends another pulse with length τ, etc. The pulse width determines the range resolution, i.e., establishes the range bins for integration by:

$$\Delta R = c\frac{\tau}{n2} \tag{4.4}$$

where n is the index of refraction. The spacing between pulses is known as the *inter-pulse period (IPP)*.Associated with the IPP is an *unambiguous range*, which is the maximum range detectable without *aliasing*, i.e., without targets from one pulse appearing in another pulse's range bins.

$$R_u = c\frac{IPP}{2} \tag{4.5}$$

A final quantity to be considered for a radar is its *duty cycle* which is a measure of transmit time as a fraction of operational time. It is calculated as shown in Equation 4.6.

$$dutycycle = \frac{\tau}{IPP} \tag{4.6}$$

The duty cycle used is based on system capabilities and limitations. For example, the radar used in this research has a maximum operational duty cycle of 10%. This is not because pulse radars typically operate at a high peak power - they do not; but, they cannot operate for an extended period of time and thus are often average power limited, and must operate with a low duty cycle. Upon receive, the series of return signals is broken up into range bins, and each bin's sequence of

returns is summed over the integration period (i.e., *integrated*), to produce a final P_r. Adjusting the integration time for an ISR is tricky, as most of the time it is dependent on *autocorrelation function (ACF)*, which essentially establishes thresholds that must be crossed before the data can be considered to be fully integrated, i.e., correct.

In order to derive electron density from an ISR's receive power, adjustments are made to the radar range equation (Equation 4.3) particular to the actual target: sensing ionospheric electron density. First, the target being sensed is a plasma that is approximated as electrically neutral, and who's backscattered signal shape is dependent on the plasma characteristics. One of these characteristics is the radar cross section, σ, of a single electron. It is derived in several references including *Evans* (1962, 1969), and presented without proof:

$$\sigma = \frac{\sigma_e}{(1 + k^2\lambda_D^2)(1 + T_r + k^2\lambda_D^2)} \tag{4.7}$$

Here, σ_e is the cross section of a single electron (known to be on the order of 10^{-29} m^2), $T_r = T_e/T_i$ is the ratio of the temperature of the electrons to those of the ions, and the term $k^2\lambda_D^2$ is comprised of the Bragg scattering number[1] (k) and the Debye wavelength (λ_D, see Equation 3.16). The denominator accounts for the bulk plasma behavior since the transmitting wavelength of the radar is much larger than the Debye wavelength ($\lambda \gg \lambda_D$), and the plasma is assumed to respond as a unit.

The second adjustment to the radar range equation for sensing the ionosphere is to account for fact that the sensed target fills the entirety of the radar beam. The cross section represented in Equation 4.7 is for a single electron, but the target is a cluster of electrons that fills a volume of radius proportional to radar beamwidth and altitude, with height corresponding to the pulse width. The beam width in meters at a distance R from the antenna is estimated as $R \sin\theta$ where θ is the angular beam width. In most cases, θ is $\sim 1^\circ$ and the small angle approximation applies. These factors combined allow for the removal of one factor of $1/(4\pi R^2)$ from the range equation. The final equation prior to integration over the gain of the ISR's antenna as a function of elevation

[1] A great tutorial on Bragg-Scattering can be found at `http://www.radartutorial.eu/07.waves/wa52.en.html`.

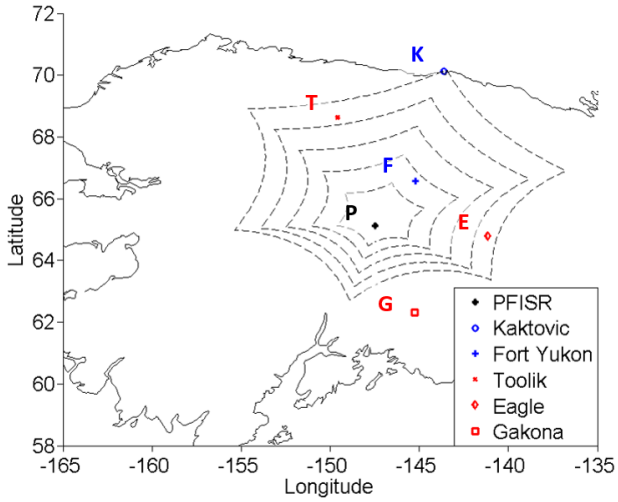

Figure 4.1: Locations of GPS receivers throughout Alaska overlaid on the PFISR beam pattern. Corresponding geographic and geomagnetic coordinates (as of 21 December 2015) are listed in Table 4.1.

angle, and assuming that the beam is spherically symmetric in azimuth, is given in Equation 4.8 (*Evans*, 1962, 1969).

$$P_r = \frac{P_t L N_e \sigma_e c \tau \lambda^2}{64\pi^2 R^2 (1 + k^2\lambda_D^2)(1 + T_r + k^2\lambda_D^2)} \int_\theta G^2(\theta) \sin\theta \mathrm{d}\theta \tag{4.8}$$

Here, system losses represented by L are a combined into on term with a value less than one, and the system is assumed to use the same antenna for transmission and receipt so that the antenna gain, $G(\theta)$, is the same. In the case of the Poker Flat Incoherent Scatter Radar discussed next, the equation after accounting for the gain of the antenna array, integrating, and solving for the electron density becomes Equation 4.9 (*Gudivada*, 2014).

$$N_e = (K_{sys})(\frac{1}{P_t \tau_p})(R^2 P_R)[(1 + k^2\lambda_D^2)(1 + T_r + k^2\lambda_D^2)] \tag{4.9}$$

A new term, the system constant K_{sys}, consolidates all of the physical constants and system parameters into one term, and P_r is modified depending on the ISR noise characteristics. Both are discussed in the next section.

4.1.3 Poker Flat Incoherent Scatter Radar

There are numerous methods for deriving electron density, N_e, at a particular point in space. For the purposes of this dissertation, we are using N_e derived from experiments run at the Poker Flat Incoherent Scatter Radar (PFISR).[2] PFISR is an incoherent scatter radar (ISR) with an electronically steered array (ESA) located at Poker Flat Research Range, near Fairbanks, Alaska. It has a northward oriented bore site, tilted 16° from zenith and aligned to a 15° azimuth. Figure 4.1 shows PFISR's geographic location, proximity to GPS receiver sites summarized in Table 4.1, and the maximum spatial extent of its beam pattern (dashed black lines) at 150, 250, 350, 450 and 550 km altitudes. While a more robust description of the PFISR antenna structure, beam patterns, and overall capabilities can be found in many sources including that by *Heinselman and Nicolls* (2008); *Dahlgren et al.* (2012); *Semeter et al.* (2009) and others, highlighted here are relevant properties.

PFISR provides close to 500 pre-programmed beam directions for a given experiment, each beam having a beamwidth of 1.1°×1°. However, a trade exists between the number of beams available and the cadence of the final data.[3] To operate, PFISR can only point in one direction for a given integration period. In order to sense in multiple directions, it must switch between them, typically in the same sequence throughout the experiment. For instance, presume that a user has chosen eight beams to operate during an experiment, and that the integration period for the experiment is 15 seconds. Then PFISR will progress through a sequence of the eight beams, each taking 15 seconds at a time, for a total of two minutes before the radar revisits the first beam in the sequence. Although the data for each beam were taken 15 seconds apart, since it is not repeated for a full two minutes, the temporal resolution of the data turns out to be two minutes. For ionospheric structures that change on the order of seconds,[4] this can provide a large scale context, but cannot provide details about what is going on at a particular location over time.

[2] More information regarding PFISR and its capabilities can be found at `http://amisr.com/amisr/about/about_pfisr/`.

[3] For a full list of PFISR beam codes see `http://amisr.com/amisr/about/about\_pfisr/pfisr-specs/`.

[4] See Section 2.3.2.

Table 4.1: Summary of PFISR and select GPS Receiver Sites.

Site	ϕ_{gd} (°)	λ_{gd} (°)	ϕ_{gm} (°)	λ_{gm} (°)
PFISR	65.130	-147.47	65.55	-92.61
PFRR	65.119	-147.43	65.37	-92.24
Kaktovic	70.132	-143.64	71.13	-92.76
Fort Yukon	66.560	-145.21	67.24	-91.21
Toolik	68.629	-149.60	68.62	-96.59
Eagle	64.777	-141.16	66.15	-86.33
Gakona	62.305	-145.27	62.86	-88.72

For the ionosphere specific radar equation in Section 4.1.2, the PFISR system constant K_{sys} is calibrated monthly based on daytime plasma line measurements (*Evans*, 1969). The receive power is modified to account for noise and calibration data taken pulse to pulse by:

$$P_R = P_{cal}\frac{Signal - Noise}{Cal - Noise} \tag{4.10}$$

where $P_{cal} = k_B T_{cal} B$ is the system noise power calculated using Boltzmann's constant, k_B, the calibrated system temperature T_{cal} and the receiver bandwidth, B. $Signal$ is the integrated receive power, while $Noise$ and Cal are noise and calibration measurements for the radar taken for each pulse. The processing of return data to account for Debye length and electron to ion temperature ratio is more complicated and beyond the scope of this discussion. For more information see the provided references, but note that because neither λ_D nor T_r are known *a priori*, their calculation requires an iterative solution based on the spectra of the return signals.

Some of the PFISR parameters described previously can be modified while others are fixed. In particular the following can be adjusted:

(1) the number of beams used during an experiment - determines the cadence

(2) integration time - sets cadence and uncertainties of the data

(3) inter-pulse-period - sets the unambiguous range

(4) coded or uncoded pulses - determines effective range of the pulses

(5) pulse width - sets the range resolution

For example, in order to achieve a maximum unambiguous range (Equation 4.5) of $R_u = 300$ km, with a 30 second cadence over two beams while maintaining the 15 second integration time, an IPP of

$$IPP = 2\frac{R_u}{c} \approx 0.002 = 2\ ms \tag{4.11}$$

is required. If additionally a range resolution of 15 km is required, then a pulse width of

$$\tau = 2\frac{\Delta R}{c} \approx 10 \times 10^{-5} s = 100\ \mu s \tag{4.12}$$

is used.

4.1.4 Pulse Description

In the experiments conducted to support this work, one or both of two pulse types are used: long pulses and coded pulses. Long pulses are comprised of a single pulse of signal at the ISR transmit frequency that last for the duration of the pulse width, τ. The initial experiment configuration presented in both the December 2015 case study (Chapter 6) and Climatology Campaign I (Chapter 7) use long pulses with a pulse width of $\tau = 480$ μs. This translates to fitted range bins determined by the pulse width of $\sim$ 36 km. Long pulses are also used as part of Climatology Campaign II (Chapter 8), however that portion of the data set was not used in the final analysis presented in this work. The benefit of using the long pulse is that the upper portions of the ionosphere can be sensed with relatively high temporal resolution. Unfortunately the temporal resolution comes at the cost of spatial resolution: 36 km range bins only yield one or two data points in the E region ($\sim$100-150 km altitude) where ionospheric structures associated with particle precipitation can be less than one km in scale.

The second type of pulse used, coded pulse, appears in Climatology Campaign II, and will be used in the multi-beam climatology campaign described in the Future Work section of Chapter 10. The pulses are coded by randomized fractional lag alternating codes developed over roughly a decade by and described in *Lehtinen and Haggstrom* (1987); *Huuskonen et al.* (1996) and *Lehtinen et al.* (1997). While a full treatment of the use of these codes is beyond the scope of this work, it

is worth noting a few key points regarding their use as compared to long pulses. In coding a radar pulse, it is subdivided into many subpulses which are in turn 'coded' via one or more changes in their phase. The simplest of these phase changes is to alternate in some manner between 0° and 180° phase, which are often represented as a series of pluses or minuses. In Climatology Campaign II (Chapter 8), the coded pulses are 480 μs in length, are subdivided into 30 μs subpulses (a total of 16 bits), and each pulse is oversampled at 10 μs [*Varney, R., personal communications 2017*]. This allows the returns from each bit to offer simultaneous information for multiple range bins using fractional lag processing, and greatly increases the spatial resolution from a pulse that is the same duration as the previous long pulse. Coded pulses do, however, require longer integration time and spatial resolution comes at the cost of temporal resolution.

4.2 GPS Data

4.2.1 Receivers

Many different civilian GPS receivers are available on the market, ranging from small hand held devices, to much larger geodetic grade devices that produce accuracies of millimeter scales with the right antenna and some post processing. The receivers in use for this analysis are primarily Atmospheric & Space Technology Research Associates' (ASTRA), Connected Autonomous Space Environment Sensor (CASES), a dual-frequency GPS receiver (*Crowley et al.*, 2011; *O'Hanlon et al.*, 2011). CASES receivers are specifically designed to provide high fidelity space weather measurements including total electron content (TEC), and both amplitude and phase scintillation data. The CASES receiver at PFRR is coupled with a reference oscillator (10 MHz Vectron MX-041) to assist in minimizing receiver clock bias. The impact on calculations is discussed later in this section. The CASES receiver at PFRR is part of an array deployed by ASTRA to span Alaska from North to South which was installed in 2012, with the purpose of monitoring high-latitude scintillation and TEC. The CASES receivers have also been used successfully for several years near Amundsen-Scott South Pole Station in Antarctica (*Deshpande et al.*, 2012; *Clauer et al.*, 2014; *Kim*

et al., 2014).

CASES receivers are deployed at each of the locations shown in Figure 4.1, summarized in Table 4.1, and operated by ASTRA. CASES provides space weather monitoring in many forms including signal phase scintillation data via the phase scintillation index (σ_ϕ).[5] This particular set of receivers calculate σ_ϕ as discussed in Section 3.2.4, with modifications discussed as follows. The calculations are performed at a cadence of 100 s with data taken from the L1 C/A and L2-C signals. Local processing can be done to achieve σ_ϕ at any number of user defined cadences (*Crowley et al.*, 2011; *O'Hanlon et al.*, 2011).

CASES receivers take steps to minimize clock biases and geometric effects without removing the ionospheric effects. Rather than calculating the geometry-free observable (as in Equation 3.20). CASES receivers first remove clock effects through the use of a reference satellite on the same frequency. At each epoch, CASES identifies the satellite with the least amount of scintillation on a particular frequency as the reference satellite, and second as the alternate. In the CASES receiver used for this experiment, the reference oscillator integrated into its system provides a stable enough environment that this subtraction is not necessary, a technique employed with other CASES receivers. The clock-free measurement is then calculated by differencing these two signals, or in the case of a reference oscillator this differencing is skipped.

The range from and given GPS satellite to the receiver is constantly changing because of orbital motion. The range is farthest when the satellite is rising or setting from the perspective of the receiver, and least when the satellite is at its peak elevation in the sky. Therefore, the resulting 102.4s interval of phase measurements are passed into the computation of a third order polynomial fit, which is then subtracted to remove the geometry. Once estimated the phase change due to a changing range to the satellite is removed. Normally this would be done by applying Equation 3.20 directly, but the effects on a single signal are being isolated. Once this process is complete, high frequency scintillation information that is not sampled by the phase tracking loop is added through

[5] CASES also provides total electron content (TEC) calculations, the amplitude scintillation index (S_4), the decorrelation time (τ_0), and the scintillation power ratio. For more information on these indices see *Crowley et al.* (2011); *O'Hanlon et al.* (2011); *Humphreys et al.* (2009).

the use of in-phase (I) and quadrature (Q) channel measurements in the form of: $\tan^{-1}(Q/I)$ (converted to cycles), yielding $\widetilde{\phi}_{npd}$ as outlined in *O'Hanlon et al.* (2011). From here, the process is the same as previously described for calculating σ_ϕ (*Crowley et al.*, 2011; *O'Hanlon et al.*, 2011).

$$\sigma_\phi = \sqrt{\frac{1}{n}\sum_{i=1}^{n}(\bar{\widetilde{\phi}}_{npd} - \widetilde{\phi}_{npd})^2} \tag{4.13}$$

For the purposes of this analysis a sliding 102.4 s interval was used for calculations and a σ_ϕ value calculated every second. Based on the receiver sampling rate of $100Hz$ and a $102.4s$ sampling interval, the number of samples processed comes out to $N = 10240$. However, we note that on the CASES receivers most measurement cadences are user-programmable, so different window lengths are possible.

4.2.2 Ephemeris Screening

GPS rays that traveled along a single PFISR beam are used in this research and discussed here. Prior to screening, satellites were discounted if their azimuths did not fit within a window around the PFISR beam in consideration, eliminating rays that were physically unable to traverse the PFISR beam window. Signals were also eliminated if they had an elevation angle to the receiver site less than 30^o. This initial screen is done both to minimize the impact of multipath errors as discussed in the literature (*Misra and Enge*, 2006), and also because the minimum elevation angle of the set of the PFISR beams is 35°.

The geometry for screening GPS signals that traveled parallel to individual PFISR beams

Table 4.2: Synopsis of vectors shown in Figure 4.2.

Vector	Description	Source
$\vec{r_1}^*$	Earth center to PFISR	Converted from lat/lon/height
$\vec{r_1}$	Earth center to CASES receiver	Converted from lat/lon/height
$\vec{r_2}$	Earth center to GPS satellite	Sidera
$\vec{r_3}$	CASES receiver to GPS satellite	$\vec{r_3} = \vec{r_2} - \vec{r_1}$
$\vec{r_{PF}}$	PFISR to various ranges along the beam	Beam codes, az/el/range

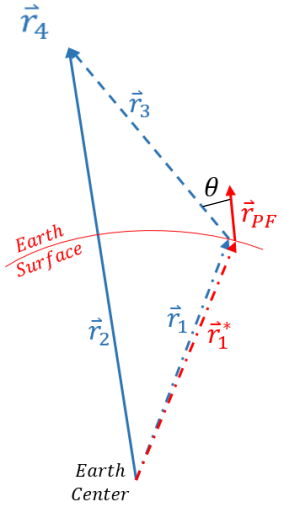

Figure 4.2: Line of site geometry for comparing PFISR beams with GPS ray paths, vectors annotated and defined in Table 4.2.

began with the geometry shown in Figure 4.2, where PFISR and the receiver site are considered to be co-located. Vectors are summarized in Table 4.2. The screening is done with a 5^o cone around the beam's East-North-Up (ENU) unit vector ($\vec{r}_{PF}$), rotated into Earth Centered Earth Fixed (ECEF) coordinates for comparison.[6] To screen GPS rays that most likely traversed a given PFISR beam, a comparison between $\vec{r}_3$ and $\vec{r}_{PF}$ using a simple vector dot product was made as shown in Equation 4.14

$$\vec{r}_3 \cdot \vec{r}_{SIP,exp} = |\vec{r}_3||\vec{r}_{SIP,exp}|cos(\theta) \tag{4.14}$$

An initial screening cone with a 5^o radius was used on ephemeris data that was spaced at one minute intervals. The total consecutive time intervals that resulted for each satellite were then used to pull one second ephemeris data that corresponded to the scintillation data spacing. Also pulled were corresponding normalized electron densities.

4.3 All Sky Imager

The Digital All Sky Camera (DASC) at PFRR was built in 2007 by KEO Scientific (Calgary, Alberta, Canada). It takes optical imagery at the previously discussed red (630.0 nm), green

[6] See Appendix B.2 for coordinate system definitions.

(557.7 nm) and blue (427.8 nm) emission lines, using an Electron Multiplying Charge-Coupled Device (EMCCD) manufactured by Andor (model BU8201). The DASC is oriented at zenith and is operational from dusk to dawn, during the winter months of October through April. When taking images it cycles through the three different wavelengths with approximately 12 seconds between consecutive images of the same wavelength. [*Hampton, D., personal communications 2016*].

Raw imagery files from the DASC at PFRR were converted from *analog to digital unit* (ADU) to Rayleighs through the application of Equation 4.15. This was done for the green, red and blue line emissions described previously in Section 2.3.4.

$$\alpha \frac{(ADU_{image} - ADU_{background})}{t} \tag{4.15}$$

Here α is a calibration conversion factor specific to the DASC for each wavelength (green: 70 R/ADU, blue: 105 R/ADU, and red: 27 R/ADU), $ADU_{background}$ was found by averaging ~100 pixels from the image corners that are not mapped to the sky, and t is the exposure time (green/blue: 1 s, red: 1.5 s) [*Hampton, D., personal communications 2016*].

Care must be taken to ensure energies are properly derived from the intensity ratios discussed in Section 2.3.4 using DASC data. Two factors are of concern: cloud cover and the storm time O/N_2 ratio. Cloud cover can increase the scattering of the emissions, translating to lower intensities of all wavelengths at the DASC, although green is disproportionately affected. As was also discussed in Section 2.3.4, the O/N_2 ratio decreases during storm time which disproportionately affects the green line as well. Since precise altitudes are not required for this research (only delineation between E and F region), adjustments based on O/N_2 ratios are not necessary (*Strickland et al.*, 1989; *Grubbs*, 2016).

Chapter 5

March 2013: Case Study I

The March 2013 equinoctial season provides an opportunity to study ionospheric disturbances during both geomagnetically quiet and disturbed conditions; and, presented here are a series of examples from this time. An experiment set was then designed and executed during the Winter Solstice of 2015 to address limitations and lessons learned from the March 2013 analysis, and this case study is presented next.

5.1 Geomagnetic Environment

During the time of 7-17 March 2013, there was one geomagnetic storm, along with a series of quasi-nightly auroras and substorms, as is evidenced by the indices shown in Figure 5.1. For the bulk of the time leading up to the 17th of March, the DST stayed at or above zero, then a geomagnetic storm occurred as the result of a solar CME on 17-19 March (discussed in Section 5.3.2). The Kp index for the pre-storm period stayed at or below 3, indicating a time of geomagnetic calm. However, as seen in the local magnetometer plot from PFRR, there was local magnetic activity, either in the form of a single auroral event or an overall auroral substorm on the nights of 7-16 March. Also evidenced in the magnetometer data is the St. Patrick's Day Storm. Presented here are data from the night of the 7th of March (auroral activity), and from the St. Patrick's Day Storm. Other analysis of this storm include *Dmitriev et al.* (2017); *Kalita et al.* (2016); *Yue et al.* (2016).

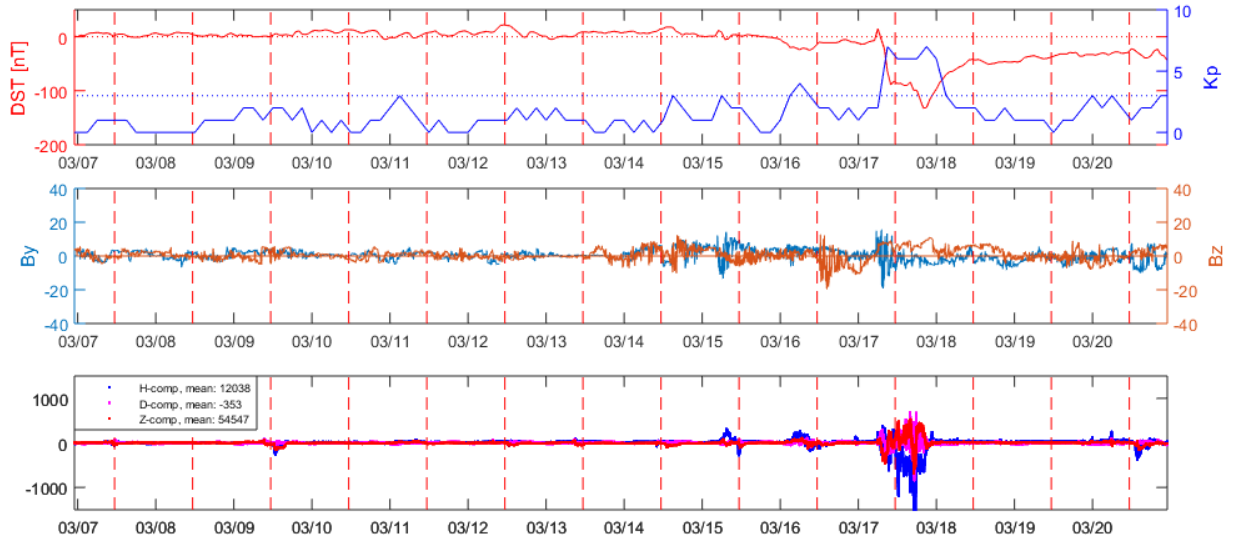

Figure 5.1: DST and Kp (top), ACE derived B_y and B_z (middle), and PFRR local magnetometer data (bottom) for select days from the month of March 2013. The horizontal red line on the top and middle plots indicates a zero line for the DST and the magnetic field components, respectively. The horizontal blue line in the top row indicates a Kp value of 3 (see Section 2.2). The magnetometer data in the bottom row are displayed as deviations from the mean values that are listed in the legend.

5.2 Sensors

Numerous experimental campaigns were performed using PFISR during the month of March 2013. For the purposes of this analysis, data from two of these campaigns are presented: the *POESsat30* (07 March) and *PINOT_Nighttime31* (17 March) experiment campaigns.[1] Beams used for each of these experiments, including azimuth and elevation data, are summarized in Table 5.1. Note that these were predefined campaigns and not observational modes that were developed as part of this research.

As was highlighted in Sections 4.1.3 and 4.1.4, PFISR is capable of using two pulse modes to characterize the E and F region ionosphere: coded pulse and long pulse, as well as a third mode for the D region: Barker Code. In general long pulses allow for better temporal resolution, while coded pulses allow for greater spatial resolution (*Nicolls et al.*, 2007; *Nicolls and Heinselman*, 2007;

[1] All experiments run on PFISR for the month of March 2013 can be browsed at `http://amisr.com/database/61/cal/2013/3/`. This includes data availability and limited visualizations.

Table 5.1: PFISR Beam List for the *PINOT_Nighttime31* experiment including azimuth and elevation for each beam, March 2013.

Beam	Azimuth	Elevation	POESsat30	PINOT_Nighttime31
63197	-35.09	66.19		x
63239	-16.23	58.68		x
63281	-2.95	47.55		x
63365	76.09	66.19		x
63401	57.23	58.68		x
63449	43.95	47.55		x
64016	14.04	90	x	x
64019	20.5	88	x	
64022	20.5	86	x	
64025	20.5	84	x	
64028	20.5	82	x	
64031	20.5	80	x	
64037	20.5	76		x
64055	20.5	64		x
64079	20.5	50		x
64103	-154.3	87.5	x	
64109	-154.3	85.5	x	
64115	-154.3	83.5	x	
64121	-154.3	81.5	x	
64133	-154.3	79.5	x	
64157	-154.3	77.5	x	x
64964	-34.69	66.09	x	
65066	75.03	65.56	x	

Semeter et al., 2009). Normally, PFISR operates in a mode combining long and coded pulses, resulting in a data cadence of one to three minutes spread out over eight to twelve beams. This was the case for both the *POESsat30* and the *PINOT_Nighttime31* experiment sets. The former was conducted with interleaved Barker Code and long pulses that cycled over 14 beams, and the latter was conducted with interleaved coded and long pulses that cycled over 11 beams (listed in Table 5.1). Long pulses each had a pulse length of 330 μs, and final processed data has a temporal resolution of 3 minutes and a spatial resolution of roughly 24 km. Alternating code pulses of 480 μs were used resulting in a 6 km spatial and 5 minute temporal resolution once processed. Barker code pulses of 130 μs were used resulting in a 0.75 km spatial and 2 minute temporal resolution once processed.

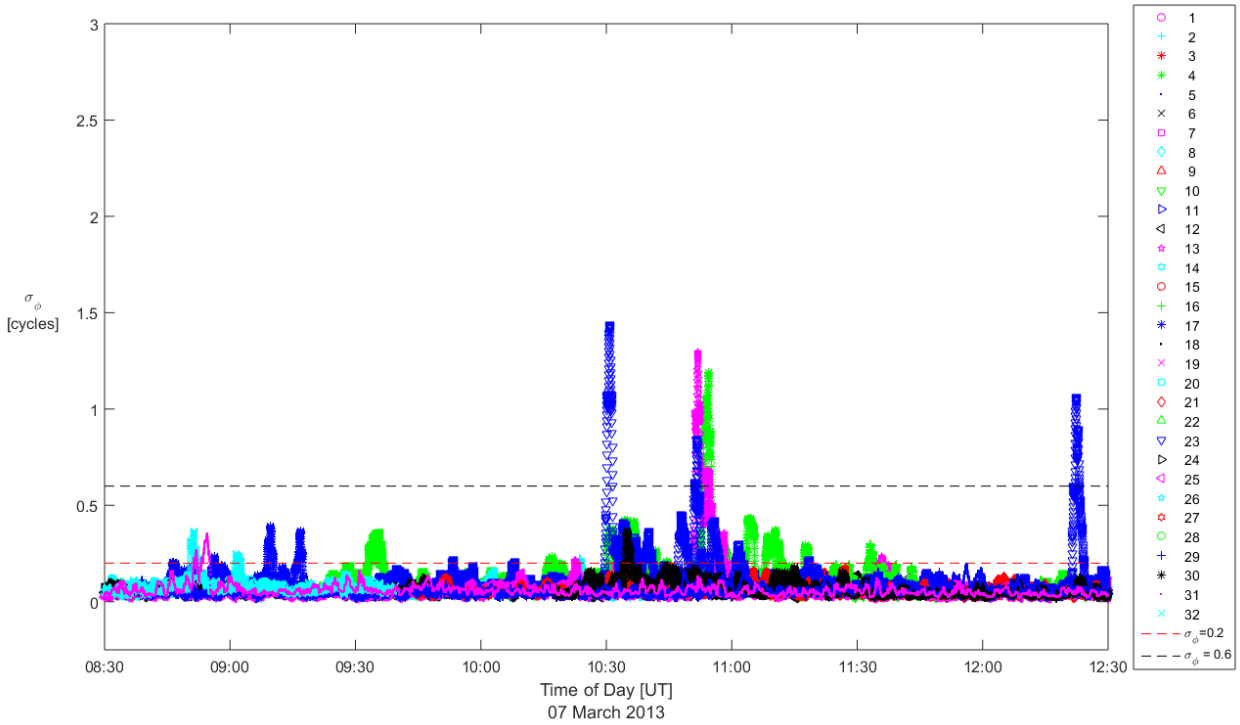

Figure 5.2: PFRR CASES σ_ϕ for 07 March 2013, all PRNs (legend on right side of plot), and zoomed to 0800-1300 UT. The red dashed line indicates $\sigma_\phi = 0.2$ cycles and the black dashed line represents $\sigma_\phi = 0.6$ cycles.

DASC imagery was taken for the month of March 2013. Imagery data was processed as previously discussed in Section 4.3. CASES receivers operated continuously during this period, and raw data was post-processed at a one second cadence for analysis. PFISR data from the 7th and 17th of March are compared to these data sets, however the correlation analysis run later used DASC and CASES data from multiple days, narrowed down to hours when scintillation was experienced. These dates and times are summarized in Section 5.3.3.

5.3 Data

5.3.1 Auroral Activity, March 2013

In Figure 5.2 a plot of σ_ϕ is shown from the CASES receiver at PFRR, plotted at one second cadence for all PRNs visible to the receiver on 07 March 2013. The times are limited from 0830-

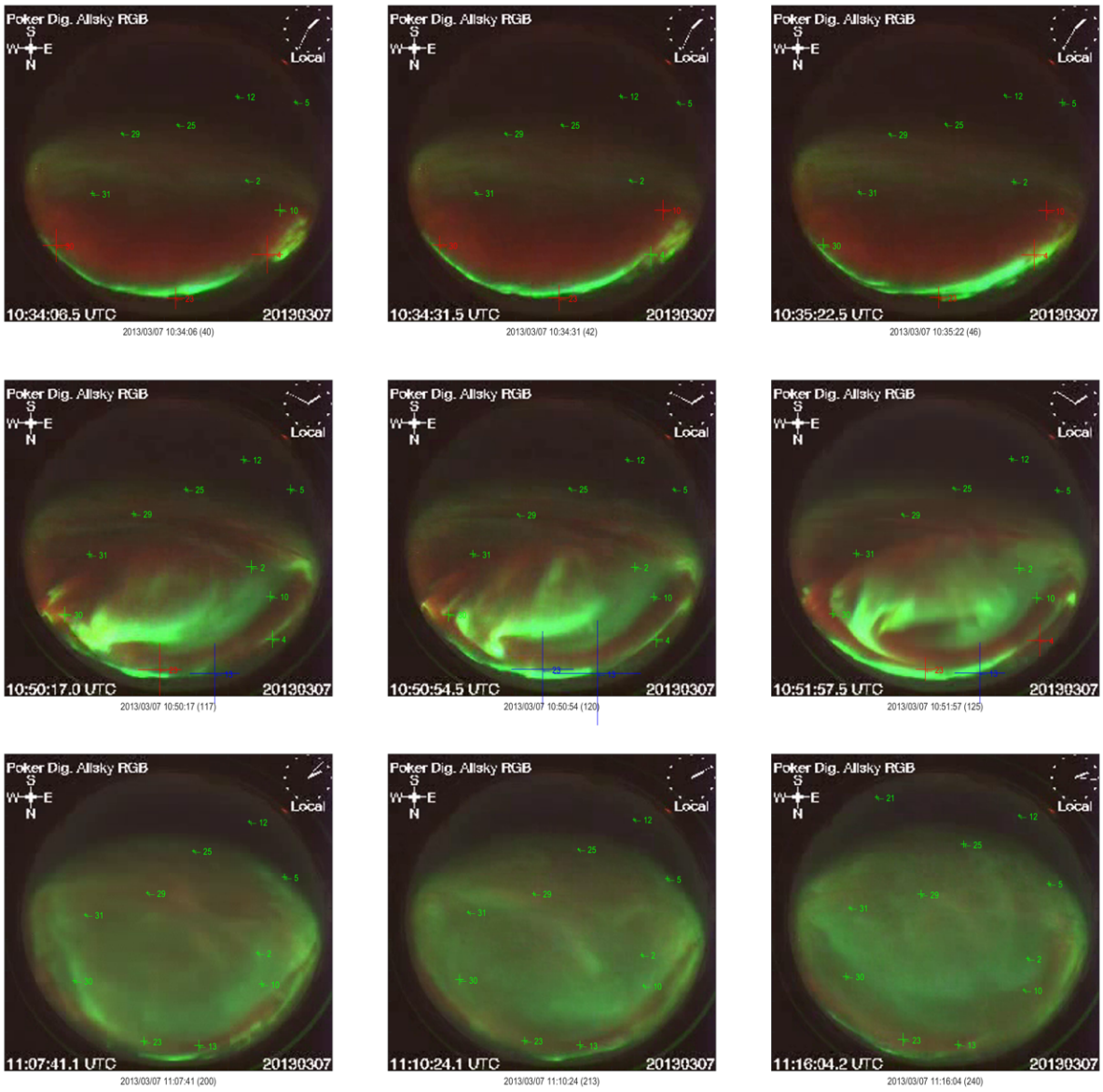

Figure 5.3: DASC consolidated images for 07 March 2013 overlaid with a colored and sized '+' for each satellite in view, proportional to the scintillation experienced at the PFRR CASES receiver for that satellite (higher intensity means a larger '+', green for $\sigma_\phi < 0.2$cycles, red for $0.2 \leq \sigma_\phi < 0.6$cycles, and blue for $\sigma_\phi \geq 0.6$cycles).

1230 UT. Notice the rapid increases in scintillation throughout the observation window. The largest variations were observed between 1030 and 1100 UT. Shown in Figure 5.3 are a sequence of image

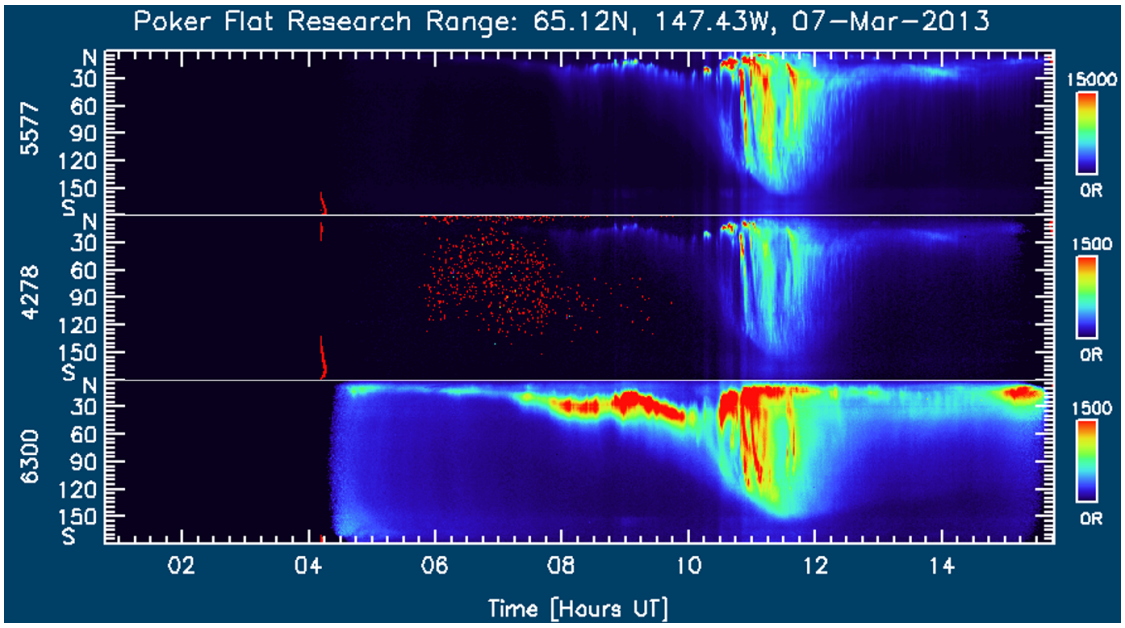

Figure 5.4: Keogram from PFRR for 07 March 2013. Shown are the North-South scans through zenith of green (top row), blue (middle row) and red (bottom row) emissions. The wavelengths are listed in Å. Note that the scales for each intensity are different and are shown in the color bar at right. Time is shown in UT across the bottom, and the elevation angle from the northern horizon is shown on the left axis of each row.

products of the DASC at PFRR. Each of the nine snapshots of DASC imagery,[2] has a '+' symbol for each PRN in view at the time of the image, placed where that satellite is visible in the sky. Recall that the images are inverted (south is up), and that times are listed in the lower left (UT) and upper right (local) corners. The symbol is sized proportionally and color-coded to the scintillation experienced at the time of the snapshot (green for $\sigma_\phi < 0.2$cycles, red for $0.2 \leq \sigma_\phi < 0.6$cycles, and blue for $\sigma_\phi \geq 0.6$cycles).

These images provide significant information and put the GPS scintillation and radar measurements into a broader spatial context. First, it is not during a geomagnetic storm. Second there are a variety of optical emissions present. These include discrete auroral arcs (green curtains that cut from southwest to northeast across the field of view and are sometimes folded), and potentially plasma blobs (large regions of red emissions). Unfortunately the DASC imagery provides

[2] These images are consolidated images with overlaid intensities of red, green and blue as was discussed in Section 4.3

emission intensities and does not indicate the altitude of the emission source. Additionally, the red emissions are too strong to be a plasma blob alone and are likely to be linked to emissions from particle precipitation.[3] Based on the location of the scintillating satellites in the images (bottom center of each of the first six images), it is clear that the emissions are spatially correlated with the scintillation; although the specific relationships and contributing factors are unclear.

Added here for reference is the keogram from PFRR on the night of the 7th of March. It

[3] See Sections 2.3.3 and 2.3.4

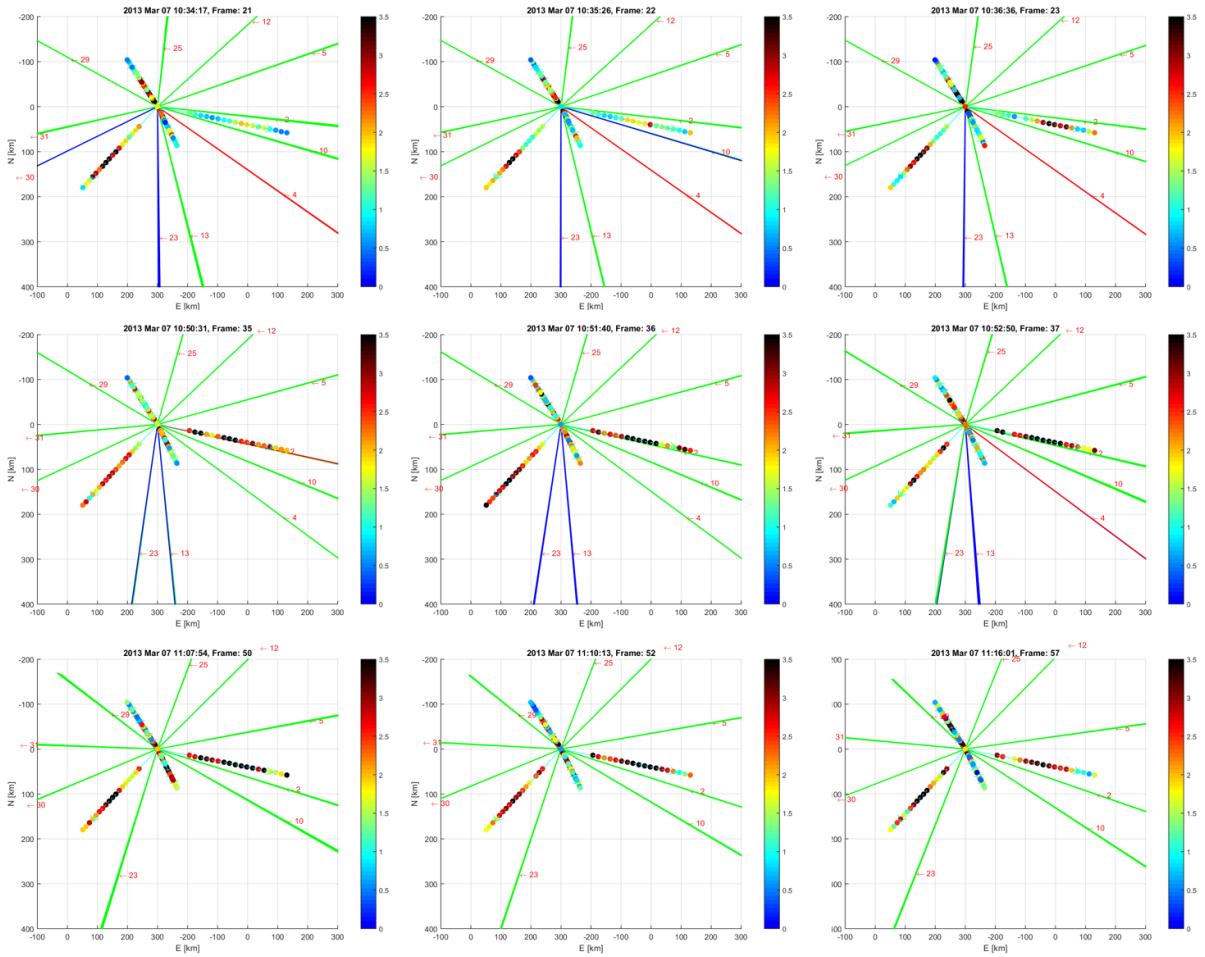

Figure 5.5: PFISR three-dimensional beam representation flattened to match the DASC orientation in Figure 5.3 (south is up). Dots correspond to electron densities measured with a long pulse experiment, scaled to $10^{11}/m^3$. Overlaid are multi-colored, numbered lines indicating GPS ray paths during the sensed period (green lines for $\sigma_\phi < 0.2$cycles, red for $0.2 \leq \sigma_\phi < 0.6$cycles, and blue for $\sigma_\phi \geq 0.6$cycles).

began taking data just after sunset (∼04:30 UT in the figure), and continued through ∼16:00 UT. Shown are the North-South scans through zenith of green (top row), blue (middle row) and red (bottom row) emissions, with wavelengths listed in Årather than in nm. Note that the scales for each intensity are different and are shown in the colorbar at right. Time is shown in UT across the bottom, and the elevation angle from the northern horizon is shown on the left axis of each row. Clearly visible in these images is the movement of PFRR into the auroral oval by what appears to be an inverted parabola starting at ∼07:00 UT near 15° elevation. This continues until ∼11:30 UT at ∼150° (vicinity magnetic midnight) when it then appears to recede, but it is really PFRR rotating out of the auroral oval.

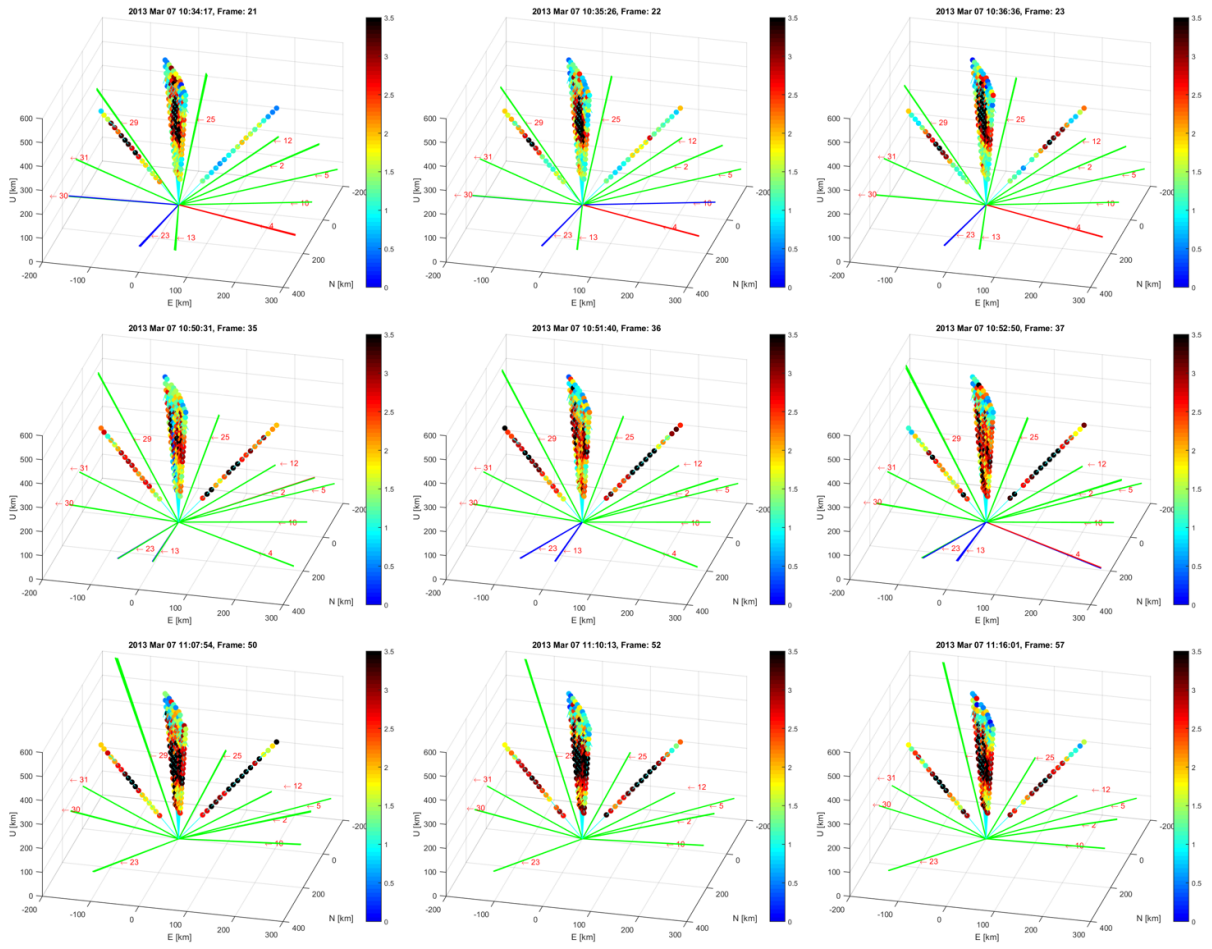

Figure 5.6: Same as Figure 5.5, except the view has been rotated into three dimensions.

To better understand the ionospheric environment, PFISR data from this time frame is evaluated. In Figures 5.5 and 5.6 two and three dimensional visualizations of PFISR data are shown, during the times of the imagery presented in Figure 5.3. In Figure 5.5 a view of the PFISR data oriented the same as the imagery is presented - flat as seen from vertical, with colored dots representing sensed electron densities per the color bars displayed, and solid lines labeled with numbers corresponding to a particular GPS satellite signal's trajectory. These lines are colored according to the scintillation experienced as was previously discussed. Because of the orientation of the figures it is difficult to see the relative positions of the signals to each of the PFISR beams of the experiment. However, clearly visible are both E and F region enhancements in various frames.

In Figure 5.6, the frames from Figure 5.5 have been rotated into a three-dimensional view. Here a better appreciation can be gained for the distribution of the GPS signals relative to the

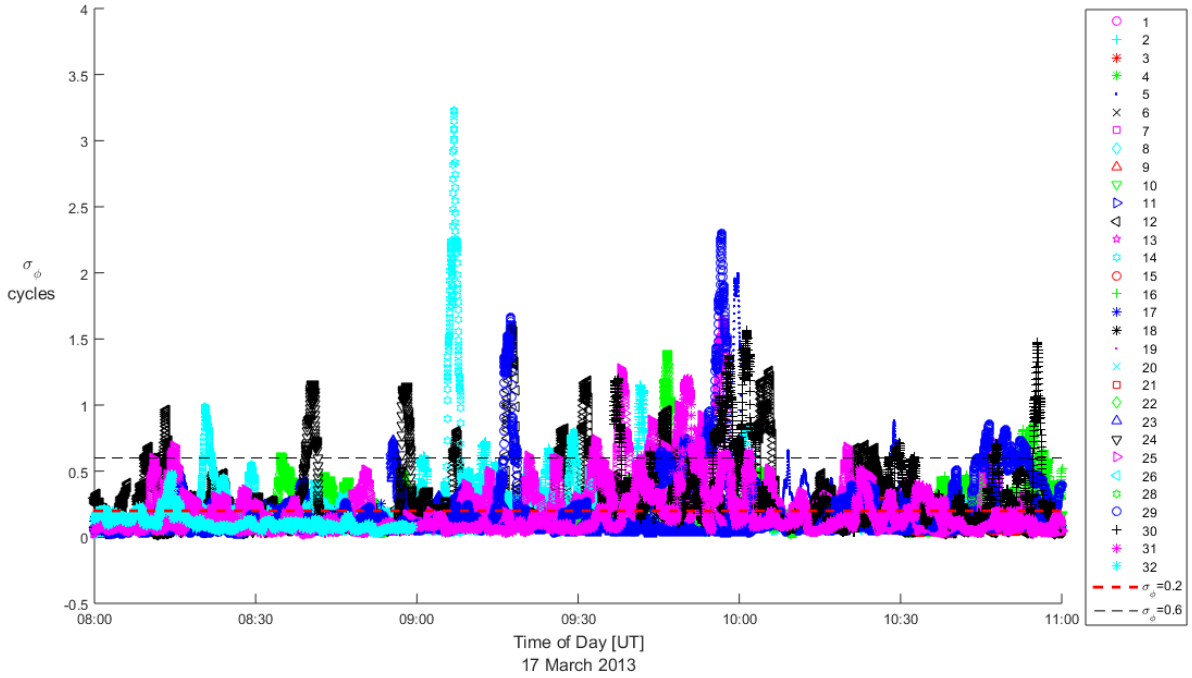

Figure 5.7: PFRR CASES σ_ϕ for 17 March 2013, all PRNs (legend on right side of plot), and zoomed to 0800-1100 UT. The red dashed line indicates $\sigma_\phi = 0.2$ cycles and the black dashed line represents $\sigma_\phi = 0.6$ cycles.

PFISR beams used for the experiment. The PFISR beams were selected to form a fan through vertical, with two beams pointing off vertical and in a plane roughly perpendicular to the central fan. The GPS signal paths are spread across of a variety of azimuths, but at lower elevation angles relative to the beams. Clearly visible to the north are the scintillating signal paths, none of which come close to intersecting the radar beams. Because of the PFISR operating mode it is difficult to determine what ionospheric activity caused the GPS scintillations.

5.3.2 St Patrick's Day Storm, 2013

The St. Patrick's Day storm was one of many quasi-annual storms that occur at or near the vernal equinox as discussed in literature (*Barkhatov et al.*, 2012; *Crooker et al.*, 1992). The 2013 storm was classified by National Oceanic and Atmospheric Administration (NOAA) as a G2 storm with the Disturbance Storm Time Index (DST) bottoming out at -132 nT and the Kp Index reaching a peak value of 6.7. Indices for this storm as well as local magnetometer data are summarized in Figure 5.1. This storm was mild compared to the Halloween Storms of 2003 (minimum DST of -383 nT); however, a measurable response in the polar ionosphere was observed.

In Figure 5.7 is another a plot of σ_ϕ from the CASES receiver at PFRR, plotted at one second cadence for all PRNs visible to the receiver on 17 March 2013. The times are limited from 0800-1100 UT. Notice the spikes in scintillation in the window, especially near 0900 UT. To better understand what might be happening, attention is focused on a single one hour segment, 0900-1000UT. Shown in Figure 5.8 (similar to Figure 5.3) are a sequence of image products of the DASC at PFRR. Each of the 12 snapshots of DASC imagery,[4] has a '+' symbol for each PRN in view at the time of the image, located where the satellite was visible in the sky. The symbol is sized proportional to and color-coded to the scintillation experienced at the time of the snapshot (green for $\sigma_\phi < 0.2$cycles, red for $0.2 \leq \sigma_\phi < 0.6$cycles, and blue for $\sigma_\phi \geq 0.6$cycles). Again, there is a great deal of information in the images. First, they were taken during a geomagnetic storm.

[4] These images are consolidated images with overlaid intensities of red, green and blue as was discussed in Section 4.3

Second, just as with the imagery from 07 March, there are a variety of optical emissions present including discrete auroral arcs and potentially plasma blobs. Based on the location of the auroral arcs with respect to the GPS signal paths, it is clear here that they likely have something to do with the scintillation, but what is not clear is exactly how, or if the red emissions might also have an impact. Note the storm was large enough to push the aurora south of zenith at Poker Flat thus the site was inside the aurora oval.

Complementary PFISR data is shown in Figures 5.10 through 5.13. In figure 5.10 the view has been flattened to match that of Figure 5.8, and in Figure 5.11 it has been rotated to allow a better of view of the orientation of the GPS rays with respect to the PFISR beams. Each GPS ray has been labeled with the appropriate PRN and color-coded in the same manner as the '+' symbols in Figure 5.8. The colored dots represent measured electron densities from PFISR along the beam at the epoch listed at the top of each image, and corresponding to the colorbar shown to the right of each plot, scaled to $\times 10^{11}/m^3$. Several things can be seen in this image. First, there are clearly night-time F Region enhancements that can be a plasma blob convecting through the PFISR ionosphere. Second, the GPS rays are all much lower in elevation than any of the PFISR beams - the closest that any one GPS ray comes to a PFISR beam is PRN 25 to the field aligned beam (back- and right-most beam shown in Frames 19 and 20). Third, when comparing the PFISR images to the DASC images, one can clearly see the effects of the auroral arcs on the field aligned beam (Frames 19 and 20).

An inspection of similar PFISR visualizations from the *PINOT_Nighttime31* AC pulse experiment reveals greater E Region detail. These are shown in Figures 5.12 and 5.13, in similar fashion to the LP experiments shown in Figures 5.10 and 5.11. The greatest scintillation on PRN 25 in Frame 10 of Figure 5.8 corresponds well to the enhancements seen in Frame 12 of these figures. More challenging to see are the enhancements associated with scintillation on PRNs 12 and 29 in Frames 7-9 of Figure 5.8, as these GPS signals are far below the southern elevation angles of the beams in use; and, because of PFISR's array setup, far below any available beams for ionospheric sensing.

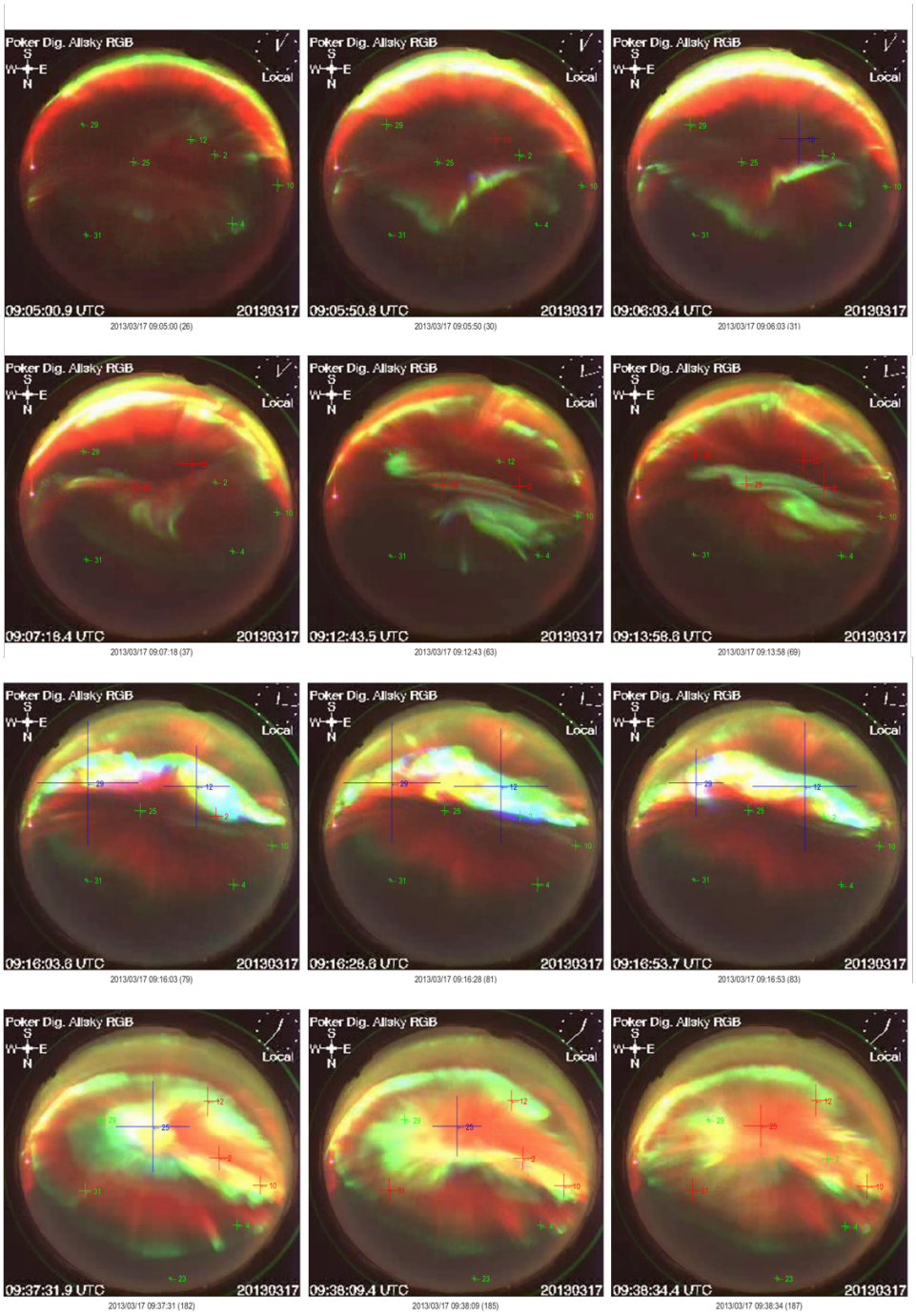

Figure 5.8: DASC consolidated images for the 2013 St Patrick's Day Storm overlaid with a colored and sized '+' for each satellite in view, proportional to the scintillation experienced at the PFRR CASES receiver for that satellite (higher intensity means a larger '+', green for $\sigma_\phi < 0.2$cycles, red for $0.2 \leq \sigma_\phi < 0.6$cycles, and blue for $\sigma_\phi \geq 0.6$cycles).

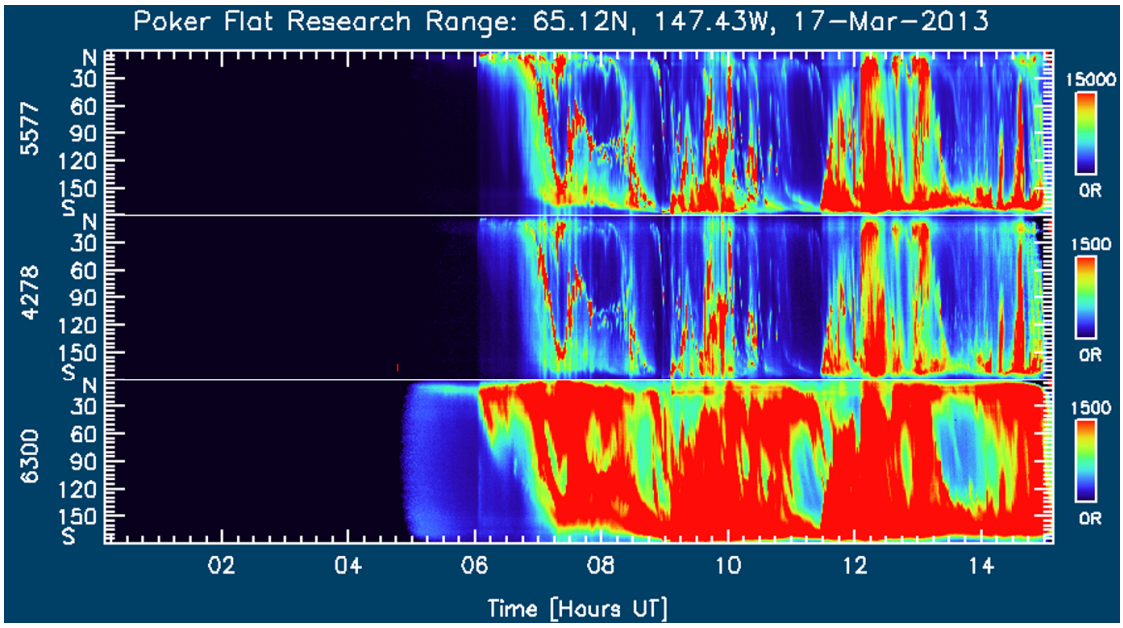

Figure 5.9: Keogram from PFRR for 17 March 2013. Shown are the North-South scans through zenith of green (top row), blue (middle row) and red (bottom row) emissions. The wavelengths are listed in Å. Note that the scales for each intensity are different and are shown in the colorbar at right. Time is shown in UT across the bottom, and the elevation angle from the northern horizon is shown on the left axis of each row.

5.3.3 Correlation Analysis

An attempt to correlate scintillation levels with emissions along the GPS line of site was made. Data used for this analysis were restricted to times of scintillation when auroral arcs were above roughly 45^o elevation in the sky. These dates and times are summarized in Table 5.2. Correlations calculated were between the phase scintillation index, σ_ϕ, and emission intensities of the red, green and blue lines discussed in Sections 2.3.4 and 4.3. Times corresponding to data used are summarized in Table 5.2. Scatter plots of blue ($R = 0.3552$, $P = 0$), red ($R = 0.4817$, $P = 0$), and green ($R = 0.3839$, $P = 0$) intensities against σ_ϕ are shown in Figure 5.14. Also shown is a scatter plot of blue vs green emission intensity which had the highest correlation value of any near 0.90. Any pass of a particular PRN over PFRR without scintillation of $\sigma_\phi \geq 0.2$ cycles was neglected for computing considerations. Otherwise, even if the PRN experienced only a few epochs above this threshold, that pass was included in the correlation analysis. It is clear that limited

Table 5.2: DASC and CASES Data used for Correlation Analysis, March 2013. Listed are dates and times for data that was used in the correlation analysis of Section 5.3.3.

Day	Start Time [UT]	Stop Time [UT]
07	10:30:00	11:30:00
15	07:00:00	09:00:00
16	06:55:00	08:30:00
17	09:00:00	10:00:00

correlations exist between emission intensities and the scintillations, however, it is unclear as to which has the most impact on GPS signals.

5.4 Summary & Lessons Learned

One of the greatest challenges noted with attributing scintillation on GPS signals to a particular ionospheric enhancement within the view of PFISR is associated with the physical attributes of the two systems. GPS signals are higher in the sky in the southern sector, while PFISR beams are generally higher in the northern sector. This leads to a limited number of potential conjunctions of any of the PFISR beams with a particular GPS signal. Often the GPS signals are well outside the beamwidth ($1^o \times 1.1^o$), and so an attribution of electron density enhancements becomes problematic. The second greatest challenge is the difference between the temporal resolution required (on the order of seconds) and the temporal resolution available with multi-beam experiments (varies from 1 to 5 minutes). The fewer beams that are used, the better the temporal resolution, which in turn limits the spatial sensing ability. Because of these two facts associated with experiment sets that were requested independent of GPS conjunctions, it is difficult to say with any certainty that a particular ionospheric enhancement was the source of the scintillation on the signal in question. This naturally points towards the requirement for a PFISR experiment with a single central beam focused on the GPS line of site, and with a surrounding cluster of beams for a volumetric view. Presented here, and in Chapters 7 and 8 are the progressions of this experiment set from a single central beam using long pulse data (Section 6 and Chapter 7), through interleaved long and coded pulse data (Chapter 8). Discussed in Chapter 10 are the initial specifications for a single

central beam surrounded by four mutually orthogonal beams, each using coded pulses for E region sensing.

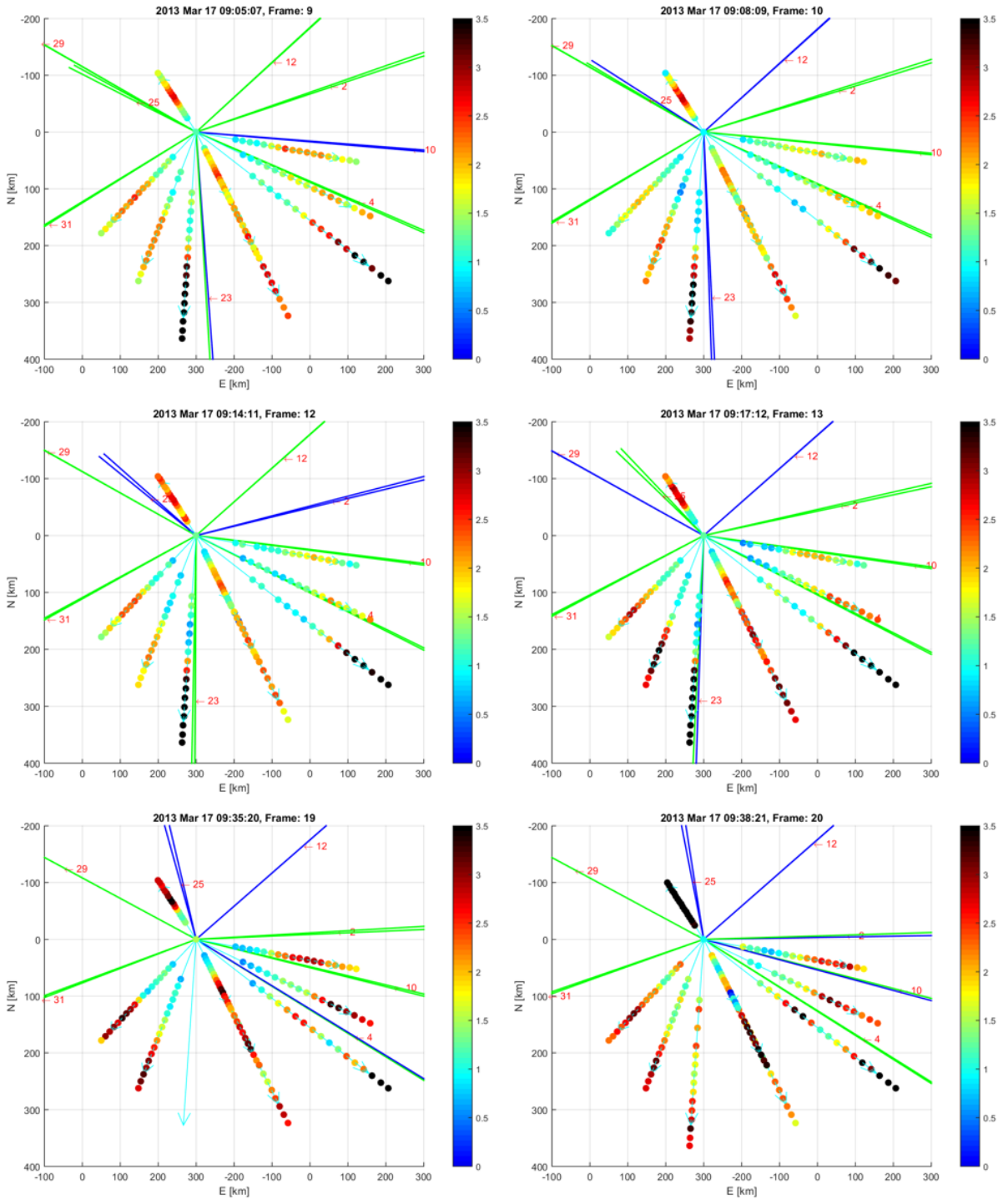

Figure 5.10: PFISR three-dimensional beam representation flattened to match the DASC orientation in Figure 5.8. Dots correspond to electron densities measured with a long pulse experiment, scaled to $10^{11}/m^3$. Overlaid are multi-colored, numbered lines indicating GPS ray paths during the sensed period (green lines for $\sigma_\phi < 0.2$cycles, red for $0.2 \leq \sigma_\phi < 0.6$cycles, and blue for $\sigma_\phi \geq 0.6$cycles).

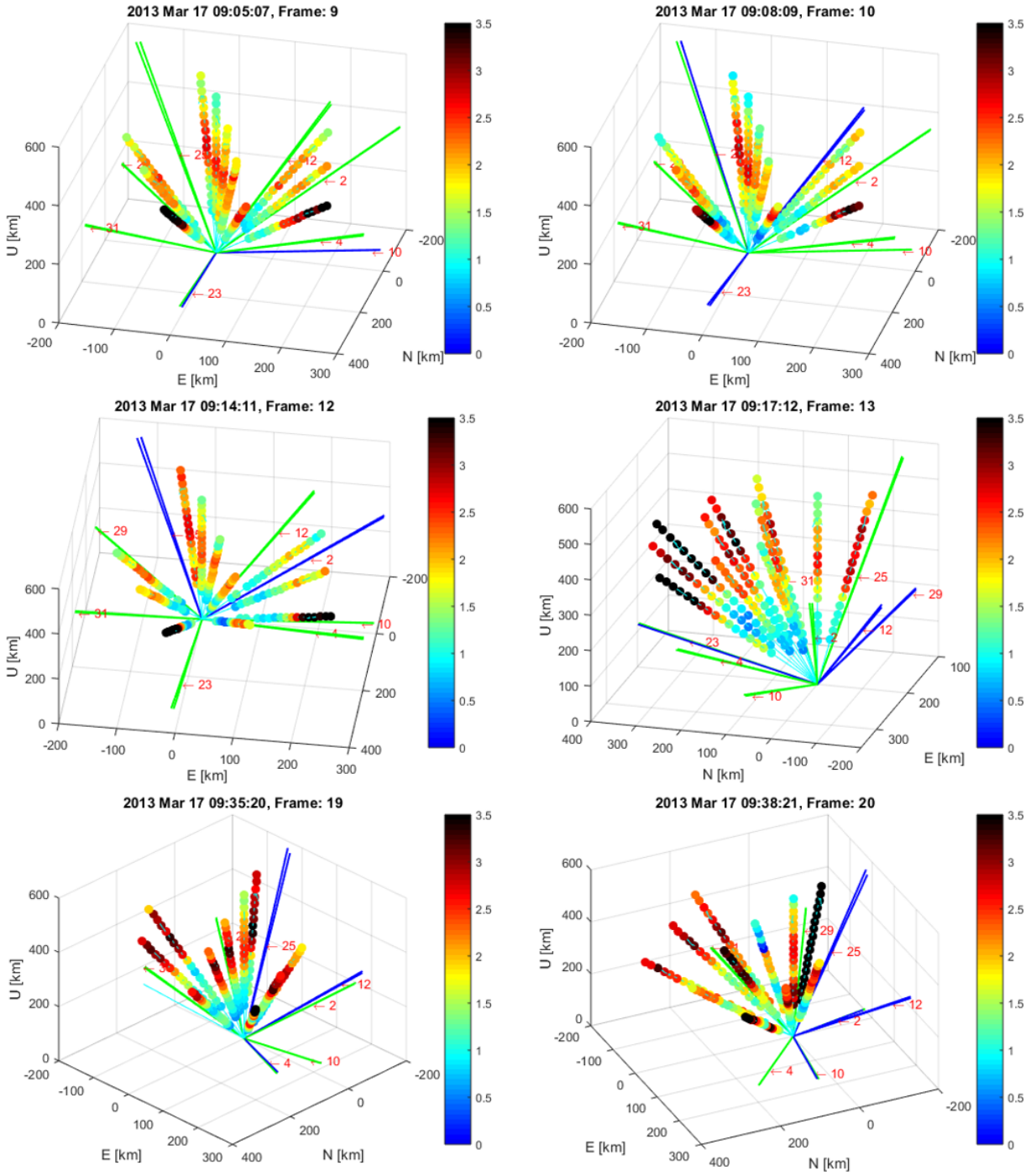

Figure 5.11: Same as Figure 5.10, except the view has been rotated into three dimensions.

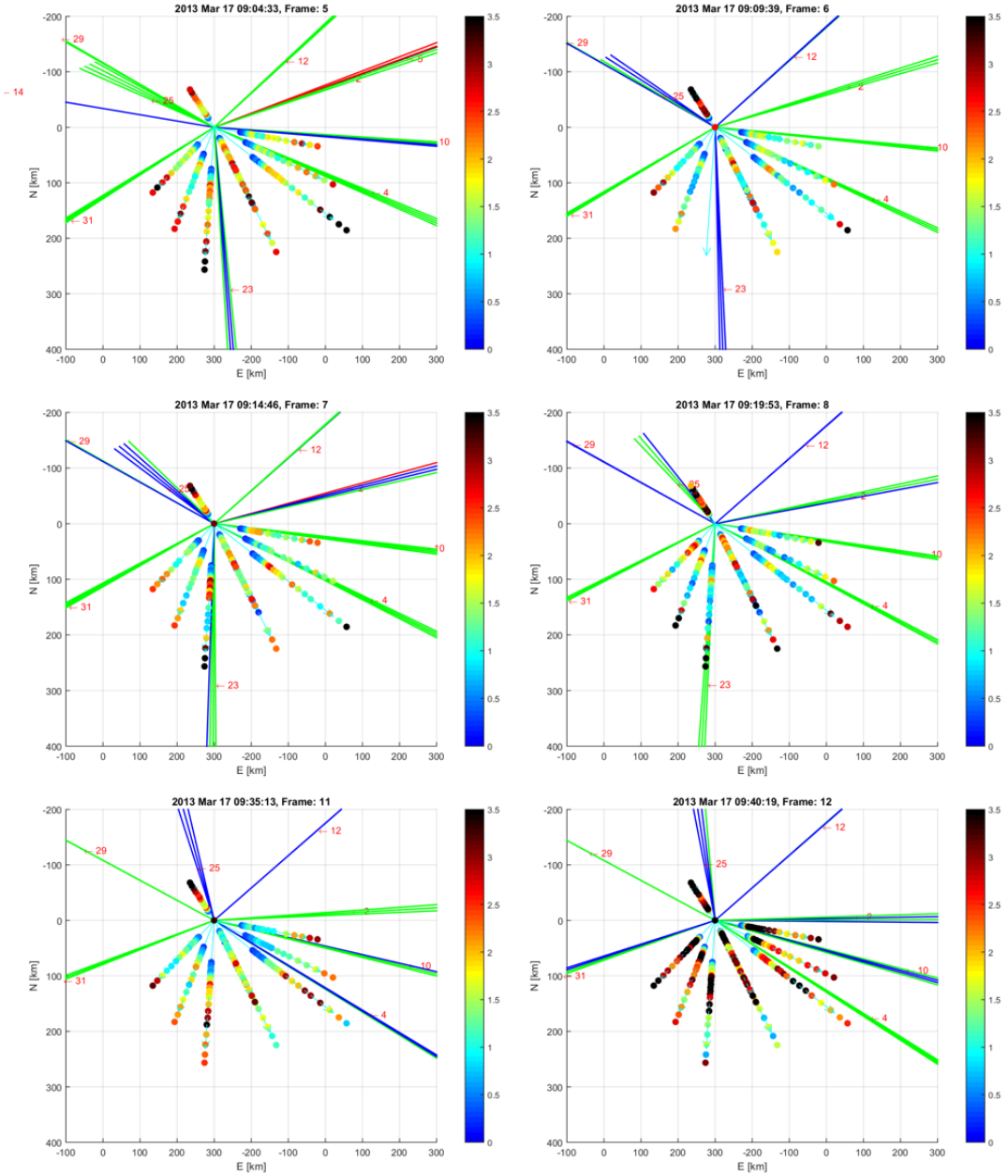

Figure 5.12: PFISR three-dimensional beam representation flattened to match the DASC orientation in Figure 5.8. Dots correspond to electron densities measured with an alternating coded pulse experiment, scaled to $10^{11}/m^3$. Overlaid are multi-colored, numbered lines indicating GPS ray paths during the sensed period (green lines for $\sigma_\phi < 0.2$cycles, red for $0.2 \leq \sigma_\phi < 0.6$cycles, and blue for $\sigma_\phi \geq 0.6$cycles).

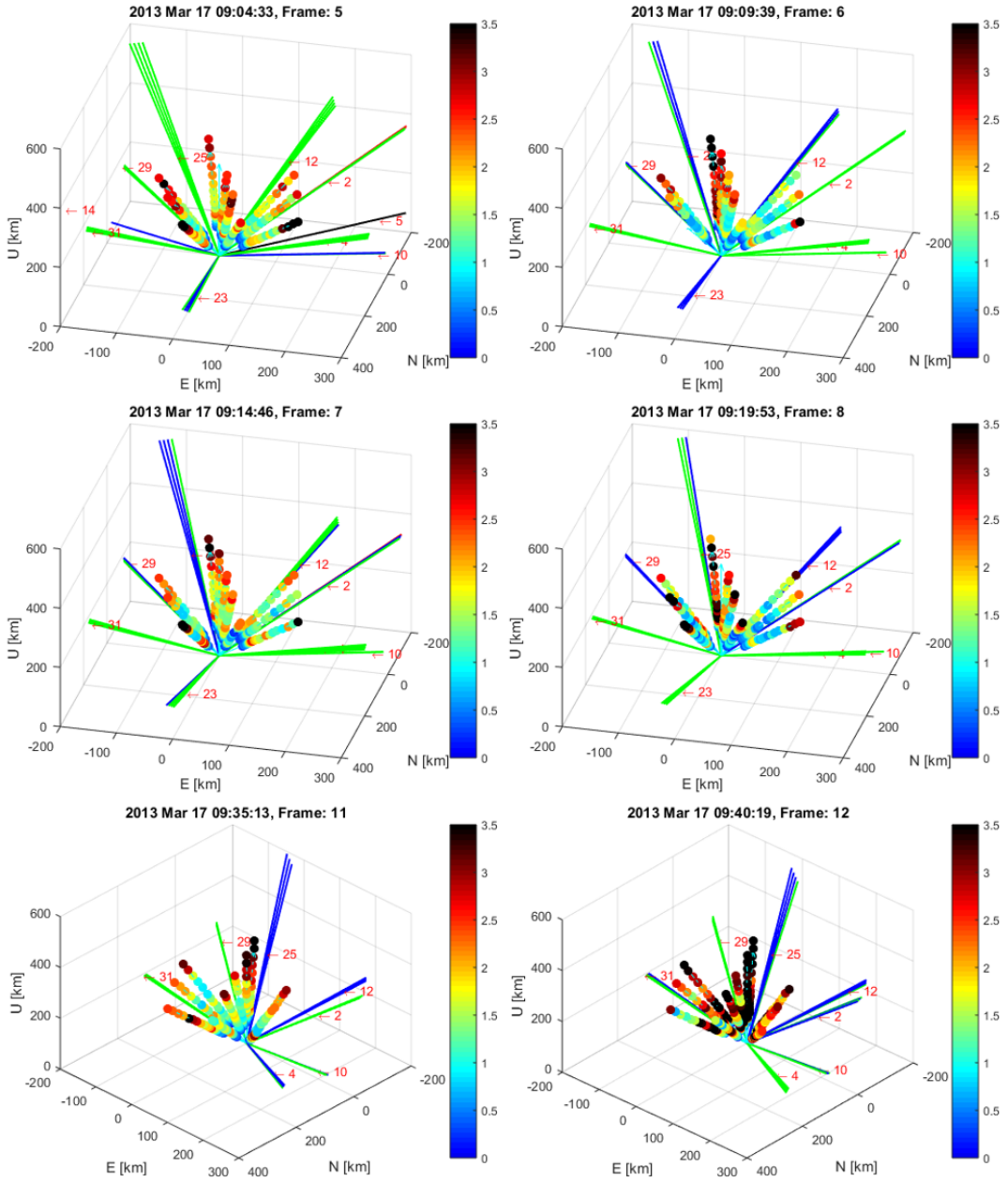

Figure 5.13: Same as Figure 5.12, except the view has been rotated into three dimensions.

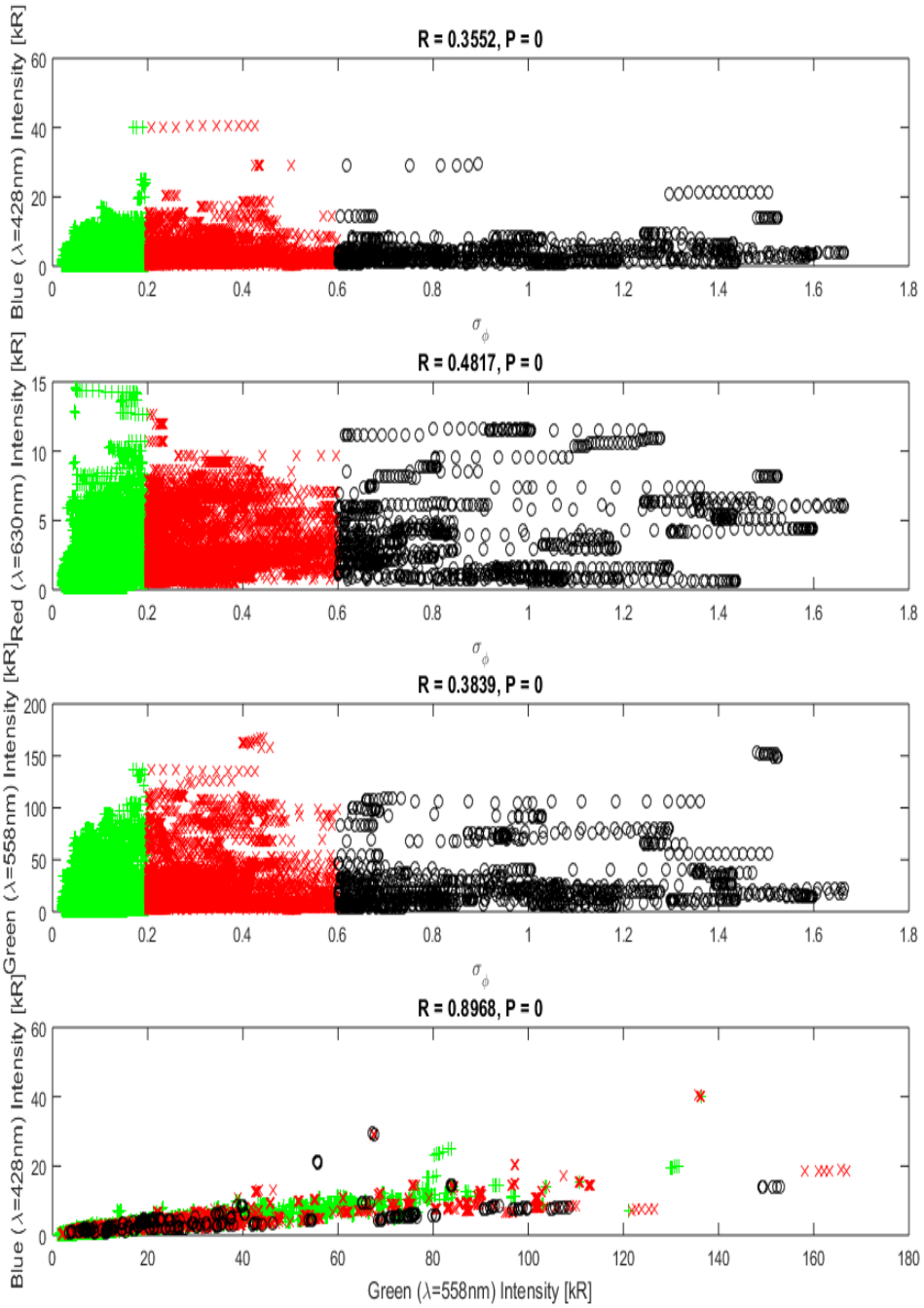

Figure 5.14: Top row: Scatter plots of blue emission intensities vs σ_ϕ across each PRN visible to the PFRR CASES receiver. Green '+' indicates $\sigma_\phi < 0.2$ cycles, black 'o' indicates $\sigma_\phi \geq 0.6$ cycles, and red '× is everything in between. Second row is the same but for red emissions, third row is for green emissions. The last row shows blue emissions plotted against green emissions.

Chapter 6

December 2015: Case Study II

In the St Patrick's Day 2013 case study discussed in the previous chapter, evidence was presented of an apparent spatial correlation between auroral activity and GPS phase scintillation ($\sigma_\phi \geq 0.2$ cycles). But previous experiments on PFISR were not designed to discern electron densities along the GPS signal path, therefore conclusive attribution of scintillation with ionospheric irregularities was impractical. As the most efficient method to correlate GPS scintillation with electron density enhancements was along the GPS signal path, an experiment was designed that would sense the ionosphere along the line of site of GPS signals received at PFRR. The series of experiments was conducted nightly over a nine day window surrounding the Winter Solstice Storm of 2015, described in detail in Section 6.1. A sequence of geomagnetic disturbances during this window allowed investigation of the temporal and spatial electron density gradients along the GPS line of slight using PFISR which were used to diagnose scintillation. Of the nine experiments conducted, only two scintillation events were detected. Although data from only three of those experiments are presented here (two sequentially disturbed nights and the preceding quiet night), all experiments were used as part of the final correlation analysis presented in this chapter.

6.1 Storm Summary

A series of three storms took place near the 21 December 2015, as indicated by the DST values shown in Figure 6.1 and summarized in Table 6.1. The largest of the three storms (21 December) is the focus of this analysis. Also shown in Figure 6.1 are the interplanetary magnetic field (IMF)

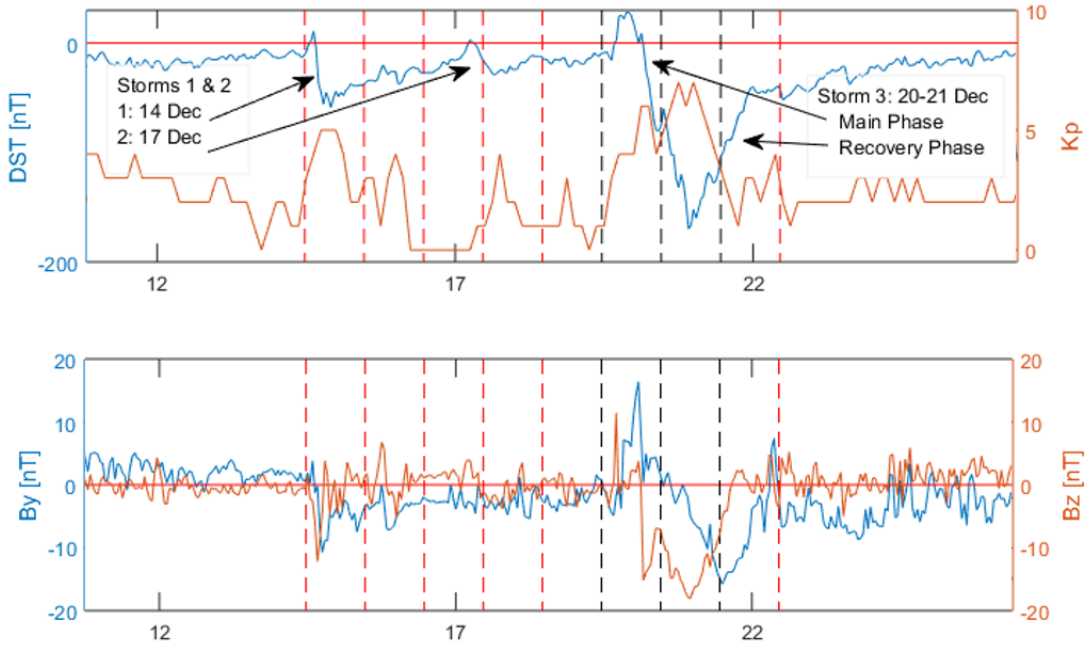

Figure 6.1: DST and Kp (top), and ACE derived B_y and B_z (bottom) for the month of December 2015. The horizontal red line on both plots indicates a zero line for the DST and the magnetic field components components, respectively. The vertical dashed lines indicate times corresponding to experimental data taken by PFISR (discussed in Section 6.3.1). Data presented in this chapter are from 19, 20 and 21 December, indicated by vertical black dashed lines.

components derived from the Advanced Composition Explorer (ACE) solar wind measurements. DST values are derived from the World Data Center (WDC) repositories at `http://wdc.kugi.kyoto-u.ac.jp/`, Kp values from the WDC files at `ftp://ftp.gfz-potsdam.de/pub/home/obs/kp-ap/wdc/`, and IMF components from the Space Weather Prediction Center archives at `ftp://ftp.swpc.noaa.gov/pub/lists/ace/`.

For reasons discussed in Chapters 2 and 3, only local magnetometer data were used to evaluate the level of local magnetic disturbance. Shown in the top row of Figure 6.2 are the magnetometer data from PFRR for the time frame shown in Figure 6.1. Locally disturbed times during experiment windows can be seen clearly in the data, but especially on the nights of 20-22 December. Toolik

Table 6.1: Summary of indices for geomagnetic storms that occurred during the Winter Solstice season of 2015.

Date	DST [nT]	Kp
December 14, 2015	-50	5
December 17, 2015	-29	4
December 20-21, 2015	-170	7

magnetometer data are shown in the bottom row with similar features as PFRR. The disturbances at each location contrast in occurrence, duration and severity - an indicator of their localized nature.

6.2 Experimental Setup

Discussed previously, PFISR is capable of using two pulse modes to characterize the E and F region ionosphere: coded pulse and long pulse. A special PFISR GPS-scintillation mode was created to support this study. PFISR was operated using long pulses of 480 μs width at 6.9%

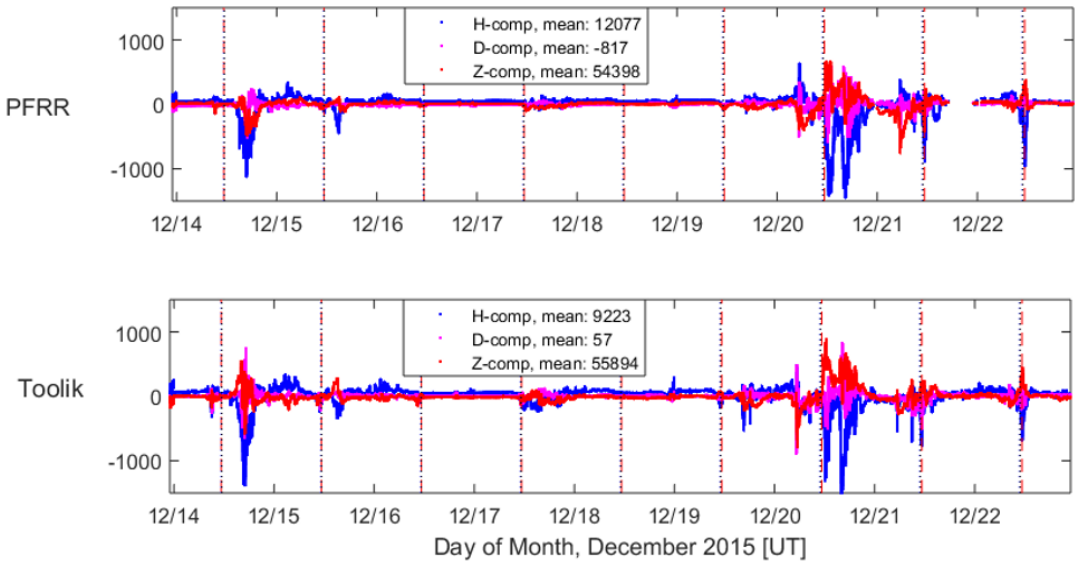

Figure 6.2: Magnetometer data from PFRR (top row) and Toolik station (bottom row), with mean value indicated the in legend subtracted for ease of comparison.Vertical red dotted lines indicate the experiment windows, and the dates shown correspond to those shown in Figure 6.1.

duty cycle, resulting in an inter-pulse period (IPP) of roughly 7 ms. The maximum unambiguous range for this experiment was 1050 km (Eqn 4.5). Unlike standard PFISR pulses, this mode placed more emphasis on temporal resolution than spatial resolution. Returns were oversampled with data parsed into 4.5 km range bins. Even though the received signal is oversampled, the effective range resolution for this experiment is 72 km consistent with the pulse width. Long pulses have post-processed range bins of 36 km as opposed to 72 km per the pulse width, even though the raw data is sampled at 4.5 km range resolution. The IPP configuration is depicted in Figure 6.3.

PFISR's field aligned beam corresponds to beam #64157, azimuth of -154.3^o, elevation of 77.5^o. To achieve the best temporal and spatial resolution, this beam operated during the GPS transit. With the normal 15 s integration window on a particular beam, 1,072 samples were integrated and post-processed, resulting in a temporal uncertainty proportional to $1/\sqrt{N} = 1/\sqrt{1072}$ or roughly 3%. Data were sampled on two independent channels to reduce the uncertainty (data taking computer (dtc) 0 and dtc1). The resulting electron densities were averaged to provide a temporal uncertainty of $1/\sqrt{(2)1072}$ or roughly 2%. In the final step for calculating electron density (Equation 4.9), the temperature ratio (T_r) of electrons to ions is used to account for thermal motions of the populations. Although a temperature ratio of unity can be assumed in most cases for the E region, it does not apply at higher altitudes (*Semeter et al.*, 2009). PFISR provided ion and electron temperature fits at one-minute cadence. Temperatures were assumed

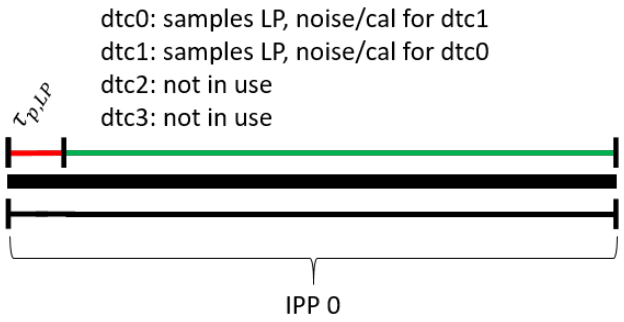

Figure 6.3: Configuration for the Experimental Campaign I (GPS35, LP only) mode IPP configuration.

Table 6.2: PFISR Experiment start and stop times, December 2015.

Day	Start Time HH:MM:SS	End Time HH:MM:SS	Figure[a]
14	11:18:41	11:27:41	-
15	11:14:40	11:23:40	-
16	11:10:49	11:19:34	-
17	11:06:47	11:15:32	-
18	11:02:48	11:11:33	-
19	10:58:44	11:07:44	6.6
20	10:54:50	11:03:35	6.8
21	10:50:47	10:59:32	6.9
22	10:46:47	10:55:47	-

[a] Where applicable.

constant across the previous one minute window and 36 km range bins. These temperatures were used at corresponding 15 s intervals to further refine the calculated N_e, at a higher resolution.

DASC imagery was available for December; and, was processed as discussed in Section 4.3. CASES receivers continued to operate as discussed in Section 4.2, and raw data was post-processed at a one second cadence for analysis.

6.3 Results

6.3.1 Data

Table 6.2 shows the experiment intervals for December 2015 (experiment times are summarized in Table 6.2). Three intervals with figure numbers are discussed in detail. Data from all intervals are included in the correlation analysis discussed in Section 6.3.2. The PFRR DASC image sequence is shown in Figure 6.4 for 21 December. Included are four snapshots of DASC imagery,[1] each of which has a '+' symbol that is sized proportional to and color-coded to the scintillation experienced at the time of the snapshot (green for $\sigma_\phi < 0.2$ cycles, red for $0.2 \leq \sigma_\phi < 0.6$ cycles, and blue for $\sigma_\phi \geq 0.6$ cycles). Similar to the data evaluated in Section 5.3.2, it is clear here that the auroral arcs moving through the path of the GPS signal are spatially correlated with the

[1] These images are consolidated images with overlaid intensities of red, green and blue as was discussed in Section 4.3

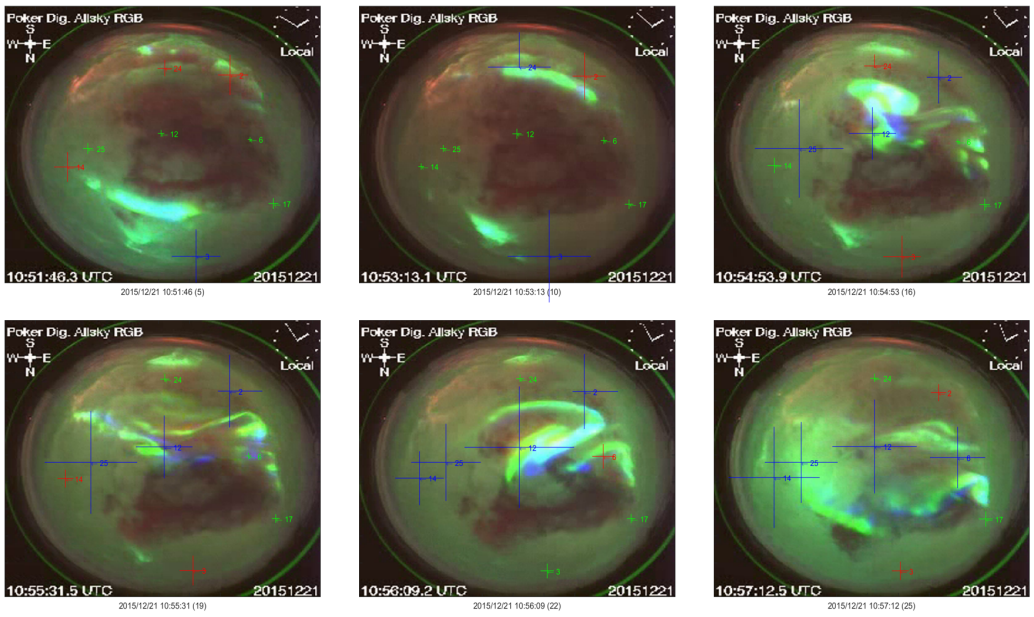

Figure 6.4: DASC consolidated images overlaid with a colored and sized '+' for each satellite in view, proportional to the scintillation experienced at the PFRR CASES receiver for that satellite (higher intensity means a larger '+', green for $\sigma_\phi < 0.2$ cycles, red for $0.2 \leq \sigma_\phi < 0.6$ cycles, and blue for $\sigma_\phi \geq 0.6$ cycles). Note that there is some cloud cover in the imagery.

scintillation. In the data sets that follow, auroral precipitation will be directly linked to electron density gradients along the GPS signal's line of site and hence shown to be a primary source of scintillation.

6.3.1.1 Amplitude Scintillation

Based on scintillation statistics and climatologies discussed in Section 3.3, amplitude scintillation was not expected to be a a factor in this study. Shown in Figure 6.5 are CASES reported S4 and σ_ϕ indices at 100 s cadence during an hour long interval that includes the times of the experiment on 21 December. As expected, even though the signal phase is scintillating, the amplitude remains mostly unaffected.

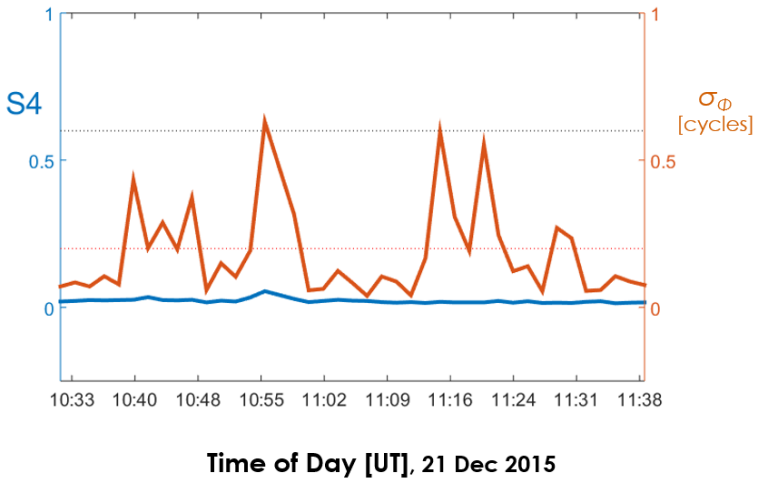

Figure 6.5: Amplitude (S4, left axis) and phase scintillation (σ_ϕ, right axis) during the 21 December 2015 experiment window.

6.3.1.2 Phase Scintillation

PFISR, CASES and DASC data from 19 December (quiet day prior to the storm), and 20 and 21 December (storm days) are presented in Figures 6.6, 6.8 and 6.9, respectively. Each figure has seven rows of data. The first row (a) contains N_e altitude time profiles, calculated as described in Section 4.1.3. This data is presented at 15 s cadence and at 4.5 km vertical spacing, consistent with the spatial oversampling and the resolution set by the pulse length (36 km). Vertical profiles at times corresponding to each of the vertical red dashed lines are shown in Figure 6.7, color-coded according to the experiment from which they are taken with dates and times summarized in Table 6.3. The second and third rows (b and c) are the temporal and spatial gradients, respectively, presented at the same spatial and temporal resolutions as N_e. The horizontal black dashed line in the first three rows highlights the data at 137 km in altitude. Note that all three rows are plotted against *altitude* and not range along the beam. Rectangular shaped anomalies shaded in grey are artifacts associated with one of the radar antenna cables,[2] and are not electron density enhancements. The fourth row (d) contains σ_ϕ in cycles for PRN 12 on the left (blue) axis, and

[2] The returns from the pulse corresponding to the anomaly are normally excluded during post processing.

dNe/dt (brown '*') and dNe/dr (black '×') at 137 km altitude on the right axis, scaled the same as rows (b) and (c). Note that σ_ϕ values of less than 0.2 cycles are shown as green, at least 0.2 cycles but less than 0.6 cycles are shown as red if present, and at least 0.6 cycles are shown as black if present (they are blue in Figure 6.4 for visibility).

The fifth, sixth and seventh rows (e, f and g) contain various types of DASC data. The fifth row (e) contains images where all three emission lines have been overlaid, with the red and blue lines enhanced for visibility. The times of the images correspond to the times of the vertical red dashed lines in the first four rows and the images are inverted (North is down). Over-plotted on the images are: (1) a white circle at the center of which is the direction of the radar beam, with the circle enlarged for visibility; (2) a red dotted arc representing the trajectory of the GPS satellite throughout the day with (3) a red '*' indicating its location at the epoch represented in each image. In the next row (f) are plots of the emission intensity ratios against the 427.8 nm intensities, processed in the same manner as *Rees and Luckey* (1974), where the green to blue ratio is represented by a green '+', the red to blue ratio by a red '*', and the red to green ratio by a brown 'o'. In the last row is the keogram for the day zoomed in to 1015 to 1115 UT, with white vertical dashed lines corresponding to the times of the images in row (e), and a red box outlining the time interval of the radar data. The intensity scale for the data shown in the keogram is located to the right.

The first day, 19 December, was a quiet day, with no significant scintillation ($\sigma_\phi \leq 0.2$ cycles), and only mild disturbances of electron density in time and space. Seen in the DASC consolidated video (not shown) shortly before the experiment window, and visible in the keogram in the last row of Figure 6.6, is evidence of a substorm to the north with resulting pulsating aurora that expands south through the field of view. This was confirmed through magnetometer data at Toolik (Fig 6.2) showing activity that spans the time before and after the experiment window (data available from `https://www.asf.alaska.edu/magnetometer/`). There is cloud cover present that scatters the green emissions more than the red reducing the intensities observed at the DASC.

On the second day, 20 December, a mild scintillation event (peak $\sigma_\phi = 0.49$ cycles) was

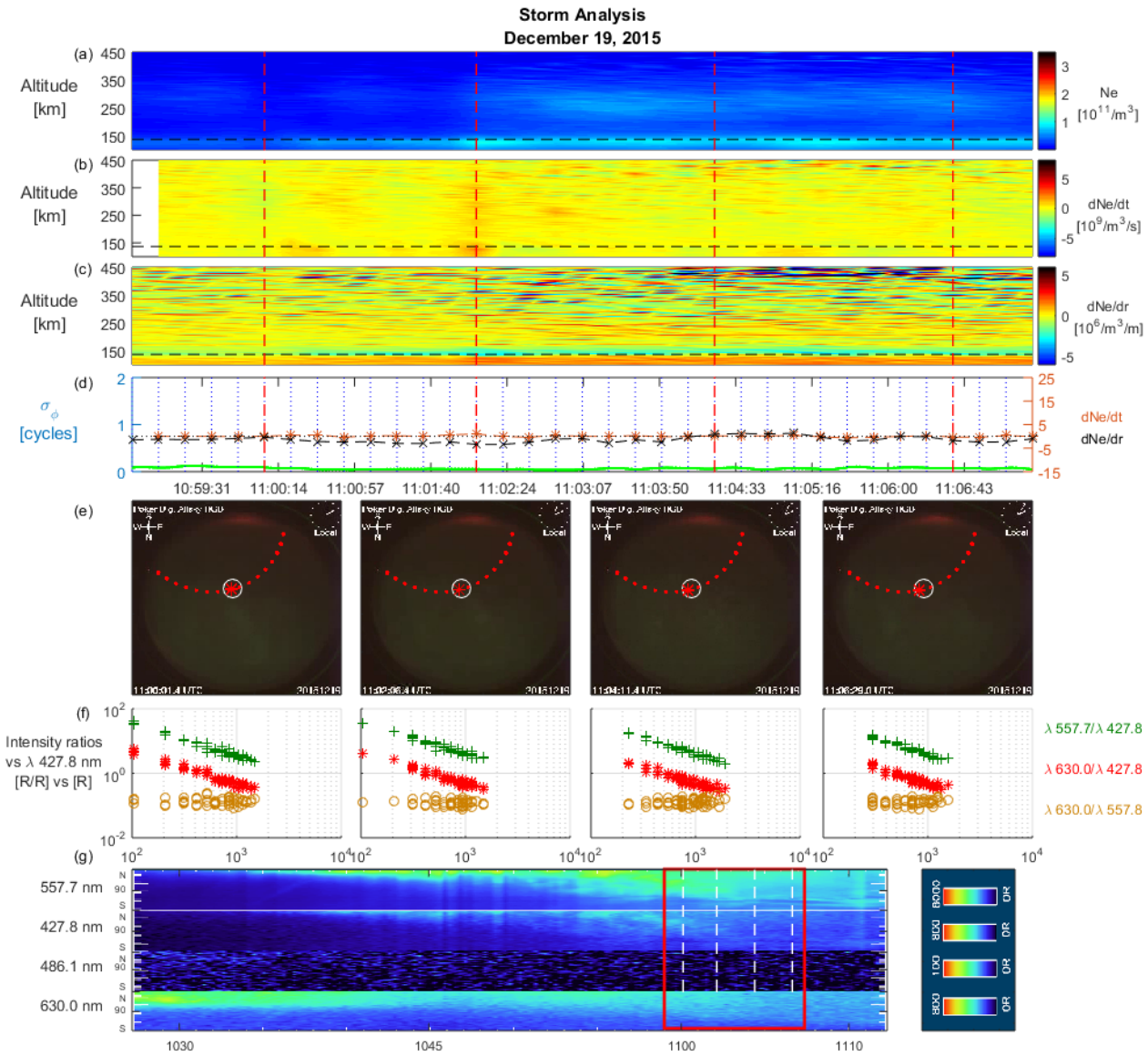

Figure 6.6: Results from PFISR experiment on December 19, 2015 (10:58:44 - 11:07:44 UT, magnetic midnight is ∼11:20 UT), beam #64157 (azimuth -154.3°, elevation 77.5°). Data displayed in each row are (a) PFISR derived electron density processed as described in Section 6.2; (b) temporal electron density gradient from epoch to epoch (dNe/dt); (c) spatial electron density gradient along the beam (dNe/dr); (d) $\sigma_\phi \geq 0.2$ cycles (left axis, red dot not present in this figure), $\sigma_\phi < 0.2$ cycles (left axis, blue dot not present in this figure), temporal gradient at 137km altitude (right axis, orange * and dashed line), spatial gradient at 137km altitude (right axis, black + and dashed line, doubled for clarity); (e) composite display of DASC imagery data from the 557.7 nm, 428.7 nm, and 630.0 nm exposures with the 428.7 nm and 630.0 nm intensities enhanced for visibility, with each image corresponding to the time of the vertical red dashed lines in rows (a) through (d) and the vertical black dashed lines in row g, red dotted arcs represent the trajectory of this pass for context; (f) DASC intensity ratios (557.47 nm/427.8 nm, 630.0 nm/427.8 nm, and 630.0 nm/557.8 nm) plotted against the 427.8 nm intensity (in Rayleighs) for the images shown in row e.; (g) keogram for the day zoomed into the 1015 to 1115 UT window, with the experiment window outlined by a red box, vertical white dashed lines corresponding to the images in rows e and f, and color bars for each row to the right. The keogram color bar represents a lower limit of 0 R for all wavelengths, and an upper limit of 8000 R (557.7 nm), 800 R (428.7 nm), and 800 R (630.0 nm).

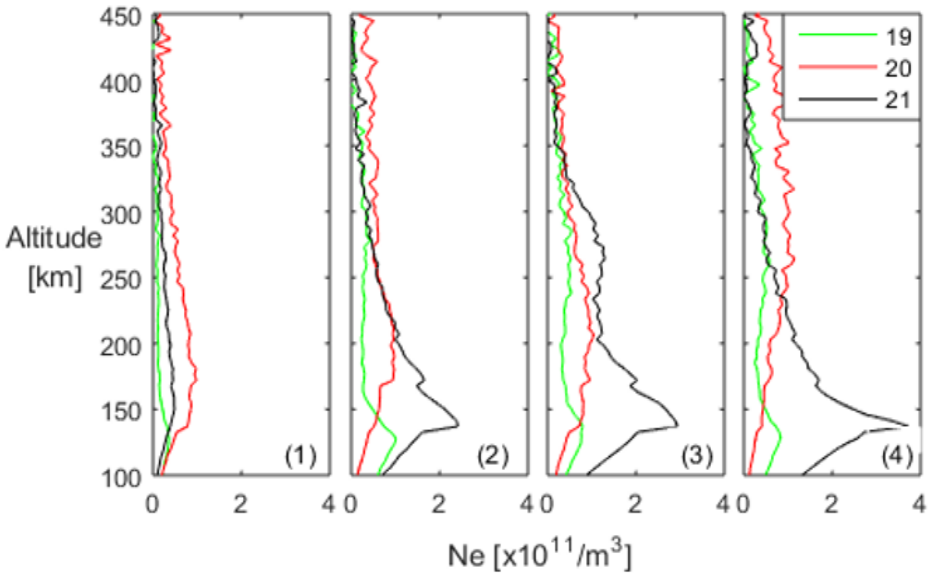

Figure 6.7: Vertical N_e profiles for each day and time corresponding to the DASC images in Figures 6.6, 6.8 and 6.9.

recorded at the start of the interval. Clearly evident in the electron density is a peak near 200 km, along with stronger spatial and temporal gradients during the time of the event than in the previous window. Peak spatial and temporal gradient magnitudes at 137 km altitude were 8.992 $\times 10^6$ per m^3/m and 2.954 $\times 10^9$ per m^3/s, respectively. Also visible in the DASC images and the keogram are strong red line emissions, even though there is some obscuration due to clouds. Results from the third day, 21 December, are shown in Figure 6.9. A major scintillation event was recorded in the latter half of the interval with a peak $\sigma_\phi = 1.571$ cycles. Corresponding to this are significant temporal and spatial gradients in the E region. The spatial and temporal gradients vary widely across this time with peak magnitudes of 24.67 $\times 10^6$ per m^3/m and 13.73 $\times 10^9$ per m^3/s

Table 6.3: N_e Profile Times

	Subfigure			
Day	1	2	3	4
19	11:00:06	11:02:06	11:04:21	11:06:36
20	10:55:27	10:56:57	10:58:27	11:00:27
21	10:51:54	10:54:54	10:55:39	10:56:39

Times of electron density (N_e) profiles shown in Figure 6.7.

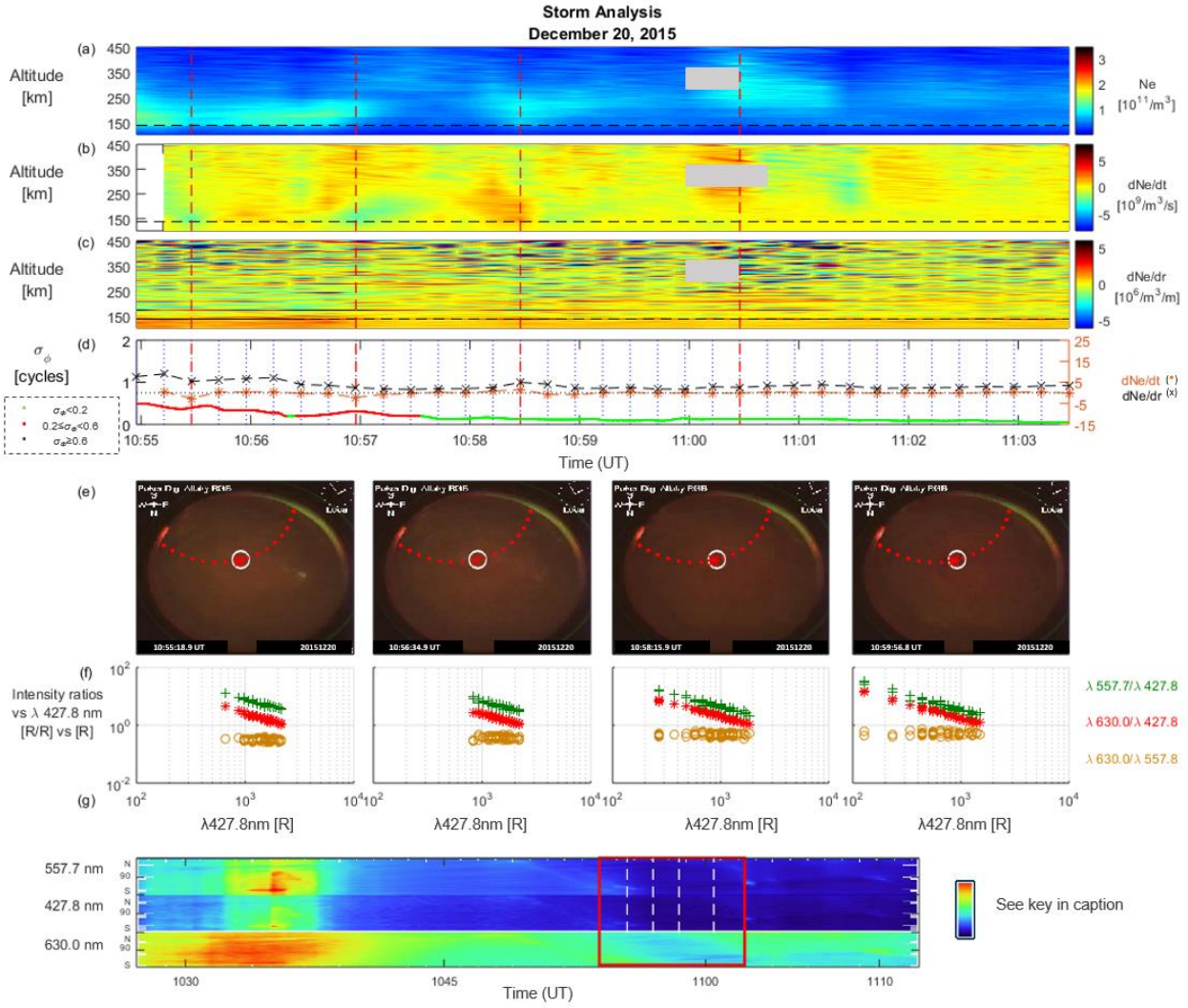

Figure 6.8: Same as Figure 6.6 except for December 20, 2015, 10:54:50-11:03:35 UT. The grey rectangles are locations where cable anomalies are present (discussed in the text). The keogram color bar lower limit is 0 R for all wavelengths and has upper limits of 25000 R (557.7 nm), 2000 R (428.7 nm), and 3000 R (630.0 nm).

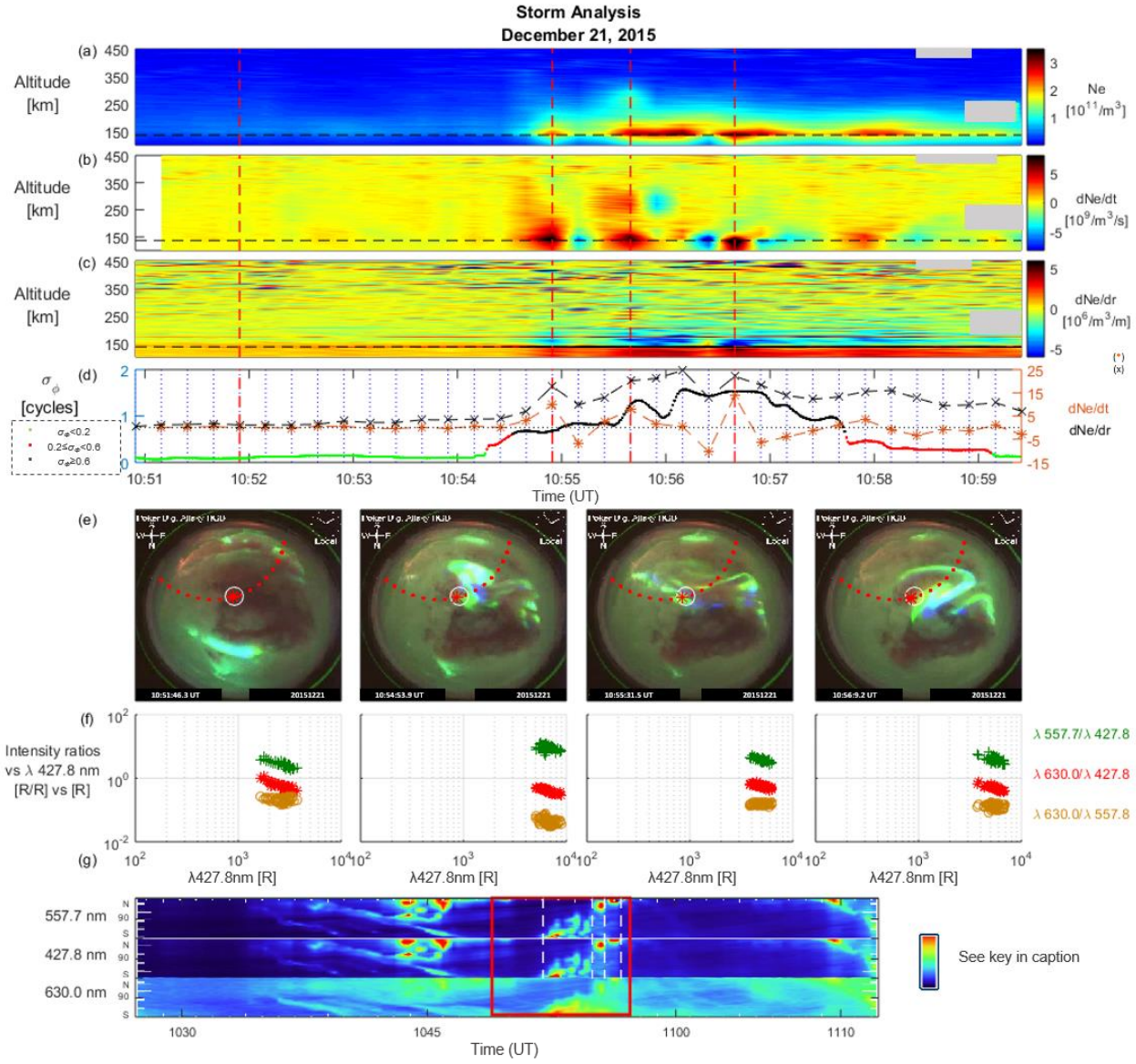

Figure 6.9: Same as Figure 6.8 except for December 21, 2015, 10:50:47-10:59:32 UT. The grey rectangles are locations where cable anomalies are present (discussed in the text). The keogram color bar lower limit is 0 R for all wavelengths and has upper limits of 70000 R (557.7 nm), 5000 R (428.7 nm), and 3000 R (630.0 nm).

respectively. The peak spatial gradient is 2.7 times larger on the 21st than the 20th, and the peak temporal gradient is approximately 4.7 times larger. Corresponding to the scintillation event and the gradients are consecutive discrete auroral arcs that move through the path of the GPS signal and the radar beam.

On each of the Figures 6.6, 6.8 and 6.9 are emission intensity ratios plotted against the blue line emission intensity. All three ratios were compared to the work of *Rees and Luckey* (1974), however only the ratio of red to blue was evaluated here. On all three days, ratio plots are relatively linear with a decreasing slope. The ratios on 19 December decrease from 5 to 0.3, across blue intensities that vary from just over 100 R to nearly 2 kR. This ratio on 20 December varies from approximately 17 down to 1, but is clustered around a range of blue intensities ranging from near 0.1 kR to just under 2.2 kR. On the 21st the grouping is tighter and varied across the scintillation event window, with just as varied blue intensities. The first, third and fourth frames have intensity ratios from approximately 1 down to 0.4 that are tightly clustered in the first image between 1.6 kR and 3.7 kR, and in the third and fourth images ranging between 3.8 kR and 6.8 kR. In the second image the ratio dips even further to a range of 0.5 down to 0.2, and is clustered around blue intensities of 5.1 kR to 8.9 kR. As will be discussed further in the next section, these ratios indicate precipitation energies near $\alpha \sim$ 0.6-3 keV on 19 December, $\alpha \sim$ 0.6-1 keV on 20 December, and $\alpha \sim$ 1.5-4 keV on the 21st. These values are interpreted in Section 6.3.3.

6.3.2 Correlation Analysis

A correlation analysis across all altitudes aids in determining the relationship of the magnitude of the temporal and spatial gradients at each altitude with the observed scintillation level. Correlation coefficients (R-values) can occur in the range $[-1, 1]$, with a value closest to one indicating a strong correlation, and R near -1 a strong anti-correlation, presuming that the R-value is statistically highly significant (corresponding p-value$\leq$ 0.005) (*Taylor*, 1997). Data from all experiment windows (see Table 6.2) was used in this calculation. The 15 s data resolution supported comparison of σ_ϕ with a total of 360 data points of dNe/dr, and 351 data points of dNe/dt. The

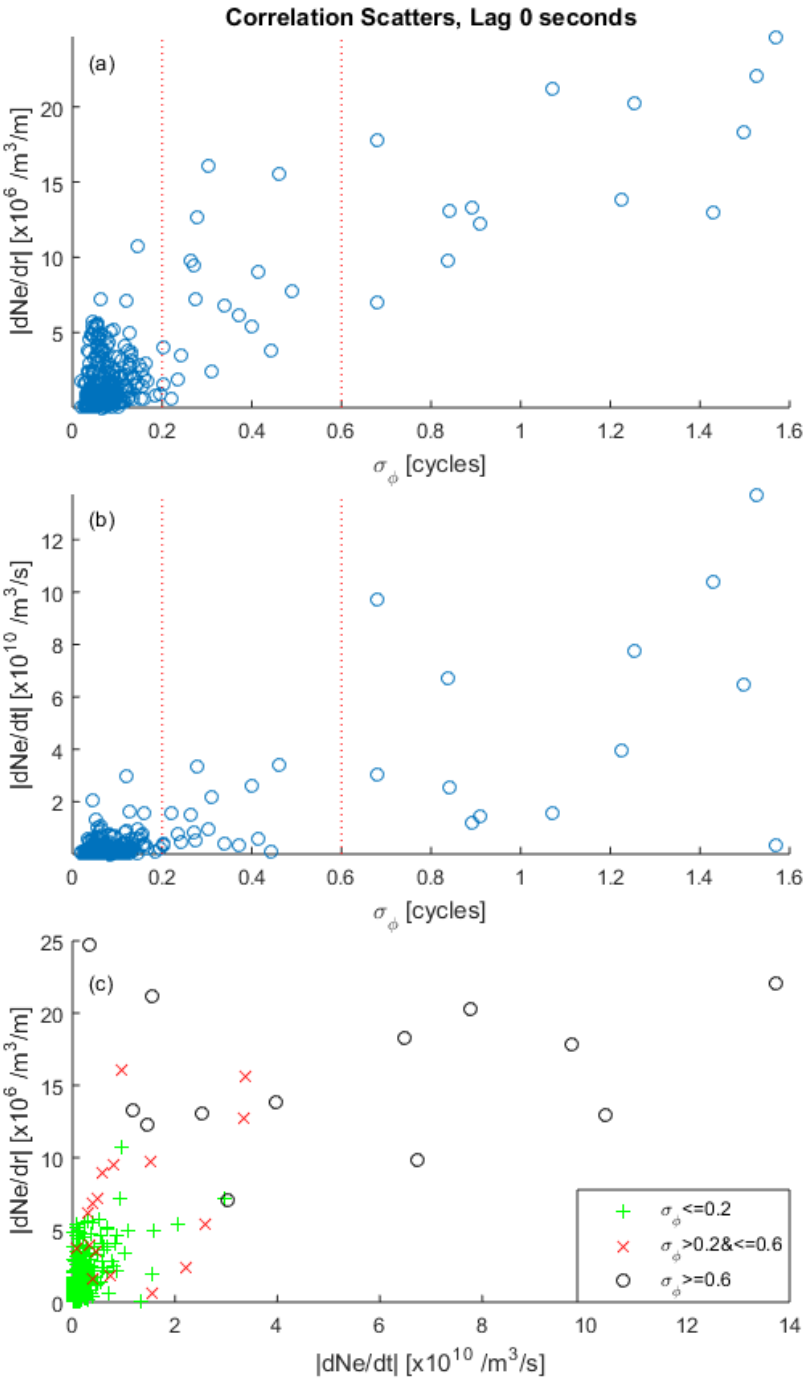

Figure 6.10: Correlation scatter plots between (a) dNe/dr and σ_ϕ, (b) dNe/dt and σ_ϕ, and (c) dNe/dr and dNe/dt for three intervals of σ_ϕ: less than 0.2 cycles (green '+'), between 0.2 and 0.6 cycles (red '×'), and above 0.6 cycles (black 'o').

maximum correlation is at an altitude of 137 km. A cross-correlation between the gradient and the scintillation showed that zero lag between these parameters yielded the best agreement, and indicated that the electron density irregularities and scintillation both appeared to occur within the 15 second PFISR observational cadence. A positive lag indicates the scintillation occurred after the gradient and negative lag the scintillation occurred before the gradient. Scintillation data in the analysis window was screened for values of $\sigma_\phi < 0.2$ cycles, $0.2 \leq \sigma_\phi < 0.6$ cycles and $\sigma_\phi > 0.6$ cycles. The resulting scatter plots for a lag of zero are shown in Figure 6.10.

In the top row (a), $|dNe/dr|$ is plotted against σ_ϕ, in the second row (b), $|dNe/dt|$ is plotted

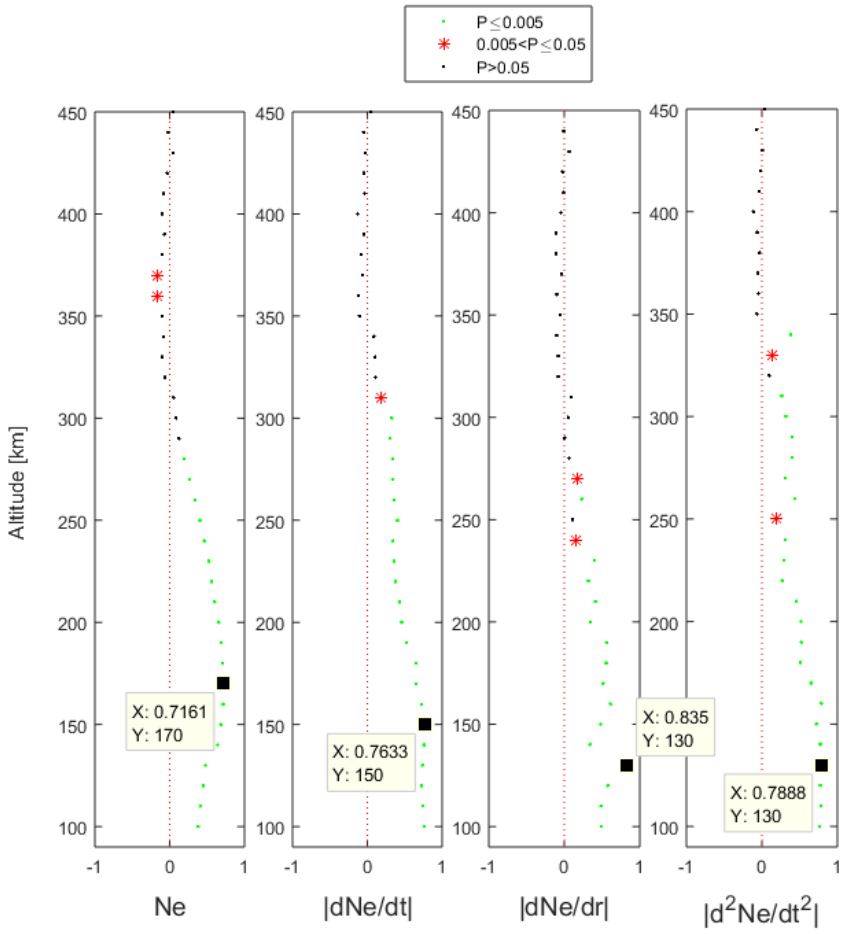

Figure 6.11: Correlation coefficients for σ_ϕ against each of N_e, $|dN_e/dt|$, $|dN_e/dr|$ and $|d^2N_e/dt^2|$ for December 2015 experiment.

against σ_ϕ, and in the third row (c) $|dNe/dr|$ is plotted against $|dNe/dt|$.There is a relatively strong correlation between $|dNe/dr|$ with σ_ϕ at 0.835 (p-value = 0), and the slightly weaker correlation coefficient between $|dNe/dt|$ and σ_ϕ at 0.769 (p-value = 0). An attempt was taken to see if the value of σ_ϕ was correlated to a combination of the two, and the result is row (c). All of the data for $\sigma_\phi \geq 0.6$ cycles (black 'o') are from the large scintillation event on the 21 December, whereas the other two intervals are a mixture from all three days. Where the red '×' and the green '+' overlap, there is mostly data from the 20th; and, where the red '×' and black 'o' overlap there is data from the 21st. All of the data from the 19th falls into the green '+' category.

Of note are several high scintillation data points ($\sigma_\phi \geq 0.6$ cycles) that have a large spatial gradient but a small temporal gradient. Each of these occur on 21 December; and, each is at a time when an auroral arc has just moved into or out of the signal path (see Figure 6.9). The two most extreme of these occurred at 10:55:55 ($|dNe/dr| \sim 21$ /m^3/m, $|dNe/dt| \sim 1.5$ /m^3/s) and 10:56:10 ($|dNe/dr| \sim 25$ /m^3/m, $|dNe/dt| \sim 0.5$ /m^3/s) - two consecutive radar measurements that fall in the middle of a large electron density peak. This peak is caused by a large folded auroral arc that moved from southwest to northeast through the signal line of site, in effect maintaining a large ionization peak in this area.

Electron densities, temporal and spatial gradients for the events of 14-21 December were then averaged over altitude bins of ten km starting at 90 km through 450 km.[3] Additionally, the second derivative of the temporal gradient, equivalently how fast the gradients were changing in time, was also computed. A subsequent correlation analysis between σ_ϕ and each of the original quantities plus $\mathrm{d}^2N_e/\mathrm{d}t^2$, is shown in Figure 6.11. There is a clear peak in correlation at altitudes in the vicinity of 130 km. The peak for the $\mathrm{d}N_e/\mathrm{d}r$ correlations is less evident. Scatter plots of $\mathrm{d}N_e/\mathrm{d}r$ against dN_e/dt for various E region altitudes are shown in Figure 6.12. The apparent correlation at 130km altitude corresponds to the peak in the $\mathrm{d}^2N_e/\mathrm{d}t^2$ correlation values shown in Figure 6.11. Even though the greatest correlation appeared between the spatial gradient and the

[3] This was done to ensure that this data could be compared to that from future experiments, which did not necessarily use the same beam.

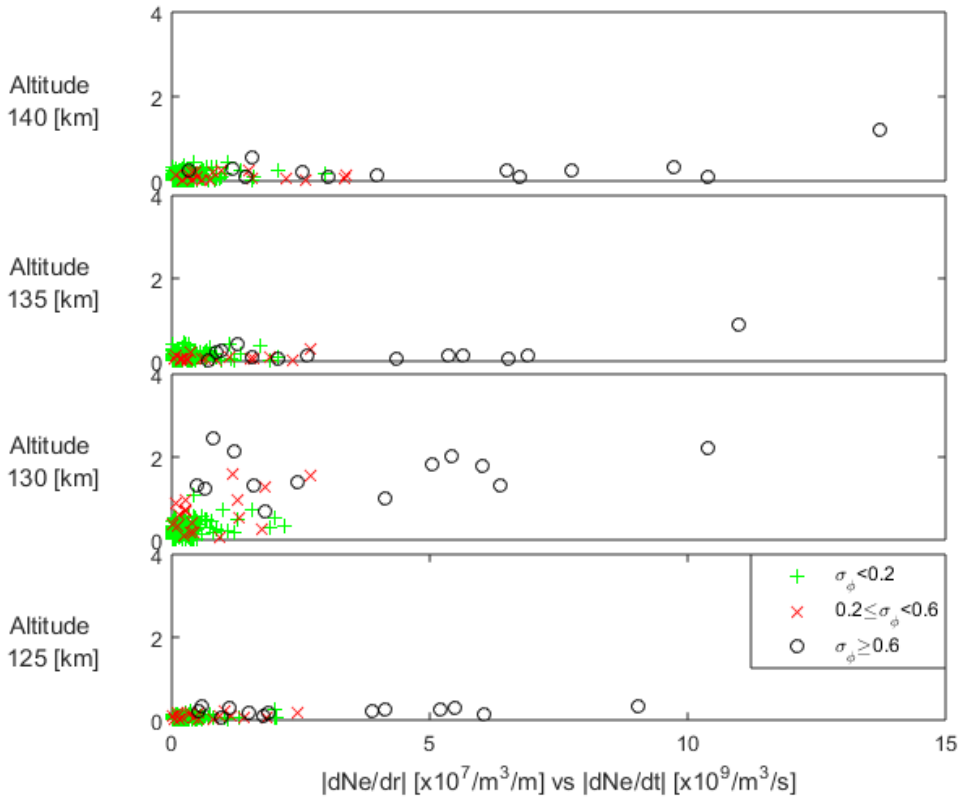

Figure 6.12: Scatter Plots of $|dN_e/dr|$ vs $|dN_e/dt|$ at five E Region altitudes (120km - 140km), 19-21 December 2015. Symbols and colors correspond to σ_ϕ intervals shown in Figure 6.10.

scintillation, it is evident there is much more to consider, especially when there is a much more consistent correlation between the temporal gradients over a range of altitudes than that of the spatial gradients.

6.3.3 Discussion

During this experiment PFISR measured the electron density along the line of sight to GPS PRN 12, which was directed along the magnetic field line, while the CASES receiver computed scintillation for this GPS satellite and the DASC provided key optical observations. On 20 and 21 December the GPS signal transited through the ionosphere with temporal and spatial gradients. These gradients in electron density correspond with variability in the index of refraction (n) along the signal's path, which introduced abrupt changes in the phase of the GPS signal recorded at

the receiver, resulting in scintillation events on two of the three days. This study addresses the following questions related to the observational campaign:

(1) What are the sources of the gradients?

(2) Where and when do they occur?

The answer to question one is that impact ionization from auroral particle precipitation with energies between 1 and 4 keV is the likely cause. Based on the intensity ratio of red to blue in the observed all-sky camera data, as plotted against blue intensities shown in row 6 of Figures 6.6, 6.8 and 6.9, one can infer the peak of the characteristic energy distribution, α [keV], of precipitating electrons from Figure 3 of *Rees and Luckey* (1974). Approximating maximum values from this chart yields for 19 December $\alpha \sim 3$ keV, 20 December $\alpha \sim 1$ keV, and 21 December $\alpha \sim 1.5$ keV for the first, third and fourth frames, but $\alpha \sim 4$ keV for the second frame. Cross-referencing these characteristic energies with the electron-ion pair production rate profiles shown in Figure 9.7 of *Schunk and Nagy* (2009), electron density peaks for each day are in the neighborhood of 120 km (19 December), 150 km (20 December) and 115-130 km (21 December). All of these correspond very well to the electron density peaks shown on each day, within the resolution of the radar range bins; and, are in line with previous results from *Garner et al.* (2011). Although the precipitating particles on 19 December have a similar energy as those on 21 December, there is a steady but smaller amount of precipitation. This results in less variation in the impact ionization and a lower and more constant electron density peak.

The answer to question two is that the scintillation causing gradients for this event occurred in the E region starting just before and lasting well into the scintillation events. To arrive at these conclusions first look at the electron densities. On December 19th, even though there is an increased density in the E region, it does not change rapidly in space nor time and no scintillation is observed. This is further supported by the keogram that shows a relatively consistent emission level at both the 557.7 nm and 630.0 nm emission lines in the southern sector over the time of the radar data (red box). The result is a steady influx of lower energy precipitating particles that

maintains the ionization in the vicinity of the affected altitudes, as represented by the steady ratio of red to green emissions. When there are scintillation events (20 and 21 December), however, note that varying gradients in electron density exist. The keogram on 20 December 20 shows a tapering of the green line emissions with a variety of levels detected on the red line. This corresponds to an increase in the ratio of red to green emissions over time, and therefore a decrease in electron density at E region altitudes, as is shown in the raw N_e data. The strongest scintillation occurs on the 21 December when large gradients exist in both time and space.

As was previously stated, correlation coefficients above 0.80 were observed between the spatial gradient at 137 km altitude and phase scintillation data, and a correlation coefficient of $\sim$0.70 was observed between the temporal gradient at the same altitude with the phase scintillation data (p-values of zero in both cases). These results indicate a stronger correlation of high scintillation ($\sigma_\phi \geq 0.6$ cycles) to the spatial gradient, and a slightly lower correlation with the temporal gradient. Additional experiments are needed to clearly delineate the relative impact of the spatial and temporal electron density gradients in the E-region on scintillation.

Relevant to this discussion are the uncertainties in the data. Stated in Section 6.2, uncertainties associated with each set of electron density measurements are approximately 2%. This implies the accuracy of the integration over the set of sampled returns, which were oversampled at a range resolution of 4.5 km. Once the data is fitted, it has a range resolution of 36 km which smooths the data, in effect reducing the spatial gradients so as to mask any subtle changes within the larger bin. So while the data presented here show an electron density peak near an altitude of 137 km, fitted data from PFISR with the appropriate resolution (not included herein) show an electron density peak near 134 km, lending credence to these findings. Further adding to this are the precipitating particle energies inferred from the emission intensity ratio analysis, which correspond to peak impact ionization production rates at altitudes between 115 km and 130 km. Clearly, the data indicate that this is an E region event.

The conclusions here are in general agreement with those presented by *Kinrade et al.* (2013), who concluded that discrete auroral arcs with green emissions along the GPS signal path were more

highly correlated to scintillation than red emissions. However, they assumed the peak green and red emission altitudes were 120 km and 200 km, respectively. In doing so, they had no ability take into account the fact that higher energy particles will statistically penetrate further into the neutral atmosphere; and, likewise lower energy particles will not penetrate as far. The use of PFISR in this study allows for the direct determination of the altitudes associated with the peak electron density, resulting in higher correlation values. Additional studies to determine if this was an isolated case or representative of GPS scintillation observed in the Alaskan sector are presented in subsequent chapters.

Pertinent to this discussion are the questions raised by *Forte et al.* (2013, 2016); *Jin et al.* (2014, 2016); *van der Meeren et al.* (2015) and others after recent studies in the polar cap aimed at determining the dominant scintillation causing ionospheric irregularity in the high-latitudes. Their conclusions that polar cap patches further structured by auroral activity after convecting into the auroral zone are the dominant causal feature have far reaching implications to our understanding of how the space environment affects trans-ionospheric communications and navigation signals. However, based on the geomagnetic and geographic difference in the experimental locations of *Jin et al.* (2014, 2016); *van der Meeren et al.* (2015) with PFRR, the comparison of these results to those found over Alaska are expected to have some contrasting elements. This is due in part to the proximity of the locations in these studies to the auroral oval. Svalbard sits in the polar cap poleward of the auroral oval, and Tromsøhas an equivalent magnetic latitue to Fairbanks. It is uniquely situated to observe phenomena as they transition between the two regions. By contrast, Alaska is situated on the day-side equatorward of the auroral oval, and transitions into and out of the auroral oval in the dusk and dawn sectors through the oval's equatorward boundary. Magnetic conditions are different in the two locations, although there are shared ionospheric phenomena. It is worth noting then that what may cause the greatest scintillation in one region, may not have the same effect in another. More targeted studies over Alaska similar to those being conducted over high-latitude sectors are required to ascertain the relative import of each phenomena, as well as what may be the source of the observed differences.

6.4 Summary & Lessons Learned

In summary, a nine day experiment using PFISR to track GPS satellites aligned with the magnetic field was conducted. GPS signals from PRN 12 traversed the ionosphere above Alaska and were received by the CASES receiver at PFRR during these experiments in December 2015. During the period of this experiment there was a geomagnetic storm that created a disturbed ionosphere which was variable in both time and space. The resulting gradients in electron density translated to a varying index of refraction (n) along the signal's path, which, in turn, introduced abrupt changes in the phase of the GPS signal recorded at the receiver. This led to a significant scintillation event on 21 December 2015. The observational data indicate that the most likely cause was electron density gradients associated with auroral precipitation in the form of discrete auroral arcs that ionized the E region ionosphere via collisions with the neutral atmosphere. Although F region impacts can not be ruled out by this case study, E region impacts appear to be of high importance based on the observed all-sky camera data and inferred energies associated with the auroral emissions and their intensity ratios. These precipitating particle energies ($\sim$1.5 keV to $\sim$4 keV) correspond to ionization production peaks in the range of 115-150 km altitude. This corresponds to the altitude of peak electron density and peak density gradients detected.

The data presented and analyzed in this chapter and the last lend themselves to several broad conclusions regarding both the ionospheric science and the experimental method used. While it is clear that E region enhancements were detected and attributed directly to GPS scintillation, more studies are required to determine the impact, if any, of F region enhancements on GPS scintillation above PFRR. Experimentally, historic PFISR E and F Region modes did not necessarily sense the ionosphere in close enough proximity to a given GPS signal's path to allow for the discernment of the source of the scintillating ionospheric enhancements. But a single beam pointed along the GPS line of sight allowed for attribution of GPS scintillation to spatial and temporal electron density gradients. Also, focusing efforts on magnetic midnight and earlier hours in accordance

with previous climatologies[4] yielded a higher likelihood of sensing environments directly related to GPS scintillation. Use of the DASC added context for interpretation of the ionospheric structures that were the source of the electron density gradients. However, use of the DASC alone was not enough to draw conclusions regarding the impact of particular emissions on GPS signals, as the energy analysis only yields the peak precipitation energy and does not always allow for the delineation between E and F region activity. Finally, the temporal resolution associated with historic PFISR experiment configurations (1 to 5 minutes), was not sufficient to discern electron densities that varied on temporal scales of seconds; but, using a single beam, a temporal scale of 15 seconds (on par with the DASC resolution) this was possible. The analyses that follow are from subsequent studies and follow-on experimental campaigns that seek to better understand the scintillation phenomenology via increasing statistical robustness of a correlation analysis, and to capitalize on lessons learned at the end of each campaign.

[4] See Section 3.3

Chapter 7

March-April 2016: Climatology Campaign I

The lessons learned from the case study of the St Patrick's Day Storm of 2013, and the initial data sets taken for the Winter Solstice Storm of 2015 centered around three things. First, only E region enhancements resulting from impact ionization due to auroral precipitation were detected and attributed directly to GPS scintillation; more studies are required to determine the impact of F region enhancements on GPS scintillation. Second, use of the DASC added context for the ionospheric phenomena that were the source of the electron density gradients; however, use of the DASC alone was not enough to draw conclusions regarding the impact of various emissions on GPS signals. Lastly, focusing efforts on magnetic midnight and earlier hours in accordance with previous climatologies yielded a higher likelihood of sensing environments directly related to GPS scintillation. Other important notes regarding the use of PRISR include the requirement for a single beam pointed along the GPS line of sight for attribution of electron density gradients to GPS scintillation; and, the ability to achieve a temporal scale of 15 s with the use of a single radar beam, which is consisitent with the DASC resolution. Based on these requirements, an experiment campaign on PFISR was designed that would minimize the temporal gradient and sense electron densities along the GPS line of site. This chapter contains an analysis of the experiment campaign based on this concept. Between March and April 2016, 68 experiments were run resulting in 13.2 hours of data; and, between May and July 2016, an addtional 52 experiments were run yielding 18.75 hours of data. Analysis of the March and April data sets are presented here.

7.1 Storm Summary

There were four periods of geomagnetic activity that occurred during the experiment windows of March and April 2016, and these are summarized in Table 7.1. Each storm was minor compared to the Winter Solstice Storm of 2015 and the St Patrick's Day Storm of 2016; however, each elicited a global storm-time response. Figures 7.1 and 7.2, top row, show the DST and Kp indices for 14-21 March and 7-15 April respectively. In the second row of each figure are the IMF B_y and B_z components, and in the third row of each are the local magnetometer readings showing deviation from average for each component. In the magnetometer data quasi-nightly auroral events and substorms appear that are not necessarily reflected in the DST and Kp values [1]

Table 7.1: Summary of indices for geomagnetic storms that occurred during the Spring Ecquinoctial season of 2016.

Date	DST [nT]	Kp
14-15 March 2016	-50	5
7-8 April 2016	-60	5.7
12-13 April 2016	-55	5
14-15 April 2016	-59	4.7

7.2 Experiment Setup

The initial focus of Climatology Campaign I were on the magnetic midnight and earlier hours of the Equinoctial months (March and April). Conjunction analyses for this time frame revealed that a total of seven beams met this criteria at various times, including the field aligned beam (beam #64157). Presented here are a subset of results from March-April 2016, all experiments, of which, were conducted with the support of the DASC. Other than the difference in beams and the length of time on a single beam, no other experimental parameters for March - April 2016 were changed from the experiments conducted in December 2015.

[1] A Kp value of at least 3 is deemed 'magnetically active'. See Chapter 2.

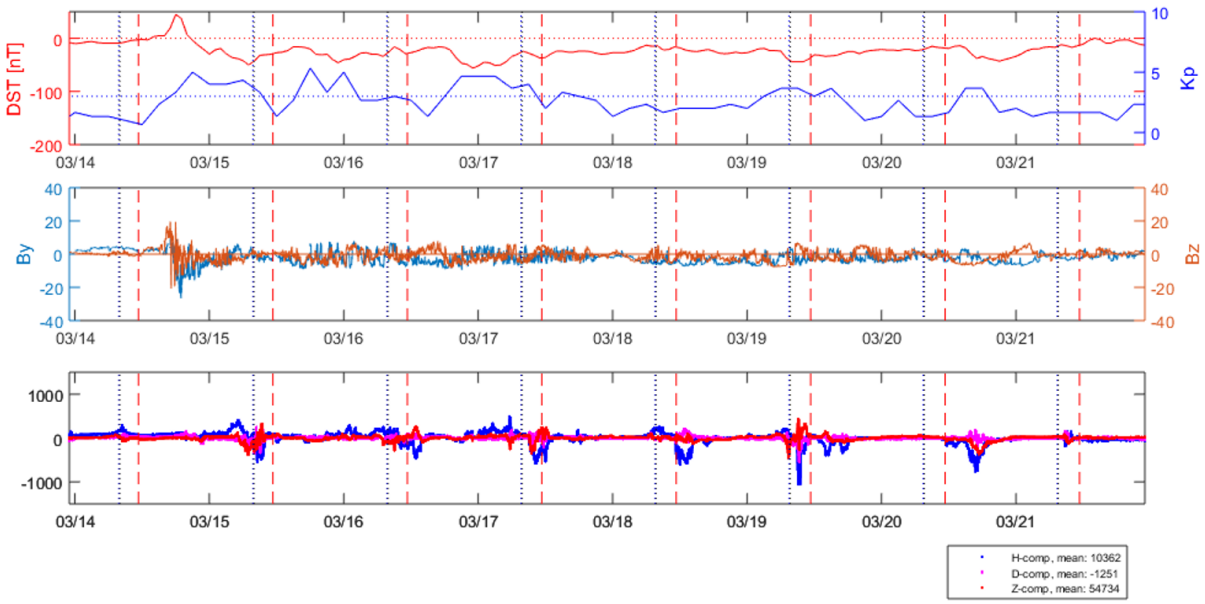

Figure 7.1: Indices for select days of March 2016.

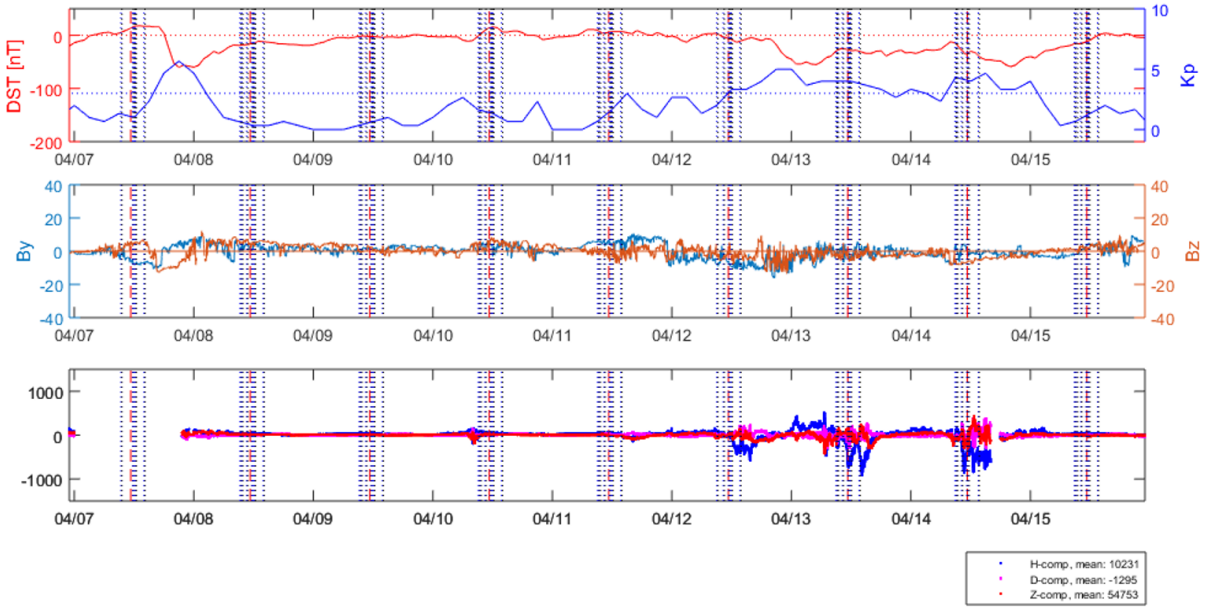

Figure 7.2: Indices for select days of April 2016.

7.3 Results

Experiments were run once per day in March on only the field aligned beam, and multiple times per day during April, all due to the occurrence of GPS conjunctions with six PFISR radar

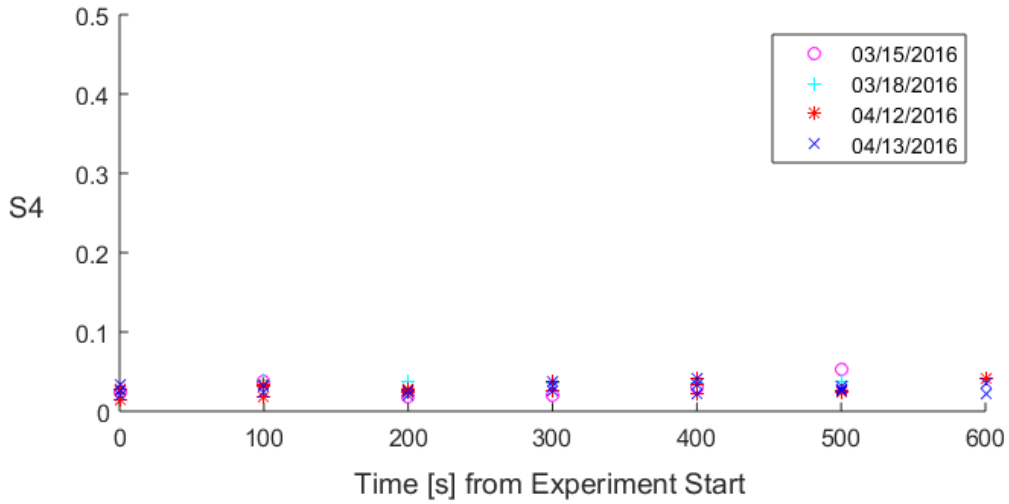

Figure 7.3: Amplitude (S4) index during the March and April 2016 experiement windows shown in Table 7.2.

beams other than the field aligned beam during the required windows. Data from six of these experiments (summarized in Table 7.2) are shown in Figures 7.6 through 7.12; and, all experiment times and beams are listed in Appendix C.

Based on scintillation statistics and climatologies discussed in Section 3.3, amplitude scintillation was not expected to be a factor in this study. Shown in Figure 7.3 are CASES reported S4 index at 100 s cadence during the experiment windows shown in Table 7.2. As expected, even though the signal phase is scintillating as is shown in subsequent sections, the amplitude remains mostly unaffected.

7.3.1 Data

Over the course of 67 experiments throughout the months of March and April, each ranging from 10 to 30 minutes in length, a total of 13.2 hours of data from the radar, imager and GPS data were analyzed. Of these, 4.6 hours of data were incorporated into the correlation study discussed in Section 7.3.2, and of these there were only only five intervals with at least one instance of $\sigma_\phi \geq 0.2$ cycles, all of which are shown here.

Presented in the following sections are examples that show mild ($\sigma_\phi < 0.2$ cycles), moderate

Table 7.2: Select PFISR Experiment start and stop times, March & April 2016. See Appendix C for a full listing of all experiment beams, dates and times for this mode.

Day	Start [UT]	Stop [UT]	Beam	Altitude [km]	PRN	Peak σ_ϕ [cycles]	Peak α [keV]	Figure
				March				
15	7:46:00	7:56:00	64157	137	29	0.67	1.6-3	7.11
18	7:34:00	7:44:00	64157	350	29	$\leq$0.2	1.6	7.6
				April				
12	11:56:46	12:08:01	65192	121	10	0.38	2-3	7.9
13	8:57:47	9:10:02	63299	118	21	0.97	10-15	7.12
13	11:16:46	11:28:01	63299	118	10	$\leq$0.2	2-3	7.4
14	10:11:43	10:23:58	65321	125	18	1.41	2-3	7.13

($0.2 \leq \sigma_\phi < 0.6$ cycles) and major ($\sigma_\phi \geq 0.6$ cycles) scintillation. Each figure has data presented in a similar manner to those from the December 2015 analysis; and, the description of these rows is briefly repeated here for reference. The first row (a) contains N_e altitude time profiles, presented at 15 s cadence and at 4.5 km vertical spacing. Vertical profiles at times corresponding to each of the vertical red dashed lines are shown in corresponding figures as referenced throughout the discussion. The second and third rows (b and c) are the temporal and spatial gradients, respectively, presented at the same spatial and temporal resolutions as N_e. The horizontal black dashed line in the first three rows highlights the data at the altitude indicated in Table 7.2. Where they appear, grey rectangles indicate artifacts associated with one of the radar antenna cables, and are not electron density enhancements. The fourth row (d) contains σ_ϕ in cycles for the PRN listed in Table 7.2 on the left (blue) axis, and dNe/dt (brown '*') and dNe/dr (black '$\times$') at indicated altitude slice on the right axis, scaled the same as rows (b) and (c). Note that σ_ϕ values of less than 0.2 cycles are shown as green, σ_ϕ of at least 0.2 cycles but less than 0.6 cycles are shown as red if present, and σ_ϕ of at least 0.6 cycles are shown as black if present.

The fifth row (e) contains images where all three emission lines have been overlaid, with the red and blue lines enhanced for visibility. The times of the images correspond to the times of the vertical red dashed lines in the first four rows and the images are inverted (North is down). Overplotted on the images are: (1) a white circle at the center of which is the direction of the radar

beam, with the circle enlarged for visibility; (2) a red dotted arc representing the trajectory of the GPS satellite throughout the day with (3) a red '*' indicating its location at the epoch represented in each image. In the next row (f) are plots of the emission intensity ratios against the 427.8 nm intensities, where the green to blue ratio is represented by a green '+', the red to blue ratio by a red '*', and the red to green ratio by a brown 'o'. The keogram for these days has been omitted, but displayed as a separate figure where relevant.

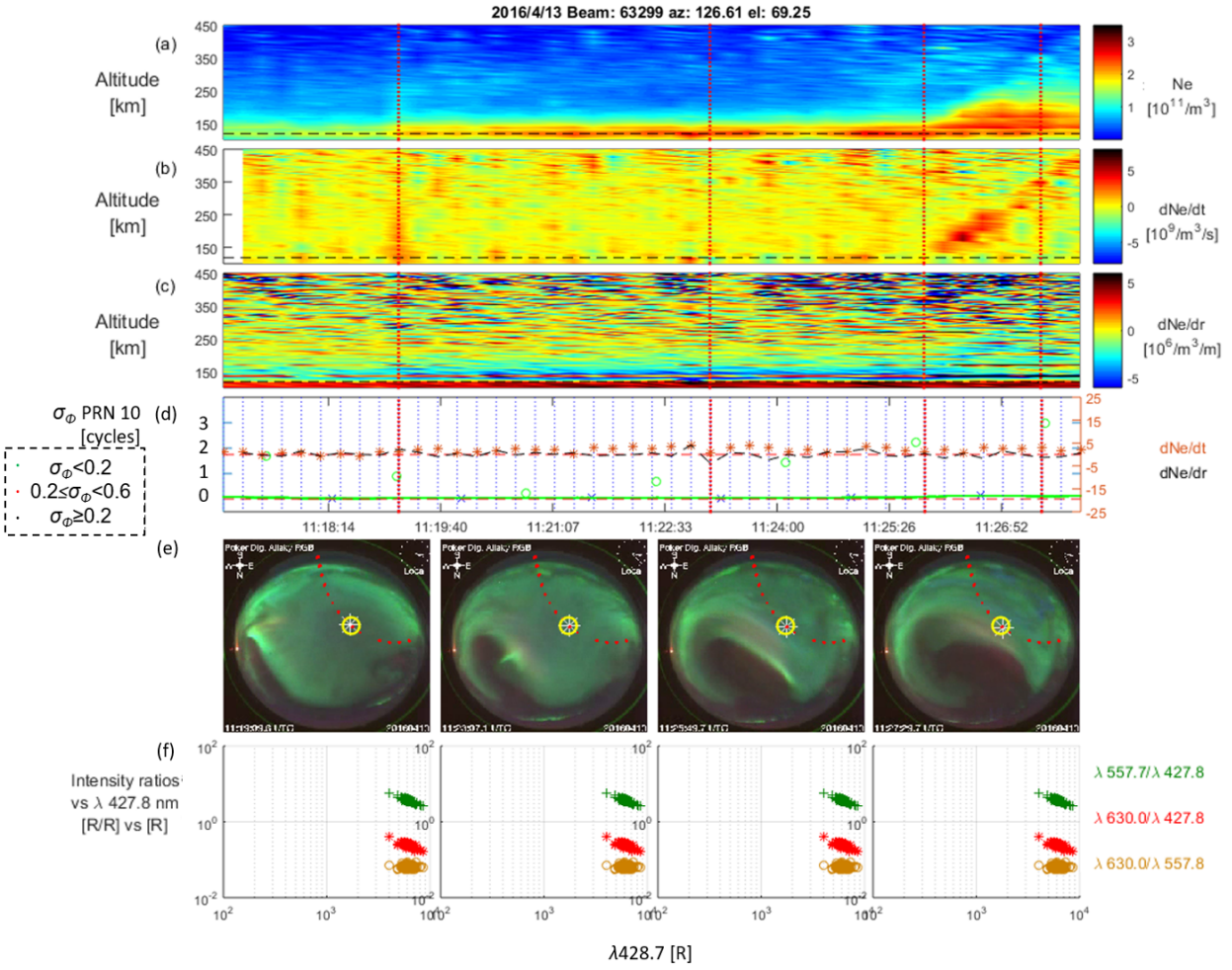

Figure 7.4: Results for 13 April 2016, PFISR Beam #63299. All rows correspond to those shown in Figures 6.6 through 6.9, except that the keogram has been left off. The altitude slice shown is for 118 km.

Table 7.3: Electron density profiles corresponding to the times indicated with vertical red dashed lines in Figures 7.6 and 7.4.

	Subfigure			
Day	1	2	3	4
18-Mar	7:36:51	7:38:06	7:40:51	7:41:36
13-Apr	11:19:08	11:23:08	11:25:53	11:27:23

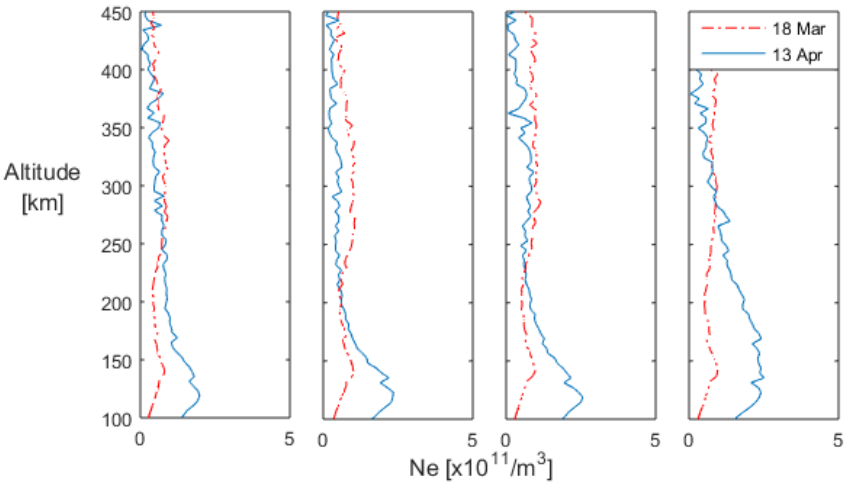

Figure 7.5: Electron Density (N_e) profiles corresponding to the vertical red lines of Figures 7.6 and 7.4, with horizontal black dashed lines corresponding the altitude slice taken in the corresponding figure.

7.3.1.1 Mild Scintillation

Two examples of mild scintillation are presented here. The first, shown in Figure 7.4, is associated with E region enhancements; the latter, shown in Figure 7.6, contains both E and F region enhancements. In both cases, scintillation values never exceed 0.2 cycles. Shown in row (e) of Figure 7.4 (13 April), are primarily green emissions filling the DASC view. Electron density enhancements associated with these emissions are evident in the electron density color plots of the figure (row a), and in profiles shown in Figure 7.5. E Region electron density is steadily increasing over time, but shows very little short term variation as evidenced by the gradient plots in rows 2 and 3. Energy estimates of the precipitating particles are $\sim 2-3$ keV. These are consistent with

the altitudes of peak E region electron density enhancements $\sim$ 118 km (*Schunk and Nagy*, 2009).

The second example of mild scintillation is shown in Figure 7.6 (18 March). Seen are red emissions filling the view of the DASC (row e), with green emissions also faintly visible, especially along the northern (bottom) edge, and across the images' central band. Electron density enhancements associated with these emissions are evident in the electron density color plots of the figure (row a), and in profiles shown in Figure 7.5. Energy estimates of the precipitating particles are $\sim$ 1.6 keV. These are consistent with the altitudes of peak E region electron density enhancements, $\sim$ 145 km (*Schunk and Nagy*, 2009). E region electron densities are roughly constant over time as

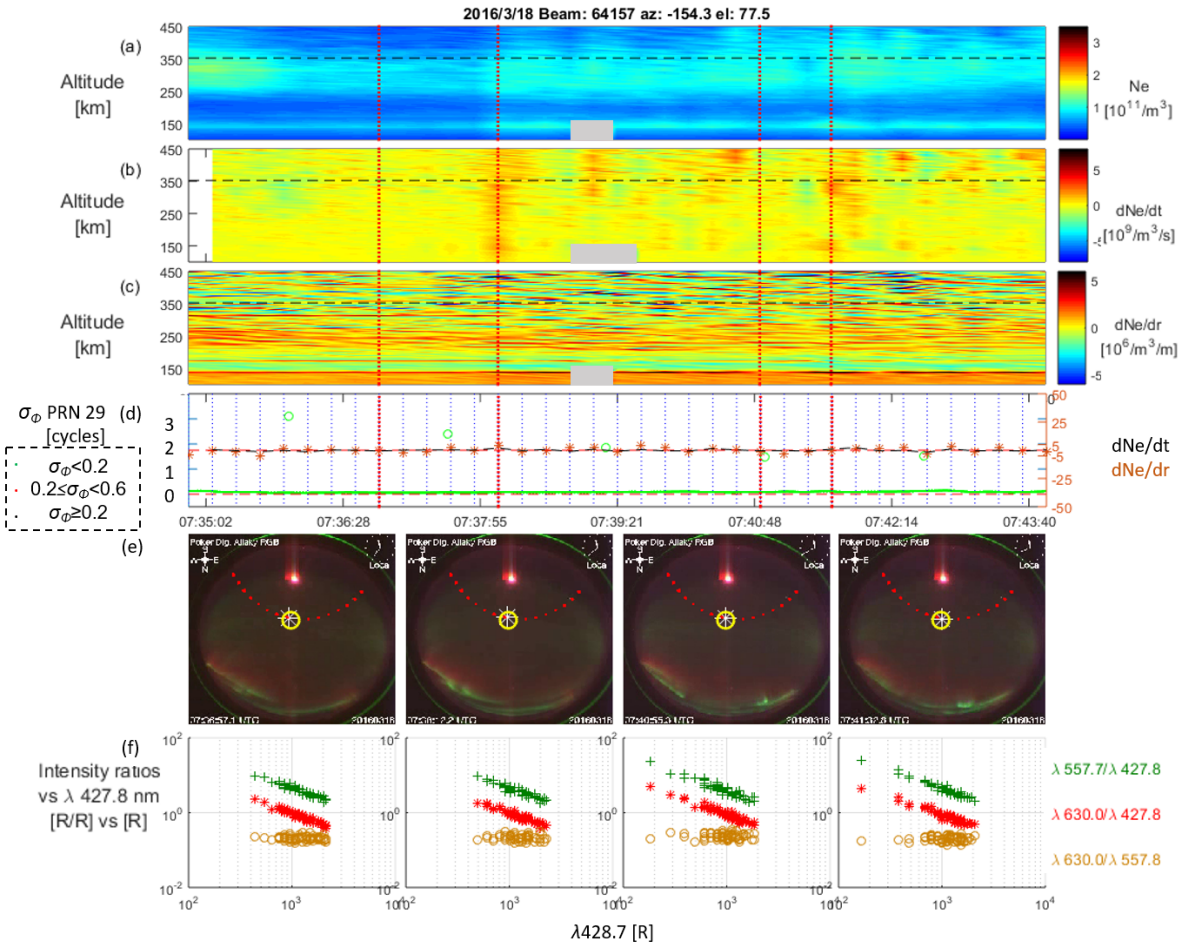

Figure 7.6: Results for 18 March 2016, PFISR Beam #64157. All rows correspond to those shown in Figures 6.6 through 6.9, except that the keogram has been left off. The altitude slice shown is for 350 km.

can be seen from the color plots of dNe/dt (row 2) and dNe/dr (row 3). Also present in Figure 7.6, are additional F region enhancements centered around an altitude of 340 km. To better understand what is happening in this experiment, additional information is gleaned from both the keogram shown in Figure 7.7, and from the PFISR experiments run immediately before and after it, shown in Figure 7.8. The keogram from 18 March reveals significant red line emissions (bottom row, experiment window highlighted with red box) during the time of the experiment. The peak green line intensities (∼15 kR) are roughly an order of magnitude greater than the peak red line intensities (∼1.5 kR). This is the typical signature of an auroral or plasma blob (*Hosokawa et al.*, 2011). To confirm the presence of the auroral blob, N_e from the WorldDay35 campaign on PFISR is evaluated, which operated both before and after the 18 March GPS conjunction experiment. Three-dimensional visualizations are shown in Figure 7.8. Each frame is roughly five minutes apart and is displayed in East-North-Up components. The dots are colored according to the electron densities on the colorbar shown and *not* proportionally sized. Electron density enhancements occur predominantly at F region altitudes in each frame. They do not, however, appear to have

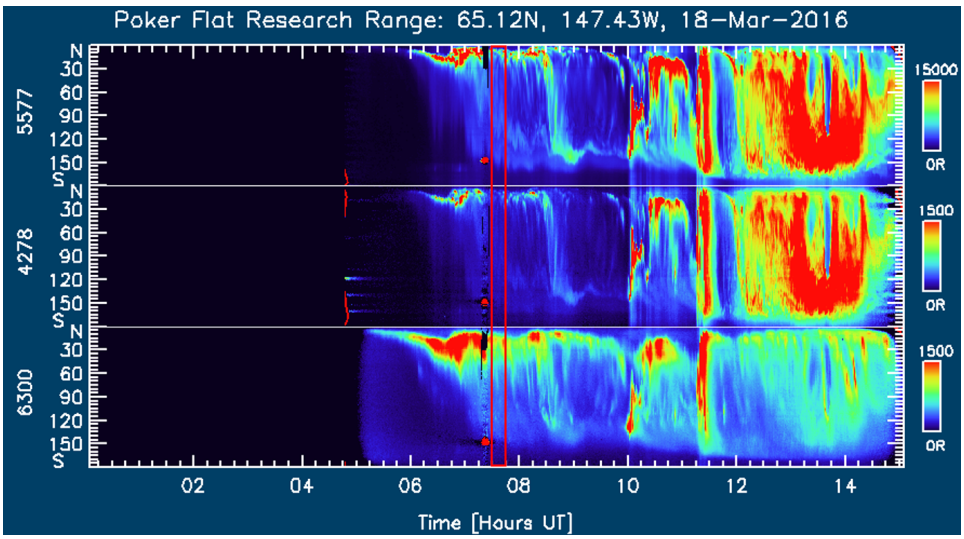

Figure 7.7: Keogram for 18 March 2016. Shown are emission intensities for the green (top row), blue (middle row) and red (bottom row) lines, with colorbars corresponding to the scales of each to the right. The peak green line intensities (∼15 kR) are roughly 10× greater than the peak red line intensities (∼1.5 kR). The experiment window from Figure 7.6 is highlighted with a red box.

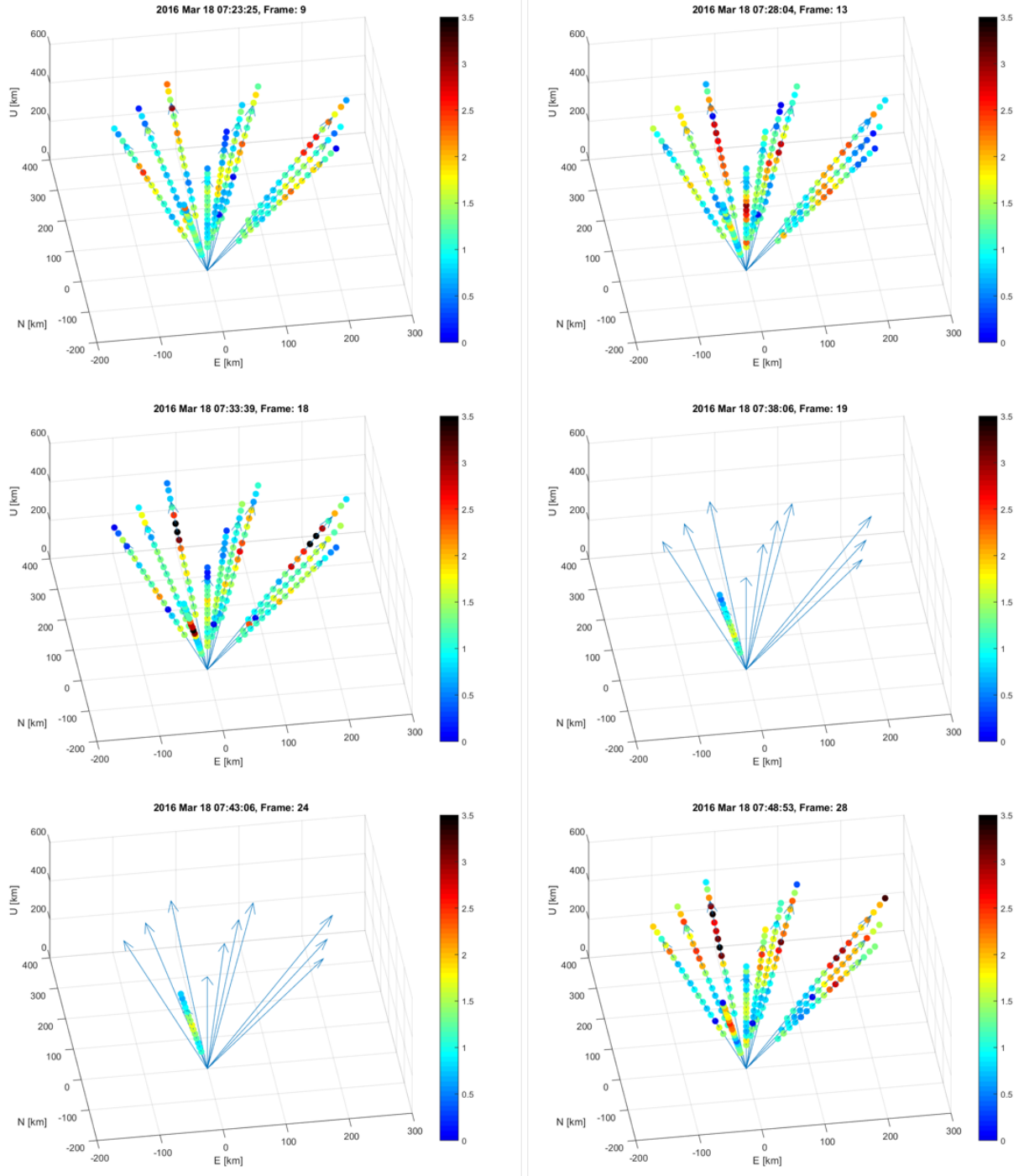

Figure 7.8: Three dimensional visualizations for 18 March 2016. Frames 9, 13, 18 and 28 are from the WorldDay35 experiment campaign that took place before and after the 18 March GPS campaign (frames 19 and 24). Vector arrows align with each beam in use for the WorldDay35 campaign and give visual reference for this experiment set.

any impact on this set of GPS signals even though resulting gradients appear along the signal line of site. This type of event occurs during the March and April experiment sets a total 15 times: each experiment revealing F region enhancements that are most likely auroral blobs that do not result in a scintillation event. Of these instances, ten occurred in the vicinity of magnetic midnight, consistent with the timing of the convection of a polar cap patch into the auroral oval (*Moen et al.*, 2015). Of the remaining five, one occured in the 07-08 UT window, and four in the 09-10 UT window; each, of which, is consistent with the continued convection of auroral blobs through the

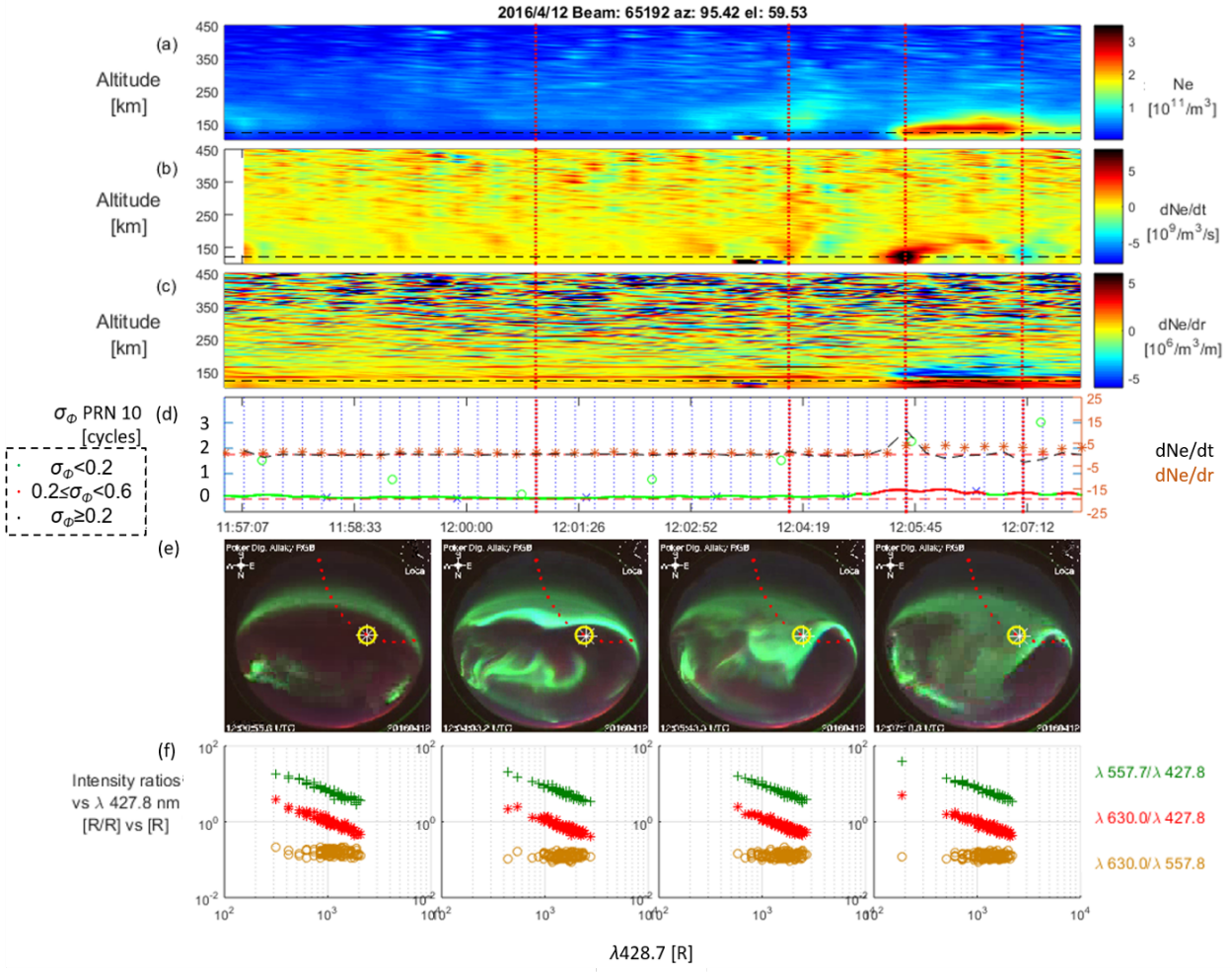

Figure 7.9: Results for 12 April 2016, PFISR Beam #65192. All rows correspond to those shown in Figures 6.6 through 6.9, except that the keogram has been left off. The altitude slice shown is for 121 km.

auroral oval before rejoining the dayside plasma.

7.3.1.2 Moderate Scintillation

An example of a moderate scintillation event is shown in Figure 7.9. Green line emissions appear in the form of a discrete auroral arc moving through the field of view of the radar and of the GPS signal path. Energies associated with the arc are on the order of 2-3 keV and consistent with the electron density enhancement centered around 120 km shown in the first row and in Figure 7.10. Unlike Figures 7.6 and 7.4, the arc is discrete, in the ray path and maintains a constant position for a time before moving on, creating a temporal and spatial gradient as can be seen in the gradients shown in rows 2 and 3. Here scintillation rises to a value of $\sigma_\phi = 0.38$ cycles before tapering off. The appearance of the scintillation is directly linked to the sudden movement of the arc into and immediately out of the GPS signal line of site. The difference between this example and those presented in the previous section is the change of N_e over time - relatively rapid increase followed by a decline, compared to steady increase in the non-scintillating examples.

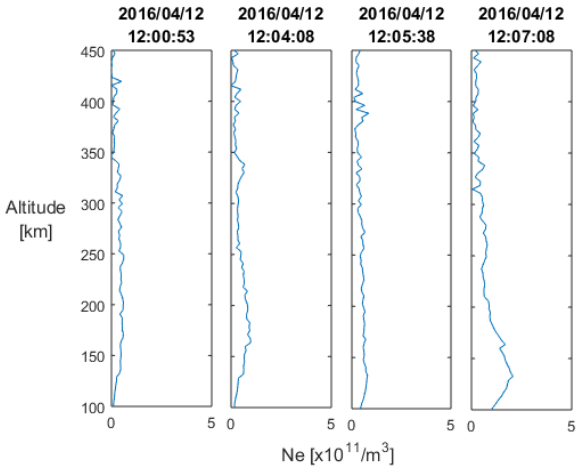

Figure 7.10: Electron Density (N_e) profiles corresponding to the vertical red lines of Figure 7.9, with horizontal black dashed lines corresponding the altitude slice taken in the same figure.

7.3.1.3 Major Scintillation

Figures 7.11, 7.12 and 7.13 show examples of major scintillation events associated with repeated movement of auroral arcs in and out of the GPS ray path. In the DASC view of Figure 7.11 there is a single auroral arc that moved through the GPS ray path and radar beam. Energies associated with this arc are 1.6-3 keV, corresponding well to the peak electron density enhancements shown in the radar data near 120 km altitude and in the electron density profiles of Figure 7.14. The difference between this example and that shown in Figure 7.9, is that the arc does not sit in the ray path for an extended period of time. Rather, it moves quickly through, creating the

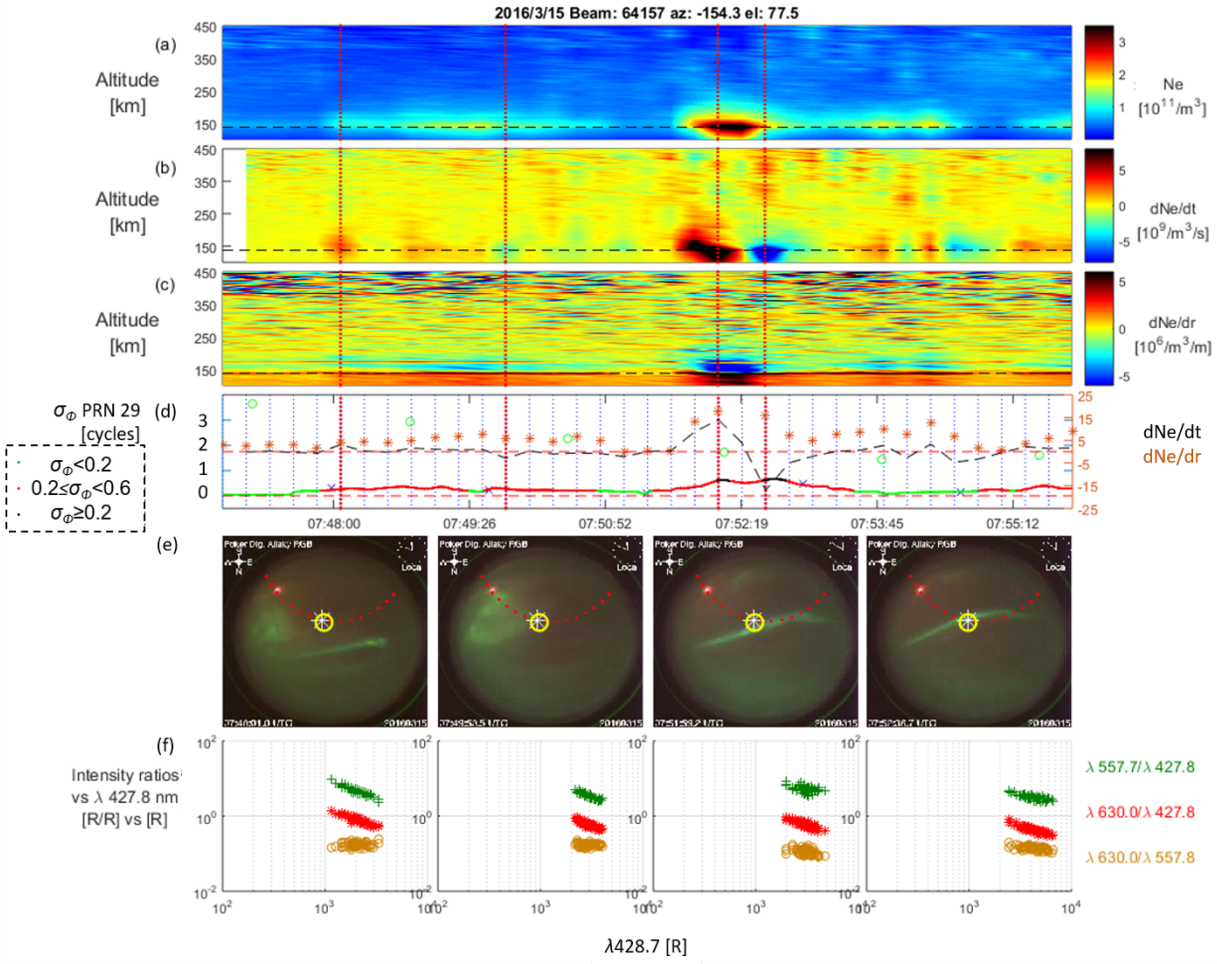

Figure 7.11: Results for 15 March 2016, PFISR Beam #64157. All rows correspond to those shown in Figures 6.6 through 6.9, except that the keogram has been left off. The altitude slice shown is for 137 km.

large temporal gradient seen in row 2. A peak scintillation value of $\sigma_\phi = 0.67$ cycles is seen. In the DASC view of Figure 7.12, a succession of auroral arcs is visible moving in and out of the view of the radar and the GPS ray path, thus creating the fluctuating temporal gradient shown in row 3. Energies associated with this arc are 10-25 keV, corresponding well to the peak electron density enhancements shown in the radar data near 115 km in altitude and in the electron density profiles of Figure 7.14. Peak scintillation values of up to $\sigma_\phi = 0.97$ cycles are recorded and the impact of the fluctuations in the gradient over time is clearly seen.

The greatest scintillation event experienced during the March - April 2016 experiment set

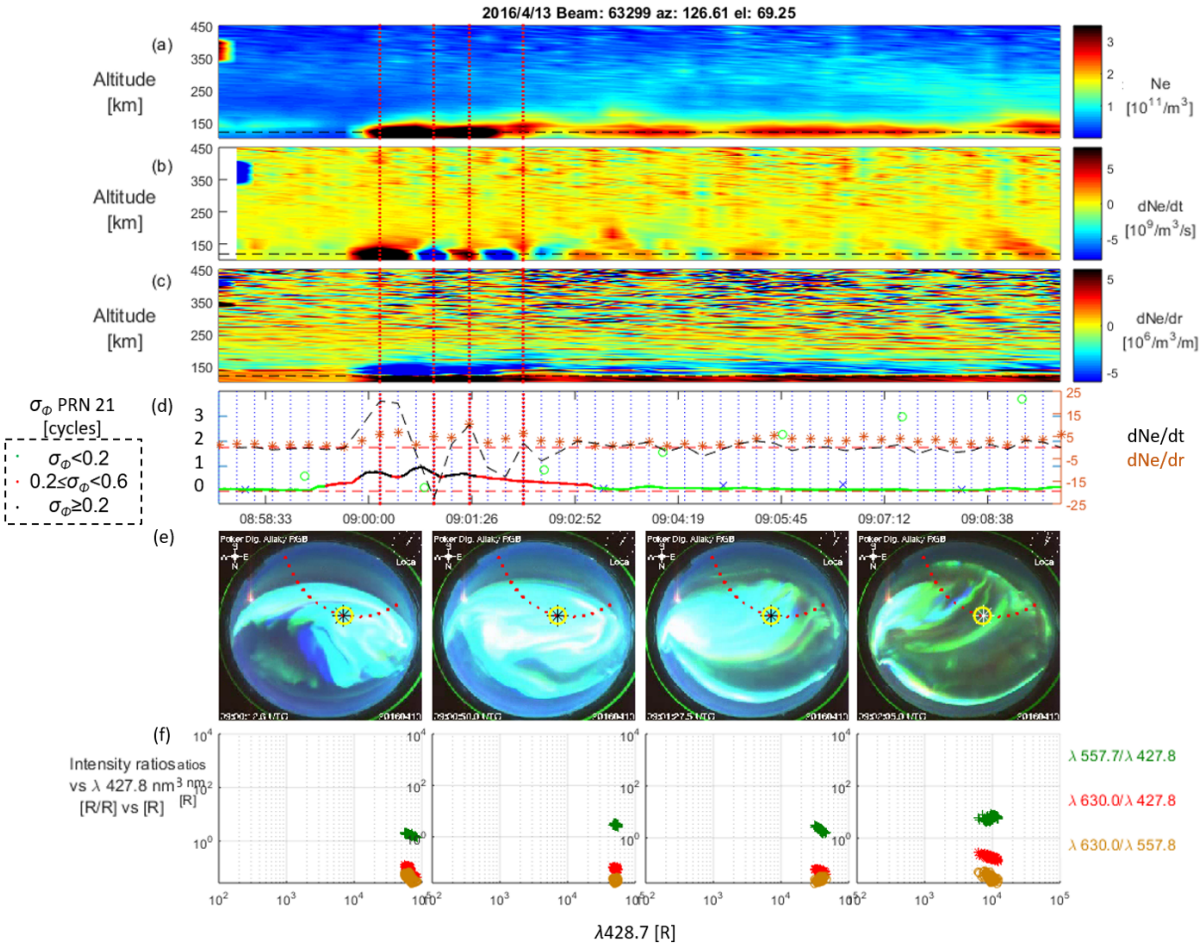

Figure 7.12: Results for 13 April 2016, PFISR Beam #63299. All rows correspond to those shown in Figures 6.6 through 6.9, except that the keogram has been left off. The altitude slice shown is for 118 km.

is revealed in Figure 7.13. Scintillation values reached a peak of $\sigma_\phi = 1.41$ cycles as a series of auroral arcs move through the GPS ray path and view of the radar. Precipitating particle energies are on the order of 2-3 keV and correspond to electron density peaks ~125 km, and in the electron density profiles of Figure 7.14. It is interesting to note here that although the experienced scintillation is greatest in this example, the fluctuations are not as severe as the previous example. It is also interesting to note that the GPS signal is scintillating at least moderately throughout the experiment window, but there are very few electron density enhancements or fluctuations seen at the onset of the interval.

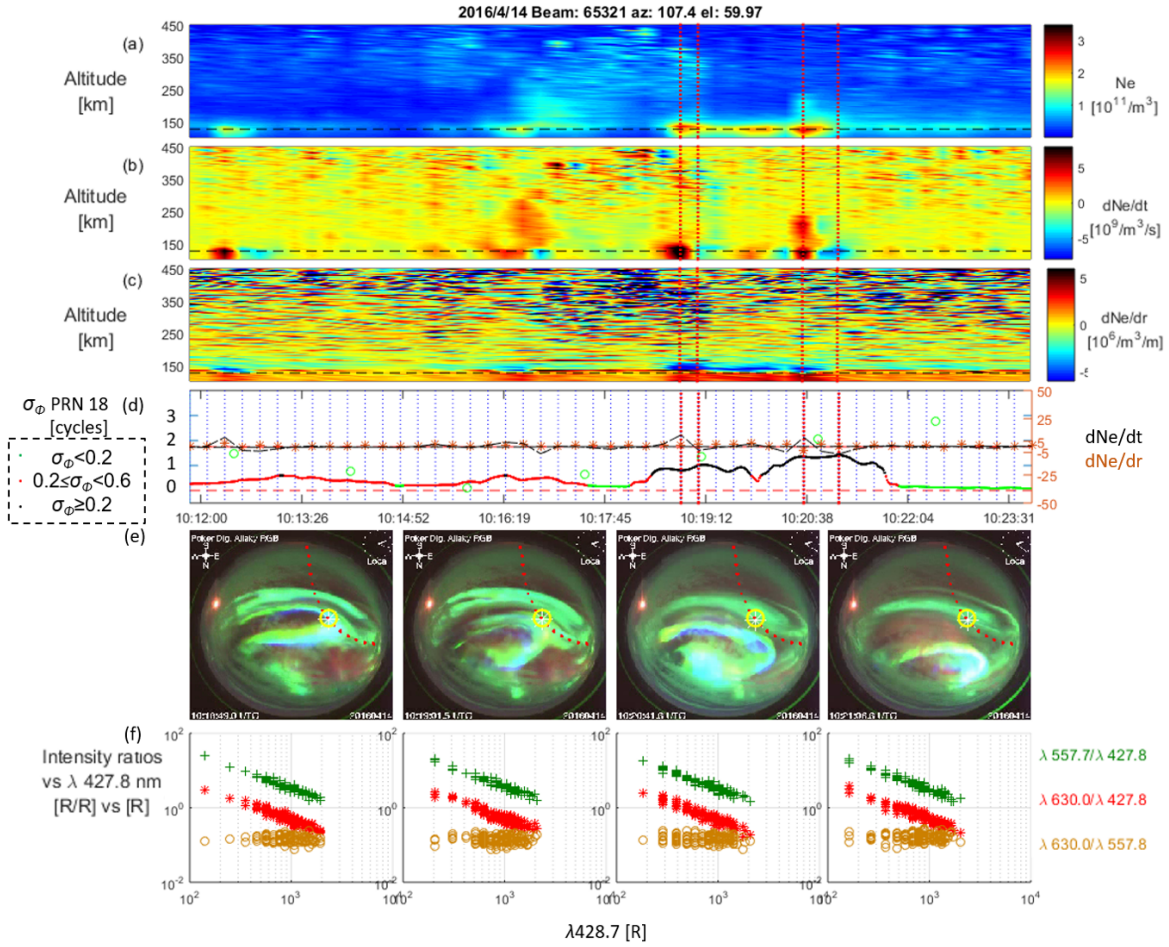

Figure 7.13: Results for 14 April 2016, PFISR Beam #65321. All rows correspond to those shown in Figures 6.6 through 6.9, except that the keogram has been left off. The altitude slice shown is for 125 km.

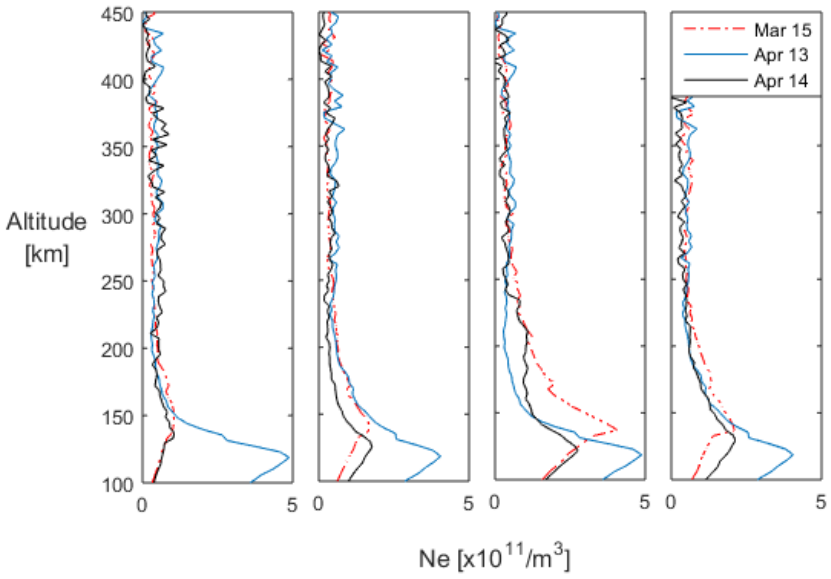

Figure 7.14: Electron Density (N_e) profiles corresponding to the vertical red lines of Figures 7.11, 7.12 and 7.13, with horizontal black dashed lines corresponding the altitude slice taken in the same figure.

7.3.2 Correlation Analysis

A correlation analysis was run across data from March and April 2016, as indicated in Table 7.5. All experimental data were averaged into ten km altitude bins to ensure an appropriate comparison of data sets. Correlation coefficients between σ_ϕ and each of N_e, $|\mathrm{d}N_e/\mathrm{d}t|$, $|\mathrm{d}N_e/\mathrm{d}r|$ and $|\mathrm{d}^2N_e/\mathrm{d}t^2|$ were calculated. Shown in Figure 7.15 are the correlation coefficients for each variable plotted versus altitude. Notice that the peak in correlation coefficients in the E region for

Table 7.4: Electron density profiles corresponding to the times indicated with vertical red dashed lines in Figures 7.11 and 7.12.

	Subfigure			
Day	1	2	3	4
15-Mar	7:48:04	7:49:49	7:52:19	7:52:49
13-Apr	9:00:09	9:00:54	9:01:24	9:02:09
14-Apr	10:18:50	10:19:43	10:20:35	10:21:05

$|dN_e/dt|$ and $|d^2N_e/dt^2|$ are much more prevalent, and that the peak for $|dN_e/dr|$ has diminished compared to those shown in Figure 6.11. Corresponding scatter plots for the same E Region altitudes as shown in Figure 6.12 are plotted in Figure 7.16. Note that the correlation is strongest between σ_ϕ and $|d^2N_e/dt^2|$ at 0.553 (altitude of 125 km), with $|dN_e/dt|$ not far behind at 0.545 (altitude of 130 km). Also note that the overwhelming majority of data points shown in Figure 7.16 with $\sigma_\phi \geq 0.6$ cycles are derived from the event on 14 April (Figure 7.13).

The next logical step in the analysis was to combine the December 2015 data with the March and April 2016 data to conduct the correlation analysis. Data were combined in the same manner as was previously discussed, and the correlation coefficients for each variable with σ_ϕ at each altitude, as well as corresponding E region scatter plots are shown in Figures 7.17 and 7.18 respectively. Here the correlation coefficient between σ_ϕ and $|d^2N_e/dt^2|$ peaked at 0.553 at an altitude of 130 km, and with $|dN_e/dt|$ at 0.545 also at an altitude of 130 km. The correlation coefficients between σ_ϕ and $|dN_e/dr|$ do appear to increase somewhat with decreasing altitude, however they are lower, with a peak correlation coefficient of 0.3978 at an altitude of 130 km.

Table 7.5: Data used for correlation analysis for March and April 2016. Also shown are the PFISR beams, PRNs in conjunction, and start and stop times for each experiment.

Beam	Day	Start	Stop	PRN	Beam	Day	Start	Stop	PRN
March									
64157	14	7:50:00	8:00:00	29	64157	15	7:46:00	7:56:00	29
64157	16	7:42:00	7:52:00	29	64157	17	7:38:00	7:48:00	29
64157	18	7:34:00	7:44:00	29	64157	19	7:30:00	7:40:00	29
April									
63299	11	9:05:21	9:18:01	21	63299	11	11:24:21	11:36:41	10
65315	11	11:43:01	11:54:21	10	65192	11	12:00:01	12:12:21	10
63299	12	9:01:46	9:14:01	21	65321	12	10:19:45	10:32:00	18
63299	12	11:20:51	11:31:51	10	65315	12	11:39:46	11:50:01	10
65192	12	11:56:46	12:08:01	10	63299	13	8:57:47	9:10:02	21
65381	13	9:17:45	9:29:00	21	63299	13	11:16:46	11:28:01	10
65315	13	11:35:45	11:46:00	10	65192	13	11:52:43	12:03:58	10
63299	14	8:53:51	9:05:51	21	65381	14	9:13:44	9:24:59	21
65321	14	10:11:43	10:23:58	18	63299	14	11:12:47	11:24:02	10
65315	14	11:31:46	11:42:01	10					

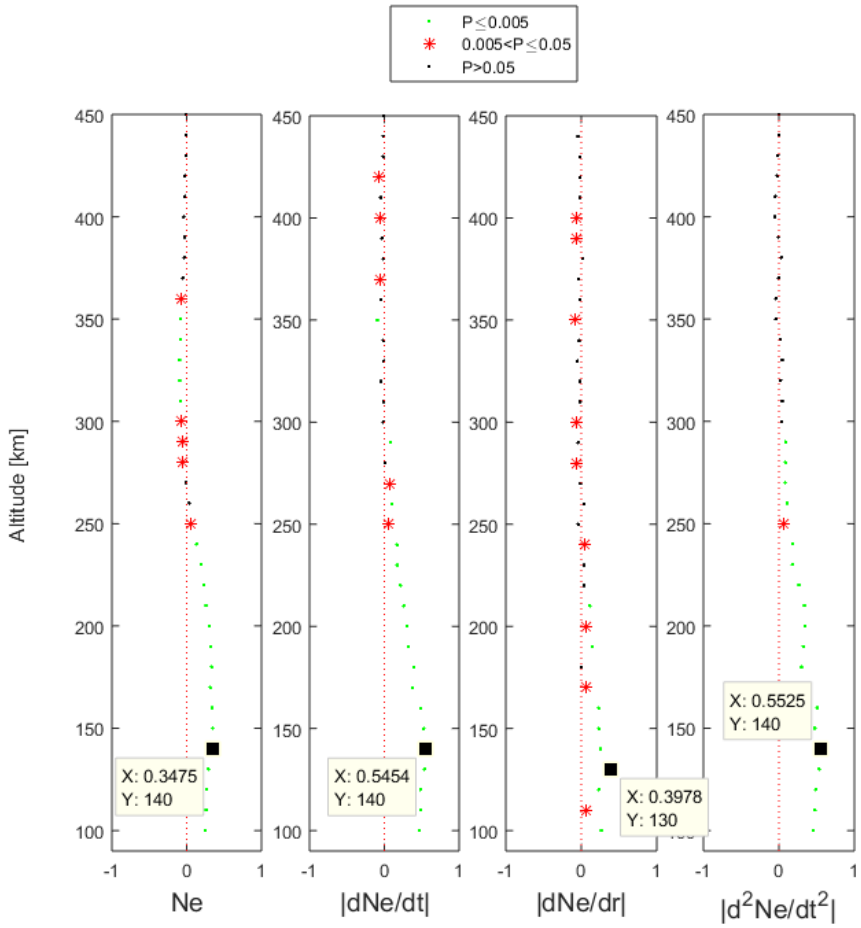

Figure 7.15: Correlation coefficients for σ_ϕ against each of N_e, $|dN_e/dt|$, $|dN_e/dr|$ and $|d^2N_e/dt^2|$. Data used are from the March-April 2016 experiment sets.

7.3.3 Discussion

In two of the six examples shown in Section 7.3, no scintillation is apparent but clearly seen is evidence of E Region enhancements, and in one case additional F Region enhancements. In one of the six examples there is moderate scintillation with a fluctuating E region enhancement due to a single auroral arc moving through the field of view. Finally, in three of the six examples scintillation at both the moderate and major levels occurs, with rapidly fluctuating E region but no F region enhancements. These are similar to the results from December 2015, where the scintillation was a direct result of the GPS signal traversing an ionosphere disturbed by discrete aurora. It is

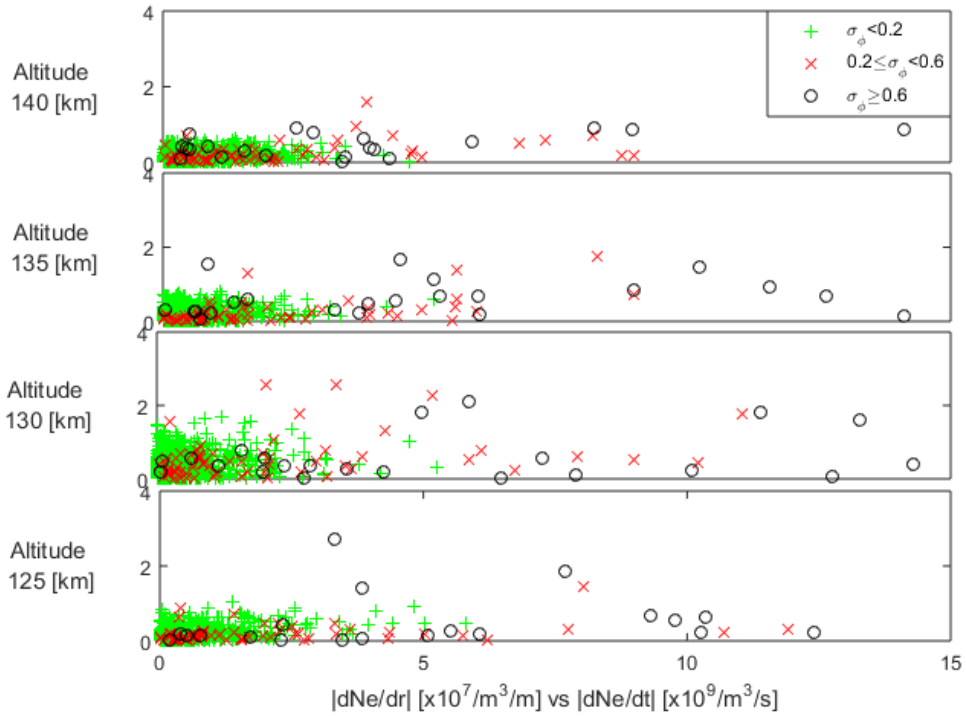

Figure 7.16: Scatter Plots of $|dN_e/dr|$ vs $|dN_e/dt|$ at five E Region altitudes (120km - 140km), March-April 2016. Symbols and colors correspond to σ_ϕ intervals shown in Figure 6.10. Data used are from the March-April 2016 experiment sets.

also interesting to note that the highest scintillation value is associated with low to moderate precipitation energies and not the highest energies. There is little in the figures to indicate why this is the case: the magnitude of the time rate of change of the temporal gradient in the former is up to 1.5 times greater than that of the latter, the altitude of greatest electron density disturbance is approximately the same, and both data sets are taken during an auroral substorm. Further analysis is required to reveal the reasons behind this phenomena.

Correlation analysis of the March and April data alone point to a conclusion that not only must a spatial gradient exist along the line of site of the GPS signal for scintillation to occur, but that it must be changing in time. This is even more evident when the data is combined with that of December 2015. It is striking to note that correlations of scintillation with F region enhancements appear to be near zero, contrary to the widely held belief that gradients associated with auroral

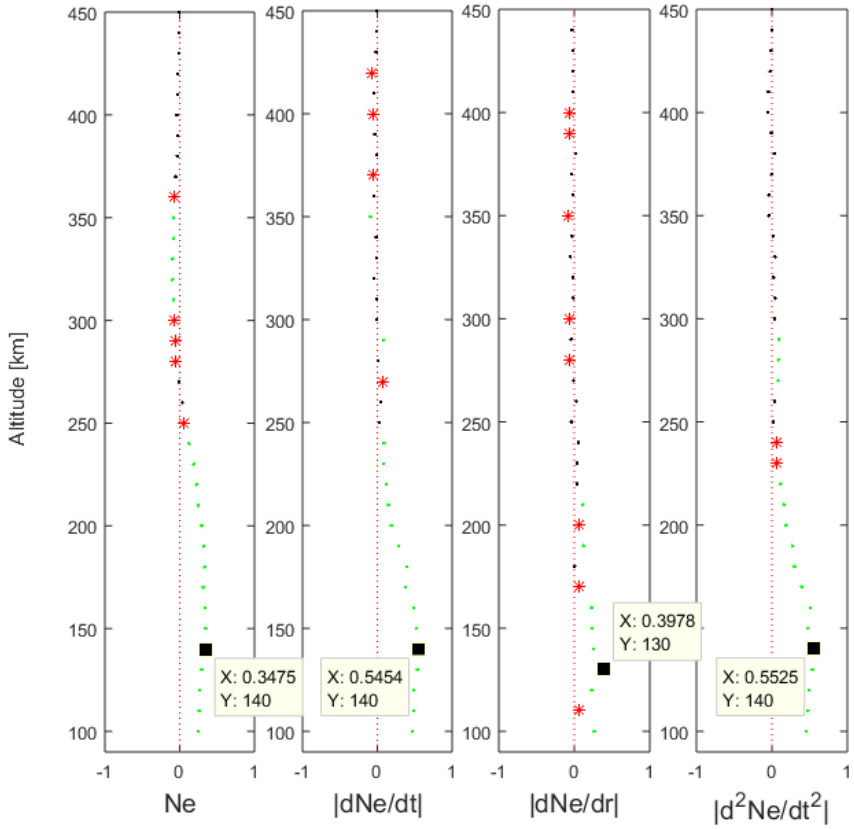

Figure 7.17: Correlation coefficients for σ_ϕ against each of N_e, $|dN_e/dt|$, $|dN_e/dr|$ and $|d^2N_e/dt^2|$. Data used are from the December 2015 and March-April 2016 experiment sets.

blobs are of greatest importance to GPS scintillation in Arctic regions. Also of interest is that the correlations between the second derivative of the temporal gradient had the greatest overall correlation with GPS scintillation than any other variable. This means that how fast the gradient is changing in time is critical to sudden deviations in phase measurements of the GPS signal at the receiver, i.e., scintillations. The highest precipitation energies did not produce the highest scintillation (corresponding to lower altitude electron density peaks), but the more rapidly the temporal gradient was changing, the higher the scintillation.

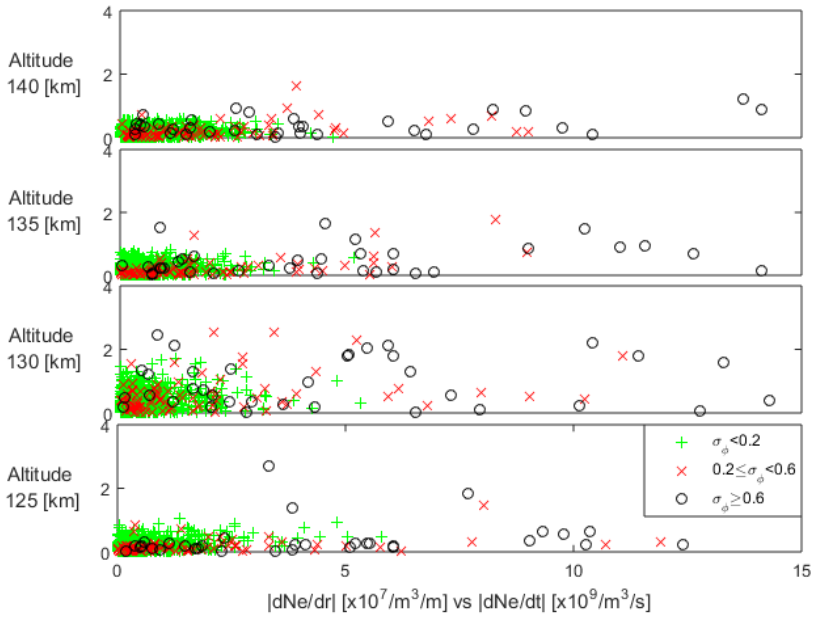

Figure 7.18: Scatter Plots of $|dN_e/dr|$ vs $|dN_e/dt|$ at five E Region altitudes (125km - 140km), December 2015 and March-April 2016. Symbols and colors correspond to σ_ϕ intervals shown in the legend (same as Figure 6.10).

7.4 Summary & Lessons Learned

A total of 52 experiments were run between March and April of 2016. Each was run in the same configuration as the December 2015 experiment from the previous chapter. Of those experiments, several examples were presented of both scintillation and non-scintillation causing ionospheric enhancements. The common feature during scintillation enhancements was a temporal and spatial gradient in electron density along the GPS line of sight, the source of which was a single or a series of discrete auroral arcs that moved across the path of the GPS signal. The presence of density gradients produced both moderate (Figure 7.9) and major scintillation (Figures 7.11, 7.12 and 7.13). Even though a spatial electron density gradient was present in the non-scintillating case, the second temporal derivative was near zero (Figure 7.4). When F region spatial gradients were detected, σ_ϕ was predominately below 0.2 cycles (Figure 7.6). Two-thirds of the detected F region enhancements occurred at times that were consistent with the transition of polar cap patches into the auroral oval (*Jin et al.*, 2016, 2014; *Moen et al.*, 2015; *Crowley et al.*, 2000). Results reported

here at first glance might seem contradictory to others from within the community, however it is likely that geographic location in the polar region plays an important factor in drivers for radio wave scintillation. Two questions follow:

(1) If E region density gradients due to dynamic energetic particle precipitation are the cause of GPS scintillation, then why are some events more severe than others?

(2) If F region density gradients consistent with the timing of convection phenomena do not produce scintillations, then are they a space weather threat?

The answer to the first question is that the time rate of change of the temporal gradient appears to control the severity of the scintillation. The key to understanding this lies in two factors: the definition of scintillation and the correlation analysis run. Scintillations by definition are produced when abrupt change(s) of the amplitude or phase of a signal occur at the receiver (*Kintner et al.*, 2007). In this case, the faster the rate of change of the electron density, the more the abrupt change in the phase of the signal at the receiver. In the moderate scintillation examples presented, a sudden change in the electron density is followed by a steady decline. In all of the major scintillation cases presented, a series of sudden increases followed by sudden decreases in electron density are seen. It is interesting to note that the greatest scintillation was seen when this sequence was most rapid (Figure 7.13), and not when the particle energies were at their highest (Figure 7.12). This explains why the highest correlations were seen between σ_ϕ and the second derivative of the temporal gradient (R =0.563, P ~0), followed by slightly lower correlations with the temporal gradient (R =0.545, P <0.005).

To address the second question a more in depth evaluation is required. The correlation analysis run in this study reveals R values tend towards zero with increasing altitude. Most of these correlations are accompanied by P values that are either statistically significant (P <0.05) or highly statistically significant (P <0.005). This implies that F region gradients and their time rate of change have little to do with GPS scintillation during these experiments. Numerous studies exist containing evidence of the linkage between the electron density gradients on the edges of high-

latitude convection phenomena and GPS scintillation. So why are the results presented in those studies so different from this one? What is it about the observation locations for those studies that would make them more vulnerable to F region enhancements? More recent studies have begun to address this at the poleward auroral boundary. *Jin et al.* (2016) placed the F region enhancements inside of the auroral oval (auroral blobs) into two categories: those that were formerly patches (i.e., convection phenomena), and those that were formed by particle precipitation. The latter of the two were from particles that did not have enough energy to penetrate into the E region (<1 keV (*Schunk and Nagy*, 2009)). The former are convection phenomena that elongate across magnetic field lines in the auroral oval, creating a tube of enhanced electron density in the F region. *Jin et al.* (2016) concluded that auroral blobs that began as polar cap patches, but that were structured by energetic particle precipitation resulted in the greatest scintillation, and that 'auroral dynamics play an important role in [their] structuring...'

Clausen et al. (2016) used satellite data to define the auroral oval, and a correlation analysis was performed between the occurrence of increased TEC and σ_ϕ, and the size and location of the polar cap. *Clausen et al.* (2016) found that polar cap patches combined with energetic particle precipitation after they had convected through the poleward auroral boundary produced the highest scintillation, in effect confirming the results of *Jin et al.* (2016). The difference between these two studies and the one presented here is the location of the instruments used. GPS data for *Jin et al.* (2016) were derived from receivers at Ny-Ålesund, Svalbard, which sits inside the nightside poleward auroral boundary. *Clausen et al.* (2016) used open source global TEC maps and scintillation data derived from a variety of sites in the Canadian High Arctic Ionospheric Network (CHAIN) that spanned 60°-90° in magnetic latitude. The bulk of the data analyzed by *Clausen et al.* (2016) were at or above 75° magnetic latitude, making the results skewed to sites in vicinity of the poleward auroral boundary. Only one conclusion is logically possible when comparing these studies with those of this analysis: that the greatest scintillation causing threat to an Arctic high-latitude site is dependent on where one is located relative to the auroral oval. If a site is inside the polar cap, then convection phenomena will dominate the scintillation-causing structures. If a site is

at or inside the poleward auroral boundary, then convection phenomena structured by particle precipitation will dominate. And if a site is at or inside the equatorward auroral boundary, then particle precipitation will dominate. This is not to say that gradients associated with any one of these, or with any combination of these will not cause scintillation, just that one or a combination of structures will dominate depending on a site's proximity to the auroral oval and its boundaries.

Chapter 8

October-November 2016: Climatology Campaign II

There are two primary lessons learned from Climatology Campaign I. First, scintillation was causally linked to E region electron density gradients that resulted from impact ionization due to energetic particle precipitation. However the severity of the scintillation experienced was linked more to the dynamic nature of the auroral activity than to the presence of the aurora itself. Greater penetration depth by precipitating particles of higher energies produced only moderate scintillation, while major scintillation resulted when streams of precipitating particles of lower energies fluctuated rapidly through the GPS signal path. Second, in the vicinity of PFRR, F region enhancements were not causally linked to scintillation. Presented in this chapter are results from a second experiment campaign designed to primarily target the E region ionosphere along the GPS line of site, while still allowing for sensing of the F region ionosphere along the same line of site. The experiments targeted months that were in the late Equinoctial season (October) and the start of winter season

Table 8.1: Summary of indices for geomagnetic storms that occurred during the Fall Equinoctial season of 2016.

Date	DST [nT]	Kp
	October 2016	
13-14	-104	6.3
16-17	-20	5
24-31	max: -15, min: -64	min: 0.7, max: 6.3]
	November 2016	
2-4	min: -50, max: -9	min: 1, max: 4.3
10	-59	4.7
22-26	-46	5.3

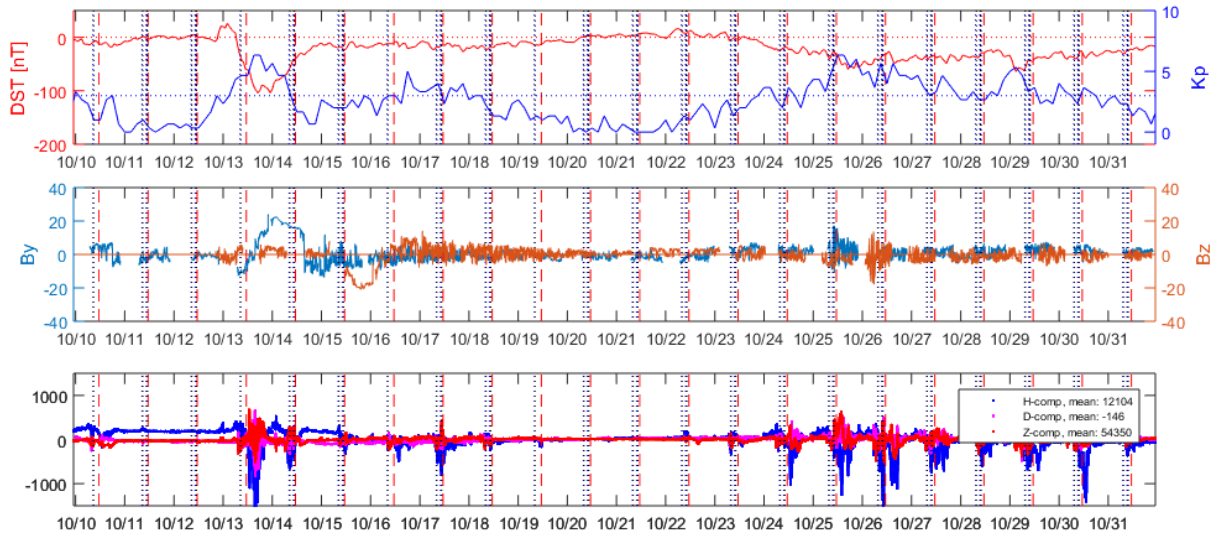

Figure 8.1: Indices for October 2016. Top row are DST (red) and Kp (blue); middle row are the IMF B_y (blue, left) and B_z (brown, right) components, and the bottom row is local magnetometer data for PFRR plotted as the deviation from the mean (indicated in the legend). Experiment times are indicated with vertical dotted lines, magnetic midnight with vertical dashed red lines.

(November), and a total of 97 experiments resulting in 36 hours of data were recorded.

8.1 Storm Summary

Shown in Figures 8.1 and 8.2 are indices for select dates from the months of October and November 2016. October was a geomagnetically active month, consistent with the equinoctial season. Of note is the geomagnetic storm on 13-14 October, as well as the geomagnetically active time starting on the 24th of October and extending through the end of the month. Key DST and Kp values for these days are listed in Table 8.1. November was geomagnetically less active, with some activity at the start of the month, a mild geomagnetic storm on 10 November. Key DST and Kp values for these days are also listed in Table 8.1. Scintillation events were recording during both months, and select data from those corresponding experiments listed in Table 8.2 are presented in figures as indicated in the last column of the table.

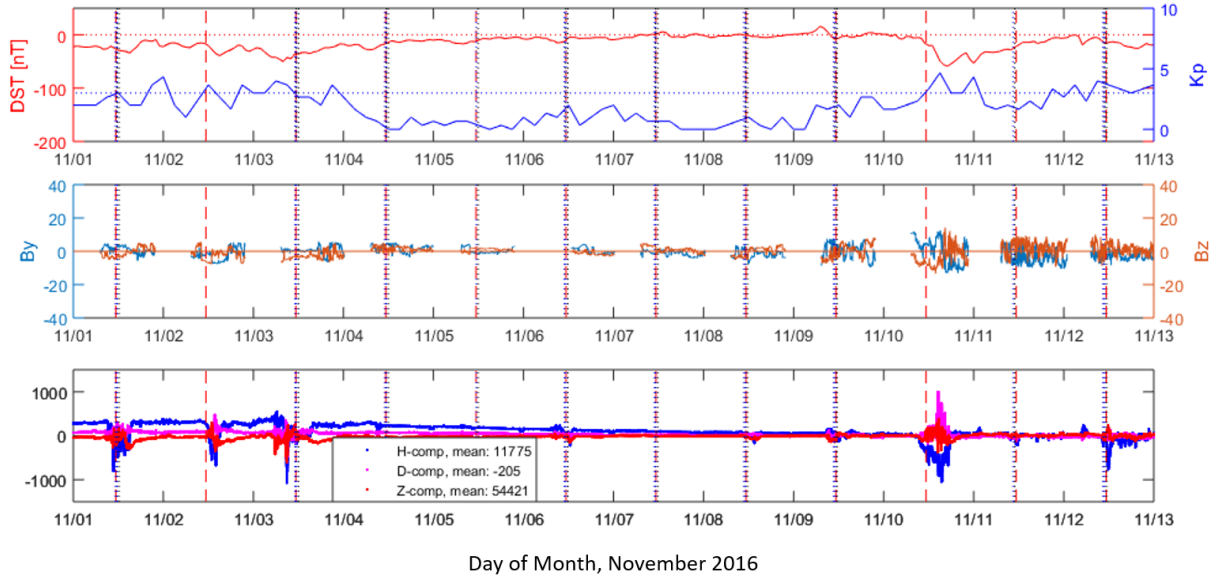

Figure 8.2: Indices for November 2016. Top row are DST (red) and Kp (blue); middle row are the IMF B_y and B_z components, and the bottom row is local magnetometer data for PFRR. Experiment times are indicated with vertical dotted lines.

8.2 Experimental Setup

The PFISR mode for this set of experiments was adjusted to further target the E region ionosphere along the GPS line of site by interleaving coded and long pulses along a single beam. As will be seen in the results, the coded pulse allowed for finer spatial resolution in the E region, while the long pulse still gave the ability to sense F region altitudes. The balance between the two was achieved through the inter-pulse period (IPP) sequence depicted pictorially in Figure 8.3. The sequence begins with a 5 ms long IPP0, consisting of a 480 μs alternating code (AC) pulse, followed by a period of listening during which the data taking computer number 0 (dtc0) samples the AC pulse at 10 μs per sample, dtc3 takes noise and calibration samples, and dtc's 1 and 2 do nothing. Next in the sequence is a 4.9 ms long IPP1 consisting of a 330 μs long pulse (LP) followed by a 30 μs short pulse (SP) on a slightly different frequency. During the listening period, dtc0 samples the SP at 10 μs for noise and calibration data, while dtc's 1 and 2 sample down and up

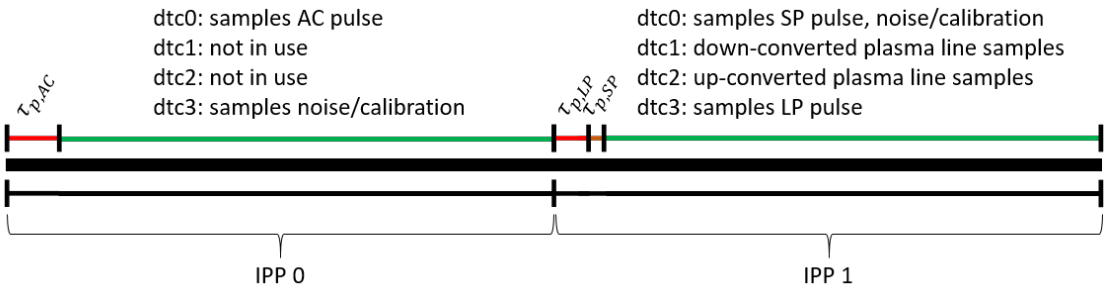

Figure 8.3: Configuration for the Experimental Campaign II (GPS35) mode IPP configuration. Further detail on parameter values are provided in Section 8.2.

converted plasma line samples respectively, and dtc3 samples the LP at 20 μs. The net IPP is then 9.9 ms long, and yields a net duty cycle of 8.48% [*personal communications with Roger Varney, 30 January 2017*].

For the purposes of the analysis presented in this chapter, only electron density data that was post-processed by SRI are presented and used. The range resolution was established by the pulse width of IPP1, with range bins of 49.5 km and post processed range resolution of 24 km. For each LP experiment 128 pulses were sampled and integrated resulting in an uncertainty

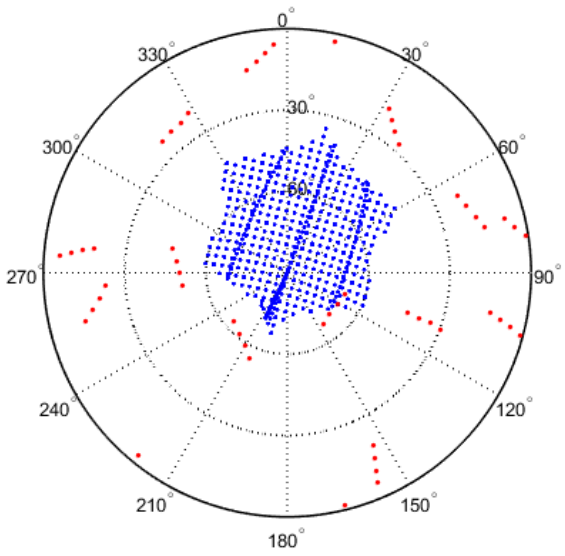

Figure 8.4: Overlay of GPS visilbity for the times of 09:15-09:45 UT, 28 October 2016 (red dots) onto the PFISR beam pattern directions (blue dots).

Table 8.2: Select Experiment Dates and Times for October and November 2016. All times are in UT. Data sets with three asterisks ('***') following the beam number were included in all correlation runs, those with '**' only in the first two, and those with '*' in only the first correlation run.

Beam	Experiment Start Day	Time [UT]	PRN	Peak σ_ϕ [cycles]	Altitude Slice [km]	Figure
			October			
65258**	13	08:18	7	0.3702		
65258***	16	08:06	7	0.9274	118	8.10
65258**	17	08:02	7	0.3726		
63299***	17	10:02	28	0.9987	112	8.8
65315**	25	09:52	28	0.5443		
65315***	26	09:48	28	0.6399		
63299*	27	09:22	28	$\leq$0.2		
65315**	27	09:44	28	0.2162		
63299***	28	09:18	28	0.6152	112	8.9
65258**	29	07:14	7	0.3539	110	8.6
63299*	29	09:14	28	$\leq$0.2		
65315*	29	09:36	28	$\leq$0.2		
65258***	30	07:10	7	0.7057		
			November			
65258*	1	11:12	17	$\leq$0.2	102	8.11
65258**	3	11:04	17	0.3147		
65258**	9	10:40	17	0.2996		

of $1/sqrt(N) = 1/\sqrt{(}128)$ or roughly 8.8%. Because SRI provided fits for both the long and coded pulse data, they were also able to propagate the uncertainties associated with each specific measurement to the final N_e calculation, and those are represented by error bars on any of the individual electron density profiles displayed (*Farley*, 1969).

The PFRR CASES receiver operated as has been previously discussed, and 100Hz data was post-processed for 1s resolution σ_ϕ. To minimize bandwidth demands, CASES data were initially screened at 100s cadence, and then only 100Hz data corresponding to times of scintillation were analyzed.[1] The PFRR digital all-sky camera (DASC) was employed as was discussed in Sections 4.3 and 5.2, except precipitating particle energies after *Rees and Luckey* (1974) are not presented here. Experiment dates and times are summarized in Appendix C, with those analyzed here

[1] Data files for a full day of 100 s cadence data are approximately 1.5-2 MB in size. Data files for raw iq data sampled at 100 Hz are approximately 3-4 GB for a two hour window.

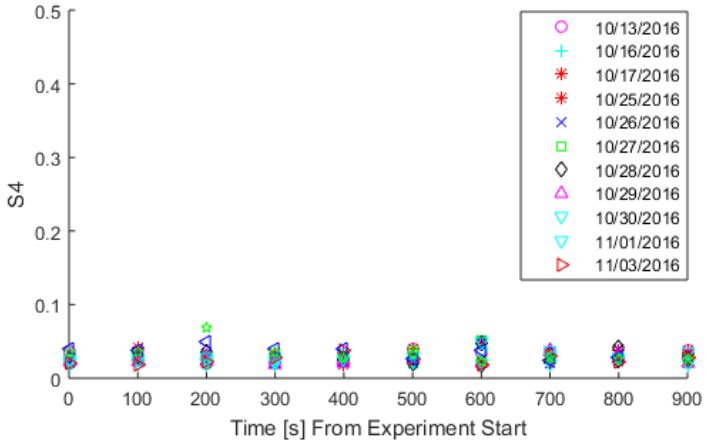

Figure 8.5: S4 presented at 100 s cadence for each of the October and November experiments listed in Table 8.2.

highlighted in Table 8.2. GPS visibility for the day of 28 October overlaid onto the PFISR beam pattern and restricted to 09:15-09:45 UT is shown in Figure 8.4 for reference.

8.3 Results

Results from these experiments are analyzed for the times indicated in Table 8.2. The experiments that have a figure number indicated in the last column of the table are discussed here. All others are available upon request. A brief note up front regarding amplitude scintillation: based on scintillation statistics and climatologies discussed in Section 3.3, it was not expected to be a factor in this study. Shown in Figure 8.5 are CASES reported S4 index at 100 s cadence during the experiment windows shown in Table 8.2. As expected, even though the signal phase is scintillating as is shown in subsequent sections, the signal amplitude remains mostly unaffected.

8.3.1 Data

In general, the data sets in this analysis are similar to those seen in the previous chapters, except there is higher fidelity E region information to evaluate. Each of Figures 8.6, 8.8, 8.9 and 8.11 show PFISR, scintillation and DASC data displayed across six rows. The first row (a) contains N_e altitude time profiles derived from long pulses, calcuated by the SRI fitting algorithm. This data

is presented at 15 s cadence and at 21 km vertical spacing, consistent with the range resolution set by the pulse length (24 km). Vertical profiles at times corresponding to each of the vertical red dashed lines are shown in Figure 8.7, with the day and time indicated at the top of each profile. The second and third rows (b and c) are the temporal and spatial gradients, respectively, presented at the same spatial and temporal resolutions as N_e. The horizontal black dashed line in the first three rows highlights the data at the altitude indication in the caption and in Table 8.2. Note that all three rows are plotted against *altitude* and not range along the beam. White rectangular shaped areas represent blocks where the SRI fitting algorithm failed to produce a value for N_e. The fourth row (d) contains σ_ϕ in cycles for the indicated PRN on the left (blue) axis, and dNe/dr (brown '*') and dNe/dt (black '$\times$') at the sliced altitude on the right axis, scaled the same as rows (b) and (c). Note that σ_ϕ values of less than 0.2 cycles are shown as green, at least 0.2 cycles but less than 0.6 cycles are shown as red if present, and at least 0.6 cycles are shown as black if present.

The fifth row (e) contains images where all three emission lines have been overlaid, with the red and blue lines enhanced for visibility. The times of the images correspond to the times of the vertical red dashed lines in the first four rows and the images are inverted (North is down). Overplotted on the images are: (1) a yellow or white circle at the center of which is the direction of the radar beam, with the circle enlarged for visibility; (2) a red dotted arc representing the trajectory of the GPS satellite throughout the day with (3) a white '*' indicating its location at the epoch represented in each image. Shown in the final row (g) are N_e altitude time profiles derived from coded pulses, calculated by the SRI fitting algorithm. This data is presented at 15 s cadence and at varied vertical spacing (ranging from 4 km to 24 km spacing, with the closest in the E region and furthest in the F region). Vertical profiles at times corresponding to each of the vertical red dashed lines are shown in Figure 8.7, with the day and time indicated at the top of each profile.

Shown in Figure 8.6 is one example of a recorded mild scintillation event with an auroral arc that appears to sit in the path of the GPS signal and the radar beam. This is followed by an arc that moves quickly through beam and the GPS line of sight creating a moderate scintillation event. Note here that there are white spaces spread throughout the pcolor plots of the long pulse

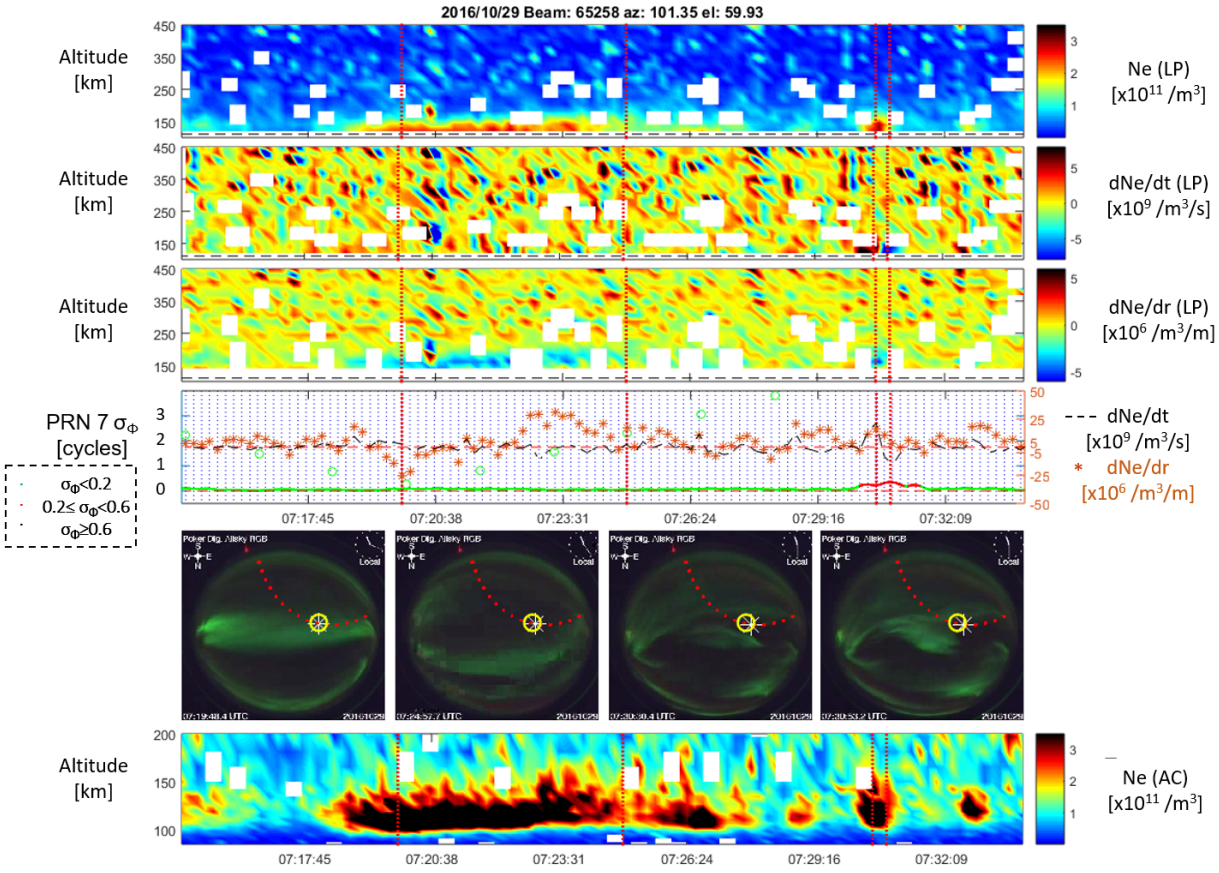

Figure 8.6: Results for 29 October 2016, PFISR Beam #65258 (azimuth: 101.35°. Data displayed in each row are a) SRI fitted long pulse (LP) electron density (N_e, $[\times 10^{11}/m^3]$); b) temporal electron density gradient from epoch to epoch (dNe/dt $[\times 10^9/m^3]$); c) spatial electron density gradient along the beam (dNe/dr $[\times 10^6/m^3]$); d) $\sigma_\phi \geq 0.2$ cycles (left axis, red dot), $\sigma_\phi < 0.2$ cycles (left axis, green dot), angle between the GPS signal ray path and the PFISR beam (left axis, green circle), temporal gradient at 110 km altitude (right axis, black + and dashed line), spatial gradient at 110 km altitude (right axis, orange '*'); e) composite display of DASC imagery data from the 557.7 nm, 428.7 nm, and 630.0 nm exposures with the 428.7 nm and 630.0 nm intensities enhanced for visibility, and each image corresponding to the time of the vertical red dashed lines in rows a through d and row g; f) SRI fitted alternating code N_e, $[\times 10^{11}/m^3]$. The altitude slice shown is for 120 km. The white blocks throughout the data are a result of the fitting process at SRI and indicated times and altitudes where the fitting algorithm failed to produce a value.

electron density. This is because the data shown here are the SRI produced fitted electron densities and not the post-process raw data returns as were shown in Chapters 5 and 7. SRI was able to fit the data at 15 s intervals, on par with the previous campaign's temporal resolution and that

Table 8.3: Summary of electron density (N_e) and associated gradients (dN_e/dr,dN_e/dt) for displayed figures. Altitudes at which the N_e values were taken correspond to those indicated on the profiles in Figure 8.7. Values for the gradients were taken at the altitude slice indicated for each experiment in Table 8.2.

Experiment			Epoch			
Day	Figure	Quantity	1	2	3	4
16 October	8.10	N_e	2.603	2.329	11.21	5.565
		dN_e/dt	-1.332	-16.22	-28.3	-8.907
		dN_e/dr	-1.298	-13.93	17.53	0.4372
17 October	8.8	N_e	38.47	8.016	6.947	5.675
		dN_e/dt	33.38	-36.23	18.28	-15.31
		dN_e/dr	-94.18	8.821	19.81	5.156
28 October	8.9	N_e	7.507	5.046	12.98	6.682
		dN_e/dt	-3.287	-1.131	31.61	-3.364
		dN_e/dr	-19.86	31.38	6.91	7.188
29 October	8.6	N_e	7.501	2.577	5.884	4.691
		dN_e/dt	2.756	2.612	21.39	-7.957
		dN_e/dr	-25.89	17.58	16.41	10.73
01 November	8.11	N_e	5.454	5.685	5.672	4.095
		dN_e/dt	10.34	-2.823	-0.4611	1.861
		dN_e/dr	-12.38	-35.57	-29.34	-15.97

of the DASC, as well as to provide measurement uncertainties, however fitting to such a short interval causes the fitting algorithm to fail more often as evidenced by the white squares that appear throughout the plots. Electron density profiles corresponding to the vertical red dashed lines and the all-sky images are shown in Figure 8.7. Peak electron densities recorded are in the lower E region: 7.501×10^{11} per m^3 at 106.7 km altitude in the first frame, and at 110.6 km altitude in the remaining frames with values of 2.577×10^{11} per m^3, 5.884×10^{11} per m^3 and 4.691×10^{6} per m^3. Corresponding spatial gradients at each epoch are: -25.89 $\times10^6$ per m^3/m, 17.58 $\times10^6$ per m^3/m, 16.41 $\times10^6$ per m^3/m, and 10.73 $\times10^6$ per m^3/m. Corresponding temporal gradients at each epoch are: 2.756 $\times10^9$ per m^3/s, 2.612 $\times10^9$ per m^3/s, 21.39 $\times10^9$ per m^3/s and -7.957 $\times10^9$ per m^3/s. All values are summarized in Table 8.3. In this case, scintillation increases only when a spatial gradient is coupled with a strong temporal gradient, as in the last two epochs where scintillation rises to moderate levels at a peak of 0.3539 cycles.

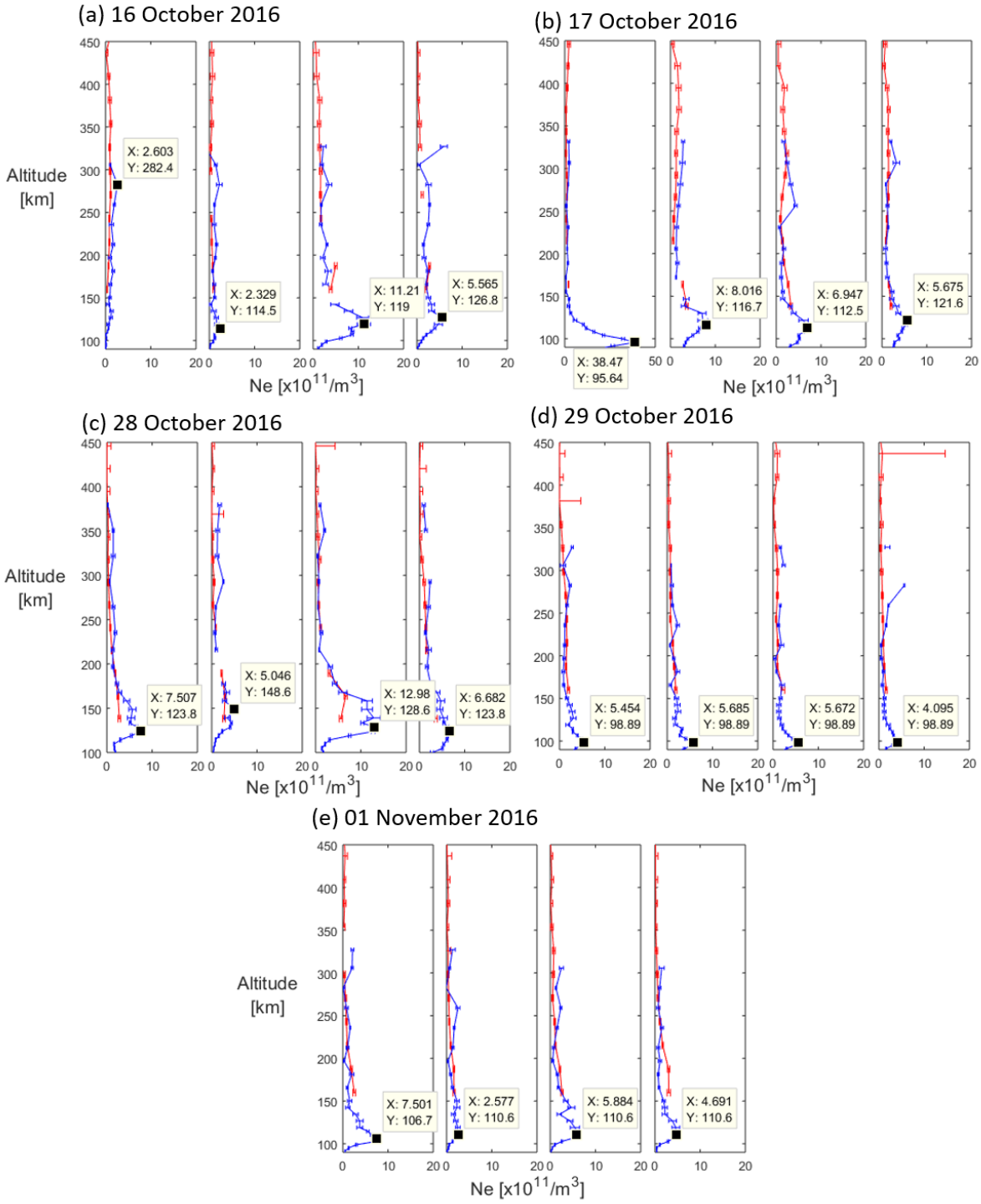

Figure 8.7: Electron Density (N_e) profiles corresponding to the vertical red lines of Figures 8.6, 8.8, 8.9, 8.10 and 8.11. Peak electron densities are highlighted in each profile and summarized in Table 8.3. Horizontal bars at each data point indicate the error in each measurement provided by SRI data fits of PFISR sensed data.

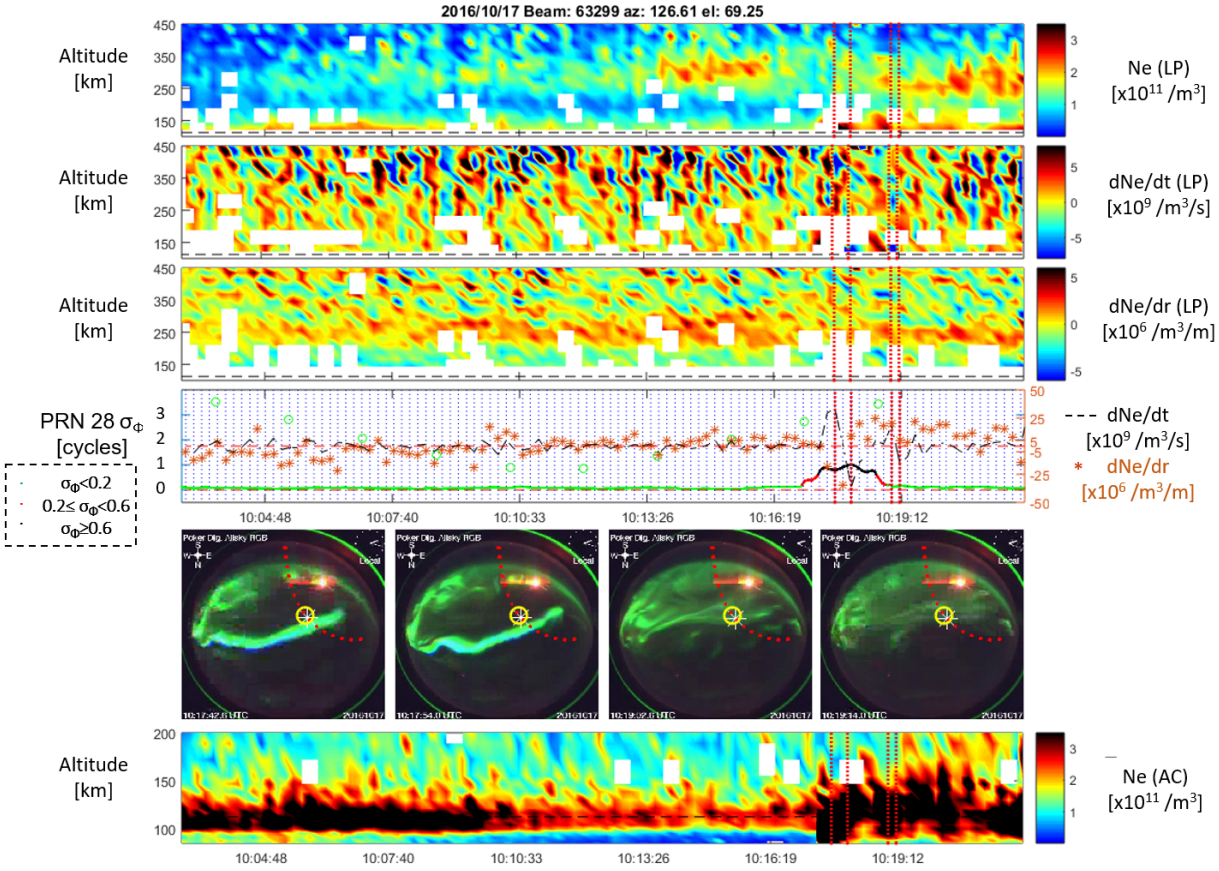

Figure 8.8: Results for 17 October 2016, PFISR Beam #63299. All rows correspond to those shown in Figure 8.6. The altitude slice shown is for 112 km.

Results indicating the source of major scintillation events are shown in Figures 8.8, 8.9 and 8.10. In the first a single auroral arc moves through the signal line of sight, while in the latter two a series of arcs move in and out of the field of view. Electron density profiles corresponding to the vertical red dashed lines of each of these figures are shown in Figure 8.7. For 17 October peaks vary across altitudes as low as 95 km and as high as 122 km, with little to no activity in the F region. Electron density peaks on 28 October vary across E region altitudes but not as widely (108 km to 130 km), but also show few if any enhancements in the F region. Electron density peaks on 16 October indicate activity primarily in the E region (115 km to 127 km) with some evidence of

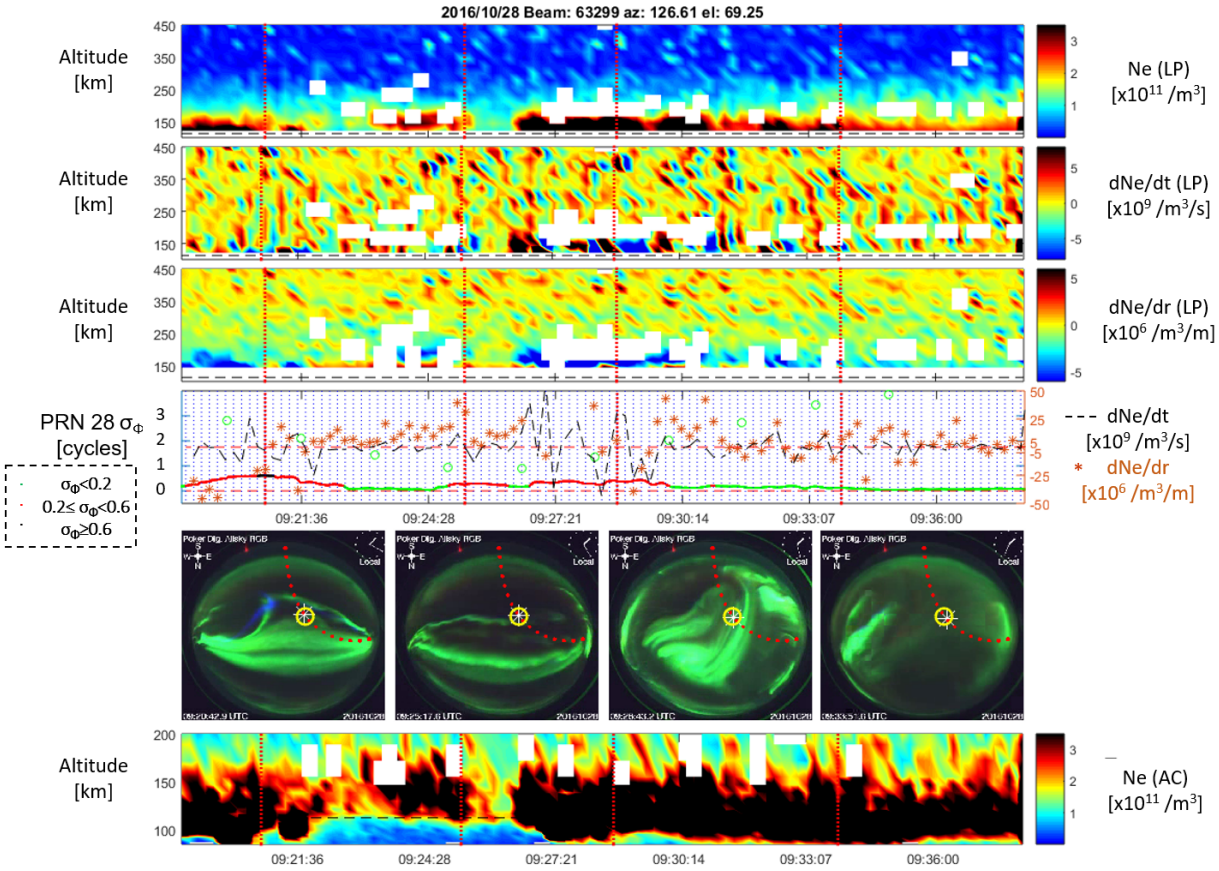

Figure 8.9: Results for 28 October 2016, PFISR Beam #63299. All rows correspond to those shown in Figure 8.6. The altitude slice shown is for 112 km.

F region enhancements. Values for N_e, dN_e/dr and dN_e/dt are summarized in Table 8.3.

In contrast to the previous examples where varying E region densities exists, the data shown in Figure 8.11, taken on 01 November, show clearly visible electron density gradients in the lower F region. This data is taken around magnetic midnight, so it is possible that the F region enhancement is a plasma blob moving through the area. While red line emissions are not evident in the imagery overlays, they are visible in the third row of the keogram shown in Figure 8.12. Electron density profiles corresponding to the red vertical dashed lines on Figure 8.11 are shown in the bottom row of Figure 8.7. E region enhancements are seen, and the F region enhancements, while small, are

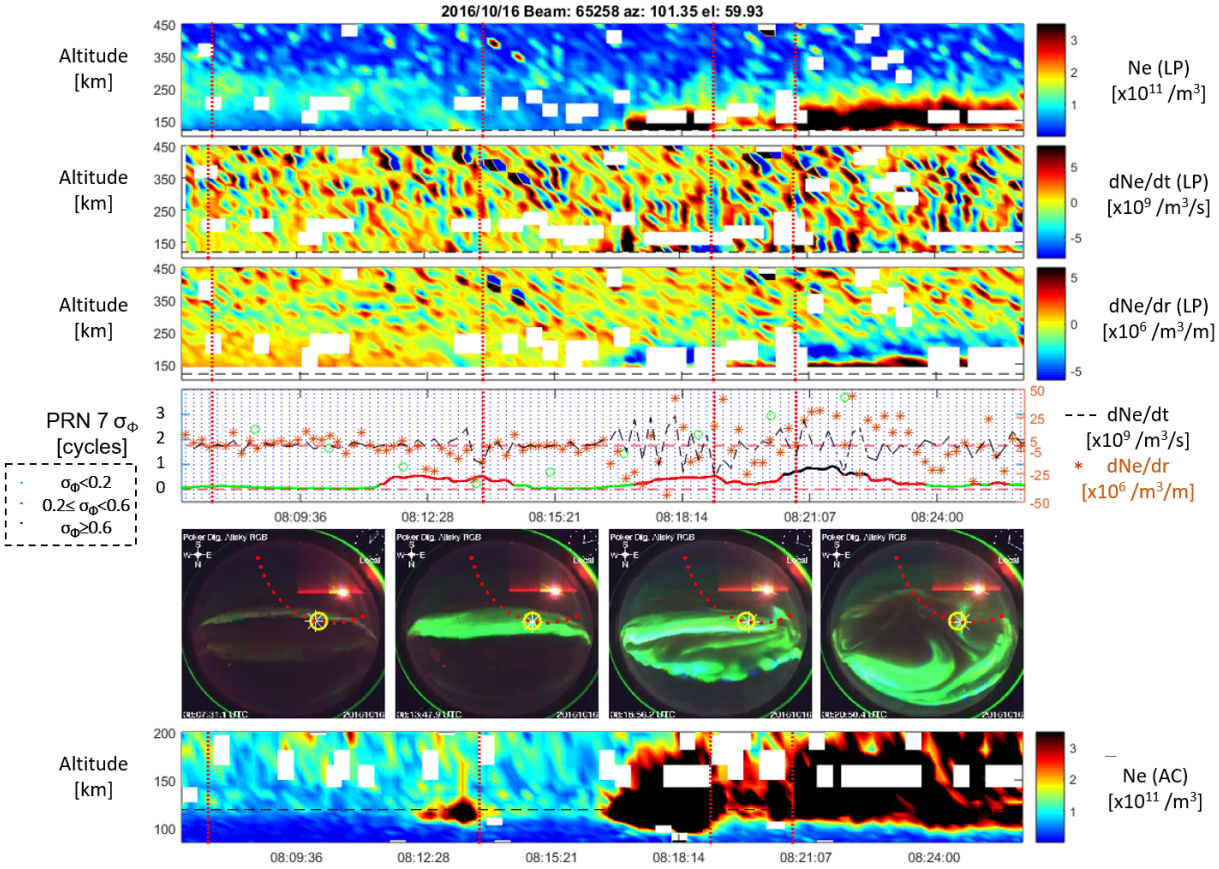

Figure 8.10: Results for 16 October 2016, PFISR Beam #65258. All rows correspond to those shown in Figure 8.6. The altitude slice shown is for 118 km.

still visible.

8.3.2 Correlation Analysis

A correlation analysis was conducted between σ_ϕ and each of N_e, $|dN_e/dt|$, $|dN_e/dr|$ and $|d_e^N/dt^2|$ for the data in this experiment campaign. Long pulse (LP) data were separated into 20 km altitude bins, and where two or more data points existed from a single experiment in a single bin the maximum value was taken. Note that the magnitude of the gradients was used rather than the actual value. Coded pulse (AC) data were binned in the same manner as LP data except

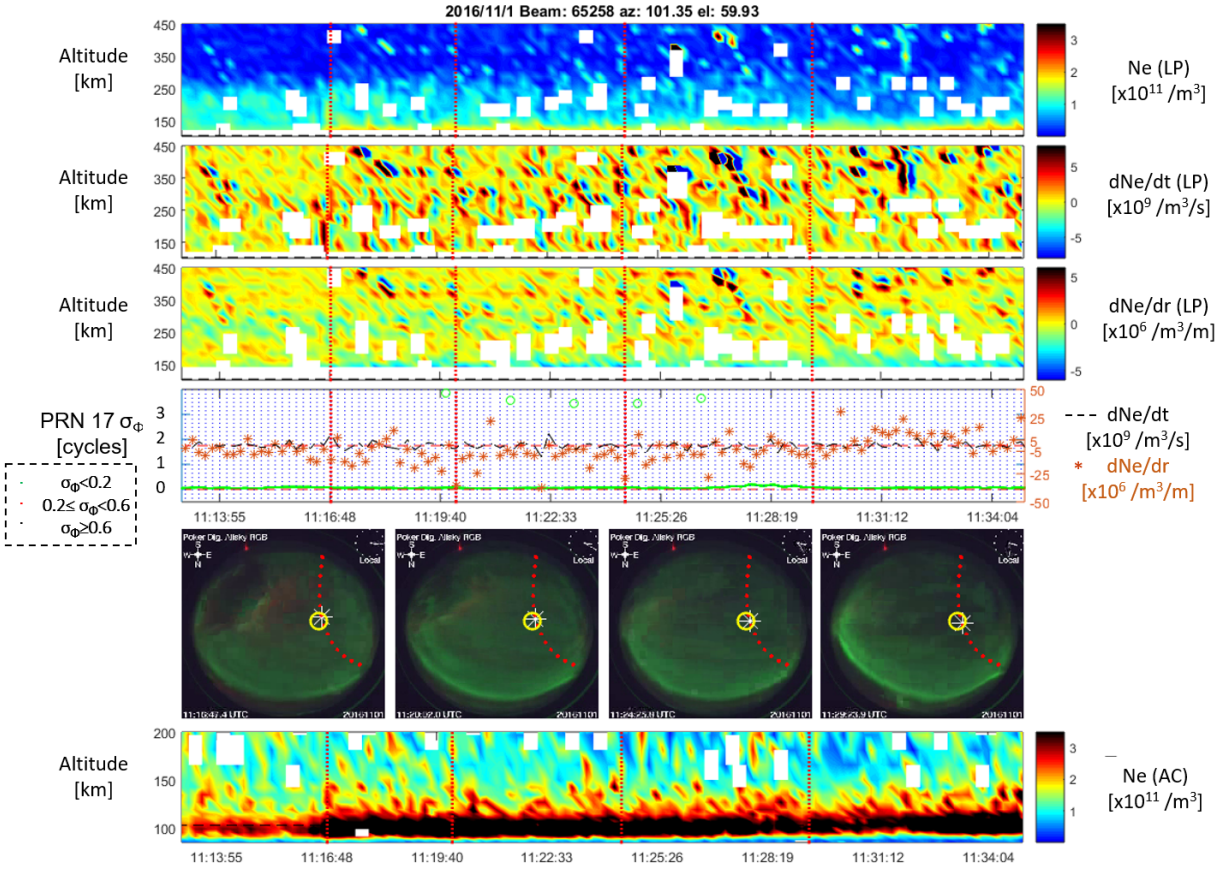

Figure 8.11: Results for 01 November 2016, PFISR Beam #65258. All rows correspond to those shown in Figure 8.6. The altitude slice shown is for 102 km.

that they were spread across altitude bins of 4 km, 8 km, 16 km and 24 km consistent with the distribution of the data's altitude bins so as not to lose any information when taking the maximum of multiple data points. Shown in Table 8.4 are the results of three iterations of this analysis. In the first iteration, all data from Table 8.2 was included in the analysis (indicated with at least one '*' by the beam number in Table 8.2). In the second iteration, only those data sets with at least a moderate scintillation event (0.2 cycles $\leq \sigma_\phi <$ 0.6 cycles) in them were included (at least two '*' by the beam number). In the last iteration, only those data sets with at least a major scintillation event ($\sigma_\phi \geq$ 0.6 cycles) in them were included (three '*' by the beam number). Mild

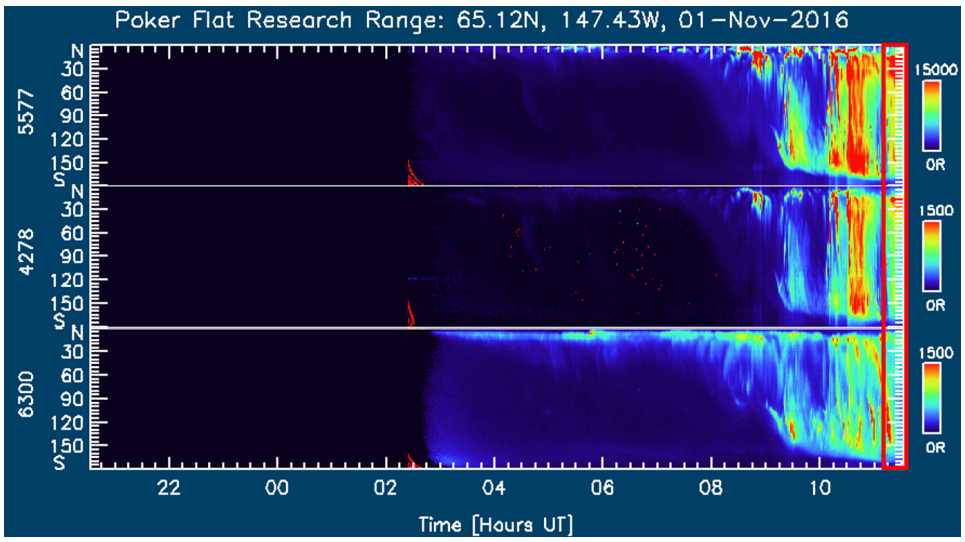

Figure 8.12: Keogram for 01 November 2016. The rows from top to bottom are green, blue, red emission lines. Each line has a different colorbar that is indicated on the right, measured in Rayleigh [R]. The red outlined box corresponds to the experiment window shown in Figure 8.11.

scintillation as shown in the table is for data where $\sigma_\phi < 0.2$ cycles. Figure 8.13 shows the results of the final iteration (3), for both LP data ('+') and AC data ('o'). Note that the symbols are color coded according to their statistical significance: highly statistically significant ($P \leq 0.005$) are shown in green, statistically significant ($0.005 < P \leq .05$) are shown in red, and shown in black are not statistically significant ($P > 0.05$). Both correlation coefficient plots appear to have the

Table 8.4: Correlation analysis results by iteration, October - November 2016. Data categories are: 'mild': $\sigma_\phi < 0.2$ cycles, 'moderate (mod)': 0.2 cycles $\leq \sigma_\phi < 0.6$ cycles, and 'major': $\sigma_\phi \geq 0.6$ cycles. The number of data points in each category are indicated for each run (1, 2 or 3), and for each pulse type (long (LP) or coded (AC) pulse).

Run	Pulse	Msmts by Category			R Value (Altitude [km])$^\alpha$			
		Mild	Mod	Major	N_e	dN_e/dr	dN_e/dt	d^2N_e/dt^2
1	LP	1520	200	23	0.4439 (160)	0.3909 (120)	0.4217 (140)	0.3255 (140)
	AC	1525	194	24	0.4111 (127)	0.3795 (103)	0.3799 (103)	0.3296 (107)
2	LP	1080	200	23	0.4889 (160)	0.4516 (120)	0.4357 (140)	0.3567 (140)
	AC	1085	194	24	0.4894 (127)	0.4088 (103)	0.4378 (107)	0.4243 (107)
3	LP	386	121	23	0.6031 (120)	0.6058 (120)	0.4547 (120)	0.3453 (120)
	AC	391	115	24	0.4587 (127)	0.4173 (103)	0.4364 (103)	0.4081 (107)

$^\alpha$ For each measurement, $P \leq 0.005$.

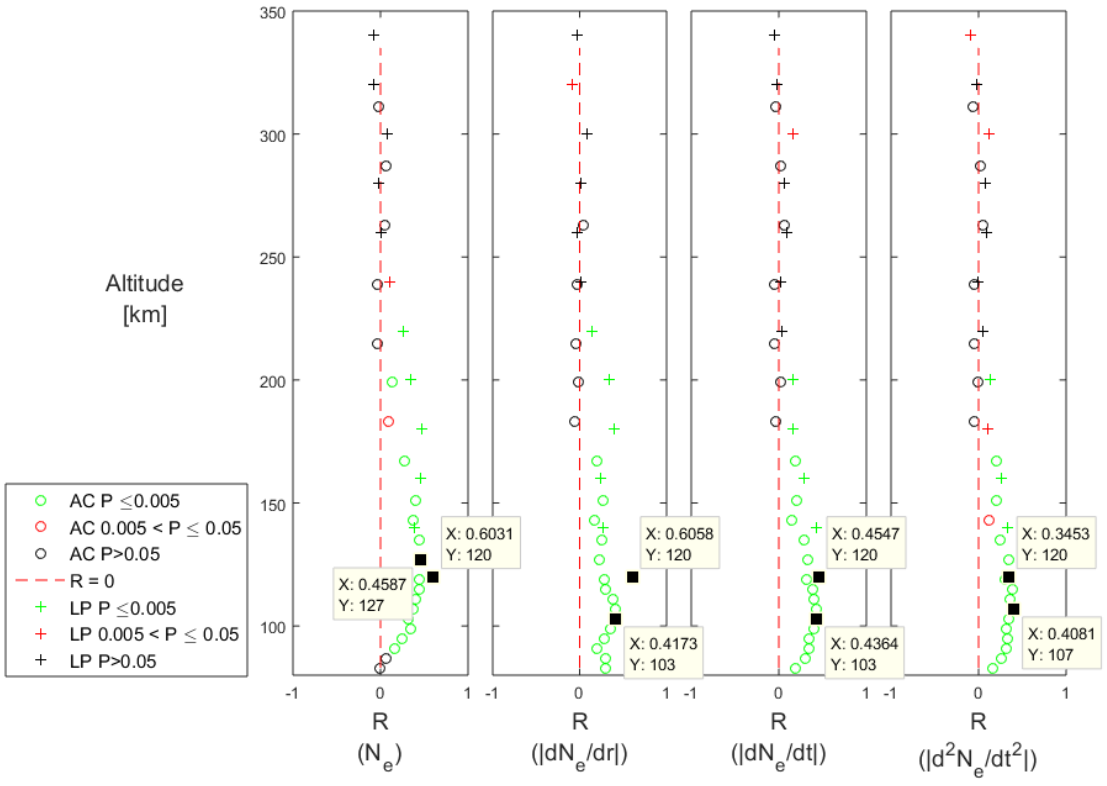

Figure 8.13: Correlation Coefficients by Altitude for long pulse (LP) data ('+') and coded pulse ('o'), October-November 2016. The color indicates the statistical significance of the data: green represents $P \leq 0.005$, red represents $0.005 < P \leq .05$, and black represents $P > 0.05$.

same general structure by altitude as those previously seen (peaked in the E region, with mostly insignificant correlations at F region altitudes). Although the peak correlations shown are less than 50%, it is encouraging that the E region correlations are highly statistically significant.

The question of why the correlation coefficients were so much less than those seen in Experiment Campaign I has several possible answers. First, the data sets being used for the correlations are heavily biased by mild scintillation. This is most evident in iteration 1 where there are over 1500 data points in the mild category, but only 223 total for moderate and major. The bias is lessened by excluding those experiments where only mild scintillation is seen (iteration 2), and even more when excluding experiments without at least major scintillation where just under 400 data points are in the mild category compared to nearly 150 across the major and moderate categories.

A second possibility are the number of missing data points from the PFISR data. While our eyes naturally fill in the missing data points, the SRI fitting algorithm did not always return results at every time step, which translates to no data points in the gradients, which in turn limits the correlations. A third contributing factor is the variety of peak altitudes seen across the events. Notice that the LP correlation peaks tended towards 120 km in altitude, while the AC correlation peaks tended towards 100 km in altitude. Comparing these results to the previous experiment sets, note that in the December 2015 data the peak correlation occurred at 137 km, while those in March and April tended towards 130 km. And one final contributing factor to note are the dispersion of the directions associated with the GPS signals and the PFISR beams used to sense the ionosphere. What is important here are that the relative strengths, both in correlation value and statistical significance, of the E region altitudes compared against those in the F region. Clearly the E region is dominating the source of gradients, but other factors cannot be definitively ruled out.

8.3.3 Discussion

In one of the five examples shown in Section 7.3, no scintillation is apparent but clearly seen is evidence of E Region enhancements with only minor F region gradients. In two of the five examples, evidence of both E and F region gradients is present, however only when there is rapid change in the E region does scintillation occur. Finally, in two of the five examples scintillation is observed at both the moderate and major levels occurs, with rapidly fluctuating E region but no F region enhancements. These results are similar to those that were observed in both December 2015, and in March and April 2016, where the scintillation was a direct result of the GPS signal traversing an ionosphere disturbed by discrete aurora.

Correlation analysis of the October and November data point to an affirmation of conclusions drawn from the previous two analyses: First, the E region ionosphere disturbed by dynamic particle precipitation dominates the correlations. Consistent with previous observations in this work, correlations of scintillation with F region enhancements appear to be infrequent, contrary to the widely held belief that gradients associated with auroral blobs are of greatest significance to GPS

scintillation in Arctic regions. Second, analysis points to the need for some combination of both a spatial and temporal gradient, or a strong transient gradient to exist for scintillation to occur. Correlations are non-zero and highly statistically significant between σ_ϕ and the spatial gradient, the temporal gradient, and the second derivative of the temporal gradient. Loosely translated, not only does the aurora have a direct impact on the scintillation of GPS signals, but dynamic aurora have the greatest impact.

8.4 Summary & Lessons Learned

A total of 97 experiments were conducted between the Equinoctial month of October and the winter month of November 2016. Each experiment used interleaved long and coded pulses to provide high fidelity measurements in the E region ionosphere while maintaining an ability to sense the F region. Of those experiments, several examples were presented of both high and low scintillating E region enhancements. The common feature across the causal structures is a change in both time and space of the electron density gradients along the GPS line of sight, the source of which was a single or a series of discrete auroral arcs that moved across the path of the GPS signal. These enhancements produced both moderate (Figure 8.6) and major scintillation (Figures 8.8, 8.9, and 8.10). Even though an electron density gradient was present in the non-scintillating case, it was not evolving in time (Figure 8.11). When F region enhancements were detected, they failed to cause σ_ϕ to rise above 0.2 cycles (Figures 8.8, 8.10 and 8.11). Answers to the questions previously raised did not change with the outcome of this experiment set, however the domination of dynamic E region enhancements with respect to GPS scintillation over F region enhancement effects was affirmed.

Questions now remain regarding the correlation values and why they were so much lower than previously achieved. Perhaps more data sets containing moderate and major scintillation push the correlation values in the E region higher as is expected. Not presented in this analysis are the results of 121 experiments containing over 55 hours of data from the latter half of November 2016, all of December 2016 and January 2017. It is expected that as the number of scintillation events

detected increases, and as the correlation data sets are restricted to only those with at least a major scintillation event in the window, the correlation values by altitude will increase. In adding these experiment sets to the analysis, many of the missing data points from the PFISR data will begin to fill in adding to this effect.

Chapter 9

Other High-Latitude Sectors

9.1 The Debate

Shortly before the turn of the twenty-first century, an expansion of deployed observational sensors occurred in the Arctic high-latitudes that supported analyses conducted to investigate the high-latitude ionospheric threat(s) to transionospheric signals. Many of these studies have led the scientific community to conclude that electron density gradients associated with plasma patches are the primary 'space weather threat' [e.g., *Moen et al.* (2013); *Prikryl et al.* (2011); *Spogli et al.* (2009a); *Moen et al.* (2007); *Mitchell* (2005)]. But studies conducted over the last decade including the analyses presented in this work, and those conducted by *Clausen et al.* (2016) and *Jin et al.* (2014), have found cause to refute that claim. In the case of *Clausen et al.* (2016), satellite data was used to define the auroral oval, and a correlation analysis was run between the occurrence of increased σ_ϕ and the size and location of the polar cap. In *Jin et al.* (2014), emission data and σ_ϕ were compared. In both cases, the focus was in the polar cap and at the poleward boundary of the auroral oval; and, in both cases the primary contributor to scintillation was not the polar cap patch alone. Rather it was the polar cap patch combined with energetic particle precipitation after it had convected through the poleward auroral boundary.

The focus of the study in this work is at or inside of the equatorward boundary the auroral oval, and the results indicate that particle precipitation is the primary cause of scintillation. At first glance this seems contradictory, but in the discussion that follows it is shown that these conclusions are consistent with the different physical processes that exist at both locations. In this chapter,

Table 9.1: An abbreviated list of evaluated sites in other Arctic Sectors, including geographic and geomagnetic coordinates. Also noted are their relative positions to the auroral oval throughout the analyses discussed in this chapter.

		Geographic		Geomagnetic[a]		
Site	Country	ϕ_{gd}	λ_{gd}	ϕ_{gm}	λ_{gm}	Relative Position
1 PFISR	AK (USA)	65.13	212.53	65.37	267.72	Equatorward
2 Reykjavik	Iceland	64.10	338.00	64.14	65.13	Equatorward
3 Tromso	Norway	70.00	18.90	67.10	101.61	Equatorward
4 Kiruna	Norway	67.70	21.00	64.63	101.77	Equatorward
5 Yellowknife	Canada	62.48	245.52	68.84	304.60	Equatorward
6 Eureka	Canada	79.99	247.10	84.67	276.28	Poleward
7 Thule	Greenland	77.00	291.00	83.55	26.05	Poleward
8 Resolute Bay	Canada	74.75	265.00	82.33	327.33	Poleward
9 Ny Alesund, Svalbard	Norway	78.90	11.90	76.41	107.43	Poleward

[a] Geomagnetic coordinates are displayed in AACGM (Appendix B) at the time of the Winter Solstice Storm of 2015

the sectors being considered are defined, and climatologies and case studies conducted in each of the sectors are examined. Although many papers present results of case studies and climatologies, they normally assume one broad category: the Arctic high-latitude. This is the first attempt to categorize them into two specific sectors:

(1) at or inside the poleward boundary of the auroral oval;

(2) at or inside the equatorward boundary of the auroral oval.

Analysis points to the conclusion that the primary high-latitude space weather threat to transionospheric signals is dependent on a site's location relative to the auroral oval. That is, if one is located at the poleward boundary of the auroral oval or in the polar cap, then convection phenomena (e.g., plasma patches, an F region phenomenon) will dominate the source of GPS scintillation. But, if one is located at or inside of the equatorward boundary of the auroral oval, then particle precipitation (an E region phenomenon) will dominate.

9.2 The Sectors Defined

Broadly speaking the Arctic high-latitude ionosphere is characterized by those sites that are in the polar cap or that would normally rotate into the auroral oval, either through its poleward or equatorward boundary. These sites can be fully immersed by the auroral oval, depending on their geographic location, local time of day, and the local geomagnetic conditions. During a moderate geomagnetic storm,[1] or during times of extreme geomagnetic calm, their location relative to and hence their interaction with the auroral oval can dramatically change. For the purposes of this anlaysis, the Arctic high-latitudes can be broken down into two major sectors, based on the local geomagnetic conditions at the time of the analyses conducted:

(1) Equatorward Auroral Boundary (EAB): locations at or above 60° magnetic latitude ($\phi_{gm} \geq 60°$), but equatorward of the auroral oval at some point in a 24-hour period;

(2) Poleward Auroral Boundary (PAB): locations at or above 60° magnetic latitude ($\phi_{gm} \geq 60°$), but poleward of the auroral oval at some point in a 24-hour period.[2]

Shown in Table 9.1 is an abbreviated list of these sites along with both their geodetic coordinates and their geomagnetic coordinates as of 21 December 2015.[3] Geographically, these two categories normally include most of Alaska, the northern coastline of Asia, the island of Svalbard and the northern portion of continental Norway, Greenland, Iceland, most of Canada, as well as the entirety of the Arctic Ocean. A representation of the included regions is shown in Figure 9.1 with EAB sites noted in blue and PAB sites in red. Site numbers correspond to the those listed in Table 9.1

Each site in the high-latitudes was characterized by the local conditions at the time of the study conducted. These characteristics include the local and global geomagnetic environment, the site's location relative to the auroral oval (PAB versus EAB region), the scintillation timing (magnetically), and the scintillation source (causal links). By evaluating each of these parameters more fully, a common picture emerges that allows conclusions regarding the source of the GPS

[1] Storms such as the St Patrick's Day Storm of 2013, or the Winter Solstice Storm of 2015, were classified by NOAA as G2 storms that subsided to G1 storms. See `http:\\www.swpc.noaa.gov` for more information.

[2] For the purposes of this discussion, altitude adjustment corrected geomagnetic (AACGM) coordinates will be used. See Appendix B for more details.

[3] See Chapter 6.

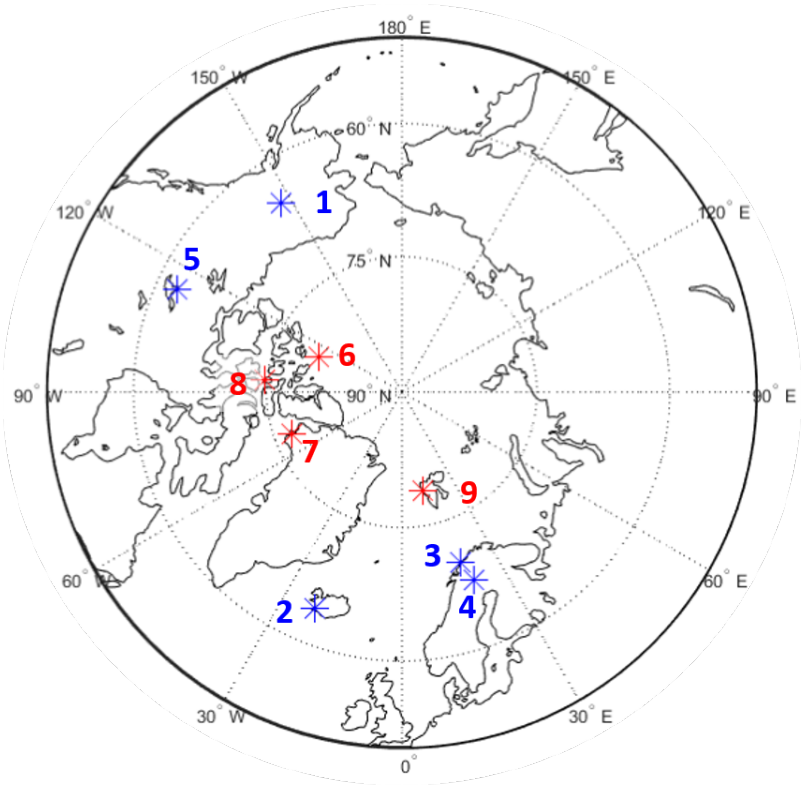

Figure 9.1: Arctic locations shown in geodetic coordinates (Appendix B); numbers correspond to the sites listed in Table 9.1.

scintillations to be drawn. It is worth noting that using the auroral oval to define the boundaries creates a situation where each case study must be considered based upon where the site was located at the time of data collection. During stronger geomagnetic storms, sites that were equatorward of the auroral oval during 'normal' conditions can find themselves at or inside the poleward boundary. Likewise, during times of low geomagnetic activity sites that were poleward of the auroral oval may find themselves at or inside the equatorward boundary.

9.3 Equatorward Auroral Boundary Sector

9.3.1 Climatologies

Many climatologies for the Arctic high-latitude GPS scintillation have been conducted since the advent of GPS and other GNSS systems; and, many of these include data from both the

equatorward and poleward boundary sectors. As a result, several climatologies will be discussed in both this section and Section 9.4. Recall that the Arctic High-Latitude Equatorward Auroral Boundary (EAB) sector is comprised of locations at or above 60° magnetic latitude ($\phi_{gm} \geq 60°$), but equatorward of the auroral oval. For the purposes of this discussion it includes PFRR, southern Canada, southern Greenland, mainland Norway, Iceland and northern Asia. Refer back to Table 9.1 for an abbreviated list.

In one of the earliest climatologies conducted, *Aarons* (1997) evaluated scintillation on GPS receivers at many high-latitude stations including Fairbanks, Alaska;[4] Yellowknife, Canada; Reykjavik, Iceland; Thule, Greenland; Ny-Ålesund, Trømso and Kiruna, Norway. Of these, Fairbanks, Yellowknife, Reykjavik, Trømso and Kiruna are considered to be in the EAB sector at the time of the study. Each of these sites is equatorward of the auroral boundary on the dayside, rotates into the auroral oval in the dusk or pre-magnetic midnight sector, then rotates out in the post-magnetic midnight sector towards dawn. The difference in the sites is the extent to which each stays within the auroral oval. Ordered in terms of the longest to shortest amount of time spent in the auroral oval, the sites are: Yellowknife, Trømso, Fairbanks, Kiruna, and lastly Reykjavik. It was noted in the study that there was a significant delay (on the order of 12-14 hours) between when Yellowknife experienced scintillations, and when Trømso and Kiruna, sites that have similar geomagnetic longitudes, experienced them. This delay corresponded to their entry into the auroral oval. *Aarons* (1997) hypothesized a link between scintillation and signals that travel through the auroral oval; but, his climatology was limited in its ability to discern E versus F region enhancements, mostly due to ground sensor limitations. In any event, he was able to draw the conclusion that the aurora was spatially correlated to scintillation and that '[d]uring a magnetic storm ... the E layer or the F layer may dominate...' at one time or the other. He noted that '...during periods of magnetic quiet, the motion of the station into the irregularity oval is a dominant factor in the development of irregularities...E layer irregularities play an important role in the totality of irregularity effects

[4] PFISR did not exist until 2007.

on transionospheric signals.[5]

In a later study by *Aarons et al.* (2000), multiple locations similar to those in the 1997 study were evaluated. They were able to better discern the altitudes of the irregularities involved using auroral imagery and known statistical emission altitudes, concluding that the irregularities must exist from 100 km up into the lower F region. They used the Kp index as well as local magnetometers for storm time indicators; and, concluded that during storm times, IMF orientation (and the resulting storm conditions) dominates and can cause scintillation any time. But when no storm is present, magnetic local time dominates. Comparable elements between these two studies and the data presented in this document are found: energetic particle precipitation and scintillation are spatially and causally linked.

A later article by *Kintner et al.* (2007) presented a climatology at PFRR, and showed evidence of refractive scintillations[6] on 6 March 2005, similar to those presented throughout Chapters 5 through 8. TEC spikes of ∼5 TECU followed by a cycle slip were reported, and they noted that '... rapid changes in TEC coincident with a bright auroral arc support the conclusion of *Coker et al.* (1995) that E region ionization is the causal factor of fast TEC fluctuations at high-latitudes.' The conclusions reached were in part contradictory to those of the previously discussed *Aarons* (1997) and *Aarons et al.* (2000) that found scintillation causes would be different depending on where one was located. *Kintner et al.* (2007) had drawn a broad conclusion regarding scintillations in the high-latitudes based only on the evidence from PFRR, even though the geomagnetic conditions across the region are widely varied.

Subsequent climatologies over similar stations by *Spogli et al.* (2009a,b) and by *Prikryl et al.* (2011, 2015a) further refined the statistical distribution of scintillation in the high-latitudes, but did not address the source. *Spogli et al.* (2009a) affirmed the previous conclusions regarding the high-latitudes that during quiet conditions phase scintillation peaked in the pre-magnetic midnight hours,

[5] *Aarons* (1997) defined the irregularity oval as a subset of the auroral oval with an intensity scale to indicate where scintillations are most intense.

[6] Recall that refractive scintillations occurr when signals encounter structures that are much greater in size than the Fresnel Radius.

while during disturbed days a bimodal peak appeared at magnetic noon and in the pre-magnetic midnight hours. They also concluded that the high-latitudes are more prone to phase scintillation than amplitude scintillation, but again did not address the causal structures. *Spogli et al.* (2009b) conducted a climatology over high and mid-latitude Europe based on the understanding that '... poleward and equatorward boundaries of the auroral oval and the walls of the ionospheric trough are privileged sites to host irregularities associated with scintillation phenomena at mid- and high-latitudes.' Of interest in this study is that they evaluated scintillation during the Hallowe'en storms of 2003, and looked at over four million data points to find a peak in σ_ϕ occurrence at magnetic midnight for sites near 65° magnetic latitude, which was found to be at the equatorward boundary of the midnight oval. They concluded for these sites that the distribution favored the pre-magnetic midnight sector. They also concluded that the scintillation regions are displaced equatorward during disturbed times, although for quiet and disturbed days the scintillation was on the same order of magnitude. *Spogli et al.* (2009b) note that their findings were '...in agreement with the polar cap patches distribution' (*Spogli et al.*, 2009b), even though they did not attempt to attribute the ionospheric source of each scintillation event.

In the climatology published by *Prikryl et al.* (2011) during the 2008-2009 solar minimum, it was concluded that for EAB sites '[P]hase scintillation occurs predominantly in the nightside auroral oval ... The strongest phase scintillation is associated with auroral arc brightening and substorms...' *Prikryl et al.* (2011) also concluded that a link existed between auroral phase scintillation and an equinoctial maximum for aurora. They combined this linkage with a dependence of scintillation in the cusp on an annual cycle to conclude that different mechanisms must exist in both regions. Specifically they divided scintillating structures into two categories: '...energetic electron precipitation [and] dynamic auroral arcs versus cusp ionospheric convection dynamics.' They further noted that '[a]uroral phase scintillation tends to be intermittent, localized and of short duration.' In a subsequent climatology covering the years 2008-2013 (roughly half of a solar cycle), *Prikryl et al.* (2015a) further refined their conclusions by drawing a link between scintillation occurrence in the auroral zone and the IMF B_z component orientation stating that the tendency is to have

'...enhanced scintillation occurrence in the expanded auroral oval and subauroral regions because of strongly southward IMF.' They further linked the scintillation with 'field-aligned irregularities in the auroral oval.'

9.3.2 Case Studies

Aside from the data presented in Chapters 5 through 8, other case studies specific to the area around Poker Flat present evidence of energetic particle precipitation linked to GPS scintillations in Alaska. Only a few case studies show a link between scintillation and convection phonemona. An early study by *Coker et al.* (1995) proposed a technique to use filtered GPS derived TEC 'to detect auroral-E ionization (AEI) at all satellite line-of sight elevations.' This was used in conjunction with satellite derived energetic particle precipitation data to identify the equatorward boundary of the auroral oval. They concluded that it is '...possible using GPS satellites and a single Earth station to determine areas and time periods affected by AEI.' Indeed, they recommended doing this in real time. Over a decade later, *Garner et al.* (2011) observed scintillation that '... was collocated with an auroral arc and a slant total electron content (TEC) increase of 5.71 TECU (TECU = $1016/m^2$),' and precipitating energies of 3-4 keV. A number of other studies of auroral activity over Poker Flat exist. In the end, the conclusion is still the same: over Poker Flat the top reported scintillation causing ionospheric structure exists because of energetic particle precipitation that results in discrete aurora and impact ionization. This is consistent with the findings of the PFISR GPS tracking experiments presented earlier in this work.

Studies have been conducted at sites that are magnetically similar to Poker Flat for years. Case studies across Canada at sites within $\pm 5^\circ$ magnetic latitude include those of *Skone et al.* (2008), who evaluated three case studies selected from scintillation events that occurred across the years 2003-2007, and for sites that were either auroral or sub-auroral but certainly part of the EAB sector in Canada. For all three events considered, they '...attributed [the scintillation effects] to nightside auroral substorm activity,' although some F region enhancements were present in each case. *Hosokawa et al.* (2014) looked at an isolated auroral substorm in November 2009 in Tromsø,

Norway in order to evaluate the temporal evolution of scintillation in conjunction with substorm phasing. Their observations were that

> During this period, bright and discrete auroral forms covered the entire sky, which implies that structured precipitation on the scale of a few kilometers to a few tens of kilometers dominated the electron density distribution in the E region. Such inhomogeneous ionization structures probably produced significant changes in the refractive index and eventually resulted in the enhancement of the phase scintillation.

These conclusions were drawn from data that had negligible F region enhancements present; and, the bulk of the scintillation from precipitation occurred at the onset of the substorm expansion phase. This was a purely E region event similar to that presented in Chapter 6.

Two other studies were conducted first as a demonstration of capability (*Forte et al.*, 2013), followed by a more in-depth evaluation of causal structure altitudes by evaluating their results within the confines of a scintillation model (*Forte et al.*, 2016). In the former, GPS derived temporal fluctuations in TEC from Trømso, Norway, were compared to electron density profiles taken from the EISCAT radar. They concluded the source of TEC variations were from both E and F region '...ionization enhancements possibly caused by particle precipitation in the nighttime sector.' In the latter study, they found that E and F region enhancements were linked to the scintillations...' These case studies are similar to the PFISR tracking mode studies in the sense that they used GPS measurements compared with radar derived electron density profiles along the same line of sight; and, the majority of the experiments were conducted at night. By contrast, however, the PFISR tracking mode studies additionally use multi-spectral imagery to confidently state the source of the enhancements. *Prikryl et al.* (2015b), who looked at the St Patrick's Day time frame of 2012 through the eyes of GPS receivers that covered a range of magnetic latitudes, concluded that the magnetic midnight auroral oval was impacted most by a southward IMF B_z combined with '...high solar wind dynamic pressure.' These were linked to nightside magnetic reconnection, a known acceleration mechanism for particle precipitation. A later study by *Prikryl et al.* (2016) furthered this concept and concluded that '[a]uroral events that include substorms, auroral breakups, and

[polar boundary intensifications] but also the ionospheric blobs are the main sources of scintillation in the nightside auroral oval.'

A case study conducted by *Astafyeva et al.* (2014) evaluated the use of two parameters, loss of lock (LoL) and TEC slips, to map out the sectors of the globe that were subject to irregularities that degraded GPS performance. In this study, two major and two moderate storms were evaluated and similar conclusions to those drawn here were reached: '...[B]esides the geomagnetic storms, quiet time auroral activity can cause increase of LoL rate, and, in particular conditions, even a singular GPS station can largely contribute in the global rate of GPS lock. In other words, auroral activity can impede the performance of GPS signals and this impediment is highly localized. As the preponderance of TEC slips at high-latitudes coincided spatially with data indicating the position of the auroral oval during each of the storms, they proposed exploring methods that would allow the use of a map of TEC slips to '...mark the storm time position of the auroral oval.'

9.3.3 EAB Summary

Throughout the climatologies and case studies presented here, the evident trends are that GPS scintillation is linked to the aurora, and that generalizations across the broader Arctic high-latitudes were improperly applied to locations with vastly different geomagnetic conditions. Also seen throughout these analyses is a lack of comparison in the relative magnitudes of the scintillations, save for the statistical existence of higher scintillation values in the night-time auroral oval than in the dayside cusp. By contrast, the PFISR tracking mode studies presented in this work are aimed at considering the local environmental factors that primarily contribute to scintillation, distinguishing between the relative contribution of each.

9.4 Poleward Auroral Boundary Sector

9.4.1 Climatologies

As was stated at the start of this chapter, many Arctic high-latitude GPS scintillation climatologies have been conducted over the last quarter century; and, many of these include data from both the equatorward and poleward boundary sectors. As a result, several of the climatologies discussed in Section 9.3.1 are also discussed here. Recall that the Arctic High-Latitude Poleward Auroral Boundary (PAB) Sector is comprised of locations at or above 60° magnetic latitude ($\phi_{gm} \geq 60°$), but poleward of the auroral oval. For our purposes this includes Resolute Bay, Canada; Thule, Greenland; and the island of Svalbard, Norway. Refer back to Table 10.1 for an abbreviated list.

The climatology by *Aarons* (1997), focused not only on sites in the equatorward boundary sector, but also on those in the poleward sector. Specifically it looked at Thule, Greenland, and Ny-Ålesund, Norway. He highlighted that 'Ny-Ålesund is at a higher latitude than the quiet nighttime auroral oval but moves under the auroral oval in the daytime. It therefore has a different morphology than those stations [equatorward of the auroral oval]...' In essence he expected that the causal structures would not only be different, but that they would depend on a site's location relative to the auroral oval. He further states that while Ny-Ålesund is normally in the polar cap or at its poleward boundary, during extremely quiet times it can be found well immersed in the auroral oval. The analysis presented led to the conclusion that scintillation had both E and F layer sources, and that when conditions are highly disturbed there are typically multiple sources of the instabilities and therefore the scintillations, including particle precipitation and fast moving plasma flows. He further concluded that '[t]he irregularities might have various origins in time and at various latitudes in the oval.' But, again, he was unable to ascertain the impact of F region phenomena.

Roughly a decade later, *Kintner et al.* (2007) summarized many different sources including *Basu et al.* (1998), which found evidence of both diffractive and refractive scintillations in the polar

cap, poleward of the auroral oval and associated with polar cap patches.[7] In either case, the high-latitudes tend to be dominated with refractive structures and hence primarily phase scintillation. In *Spogli et al.* (2009b), the scintillations were statistically linked at the poleward boundary and in the cusp to magnetic noon near 75° magnetic latitude, which was even more pronounced when the data is separated by quiet vs disturbed days. The authors concluded that the scintillation regions are displaced equatorward during disturbed times, consistent with an expanding auroral oval, and that scintillation occurrence near magnetic midnight was consistent with the distribution of polar cap patches. Interestingly, they posed the question of which was the '...best indicator of the quiet/disturbed conditions for scintillation climatological purposes?' to which, the answer in many studies has been shown to be local magnetometer data.

A climatology by *Moen et al.* (2013) that looked at data from 2008-2012 over Svalbard directly link scintillations in the cusp and at magnetic midnight to the convection of plasma patches through the polar cap and into the auroral oval. They also noted the strong dependence of these occurrences on IMF orientation, expressing the importance that particle precipitation has in scintillation. *Prikryl et al.* (2011) conducted a climatology during the 2008-2009 solar minimum, and at poleward locations noted the predominance of scintillation in the '...footprint of the cusp,' and at magnetic midnight. The results of both of these climatologies point towards what *Aarons* (1997) stated a decade and half earlier - that the morphology would be different depending on where a site was with respect to the auroral oval. *Prikryl et al.* (2011) broke the morphology down into the two irregularity structures: auroral arcs and convection phenomena (aka patches). The interpretation of their results is simply this: if one is located inside the polar cap and rotate into and out of the auroral oval and cusp on the dayside, then convection is of primary concern; but, if located at high-latitudes and equatorward of the auroral oval on the dayside, and rotate into and out of the auroral oval at night, then particle precipitation and substorms have the greatest impact, these conclusions are consistent with results presented in this work from PFRR.

[7] Diffractive scintillations imply smaller scale structures, refractive implies larger scale sizes. Discussed in Section 3.1.2.

More recent climatologies seem to reiterate these points. In the climatology conducted by *Prikryl et al.* (2015a) for 2008-2013 that covered roughly one half of a solar cycle this point was emphatically reiterated:

> The phase scintillation mainly occurs on the dayside in the cusp where ionospheric irregularities convect at high speed, in the nightside auroral oval where energetic particle precipitation causes field-aligned irregularities with steep electron density gradients and in the polar cap where electron density patches that are formed from a tongue of ionization.

The strong dependence on the IMF orientation was restated and taken one step further to include a distinction between the effects of the B_y and B_z components: B_z south was causally linked to the occurrence of scintillation, but the distribution throughout the polar cap was dependent on the orientation of B_y.

> In the polar cap, the IMF B_y polarity controls dawndusk asymmetries in scintillation occurrence collocated with a tongue of ionization for southward IMF and with sun-aligned arcs for northward IMF...predominantly field-aligned irregularities in the auroral oval and L-shell-aligned irregularities in the cusp.

This point was echoed in *Prikryl et al.* (2015b). Lastly *Jin et al.* (2016) conducted a climatology from November of 2010 through February of 2014 at Ny-Ålesund in the night time polar cap at the poleward boundary of the auroral oval. Their conclusion: auroral blobs that began as patches and convected into the auroral oval at magnetic midnight, only to be further structured by discrete auroral arcs were the single largest threat to GPS signals at Ny-Ålesund.

9.4.2 Case Studies

Just like with the EAB sector, in the PAB sector individual case studies are common - especially on the island of Svalbard. An individual case study by *Basu et al.* (1998) at Ny-Ålesund, poleward of dayside cusp, reports amplitude scintillation and TEC variations in response to a patch transiting trough the field of view. They noted

> The presence of irregularities in a longitudinally broad region slightly poleward of the cusp is probably related to the plasma mantle at low altitudes ... The discrete

> auroral features observed by these authors in this region and the associated field-aligned currents may be the source of the observed irregularities.

This conclusion seems to be consistent with the later findings of *Jin et al.* (2014),[8] that polar cap patches and plasma blobs originating as polar cap patches and are structured by the aurora create the strongest scintillations.

Kintner et al. (2002) conducted a TEC study at Nordlysstagjonen near Longyearbyen, Svalbard. They detected discrete E region aurora that produced changes in TEC (spikes of 8 TECU) that raised significant questions for the authors. They knew that pre-magnetic midnight dynamic auroral arcs were dominated by more energetic electrons than elsewhere in the auroral oval; and, that their fluxes tended to be greater. This led them to conclude that the auroral arcs were responsible for the TEC enhancements. They wondered '[h]ow can less intense dayside aurora during minor geomagnetic activity produce TEC fluctuations comparable to nightside activity during geomagnetic storms?' Their answer was that to fully resolve the changes, at least 1 Hz samples are required (their data was a 10 second average every 30 seconds). Their conclusions are yet again, consistent with the observations in this work. *Mitchell* (2005); *van der Meeren et al.* (2014); *Jin et al.* (2015) also conducted studies at Ny-Ålesund in the dayside cusp, and *van der Meeren et al.* (2015) who conducted studies in at the night-side PAB, with findings similar to *Kintner et al.* (2002). *Jin et al.* (2015) stated that '[r]esults show that the occurrence rate of the GPS phase scintillation is highest inside the auroral cusp, regardless of the scintillation strength and the interplanetary magnetic field (IMF).' *van der Meeren et al.* (2015) took the evaluation one step further, noting that it was not until the patches convected in the auroral zone and were structured by discrete aurora did the most intense scintillations occur. Most of these studies also noted that the movement of the enhancements was in keeping with the directions imposed by IMF B_y orientation, the same thing that *Prikryl et al.* (2016) and others have consistently highlighted from their studies specific to Canada and the broader PAB sector. In Canada, similar results were seen by *Prikryl et al.* (2010)at the PAB:

[8] Discussed in Section 3.4.

We have found, as expected, that auroral arc and substorm intensifications as well as cusp region dynamics are strong sources of phase scintillation and potential cycle slips. In addition, we have found clear seasonal and universal time dependencies of TEC and phase scintillation over the polar cap region.

9.5 Response to the Debate

Many climatologies and case studies have been conducted in the Arctic high-latitudes. They evaluated data across many sites that exist under a variety of local magnetic conditions, and yet broad generalities have been drawn regarding the predominant ionospheric source of GPS scintillation. More recent studies, however, have pointed to the possibility that something other than convection phenomena are drivers for these scintillations. When viewed independently, they appear to draw contradictory conclusions regarding the causal ionospheric source of GPS scintillation. When evaluated together, however, a common theme emerges that is summarized as follows:

(1) Sites that are located poleward of the auroral oval (PAB sector) will generally experience GPS scintillation more from ionospheric convection than from auroral activity, except when they rotate into the poleward boundary of the auroral oval where both can affect them and scintillations are the most intense.

(2) Sites that are located equatorward of the auroral oval will generally experience GPS scintillation more from auroral activity than from ionospheric convection phenomena, except when the geomagnetic environment allows them to experience conditions at the poleward boundary (rare).

Essentially the climatologies and case studies that have been independently conducted for the better part of the last half century when viewed together lead to the conclusion that scintillation across the two sectors differ in severity and, more importantly, in source. Additionally, the sectors have two distinct mechanisms for causing GPS, and more broadly UHF, scintillations. These are impact ionization from particle precipitation and convection phenomena. The debate has been occurring in Journals throughout the last half century and has reached a conclusion in this work: scintillation in the equatorward auroral oval coincides with the presence of aurora, scintillation in the poleward auroral oval sector coincides with locations where both plasma patches and aurora occur.

Chapter 10

Conclusions & Future Work

Over the course of this work, the nature of high-latitude GPS scintillations over Poker Flat was investigated. The prevailing theory in the high-latitude aeronomy community is that convection phenomena, like plasma patches and auroral blobs, are *the* high-latitude space weather threat, while others would argue that ionospheric structures resulting from particle precipitation are to blame. The data in this work, combined with a thorough review of the literature point to one conclusion: they are both correct. The causal ionospheric structure for high-latitude GPS scintillation depends on the receiver's location relative to the auroral oval: convection phenomena dominate at the poleward boundary and inside the polar cap while auroral phenomena dominate inside the auroral oval. What follows is a summary of the outcome(s) for each science question along with a summary of on-going experiments and recommendations for future work.

10.1 Science Questions

In this work, research has been presented that sought to address the three science questions originally posed. First, the questions of what scintillating ionospheric structures existed and which one was more important to GPS scintillation in Alaska were addressed. Historically F region enhancements were thought to be *the* causal structures across the high-latitudes both in severity and in occurrence (*Moen et al.*, 2013; *Jin et al.*, 2014). Results of the analyses presented in this work tell a different story: over 72 total hours of experiments conducted between December 2015 and November 2016, including radar derived electron densities, the GPS scintillation index and multi-

spectral imagery, no F region enhancements were detected at PFRR that led to a scintillation event ($\sigma_\phi \geq 0.2$ cycles). However, highly localized E region enhancements resulting from impact ionization due to energetic particle precipitation were causally and correlatively linked to GPS scintillation. This is not to say that F region enhancements do not cause GPS scintillation over Alaska, only to say that they are not the primary threat. The analysis in this work reveals that Alaska primarily sees discrete auroral arcs that are linked to scintillation, which can occur any time that Alaska is in the vicinity of the auroral oval (either at the equatorward boundary or fully immersed), but are primarily seen in the magnetic midnight and pre-magnetic midnight hours.

Lastly, the analysis presented in Chapter 9 addressed the question of how the morphology of scintillating structures in Alaska compared to that in other high-latitude sectors. These sites were broken down into two categories: those that are located inside the polar cap and rotate into and out of the poleward boundary of the auroral oval (PAB), and those that rotate into and out of the equatorward boundary of the auroral oval (EAB). Alaska is usually inside the EAB sector, and results presented here point to the fact that Alaska is no different than any other EAB site: auroral phenomena dominate. Again this is not to say that F region enhancements do not cause scintillation over Alaska, only that the dominant structures are in the E region and result from impact ionization due to particle precipitation.

10.2 Future Work

It is evident from the analyses contained in this work that there is a plausible link between the observed scintillation and indeterminate factors yet to be assessed. This is seen in the moderate correlation values between E region gradients and scintillation events seen in the data from Chapters 7 and 8. Completing the analysis presented in Chapter 8, where only two-thirds of the data between October 2016 and January 2017 have been analyzed, will allow the correlation values to be better determined and will confirm whether or not other factors need to be considered.

Horizontal ionospheric structures occurring during times of F-region plasma enhancements were not able to be derived from the single beam experiments, therefore a volumetric approach is

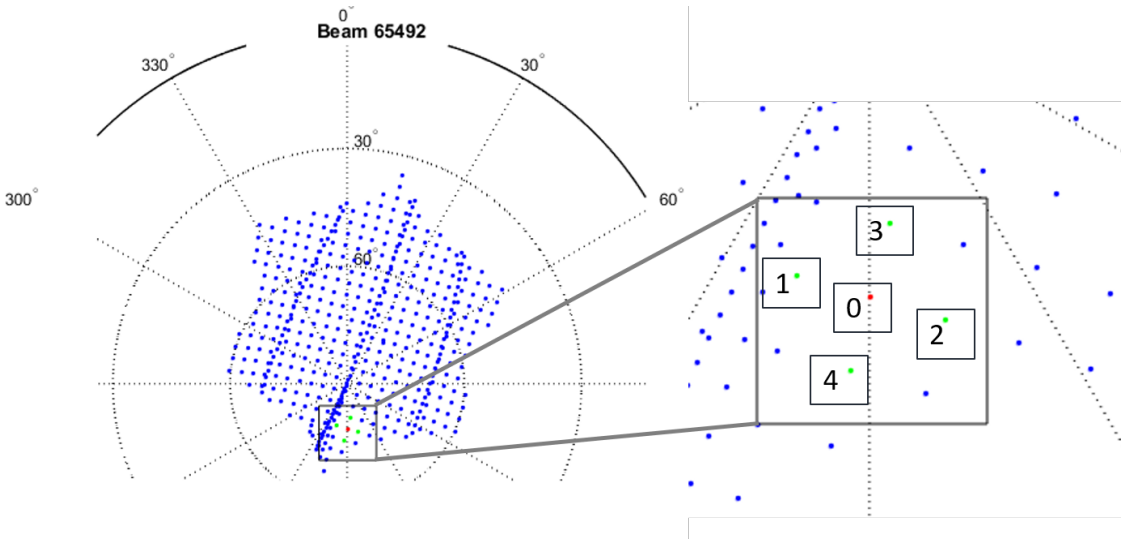

Figure 10.1: Beam configuration for Experimental Campaign III multi-beam experiment (GPSAC1.v01.ffd4).

warranted in the next experimental campaign. This may help to answer the question of whether F region enhancements seen along the GPS line of site were indeed auroral blobs and in which direction they were moving. It will also help to answer the question of what type of aurora was present and the broader context in which it was occurring without the assistance of the all-sky camera. Because of this, a third mode on the radar was developed and 337 experiments covering over six days of worth of time were requested from February through May of 2017.[1] The radar mode was adjusted to account for a new range of target altitudes for the experiments: between 100 km and 150 km. Long pulses were completely eliminated from the experiments to focus all power on the E region, and interleaved coded pulses were used. A total of six beams with the configuration shown in Figure 10.1 were used, and in each IPP the beam sequence followed the order 1-0-2-3-0-4. Note that the '0' beam is the GPS line of sight beam which appears twice in a single IPP sequence to increase the statistics of that measurement, and each of the surrounding beams form a '+' in order to sense meridional and zonal drifts. The resulting temporal resolution on the center ('0') beam is expected to be around 7.5 s or better, with at least double the resolution

[1] Not all experiments were conducted due to conflicts with other experiments of high priority. The PFISR schedule for the month of February 2017 can be found at `http://amisr.com/database/61/sched/2017/2/`, and other months' schedules can be seen through the available navigation buttons.

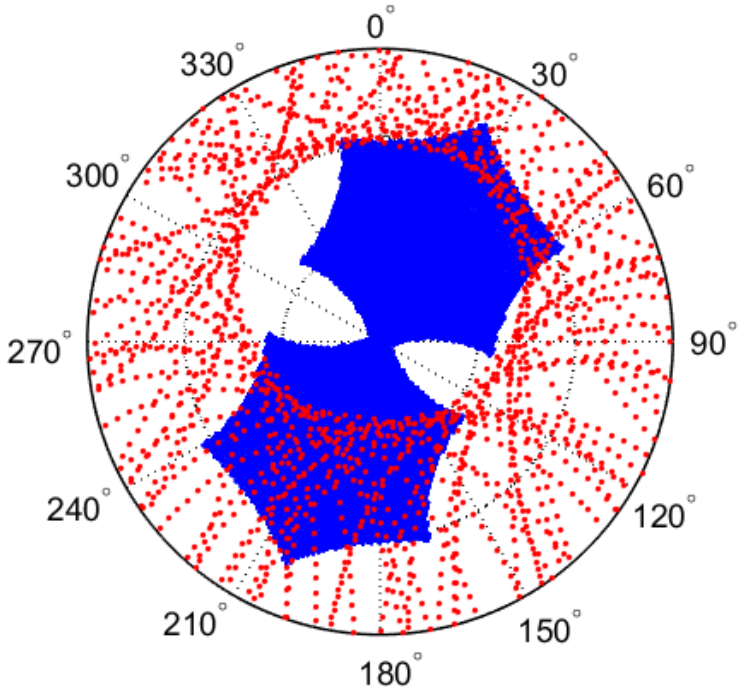

Figure 10.2: Polar plot showing visibility, and equivalently trajectories, of GPS satellites as seen by a notional CASES receiver at Resolute Bay ($\phi_{gd} = 74.72955°$, $\lambda_{gd} = -94.90576°$). Satellite positions in the sky are marked with red circles for the entire 24 hour period of 21 December. The elevation mask is 10°. See Section 3.2.2. Also shown is the Resolute Bay Incoherent Scatter Radar (RISR) beam array pattern (blue dots forming a curved hexagon).

on the surrounding beams. Observations of the F region are still attainable by integrating longer, so while the E region cadence will be fairly high (approximately 7.5 s spacing), the F region cadence will be somewhat slower - a value to be determined. The PFRR CASES receiver will be operated as has before, and select 100 Hz data will be post-processed to produce σ_ϕ at 1 s resolution.

Because PFISR only has a northward facing antenna array, and because it is limited to only 483 beams, the number of GPS conjunctions with PFISR beams are severely limited. The data sets collected have provided invaluable insight into the source of GPS scintillations over PFRR, however many more experiments could be performed if the antenna array and the GPS constellation were better aligned. Only beams on the southerly edges of PFISR's beam pattern experience conjunctions with GPS signals and as such it limits the array's ability to track a single GPS signal throughout the course of its trajectory across the sky. Unlike PFISR, the Resolute Bay Incoherent

Scatter Radar (RISR) has two antenna arrays, one pointing north *and* one pointing south. It is also located near the poleward edge of the auroral oval. Because of its design and unique location it has abilities that PFISR does not: enhanced GPS conjunctions with both arrays, as well as an ability to near-simultaneously sense both the polar cap and the auroral oval. Shown in Figure 10.2 is a 24-hour visibility plot comparing GPS signals received at RISR with its beam pattern. The blue hexagonal shapes are filled with dots representing each of the RISR-Canada and RISR-North beam patterns. Each RISR panel is capable of 3277 pre-programmed beam directions compared with 483 at PFISR. Using both panels of RISR would allow greater visibility into the poleward edge of the auroral oval, while also working with some of the northern most visible GPS satellites in the polar cap.

For many years the high-latitude aeronomy community has debated the primary ionospheric source of GPS scintillation. Broad conclusions have been drawn that plasma patches are the primary scintillating structure using a relatively small set of analyses covering observational data derived from a sparse sensory network. If one considers the distributed data geomagnetically rather than geographically, a common theme emerges with regards to the relative location of sites with respect to the auroral oval. While polar cap patches in the F region may be a primary contributor at or inside the poleward edge of the auroral oval, inside the auroral oval, particularly at the equatorward edge, dynamic particle precipitation causing impact ionization throughout the E region is the primary contributor.

Bibliography

Aarons, J. (1982), Global Morphology of Ionospheric Scintillations, in *Proceedings of the IEEE*, pp. 360–378.

Aarons, J. (1997), Global positioning system phase fluctuations at auroral latitudes, *Journal of Geophysical Research*, *102*(A8), 17,219–17,231.

Aarons, J., B. Lin, M. Mendillo, K. Liou, and M. Codrescu (2000), Global Positioning System phase fluctuations and ultraviolet images from the Polar satellite, *Journal of Geophysical Research*, *105*(A3), 5201–5213, doi:10.1029/1999ja900409.

Akasofu, S.-I. (2009), *The Northern Lights: Secrets of the Aurora Borealis*, Alaska Northwest Books, Portland, OR.

Appleton, E. V. (1946), Two Anomalies in the Ionosphere, *Nature*, *157*(3995), 691, doi:10.1038/157691a0.

Astafyeva, E., Y. Yasyukevich, A. Maksikov, and I. Zhivetiev (2014), Geomagnetic storms, superstorms, and their impacts on GPS-based navigation systems, *Space Weather*, *12*(7), 508–525, doi:10.1002/2014SW001072.

Axelrad, P., and K. Larson (2006), GNSS Solutions: Orbital precession, optimal dual-frequency techniques, and Galileo receivers, *Inside GNSS*, (July/August 2006), 16–17.

Azeem, I., G. Crowley, A. Reynolds, J. Santana, and D. Hampton (2013), First Results of Phase Scintillation from a Longitudinal Chain of ASTRA's SM-211 GPS TEC and Scintillation Receivers in Alaska, in *ION 2013 Pacific PNT Meeting*, pp. 735–742, Honolulu, Hawaii.

Baker, K. B., and S. Wing (1989), A new magnetic coordinate system for conjugate studies at high latitudes, *Journal of Geophysical Research*, *94*(A7), 9139, doi:10.1029/JA094iA07p09139.

Barkhatov, N. A., E. A. Revunova, and A. E. Levitin (2012), Geomagnetic efficiency of solar ejection depended on relative orientation of Sun and Earth rotation axes, in *"Physics of Auroral Phenomena", Proc. XXXV Annual Seminar, Apatity,*, pp. 85–87, Polar Geophysical Institute.

Basu, S., and S. Basu (1981), Equatorial scintillations - a review, *Journal of Atmospheric and Terrestrial Physics*, *43*(5), 473–489.

Basu, S., and S. Basu (1985), Equatorial scintillations: advances since ISEA-6, *Journal of Atmospheric and Terrestrial Physics*, *47*(8-10), 753–768, doi:10.1016/0021-9169(85)90052-2.

Basu, S., S. Basu, J. P. Mullen, and A. Bushby (1980), Long-term 1.5 GHz Amplitude Scintillation Measurements at the Magnetic Equator, *Geophysical Research Letters*, *7*(4), 259–262.

Basu, S., E. J. Weber, T. W. Bullett, M. J. Keskinen, E. Mackenzie, R. Sheehan, H. Kuenzler, P. Ning, and J. Bongio (1998), Characteristics of plasma structuring in the cusp / cleft region patches with total electron contents m -2 and amplitude scintillations at the GPS, *33*(6), 1885–1899.

Basu, S., K. M. Groves, S. Basu, and P. J. Sultan (2002), Specification and forecasting of scintillations in communication/navigation links: Current status and future plans, *Journal of Atmospheric and Solar-Terrestrial Physics*, *64*(16), 1745–1754, doi:10.1016/S1364-6826(02)00124-4.

Bate, R. R., D. D. Mueller, and J. E. White (1971), *Fundamentals of Astrodynamics*, Dover Publications, Inc, New York.

Beach, T. L. (1998), Global Positioning System Studies of Equatorial Scintillations, Ph.D. thesis, Cornell University, Ithica, NY.

Beniguel, Y., P. Hamel, Y. Béniguel, and P. Hamel (2011), A global ionosphere scintillation propagation model for equatorial regions, *Journal of Space Weather and Space Climate*, *1*(1), A04, doi:10.1051/swsc/2011004.

Bergeot, N., J.-M. Chevalier, C. Bruyninx, E. Pottiaux, W. Aerts, Q. Baire, J. Legrand, P. Defraigne, and W. Huang (2014), Near real-time ionospheric monitoring over Europe at the Royal Observatory of Belgium using GNSS data, *Journal of Space Weather and Space Climate*, *4*, A31, doi:10.1051/swsc/2014028.

Booker, H. (1958), The Use of Radio Stars to Study Irregular Refraction of Radio Waves in the Ionosphere, *Proceedings of the IRE*, *46*, 298–314, doi:10.1109/JRPROC.1958.286791.

Booker, H., J. Ratcliffe, and J. Shinn (1950), Diffraction from an irregular screen with applications to ionospheric problems, *Philosophical Transactions of the Royal Society of London. Series A, Mathematical and Physical Sciences*, *242*(A), 856, doi:10.1098/rsta.1979.0079.

Booker, H. G., and G. Majidiahi (1981), Theory of refractive scattering in scintillation phenomena, *Journal of Atmospheric and Terrestrial Physics*, *43*(11), 1199–1214, doi:10.1016/0021-9169(81)90035-0.

Borovsky, J. E., and M. H. Denton (2009), Electron loss rates from the outer radiation belt caused by the filling of the outer plasmasphere: The calm before the storm, *Journal of Geophysical Research: Space Physics*, *114*(11), 1–12, doi:10.1029/2009JA014063.

Borovsky, J. E., and J. T. Steinberg (2006), The "calm before the storm" in CIR/magnetosphere interactions: Occurrence statistics, solar wind statistics, and magnetospheric preconditioning, *Journal of Geophysical Research: Space Physics*, *111*(7), 1–29, doi:10.1029/2005JA011397.

Bradley, B. K. (2014), Sidera v1.1. \url{https://www.asterlabs.com/Sidera.html}.

Briggs, B. H., G. J. Phillips, and D. H. Shinn (1950), The Analysis of Observations on Spaced Receivers of the Fading of Radio Signals, *Proceedings of the Physical Society. Section B*, *B63*, 106–121, doi:10.1088/0370-1301/63/2/305.

Brito, T., M. K. Hudson, B. Kress, J. Paral, A. Halford, R. Millan, and M. Usanova (2015), Simulation of ULF wave-modulated radiation belt electron precipitation during the 17 March 2013 storm, *Journal of Geophysical Research A: Space Physics*, *120*(5), 3444–3461, doi:10.1002/2014JA020838.

Buckley, R., and P. Road (1975), Diffraction by a random phase-changing screen: A numerical experiment, *Journal of Atmospheric and Terrestrial Physics*, *37*, 1431–1446.

Chiu, Y. T., and J. M. Straus (1979), Rayleigh-Taylor and Wind-Driven Instabilities of the Nighttime Equatorial Ionosphere, *Journal of Geophysical Research*, *84*(A7), 3283–3290.

Christian, E. R., and A. J. Davis (2012), ACE Mission, http://www.srl.caltech.edu/ACE/ace_mission.html.

Chua, D., G. Parks, M. Brittnacher, G. Germany, and J. Spann (2004), Auroral substorm timescales: IMF and seasonal variations, *Journal of Geophysical Research: Space Physics*, *109*(A3), 1–16, doi:10.1029/2003JA009951.

Clauer, C. R., H. Kim, K. Deshpande, Z. Xu, D. Weimer, S. Musko, G. Crowley, C. Fish, R. Nealy, T. E. Humphreys, J. a. Bhatti, and a. J. Ridley (2014), An autonomous adaptive low-power instrument platform (AAL-PIP) for remote high-latitude geospace data collection, *Geoscientific Instrumentation, Methods and Data Systems*, *3*(2), 211–227, doi:10.5194/gi-3-211-2014.

Clausen, L. B. N., J. I. Moen, K. Hosokawa, and J. M. Holmes (2016), GPS scintillations in the high latitudes during periods of dayside and nightside reconnection, *Journal of Geophysical Research A: Space Physics*, *121*(4), 3293–3309, doi:10.1002/2015JA022199.

Cliver, E. W., Y. Kamide, and A. G. Ling (2000), Mountains versus valleys: Semiannual variation of geomagnetic activity, *Journal of Geophysical Research*, *105*(A2), 2413, doi:10.1029/1999JA900439.

Coker, C., R. Hunsucker, and G. Lott (1995), Detection of auroral activity using GPS satellites, *Geophysical Research Letters*, *22*(23), 3259–3262, doi:10.1029/95GL03091.

Colpitts, C. A. (2016), Investigations of the Many Distinct Types of Auroras, in *Auroral Dynamics and Space Weather, Geophysical Monograph 215*, edited by Y. Zhang and L. J. Paxton, first ed., chap. 1, pp. 3–18, John Wiley & Sons, Inc.

Cowley, S. W. H. (1996), A beginner's guide to the Earth's magnetosphere., *Earth in Space*, *8*(7), 9–13.

Crooker, N. U. (1975), Solar wind-magnetosphere coupling, *Reviews of Geophysics and Space Physics*, *13*(3), 955–958.

Crooker, N. U., E. W. Cliver, and B. T. Tsurutani (1992), The semiannual variation of great geomagnetic storms and the postshock Russell-McPherron effect preceding coronal mass ejecta, *Geophysical Research Letters*, *19*(5), 429, doi:10.1029/92GL00377.

Crowley, G. (1996), Critical Review of Ionospheric Patches and Blobs, *The Reivew of Radio Science 1993-1996*, pp. 619–648.

Crowley, G., A. J. Ridley, D. Deist, S. Wing, D. J. Knipp, B. A. Emery, J. Foster, R. Heelis, M. Hairston, and B. W. Reinisch (2000), Transformation of high-latitude ionospheric F region patches into blobs during the March 21, 1990, storm, *Journal of Geophysical Research*, *105*(A3), 5215–5230, doi:10.1029/1999JA900357.

Crowley, G., G. S. Bust, A. Reynolds, I. Azeem, R. Wilder, B. Co, B. W. O'Hanlon, M. L. Psiaki, S. Powell, T. E. Humphreys, and J. a. Bhatti (2011), CASES: A Novel Low-Cost Ground-based Dual- Frequency GPS Software Receiver and Space Weather Monitor, *Proceedings of the 24th International Technical Meeting of the ION GNSS Portland, OR*, pp. 1437–1446.

Dahlgren, H., J. L. Semeter, K. Hosokawa, M. J. Nicolls, T. W. Butler, M. G. Johnsen, K. Shiokawa, and C. Heinselman (2012), Direct three-dimensional imaging of polar ionospheric structures with the Resolute Bay Incoherent Scatter Radar, *Geophysical Research Letters*, *39*(L05104), 1–6, doi: 10.1029/2012GL050895.

Datta-Barua, S., Y. Su, K. Deshpande, D. Miladinovich, G. S. Bust, D. Hampton, and G. Crowley (2015), First light from a kilometer-baseline, *Geophysical Research Letters*, *42*, 3639–3646, doi: 10.1002/2015GL063556.

Davis, N. C. (1996), An Information-Based Revolution in Military Affairs, *Strategic Review*, *24*(1), 43–53.

Deshpande, K. B., G. S. Bust, C. R. Clauer, H. Kim, J. E. MacOn, T. E. Humphreys, J. a. Bhatti, S. B. Musko, G. Crowley, and a. T. Weatherwax (2012), Initial GPS scintillation results from CASES receiver at South Pole, Antarctica, *Radio Science*, *47*(5), 1–10, doi: 10.1029/2012RS005061.

Dissinger, K. (2008), GPS Goes to War - The Global Positioning System in Operation Desert Storm.

Dmitriev, A. V., A. V. Suvorova, M. V. Klimenko, V. V. Klimenko, K. G. Ratovsky, R. A. Rakhmatulin, and V. A. Parkhomov (2017), Predictable and unpredictable ionospheric disturbances during St. Patrick's Day magnetic storms of 2013 and 2015 and on 8-9 March 2008, *Journal of Geophysical Research: Space Physics*, doi:10.1002/2016JA023260.

Downes, L., and C. Mui (2000), *Unleashing the Killer App: Digital Strategies for Market Dominance*, Harvard Business School Press.

Dungey, J. W. (1961), Interplanetary Magnetic Field and the Auroral Zones, *Physical Review Letters*, *6*(2), 47–48, doi:10.1103/PhysRevLett.6.47.

Engineering, T. (2008), Trimble NetR8 GNSS Reference Receiver, (October), 1–5.

Erickson, P. J., F. Beroz, and M. Z. Miskin (2011), Statistical characterization of the American sector subauroral polarization stream using incoherent scatter radar, *Journal of Geophysical Research: Space Physics*, *116*(3), 1–8, doi:10.1029/2010JA015738.

Evans, J. V. (1962), Studies of the F-Region by the Incoherent Backscatter Method, *Tech. rep.*, MIT.

Evans, J. V. (1969), Theory and Practice of Ionosphere Study by Thompson Scatter Radar, *Proceedings of the IEEE*, *57*(4), 496–530.

Falayi, E., and N. Beloff (2009), Asymmetry in seasonal variation of geomagnetic activity, *Canadian Journal of Pure & Applied Sciences*, *3*(2), 813–820.

Farley, D. T. (1969), Incoherent scatter correlation function measurements, *Radio Science*, *4*(10), 935–953.

Fejer, B. G. (1991), Low latitude electodynamic plasma drifts: A review, *J. Atmos. Terr. Phys.*, *53*(8), 677–693.

for Policy, O. o. t. U. f. D. (2016), Report to Congress on Strategy to Protect United States National Security Interests in the Arctic Region, *Tech. rep.*

Forte, B., N. D. Smith, C. N. Mitchell, F. Da Dalt, T. Panicciari, A. T. Chartier, D. Stevanovic, M. Vuckovic, J. Kinrade, J. R. Tong, I. Haggstrom, and E. Turunen (2013), Comparison of temporal fluctuations in the total electron content estimates from EISCAT and GPS along the same line of sight, *Annales Geophysicae*, *31*(4), 745–753, doi:10.5194/angeo-31-745-2013.

Forte, B., C. Coleman, S. Skone, I. Häggström, C. Mitchell, J. Kinrade, and G. Bust (2016), Identification of scintillation signatures on GPS signals originating from plasma structures detected with EISCAT incoherent scatter radar along the same line of sight, *Journal of Geophysical Research: Space Physics*, pp. 916–931, doi:10.1002/2016JA023271.

Foster, J. C., a. J. Coster, P. J. Erickson, J. M. Holt, F. D. Lind, W. Rideout, M. McCready, A. Van Eyken, R. J. Barnes, R. a. Greenwald, and F. J. Rich (2005), Multiradar observations of the polar tongue of ionization, *Journal of Geophysical Research*, *110*(A09S31), 1–12, doi:10.1029/2004JA010928.

Garner, T. W., R. B. Harris, J. a. York, C. S. Herbster, C. F. Minter, and D. L. Hampton (2011), An auroral scintillation observation using precise, collocated GPS receivers, *Radio Science*, *46*(RS1018), 1–11, doi:10.1029/2010RS004412.

Ghafoori, F., and S. Skone (2015), Impact of Equatorial Ionospheric Irregularities on GNSS Receivers Using Real and Synthetic Scintillation Signals, *Radio Science*, pp. n/a–n/a, doi:10.1002/2014RS005513.

Ghoddousi-Fard, R., P. Prikryl, and F. Lahaye (2013), GPS phase difference variation statistics: A comparison between phase scintillation index and proxy indices, *Advances in Space Research*, *52*(8), 1397–1405, doi:10.1016/j.asr.2013.06.035.

Gjerloev, J. W., R. A. Hoffman, M. M. Friel, L. A. Frank, and J. B. Sigwarth (2004), Substorm behavior of the auroral electrojet indices, *Annales Geophysicae*, *22*, 2135–2149.

Goodwin, L. V., B. Iserhienrhien, D. M. Miles, S. Patra, C. Van Der Meeren, S. C. Buchert, J. K. Burchill, L. B. N. Clausen, D. J. Knudsen, K. A. McWilliams, and J. Moen (2015), Swarm in situ observations of F region polar cap patches created by cusp precipitation, *Geophysical Research Letters*, *42*(4), 996–1003, doi:10.1002/2014GL062610.

Griffiths, D. J. (1999), *Introduction to Electrodynamics*, 3rd ed., Prentice-Hall, Inc, Upper Saddle River, New Jersey.

Grubbs, G. I. (2016), Magnetosphere-ionosphere coupling during active aurora, Dissertation, University of Texas at San Antonio.

Gudivada, K. P. (2014), Detection of F-Region Electron Density Irrgularities using Incohere-Scatter Radar, Masters thesis, University of Alaska Fairbanks.

Halliday, D., R. Resnick, and J. Walker (2008), *Fundamentals of Physics*, John Wiley & Sons, Inc, Hoboken.

Heinselman, C. J., and M. J. Nicolls (2008), A Bayesian approach to electric field and E-region neutral wind estimation with the Poker Flat Advanced Modular Incoherent Scatter Radar, *Radio Science*, *43*(RS5013), 1–15, doi:10.1029/2007RS003805.

Hewish, A. (1951), The diffraction of radio waves in passing through a phase-changing ionosphere, *Proceedings of the Royal Society Series A: Mathematical, Physical and Engineering Scienceso*, *209*, 81–94.

Hey, J. S., S. J. Parsons, and J. W. Phillips (1946), Fluctuations in Cosmic Radiation at Radio-Frequencies, *Nature*, *158*, 234–235.

Hosokawa, K., J. I. Moen, K. Shiokawa, and Y. Otsuka (2011), Decay of polar cap patch, *Journal of Geophysical Research*, *116*(A05306), 1–13, doi:10.1029/2010JA016297.

Hosokawa, K., Y. Otsuka, Y. Ogawa, and T. Tsugawa (2014), Observations of GPS scintillation during an isolated auroral substorm, *Progress in Earth and Planetary Science*, *1*(1), 16, doi: 10.1186/2197-4284-1-16.

Huang, C. S., O. De La Beaujardiere, P. A. Roddy, D. E. Hunton, R. F. Pfaff, C. E. Valladares, and J. O. Ballenthin (2011), Evolution of equatorial ionospheric plasma bubbles and formation of broad plasma depletions measured by the C/NOFS satellite during deep solar minimum, *Journal of Geophysical Research: Space Physics*, *116*(3), 1–13, doi:10.1029/2010JA015982.

Humphreys, T. E., M. L. Psiaki, J. C. Hinks, B. O'Hanlon, and P. M. Kintner (2009), Simulating ionosphere-induced scintillation for testing GPS receiver phase tracking loops, *IEEE Journal on Selected Topics in Signal Processing*, *3*(4), 707–715, doi:10.1109/JSTSP.2009.2024130.

Huuskonen, A., M. S. Lehtinen, and J. Pirttila (1996), Fractional lags in alternating codes: Improving incoherent scatter measurements by using lag estimates at noninteger multiples of baud length, *Radio Science*, *31*(2), 245–261.

International, S. (2016), AMISR.

Jiao, Y., and Y. T. Morton (2015), Comparison of the effect of high-latitude and equatorial ionospheric scintillation on GPS signals during the maximum of solar cycle 24, pp. 886–903, doi: 10.1002/2015RS005719.Received.

Jin, Y., J. Moen, and W. Miloch (2014), GPS scintillation effects associated with polar cap patches and substorm auroral activity: direct comparison, *Journal of Space Weather and Space Climate*, *4*(A23), 1–6, doi:10.1051/swsc/2014019.

Jin, Y., J. I. Moen, and W. J. Miloch (2015), On the collocation of the cusp aurora and the GPS phase scintillation: A statistical study, *Journal of Geophysical Research A: Space Physics*, *120*(10), 9176–9191, doi:10.1002/2015JA021449.

Jin, Y., J. Moen, W. Miloch, L. Clausen, and K. Oksavik (2016), Statistical study of the GNSS phase scintillation associated with two types of auroral blobs, *Journal of Geophysical Research: Space Physics*, *121*, 4679–4697, doi:10.1002/2016JA022400.

Johnsen, M. G. (2011), The Dayside Open / Closed Field line Boundary Ground-based optical determination and examination, Ph.D. thesis, University of Tromso.

Jones, A. V. (1974), *Aurora*, D. Reidel Publishing Company, Boston, MA.

Joshi, P. P., J. B. H. Baker, J. M. Ruohoniemi, J. J. Makela, D. J. Fisher, B. J. Harding, N. A. Frissell, and E. G. Thomas (2015), Journal of Geophysical Research : Space Physics Observations of storm time midlatitude ion-neutral coupling using SuperDARN radars and NATION, pp. 8989–9003, doi:10.1002/2015JA021475.Received.

Kalita, B. R., R. Hazarika, G. Kakoti, P. K. Bhuyan, D. Chakrabarty, G. K. Seemala, K. Wang, S. Sharma, T. Yokoyama, P. Supnithi, T. Komolmis, C. Y. Yatini, M. Le Huy, and P. Roy (2016), Conjugate hemisphere ionospheric response to the St. Patrick's Day storms of 2013 and 2015 in the 100E longitude sector, *Journal of Geophysical Research: Space Physics*, *121*(11), 11,364–11,390, doi:10.1002/2016JA023119.

Kamide, Y., W. Baumjohann, I. a. Daglis, W. D. Gonzalez, M. Grande, J. a. Joselyn, R. L. McPherron, J. L. Phillips, E. G. D. Reeves, G. Rostoker, a. S. Sharma, H. J. Singer, B. T. Tsurutani, and V. M. Vasyliunas (1998), Current understanding of magnetic storms: Storm-substorm relationships, *Journal of Geophysical Research*, *103*(A8), 17,705, doi:10.1029/98JA01426.

Kil, H., Y. S. Kwak, L. J. Paxton, R. R. Meier, and Y. Zhang (2011), O and N2 disturbances in the F region during the 20 November 2003 storm seen from TIMED/GUVI, *Journal of Geophysical Research: Space Physics*, *116*(2), 1–9, doi:10.1029/2010JA016227.

Kim, H., C. R. Clauer, K. Deshpande, M. R. Lessard, A. T. Weatherwax, G. S. Bust, G. Crowley, and T. E. Humphreys (2014), Ionospheric irregularities during a substorm event: Observations of ULF pulsations and GPS scintillations, *Journal of Atmospheric and Solar-Terrestrial Physics*, *114*, 1–8, doi:10.1016/j.jastp.2014.03.006.

Kinrade, J., C. N. Mitchell, N. D. Smith, Y. Ebihara, A. T. Weatherwax, and G. S. Bust (2013), GPS phase scintillation associated with optical auroral emissions: First statistical results from the geographic South Pole, *Journal of Geophysical Research: Space Physics*, *118*, 2490–2502, doi:10.1002/jgra.50214.

Kintner, P., H. Kil, C. Deehr, and P. Schuck (2002), Simultaneous total electron content and all-sky camera measurements of an auroral arc, *Journal of Geophysical Research*, *107*(A7), 1127, doi:10.1029/2001JA000110.

Kintner, P. M. (2004), Size, shape, orientation, speed, and duration of GPS equatorial anomaly scintillations, *Radio Science*, *39*(2), n/a–n/a, doi:10.1029/2003RS002878.

Kintner, P. M., and B. M. Ledvina (2005), The ionosphere, radio navigation, and global navigation satellite systems, *Advances in Space Research*, *35*, 788–811, doi:10.1016/j.asr.2004.12.076.

Kintner, P. M., B. M. Ledvina, and E. R. De Paula (2007), GPS and ionospheric scintillations, *Space Weather*, *5*(April), 1–23, doi:10.1029/2006SW000260.

Knipp, D. (2011), *Understanding Space Weather and the Physics Behind It*, McGraw Hill Companies, Inc.

Kumar, S., and A. K. Singh (2012), Effect of solar flares on ionospheric TEC at Varanasi , near EIA crest, during solar, *Indian Journal of Radio & Space Physics*, *41*(April 2012), 141–147.

Ledvina, B. M., P. M. Kintner, and J. J. Makela (2004), Temporal properties of intense GPS L1 amplitude scintillations at midlatitudes, *Radio Science*, *39*(1), 1–8, doi:10.1029/2002RS002832.

Lehtinen, M. S., and I. Haggstrom (1987), A new modulation principle for incoherent scatter measurements, *Radio Science*, *22*(4), 625–634.

Lehtinen, M. S., A. Huuskonen, and M. Markkanen (1997), Randomization of alternating codes: Improving incoherent scatter measurements by reducing correlations of gated autocorrelation function estimates, *Radio Science*, *32*(6), 2271–2282.

Liu, J., T. Nakamura, L. Liu, W. Wang, N. Balan, T. Nishiyama, M. R. Hairston, and E. G. Thomas (2015), Formation of polar ionospheric tongue of ionization during minor geomagnetic disturbed conditions, *Journal of Geophysical Research A: Space Physics*, *120*(8), 6860–6873, doi:10.1002/2015JA021393.

Loucks, D., S. Palo, M. Pilinski, G. Crowley, I. Azeem, and D. Hampton (2017), High-latitude GPS Phase Scintillation from E Region Electron Density Gradients During the December 20-21, 2015 Geomagnetic Storm, *Journal of Geophysical Research: Space Physics*, doi:10.1002/2016JA023839.

Magnetism, D. A. C. f. G., and Space (2016), World Data Center for Geomagnetism, Kyoto.

Matassa, C. K. (2011), Comparing the Capabilities and Performance of the Ultra-high Frequency Follow-on System with the Mobile User Objective System, Ph.D. thesis, Naval Post Graduate School.

Melvin, W. L., and J. A. Scheer (2013), *Principles of Modern Radar, Volume 2 - Advanced Techniques - Knovel*, SciTech Publishing, Edison, NJ.

Milan, S. E., J. Hutchinson, P. D. Boakes, and B. Hubert (2009), Influences on the radius of the auroral oval, *Annales Geophysicae*, *27*(7), 2913–2924, doi:10.5194/angeo-27-2913-2009.

Misra, P., and P. Enge (2006), *Global Positioning System: Signal, Measurements, and Performance*, 2nd ed., Ganga-Jamuna Press, Lincoln, Massachusetts.

Mitchell, C. N. (2005), GPS TEC and scintillation measurements from the polar ionosphere during the October 2003 storm, *Geophysical Research Letters*, *32*(12), L12S03, doi:10.1029/2004GL021644.

Moen, J., N. Gulbrandsen, D. A. Lorentzen, and H. C. Carlson (2007), On the MLT distribution of F region polar cap patches at night, *Geophysical Research Letters*, *34*(14), L14,113, doi:10.1029/2007GL029632.

Moen, J., K. Oksavik, L. Alfonsi, Y. Daabakk, V. Romano, and L. Spogli (2013), Space weather challenges of the polar cap ionosphere, *Journal of Space Weather and Space Climate*, *3*, A02, doi:10.1051/swsc/2013025.

Moen, J., K. Hosokawa, N. Gulbrandsen, and L. B. N. Clausen (2015), On the symmetry of ionospheric polar cap patch exits around magnetic midnight, *Journal of Geophysical Research: Space Physics*, *120*, 7785–7797, doi:10.1002/2015JA021980.Received.

Morrissey, T. N., K. W. Shallberg, a. J. Van Dierendonck, and M. J. Nicholson (2004), GPS receiver performance characterization under realistic ionospheric phase scintillation environments, *Radio Science*, *39*(1), n/a–n/a, doi:10.1029/2002RS002838.

NCEI (2017), Auroral Electrojet (AE, AL, AO, AU) - A Global Measure of Auroral Zone Magnetic Activity.

Newell, P. T., T. Sotirelis, and S. Wing (2009), Diffuse, monoenergetic, and broadband aurora: The global precipitation budget, *Journal of Geophysical Research: Space Physics*, *114*(9), 1–20, doi:10.1029/2009JA014326.

Nicolls, M. J., and C. J. Heinselman (2007), Three-dimensional measurements of traveling ionospheric disturbances with the Poker Flat Incoherent Scatter Radar, *Geophysical Research Letters*, *34*(L21104), 1–6, doi:10.1029/2007GL031506.

Nicolls, M. J., C. J. Heinselman, E. A. Hope, S. Ranjan, M. C. Kelley, and J. D. Kelly (2007), Imaging of Polar Mesosphere Summer Echoes with the 450 MHz Poker Flat Advanced Modular Incoherent Scatter Radar, *Geophysical Research Letters*, *34*(L20102), 1–6, doi:10.1029/2007GL031476.

NSIDC (2016), SOTC: Sea Ice, National Snow & Ice Data Center.

O'Brien, T. P., and R. L. McPherron (2002), Seasonal and diurnal variation of Dst dynamics, *Journal of Geophysical Research: Space Physics*, *107*(A11), 1–10, doi:10.1029/2002JA009435.

Oh, S. Y., and Y. Yi (2011), Solar magnetic polarity dependency of geomagnetic storm seasonal occurrence, *Journal of Geophysical Research: Space Physics*, *116*(6), 1–6, doi:10.1029/2010JA016362.

O'Hanlon, B., M. Psiaki, J. Bhatti, G. Crowley, and G. Bust (2011), CASES: A Smart, Compact GPS Software Receiver for Space Weather Monitoring, *ION GNSS 2011*, pp. 1–9.

Parker, E. N. (1958), Dynamics of the Interplanetary Gas and Magnetic Fields, *The Astrophysical Journal*, *128*, 664, doi:10.1086/146579.

Prikryl, P., P. T. Jayachandran, S. C. Mushini, D. Pokhotelov, J. W. MacDougall, E. Donovan, E. Spanswick, and J.-P. St.-Maurice (2010), GPS TEC, scintillation and cycle slips observed at high latitudes during solar minimum, *Annales Geophysicae*, *28*(6), 1307–1316, doi:10.5194/angeo-28-1307-2010.

Prikryl, P., P. T. Jayachandran, S. C. Mushini, and R. Chadwick (2011), Climatology of GPS phase scintillation and HF radar backscatter for the high-latitude ionosphere under solar minimum conditions, *Annales Geophysicae*, *29*(2), 377–392, doi:10.5194/angeo-29-377-2011.

Prikryl, P., P. T. Jayachandran, R. Chadwick, and T. D. Kelly (2015a), Climatology of GPS phase scintillation at northern high latitudes for the period from 2008 to 2013, *Annales Geophysicae*, *33*(5), 531–545, doi:10.5194/angeo-33-531-2015.

Prikryl, P., R. Ghoddousi-Fard, E. Thomas, J. Ruohoniemi, S. Shepherd, P. Jayachandran, G. Danskin, E. Spanswick, Y. Zhang, Y. Jiao, and Y. Morton (2015b), GPS phase scintillation at high latitudes during geomagnetic storms of 717 March 2012 Part 1: The North American sector, *Annales Geophysicae*, *33*, 637–656.

Prikryl, P., R. G. Fard, J. M. Ruohoniemi, and E. G. Thomas (2016), GPS Phase Scintillation at High Latitudes during Two Geomagnetic Storms, in *Auroral Dynamics and Space Weather, Geophysical Monograph 215*, pp. 211–231, John Wiley & Sons, Inc, Washington, D.C.

Psiaki, M. L., A. P. Cerruti, P. M. Kintner, and S. P. Powell (2008), Diffraction Tomography of the Disturbed Ionosphere Based on GPS Scintillation Data, *Antenna*, (September), 16–19.

Rama Rao, P. V. S., K. Niranjan, D. S. V. V. D. Prasad, S. Gopi Krishna, and G. Uma (2006), On the validity of the ionospheric pierce point (IPP) altitude of 350 km in the Indian equatorial and low-latitude sector, *Annales Geophysicae*, *24*(8), 2159–2168, doi:10.5194/angeo-24-2159-2006.

Rangarajan, G. K., and T. Iyemori (1997), Time variations of geomagnetic activity indices Kp and Ap: an update, *Annales Geophysicae*, *15*(10), 1271, doi:10.1007/s005850050544.

Ratcliffe, J. A. (1956), Some Aspects of Diffraction Theory and their Application to the Ionosphere, *Reports on Progress in Physics*, *9*, 188–267, doi:10.1088/0034-4885/19/1/306.

Rees, M. H., and D. Luckey (1974), Auroral Electron Energy Derived From Ratio of Spectroscopic Emissions 1. Model Computations, *Journal of Geophysical Research*, *79*(34), 5181–5186, doi:10.1029/JA079i034p05181.

Richards, M. A., J. A. Scheer, and W. A. Holm (2010), *Principles of Modern Radar, Vol I: Basic Principles*, SciTech Publishing, Edison, NJ.

Rostoker, G. (2000), Effects of substorms on the stormtime ring current index Dst, *Annales Geophysicae*, *18*, 1390–1398, doi:10.1007/s005850000275.

Russell, C. T. (2001), The dynamics of planetary magnetospheres, *Planetary and Space Science*, *49*, 1005–1030, doi:10.1016/S0032-0633(01)00017-4.

Russell, C. T., and R. L. McPherron (1973), Semiannual Variation of Geomagnetic Activity, *Journal of Geophysical Research*, *78*(1), 92–108, doi:10.1029/JA078i001p00092.

Salpeter, E. (1967), Interplanetary Scintillations. I. Theory, *Astrophysical Journal*, *147*, 433–448, doi:10.1017/CBO9781107415324.004.

Sandholt, P., C. Farrugia, and W. Denig (2004), Dayside aurora and the role of IMF By/Bz: detailed morphology and response to magnetopause reconnection, *Annales Geophysicae*, *22*, 613–628.

Sandholt, P. E., C. J. Farrugia, J. Moen, and S. W. H. Cowley (1998), Dayside auroral configurations: Responses to southward and northward rotations of the interplanetary magnetic field, *Journal of Geophysical Research*, *103*(A9), 20,279–95, doi:10.1029/98JA01541.

Schunk, R., and A. Nagy (2009), *Ionospheres: Physics, Plasma Physics, and Chemistry*, vol. 1, second ed., Cambridge, New York.

Semeter, J., T. Butler, C. Heinselman, M. Nicolls, J. Kelly, and D. Hampton (2009), Volumetric imaging of the auroral ionosphere: Initial results from PFISR, *Journal of Atmospheric and Solar-Terrestrial Physics*, *71*, 738–743, doi:10.1016/j.jastp.2008.08.014.

Shepherd, S. G. (2014), Altitude-adjusted corrected geomagnetic coordinates: Definition and functional approximations, *Journal of Geophysical Research: Space Physics*, *119*(9), 7501–7521, doi:10.1002/2014JA020264.

Skolnik, M. I. M. I. (2008), *Radar handbook*, third ed., McGraw-Hill.

Skone, S., and M. De Jong (2000), The impact of geomagnetic substorms on GPS receiver performance, *Earth, Planets and Space*, *52*(11), 1067–1071.

Skone, S., and S. M. Shrestha (1999), Limitations in Gps Positioning Accuracies and Receiver Tracking Performance During Solar Maximum, *1*(2), 129–143.

Skone, S., F. Man, F. Ghafoori, and R. Tiwari (2008), Investigation of scintillation characteristics for high latitude phenomena, *21st International Technical Meeting of the Satellite Division of the Institute of Navigation, ION GNSS 2008*, *3*(September), 1743–1751.

Smith, F. G. (1950), Origin of the Fluctuations of the Intensity of Radio Waves from Galactic Sources, *Nature*, *165*, 422–423.

Spogli, L., L. Alfonsi, G. D. Franceschi, V. Romano, M. H. O. Aquino, and A. Dodson (2009a), Climatology of GNSS ionospheric scintillation at high latitudes, in *American Geophysical Union, Fall Meeting*.

Spogli, L., L. Alfonsi, G. De Franceschi, V. Romano, M. H. O. Aquino, and A. Dodson (2009b), Climatology of GPS ionospheric scintillations over high and mid-latitude European regions, *Annales Geophysicae*, *27*, 3429–3437, doi:10.5194/angeo-27-3429-2009.

Sridhar, M., C. S. Rao, K. P. Raju, and D. V. Ratnam (2014), Ionospheric scintillation monitoring at a low latitude Indian station during geo-magnetic storm, *2014 International Conference on Electronics and Communication Systems (ICECS)*, pp. 1–6, doi:10.1109/ECS.2014.6892778.

Stern, D. P. (2002), The Earth's Magnetic Field in Space.

Stimson, G. W. (1998), *Introduction to Airborne Radar*, 2nd ed., SciTech Publishing, Edison, NJ.

Strickland, D. J., R. R. Meier, J. H. Hecht, and A. B. Christensen (1989), Deducing Composition and Incident Electron Spectra From Ground-Based Auroral Optical Measurements: Theory and Model Results, *Journal of Geophysical Research*, *94*(A10), 13,527–13,539, doi:10.1029/JA094iA10p13553.

Taylor, J. R. (1997), *An Introduction to Error Analysis: The Study of Uncertainties in Physical Measurements*, second ed., 215–222 pp., University Science Books, Sausalito, California.

Thomas, E. G., K. Hosokawa, J. Sakai, J. B. H. Baker, J. M. Ruohoniemi, S. Taguchi, K. Shiokawa, Y. Otsuka, A. J. Coster, J. P. St.-Maurice, and K. A. McWilliams (2015), Multi-instrument, high-resolution imaging of polar cap patch transportation, *Radio Science*, *50*(9), 904–915, doi:10.1002/2015RS005672.

Vallado, D. A. (2007), *Fundamentals of Astrodynamics and Applications*, third ed., Microcosm Press/Springer, Hawthorne, CA/New York, NY.

van der Meeren, C., K. Oksavik, D. Lorentzen, and J. I. Moen (2014), GPS scintillation and irregularities at the front of an ionization tongue in the nightside polar ionosphere, *Journal of Geophysical Research: Space Physics*, *119*, 8624–8636, doi:10.1002/2014JA020114.

van der Meeren, C., K. Oksavik, D. A. Lorentzen, M. T. Rietveld, and L. B. N. Clausen (2015), Severe and localized GNSS scintillation at the poleward edge of the nightside auroral oval during intense substorm aurora, *Journal of Geophysical Research:Space Physics*, *120*, 10,607–10,621, doi:10.1002/2015JA021819.

Verkhoglyadova, O. P., B. T. Tsurutani, A. J. Mannucci, M. G. Mlynczak, L. A. Hunt, L. J. Paxton, and A. Komjathy (2016), Solar wind driving of ionosphere-thermosphere responses in three storms near St. Patrick's Day in 2012, 2013, and 2015, *Journal of Geophysical Research: Space Physics*, *121*, 8900–8923, doi:10.1002/2016JA022883.

Vulcanologia, I. N. d. G. e. (), Geomagnetic Indices.

Warnant, R. R., and E. Pottiaux (2000), The increase of the ionospheric activity as measured by GPS, *Earth Planets Space*, *52*, 1055–1060.

Yeh, K. C., and C.-H. Liu (1982), Radio wave scintillations in the ionosphere, *Proceedings of the IEEE*, *70*(4), 324–360, doi:10.1109/PROC.1982.12313.

Yue, X., W. Wang, J. Lei, A. Burns, Y. Zhang, W. Wan, L. Liu, L. Hu, B. Zhao, and W. S. Schreiner (2016), Long-lasting negative ionospheric storm effects in low and middle latitudes during the recovery phase of the 17 March 2013 geomagnetic storm, *Journal of Geophysical Research: Space Physics*, *121*(9), 9234–9249, doi:10.1002/2016JA022984.

Zhang, Q.-H., B.-C. Zhang, M. Lockwood, H.-Q. Hu, J. Moen, J. M. Ruohoniemi, E. G. Thomas, S.-R. Zhang, H.-G. Yang, R.-Y. Liu, K. A. McWilliams, and J. B. H. Baker (2013), Direct Observations of the Evolution of Polar Cap Ionization Patches, *Science*, *339*(6127), 1597–1600, doi:10.1126/science.1231487.

Appendix A

Constants and Acronyms

A.1 Constants

Table A.1: Physical Constants

Constant	Definition	Value	Units
ϵ_0	Permittivity of free space	8.85×10^{-12}	$C^2/(Nm^2)$
μ_0	Permeability of free space	$4\pi\times10^{-7}$	N/A^2
k_B	Boltzmann's constant	1.38×10^{-23}	J/K
c	Speed of light	2.998×10^{8}	m/s
q	Elementary charge	1.602×10^{-19}	C
m_e	Electron mass	9.109×10^{-31}	kg

A.2 Acronyms

Table A.2: Acronyms used throughout the text.

AACGM	Altitude Adjusted Corrected GeoMagnetic
AC	Alternating Code
ACE	Advanced Composition Explorer
ADU	Analog to Digital Unit
AE	Auroral Electrojet
AEI	Auroral E-Ionization
AL	Auroral Lower
AO	Auroral zOnal
ASI	All Sky Imager(y)
ASTRA	Atmospheric & Space Technology Research Associates
AU	Auroral Upper
C/A	Course/Acquisition

Continued on next page

Acronym	Definition
CASES	Connected Autonomous Space Environment Sensor
CME	Coronal Mass Ejection
CP	Coded Pulse
DASC	Digital All-Sky Camera
DMSP	Defense Meteorological Satellite Program
DST	Disturbance Storm Time
dtc	data taking computer
EAB	Equatorward Auroral Boundary
ECEF	Earth Centered Earth Fixed
EEJ	Eastward ElectroJet
EHF	Extra High Frequency
EMCCD	Electron Multiplying Charge-Coupled Device
ENU	East-North-Up
EUV	Extreme Ultra Violet
FAC	Field Aligned Current
GLONASS	GLObalnaya NAvigazionnaya Sputnikovaya Sistema (*GNSS*)
GNSS	Global Navigation Satellite Systems
GPS	Global Positioning System
HF	High Frequency
IMF	Interplanetary Magnetic Field
INMARSAT	International Maritime Satellite
IPP	Ionospheric Pierce Point
IPP	Inter-Pulse Period
ISR	Incoherent Scatter Radar
LF	Low Frequency
LP	Long Pulse
MF	Medium Frequency
MLT	Magnetic Local Time
MUOS	Mobile User Objective System
NOAA	National Oceanic and Atmospheric Administration
NSIDC	National Snow and Ice Data Center
OML	Order of Merit List
PAB	Poleward Auroral Boundary
PFISR	Poker Flat Incoherent Scatter Radar
PFRR	Poker Flat Research Range
PNT	Position, Navigation and Timing
PRN	Pseudo-Random Noise
RADAR	RAdio Detection And Ranging
SAID	SubAuroral Ion Drifts
SAPS	SubAuroral Polarization Streams
SED	Storm Enhanced Densities
SEM	Satellite EpheMerides
SHF	Super High Frequency
TEC	Total Electron Content
TOI	Tongue Of Ionization

Continued on next page

Acronym	Definition
UFO	UHF Follow-On
UHF	Ultra High Frequency
USA	United States of America
UT	Universal Time
VHF	Very High Frequency
VLF	Very Low Frequency
WEJ	Westward ElectroJet

Appendix B

Coordinate Systems

B.1 Geomagnetic Coordinate Systems

B.1.1 The Earth's Magnetic Field

The Earth's surface magnetic field is measured using the local coordinate system depicted in Figure B.1 The coordinate system has two angles declination, D, and inclination I, which are a measure of deviation from true north and the local horizontal respectively. There are two vectors, $\vec{H}$ and $\vec{F}$, which are the horizontal intensity and total field respectively (*Knipp*, 2011). Combined these produce the X, Y and Z components as shown in Equations B.1 throught B.5 below(*Knipp*, 2011).

$$X = H \cos D \tag{B.1}$$
$$Y = H \sin D \tag{B.2}$$
$$Y = X \tan D \tag{B.3}$$
$$Z = H \tan I \tag{B.4}$$
$$|F|^2 = |B|^2 = |Z|^2 + |H|^2 \tag{B.5}$$

B.1.2 Altitude Adjusted Corrected GeoMagnetic

For geomagnetic latitude and longitude the Altitude Adjusted Corrected GeoMagnetic (AACGM) Coordinate system is sometimes used. This system was developed in order to account for symmetries between northern and southern high-latitude sites in terms of the earth's magnetic dipole

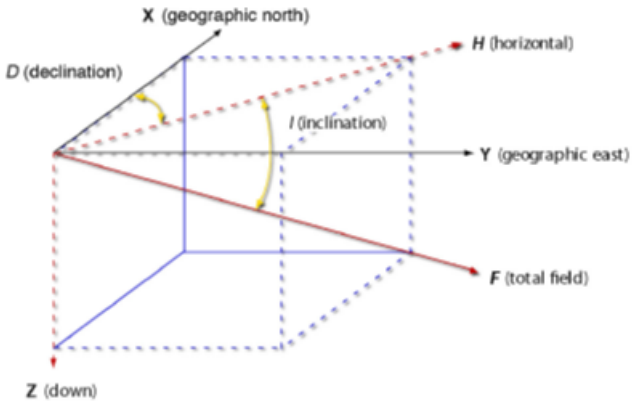

Figure B.1: Coordinates associated with the Earth's surface magnetic field and that are measured by local magnetometers (*Knipp*, 2011).

(*Baker and Wing*, 1989). The AACGM latitude and longitude are taken from the dipole line that intersects the dipole equator after tracing the magnetic field line from a given point on the earth's surface back to the dipole equator. This is depicted graphically in *Shepherd* (2014), Figure 1. Mathematically the dipole lines are calculated from the appropriate international geomagnetic reference field (IGRF) model. As the magnetic field of the earth is not static, these coordinates are dependent not only on the location of a site, but also the time of the site (*Shepherd*, 2014; *Baker and Wing*, 1989). Coefficients for calculating the coordinates, as well as more detailed information can be found in the literature and at `http://superdarn.thayer.dartmouth.edu/aacgm.html`.

B.2 Geographic Coordinate Systems

The Earth-Centered-Earth-Fixed (ECEF) coordinate system, is shown in Figure B.2a. ECEF is centered at the Earth's center of mass. Its z-axis points northward through the *International Reference Pole* (IRP), also known as the *Conventional Terrestrial Pole* (CTP), which is the average position of the north geographic pole between the years 1900 and 1905. The x-axis lies in the plane of the Earth's equator and points to the Greenwich meridian (0^o longitude). The y-axis completes the right-handed coordinate system. Associated angles are the longitude (λ), and the latitude (ϕ). Geodetic latitude (ϕ_{gd}) is used in this system and accounts for the Earth's oblateness. *Bate et al.*

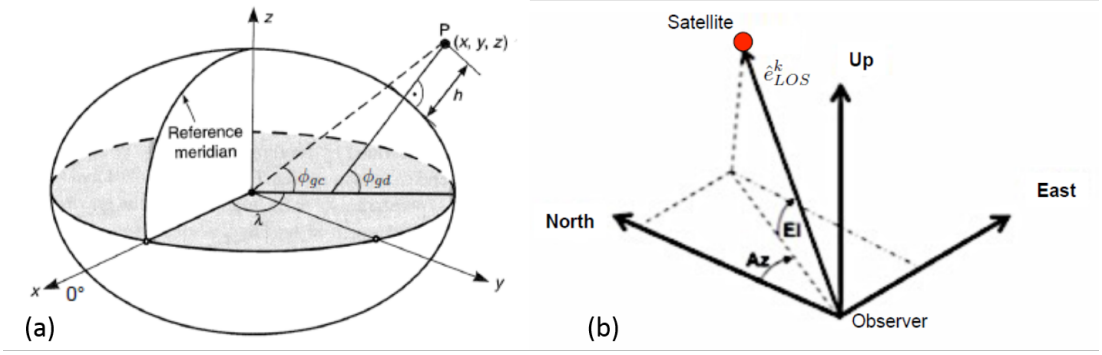

Figure B.2: (a)The Earth-Centered-Earth-Fixed (ECEF) coordinate system with associated angles, annotated. (b) The East-North-Up (ENU) coordinate system with associated angles, azimuth (Az) and elevation(El), annotated. *Bate et al.* (1971); *Misra and Enge* (2006); *Vallado* (2007)

(1971); *Misra and Enge* (2006); *Vallado* (2007)

The East-North-Up (ENU) coordinate system is fixed to the observer location and is shown in Figure B.2b. Self-explanatory are the directions - they point in the cardinal directions East (E, x-axis) and North (N, y-axis), and the right handed-coordinate system is completed with the vertical, or up (U, z-axis), component. Azimuth (Az in the picture) is the angle measured clockwise from North, and elevation (El) is measured up from the horizon. As it is fixed with the observer, this coordinate system changes at every point on the Earth. *Bate et al.* (1971); *Misra and Enge* (2006); *Vallado* (2007)

Appendix C

PFISR Experiment Times

Presented in this chapter is a list of experiment dates, times, beams, and PRNs, along with the figure where the data was presented in this document. These directly correspond to data that are, or eventually will be, shown in the Open Madrigal database found at `http://cedar.openmadrigal.org/`.

Table C.1: PFISR Experiment start and stop times, December 2015.

Day	Start [UT]	Stop [UT]	Figure[a]	Beam	Altiude[a] [km]	PRN
14	11:18:41	11:27:41		64157		12
15	11:14:40	11:23:40		64157		12
16	11:10:49	11:19:34		64157		12
17	11:06:47	11:15:32		64157		12
18	11:02:48	11:11:33		64157		12
19	10:58:44	11:07:44	6.6	64157	137	12
20	10:54:50	11:03:35	6.8	64157	137	12
21	10:50:47	10:59:32	6.9	64157	137	12
22	10:46:47	10:55:47		64157		12

[a] Where applicable.

Table C.2: Experiment times and information for March 2016.

Day	Start [UT]	Stop [UT]	Figure[a]	Beam	Altitude[a] [km]	PRN
14	7:50:00	8:00:00		64157		29
15	7:46:00	7:56:00	7.11	64157	137	29
16	7:42:00	7:52:00		64157		29
17	7:38:00	7:48:00		64157		29

[a] Where applicable.

Continued on next page

Day (Mar)	Start [UT]	Stop [UT]	Figure[a]	Beam	Altitude[a] [km]	PRN
18	7:34:00	7:44:00	7.6	64157	141	29
19	7:30:00	7:40:00		64157		29
20	7:26:00	7:36:00		64157		29
21	7:22:00	7:32:00		64157		29

[a] Where applicable.

Table C.3: Experiment times and information for April 2016.

Day	Start [UT]	Stop [UT]	Figure[a]	Beam	Altitude[a] [km]	PRN
07	9:21:21	9:34:01		63299		21
07	11:40:21	11:52:41		63299		10
07	11:59:01	12:10:21		65315		10
07	12:16:01	12:28:21		65192		10
07	14:00:41	14:13:01		63584		22
08	9:17:21	9:30:01		63299		21
08	9:37:21	9:49:41		65381		21
08	10:35:41	10:48:41		65321		18
08	11:36:21	11:48:41		63299		10
08	11:55:01	12:06:21		65315		10
08	12:12:01	12:24:21		65192		10
08	13:56:41	14:09:01		63584		22
09	9:13:21	9:26:01		63299		21
09	9:33:21	9:45:41		65381		21
09	10:31:41	10:44:41		65321		18
09	11:32:21	11:44:41		63299		10
09	11:51:01	12:02:21		65315		10
09	12:08:01	12:20:21		65192		10
09	13:52:41	14:05:01		63584		22
10	9:09:21	9:22:01		63299		21
10	9:29:21	9:41:41		65381		21
10	10:27:41	10:40:41		65321		18
10	11:28:21	11:40:41		63299		10
10	11:47:01	11:58:21		65315		10
10	12:04:01	12:16:21		65192		10
10	13:48:41	14:01:01		63584		22
11	9:05:21	9:18:01		63299		21
11	9:25:21	9:37:41		65381		21
11	10:23:41	10:36:41		65321		18
11	11:24:21	11:36:41		63299		10
11	11:43:01	11:54:21		65315		10
11	12:00:01	12:12:21		65192		10
11	13:44:41	13:57:01		63584		22

[a] Where applicable.

Continued on next page

Day (Apr)	Start [UT]	Stop [UT]	Figure[a]	Beam	Altitude[a] [km]	PRN
12	9:01:46	9:14:01		63299		21
12	10:19:45	10:32:00		65321		18
12	11:20:51	11:31:51		63299		10
12	11:39:46	11:50:01		65315		10
12	11:56:46	12:08:01	7.9	65192	121	10
12	13:40:46	13:53:01		63584		22
13	8:57:47	9:10:02	7.12	63299	118	21
13	9:17:45	9:29:00		65381		21
13	10:15:45	10:28:00		65321		18
13	11:16:46	11:28:01	7.4	63299	118	10
13	11:35:45	11:46:00		65315		10
13	11:52:43	12:03:58		65192		10
13	13:36:47	13:49:02		63584		22
14	8:53:51	9:05:51		63299		21
14	9:13:44	9:24:59		65381		21
14	10:11:43	10:23:58	7.13	65321	125	18
14	11:12:47	11:24:02		63299		10
14	11:31:46	11:42:01		65315		10
14	13:32:44	13:44:59		63584		22
15	8:49:49	9:01:49		63299		21
15	9:09:45	9:27:00		65381		21
15	10:07:49	10:20:04		65321		18
15	11:08:46	11:20:01		63299		10
15	11:27:44	11:37:59		65315		10
15	11:44:44	11:55:59		65192		10
15	13:28:51	13:40:51		63584		22

[a] Where applicable.

Table C.4: Experiment times and information for October 2016.

Day	Start [UT]	Stop [UT]	Figure[a]	Beam	Altitude[a] [km]	PRN
10	8:30:00	8:50:00		65258		7
11	8:26:00	8:46:00		65258		7
11	10:26:00	10:44:00		63299		28
11	10:48:00	11:06:00		65315		28
12	8:22:00	8:42:00		65258		7
12	10:22:00	10:40:00		63299		28
12	10:44:00	11:02:00		65315		28
13	8:18:00	8:38:00		65258		7
14	8:14:00	8:34:00		65258		7
14	10:14:00	10:32:00		63299		28

[a] Where applicable.

Continued on next page

Day (Oct)	Start [UT]	Stop [UT]	Figure[a]	Beam	Altitude[a] [km]	PRN
14	10:36:00	10:54:00		65315		28
15	8:10:00	8:30:00		65258		7
15	10:10:00	10:28:00		63299		28
15	10:32:00	10:50:00		65315		28
16	8:06:00	8:26:00	8.10	65258		7
17	8:02:00	8:22:00		65258		7
17	10:02:00	10:20:00	8.8	63299		28
17	10:24:00	10:42:00		65315		28
18	7:58:00	8:18:00		65258		7
18	9:58:00	10:16:00		63299		28
18	10:20:00	10:38:00		65315		28
19	7:54:00	8:14:00		65258		7
20	7:50:00	8:10:00		65258		7
20	9:50:00	10:08:00		63299		28
20	10:12:00	10:30:00		65315		28
21	7:46:00	8:06:00		65258		7
21	9:46:00	10:04:00		63299		28
21	10:08:00	10:26:00		65315		28
22	7:42:00	8:02:00		65258		7
22	9:42:00	10:00:00		63299		28
22	10:04:00	10:22:00		65315		28
23	7:38:00	7:58:00		65258		7
23	9:38:00	9:56:00		63299		28
23	10:00:00	10:18:00		65315		28
24	7:34:00	7:54:00		65258		7
24	9:34:00	9:52:00		63299		28
24	9:56:00	10:14:00		65315		28
25	7:30:00	7:50:00		65258		7
25	9:30:00	9:48:00		63299		28
25	9:52:00	10:10:00		65315		28
26	7:26:00	7:46:00		65258		7
26	9:26:00	9:44:00		63299		28
26	9:48:00	10:06:00		65315		28
27	7:22:00	7:42:00		65258		7
27	9:22:00	9:40:00		63299		28
27	9:44:00	10:02:00		65315		28
28	7:18:00	7:38:00		65258		7
28	9:18:00	9:36:00	8.9	63299		28
28	9:40:00	9:58:00		65315		28
29	7:14:00	7:34:00	8.6	65258		7
29	9:14:00	9:32:00		63299		28
29	9:36:00	9:54:00		65315		28
30	7:10:00	7:30:00		65258		7
30	9:10:00	9:28:00		63299		28

[a] Where applicable.

Continued on next page

Day (Oct)	Start [UT]	Stop [UT]	Figure[a]	Beam	Altitude[a] [km]	PRN
30	9:32:00	9:50:00		65315		28
31	7:06:00	7:26:00		65258		7
31	9:06:00	9:24:00		63299		28
31	9:28:00	9:46:00		65315		28

[a] Where applicable.

Table C.5: Experiment times and information for November 2016.

Day	Start [UT]	Stop [UT]	Figure[a]	Beam	Altitude[a] [km]	PRN
01	11:12:00	11:35:00	8.11	65258		17
01	11:40:00	12:10:00		65384		19
03	11:04:00	11:27:00		65258		17
03	11:32:00	12:02:00		65384		19
04	11:00:00	11:23:00		65258		17
04	11:28:00	11:58:00		65384		19
05	11:24:00	11:54:00		65384		19
06	10:52:00	11:15:00		65258		17
06	11:20:00	11:50:00		65384		19
07	10:48:00	11:11:00		65258		17
07	11:16:00	11:46:00		65384		19
08	10:44:00	11:07:00		65258		17
08	11:12:00	11:42:00		65384		19
09	10:40:00	11:03:00		65258		17
09	11:08:00	11:38:00		65384		19
11	10:32:00	10:55:00		65258		17
12	10:28:00	10:51:00		65258		17
12	10:56:00	11:26:00		65384		19
14	10:20:00	10:43:00		65258		17
14	10:48:00	11:18:00		65384		19
15	10:16:00	10:39:00		65258		17
15	10:44:00	11:14:00		65384		19
15	12:12:00	12:42:00		64157		12
16	12:08:00	12:38:00		64157		12
17	10:08:00	10:31:00		65258		17
17	10:36:00	11:06:00		65384		19
17	12:04:00	12:34:00		64157		12
18	10:04:00	10:27:00		65258		17
18	10:32:00	11:02:00		65384		19
18	12:00:00	12:30:00		64157		12
20	9:56:00	10:19:00		65258		17
20	10:24:00	10:54:00		65384		19

[a] Where applicable.

Continued on next page

Day (Nov)	Start [UT]	Stop [UT]	Figure[a]	Beam	Altitude[a] [km]	PRN
20	11:52:00	12:22:00		64157		12
26	10:00:00	10:30:00		65384		19
26	11:28:00	11:58:00		64157		12
27	9:56:00	10:26:00		65384		19
27	11:24:00	11:54:00		64157		12
28	9:52:00	10:22:00		65384		19
28	11:20:00	11:50:00		64157		12

[a] Where applicable.